Development of Magnetic Models to Assess Transformers' Susceptibility to Geomagnetic Disturbances

A thesis submitted to The University of Manchester for the degree of Doctor of Philosophy in the Faculty of Science and Engineering

2018

Yufan Ni

School of Electrical and Electronic Engineering

Contents

List of Figures

List of Tables

List of Abbreviations

ATP/EMTP	Alternative Transient Program/Electromagnetic Transients Program
AC	Alternating Current
CGO	Conventional Grain-oriented Steels
DC	Direct Current
EMF	Electromotive Force
EMR	Ministry of Energy, Mines and Resources
FEM	Finite Element Method
GIC	Geomagnetically Induced Current
GMD	Geomagnetic Disturbances
GSU	Generator Step-up
HGO	High Permeability Grain-oriented Steels
HV	High Voltage
LV	Low Voltage
MMF	Magnetomotive Force
NG	National Grid Electricity Transmission plc
NOAA	National Oceanic and Atmospheric Administration
RMS	Root Mean Square
SESC	Space Environmental Service Centre
SSN	Smoothed Sunspot Number
STC	Saturable Transformer Component
SVC	Static VAR Compensator

List of Symbols

Symbol	Meaning	Unit
$[A]$	Cross-section area	(m^2)
A_{aurora}	Vector potential of aurora-zone current	(A)
$[A_a, A_b, A_c]$	Cross-section area of main limbs	(m^2)
$[A_l]$	Cross-section area of side limbs $[A_{l1}, A_{l2}]$	(m^2)
$[A_o]$	Cross-section area of oil gaps $[A_{o1}, A_{o2}, A_{o3}, A_{o4}, A_{o5}]$	(m^2)
$[A_t]$	Cross-section area of tank paths $[A_{t1}, A_{t2}, A_{t3}, A_{t4}, A_{t5}]$	(m^2)
$[A_y]$	Cross-section area of yokes $[A_{y1}, A_{y2}, A_{y3}, A_{y4}]$	(m^2)
B	Magnetic flux density	(T)
$[B_a, B_b, B_c]$	Flux density at main limbs	(T)
$[B_l]$	Flux density at side limbs $[B_{l1}, B_{l2}]$	(T)
$[B_o]$	Flux density at oil gaps $[B_{o1}, B_{o2}, B_{o3}, B_{o4}, B_{o5}]$	(T)
$[B_t]$	Flux density at tank paths$[B_{t1}, B_{t2}, B_{t3}, B_{t4}, B_{t5}]$	(T)
$[B_y]$	Flux density at yokes $[B_{y1}, B_{y2}, B_{y3}, B_{y4}]$	(T)
d	Thickness of laminations	(m)
E	Electric field	(V/km)
E_E	Electric field in eastward	(V/km)
E_N	Electric field in northward	(V/km)
E_1	Electromotive force on HV side	(V)
f	Frequency	(Hz)
G^{-1}	Inverse admittance	(Ω^{-1})
H	Magnetic field intensity	(A/m)
$[H_a, H_b, H_c]$	Magnetic field intensity at main limbs	(A/m)
$[H_l]$	Magnetic field intensity at side limbs $[H_{l1}, H_{l2}]$	(A/m)
$[H_o]$	Magnetic field intensity at oil gaps $[H_{o1}, H_{o2}, H_{o3}, H_{o4}, H_{o5}]$	(A/m)
$[H_t]$	Magnetic field intensity at tank paths	(A/m)

	$[H_{t1}, H_{t2}, H_{t3}, H_{t4}, H_{t5}]$	
$[H_y]$	Magnetic field intensity at yokes $[H_{y1}, H_{y2}, H_{y3}, H_{y4}]$	(A/m)
I_c	Current supplying core loss	(A)
I_{dc}	DC current	(A)
I_{hv}	HV winding current	(A)
$I_{lv}{}'$	LV winding current referred to HV side	(A)
I_m	Magnetising current	(A)
$I_{tv}{}'$	TV winding current referred to HV side	(A)
I_0	No-load current	(A)
K_p	Geomagnetic intensity	NA
k	Reluctance	(A/Wb)
k_a	Anomalous loss constant	NA
k_h	Hysteresis loss constant	NA
k_{loss}	Coefficient of reactive power loss	MVar/A
L_{hv}	HV winding inductance	(mH)
$L_{lv}{}'$	LV winding inductance referred to HV side	(mH)
L_m	Core inductance	(mH)
$L_{tv}{}'$	TV winding inductance referred to HV side	(mH)
l	Distance between substations	(km)
$[l_a, B_b, B_c]$	Length of main limbs	(m)
l_E	Distance between substations in eastward	(km)
$[l_l]$	Length of side limbs $[l_{l1}, l_{l2}]$	(m)
l_{loop}	Magnetic path length for all loops	(m)
l_N	Distance between substations in northward	(km)
$[l_o]$	Length of oil gaps $[l_{o1}, l_{o2}, l_{o3}, l_{o4}, l_{o5}]$	(m)
$[l_t]$	Length of tank paths $[l_{t1}, l_{t2}, l_{t3}, l_{t4}, l_{t5}]$	(m)
$[l_y]$	Length of yokes $[l_{y1}, l_{y2}, l_{y3}, l_{y4}]$	(m)
N	Winding turn number	NA
n	Stein exponent	NA
$P_{anomalous}$	Anomalous loss	(W/kg)

P_{core}	Core loss	(W/kg)
P_{eddy}	Eddy current loss	(W/kg)
$P_{hysteresis}$	Hysteresis loss	(W/kg)
R_c	Core resistance	(Ω)
R_{hv}	HV winding resistance	(Ω)
$R_{lv}{}'$	LV winding resistance referred to HV side	(Ω)
$R_{tv}{}'$	TV winding resistance referred to HV side	(Ω)
S_b	Power base	(VA)
V_{AC}	AC voltage source matrix	(V)
V_{DC}	DC voltage source	(V)
V_{hv}	HV wide terminal voltage	(V)
V_{LL}	Rated line voltage	(kV)
$V_{lv}{}'$	LV wide terminal voltage referred to HV side	(V)
ΔV	Voltage drop between substations	(V)
Z_{load}	Load impedance	(Ω)
$\boldsymbol{\mathcal{R}}$	Reluctance	(A/Wb)
Φ	Magnetic flux	(Wb)
$\Phi_{initial}$	Limb initial magnetic flux	(Wb)
Φ_{peak}	Magnitude of limb nominal flux	(Wb)
ρ	Steel lamination resistivity	(Ω·m)

Abstract

During the peak years of solar activity, the magnetic field held by the solar wind has an impact on the Earth's magnetic field and induce an electric field on the Earth's surface. The Geomagnetically Induced Current (GIC) is generated between two neutral points of transformers. The GIC can do severe harm to a power system, including to its transformers. The worst GIC event caused a power system blackout for several hours in Quebec in 1989.

The research aims to build a representative model of core saturation and carry out simulation studies to understand the performance of transformer cores in the high flux density region. This in turn helps to identify the design features that need to be taken into account when assessing the capability of a transformer to withstand over-excitation.

ATP is a kind of user-maintained software so it allows self-developed code to be added into the software package. The results simulated by the existing ATP models are inaccurate compared to the measured results. In addition, the existing models cannot provide flux distribution results, so it is difficult to understand the process of how the core is pushed into the deep saturation region by DC offset.

A new model is developed to include the equivalent electric and magnetic circuit representations, taking flux leakage, in particular, into consideration. The flux leakage paths are composed of the oil gaps and tank in series. This model is validated by the consistency shown between the measured and simulated HV winding currents of a 5-limb transformer. The peaks of magnetising currents are identified with the peaks of magnetic flux which saturate the core.

The model can identify the design features, such as the core structure, dimension of flux leakage paths and winding impedance that need to be taken into account when assessing the capability of a transformer to withstand over-excitation. A 3-limb model and a 5-limb core model are built to assess the susceptibility to GIC for different core types in high flux density region. The delta winding plays a role in holding the 3^{rd} harmonics and unbalanced current generated by core saturation, and in delaying the core saturation. Lastly, Transformers are simulated under realistic GIC waveforms, for situations with and without load.

The new model is expected to be coded into ATP to conduct a GIC study for a power system.

Declaration

I declare that no portion of the work referred to in the thesis has been submitted in support of an application for another degree or qualification of this or any other university or other institute of learning.

Copyright Statement

Acknowledgement

First of all, I would like to express sincere gratitude to Professor Zhongdong Wang. My PhD research has greatly benefited from her patience, motivation and immense knowledge. She has been my supervisor since I was an undergraduate student at the University of Manchester. She has given me extensive personal and professional guidance and taught me a great deal about both scientific research and life in general. It is a great honour for me to have such an outstanding and kind supervisor

My sincere thanks also go to my co-supervisor Professor Peter Crossley and Dr Qiang Liu. I would particularly like to thank Dr Liu for his selfless support and valuable advice.

I am especially indebted to Professor Paul Jarman and Dr Philip Anderson for their technical support and invaluable suggestions.

I greatly appreciate the financial scholarship from National Grid and the University of Manchester that has supported my PhD research.

I am very fortunate to have spent four memorable years at the University of Manchester to complete my PhD study. My lovely colleagues in the transformer research group have made me feel at home. I would like to express my heartfelt gratitude to them for their company and friendship.

Last but not least, I would like to thank my parents and my grandparents whose love and guidance are with me in whatever I pursue. Their unconditional support and encouragement always drive me forward

Chapter 1: Introduction

1.1 Background

1.1.1 Transformer

Transformers are widely used in electrical power systems to step up or step down voltages between different parts of the network. The voltage step up by a transformer contributes to a reduction in power losses in transmission lines, while step-down transformers convert electric energy to a voltage level accessible by both industrial and household users.

A transformer is electrical-magnetic equipment, involving two closely magnetically coupled windings as the electrical circuit where electrical energy is transmitted from one voltage level to the other. An ideal transformer will neither store nor dissipate energy [1]. Perfect magnetic coupling contributes to infinite core magnetic permeability and zero magnetomotive force. In reality, the core steel permeability cannot be infinite, and therefore it is inevitable that a magnetomotive force is produced, and hence a magnetising current too. A transformer is designed in such a way that the magnetising current normally remains at a low level when a transformer is operated at its nominal voltage and frequency. This is achieved by utilising the electrical steel's B-H curve characteristics and selecting the nominal operating point around the knee point. It should be also noted that core permeability has increased significantly since the invention of power transformers with the application of optimized electrical steel material.

Transformers are mainly divided into two categories: shell type and core type, depending on the physical arrangement of the magnetic and electrical circuits. Core type transformers are more popular worldwide than shell type transformers which exist in several countries, such as the United States and Japan. Three-phase transformers are more economical than three single-phase transformer banks due to the shared magnetic circuit, the shared tank and other design features, so the majority of power transformers are three-phase transformers. Transformer banks tend to be used for high power rating transformers (e.g. generator transformer exceeding 600 MVA) or due to transportation restrictions or reliability considerations.

Historically, power transformers, just like the power systems, were developed gradually from low voltage to high voltage rating. For core type transformers, 3-limb transformers are almost the only type used in distribution systems. With the increase in power rating, 5-limb core has become an optional design for large transmission transformers, since this type of design reduces the height of core and tank, making it easier to transport. However, 3-limb transformers without outer limbs save core material and reduce core losses as compared to 5-limb transformers.

Auto-connected transformer design aims to save winding and core material and to reduce the transformer size and the construction cost [2]; therefore, it is popular in transmission interbus transformers, where the voltage ratio between two windings is generally less than 3:1. Installation of a delta winding is recommended in three-phase auto-transformers because it can provide a low impedance path for triplen harmonics, so that the system is potentially less impacted by the harmonics. In addition, a delta winding holds the unbalanced current produced by the unbalance load. Lastly, tertiary windings are also sometimes used to connect reactors at some substations to control voltage as well as reactive power.

1.1.2 UK power system network

Figure 1-1 shows the schematic diagram of the UK network [3]. The transmission network in the UK normally refers to the part operating above 132 kV, while the maximum voltage level in the UK network is 400 kV. In England and Whales, the transmission network is operated by National Grid Electricity Transmission plc [4], while Scottish Power Transmission Limited operates the network for southern Scotland and Scottish Hydro Electric Transmission plc for northern Scotland and the Scottish islands groups [5].

According to the National Grid database in 2010, among the 950 transmission transformers, the percentages of the 400/275 kV, 400/132 kV, 275/132 kV and 275/33 kV transformers were 14.8%, 27.8%, 33.8% and 6.8% respectively. According to the data in National Grid Electricity Ten Year Statement, the 400/275 kV and 275/132 kV transformers are mainly located in densely-populated areas or near to large industrial loads, such as London, Birmingham, Cardiff, Manchester, Edinburgh and Glasgow. Naturally, a higher nominal voltage is associated with a higher power rating of a power

transformer. Among the 400/275 kV transformers, 43.6% of the transformers are specified at the nominal power rating of 750 MVA, while the transformers rated at 1000 MVA and 500 MVA account for 30.7% and 16.4%. The remaining 400/275 kV transformers operate at 900 MVA, 950 MVA and 1100 MVA. 95.1% of the 400/132 kV transformers are specified at a nominal power rating of 240 MVA, while the remaining 400/132 kV transformers have a power rating of 120 MVA, 220 MVA, 276 MVA or 288 MVA. Moreover, the power rating of the 275 kV (HV side) transformers will normally not exceed 240 MVA. Regarding the 275/132 kV transformers, the majority of the them operate at 120 MVA, 180 MVA and 240 MVA (19.0%, 53.6% and 24.9%), while the power rating of the rest are 150 MVA and 155 MVA.

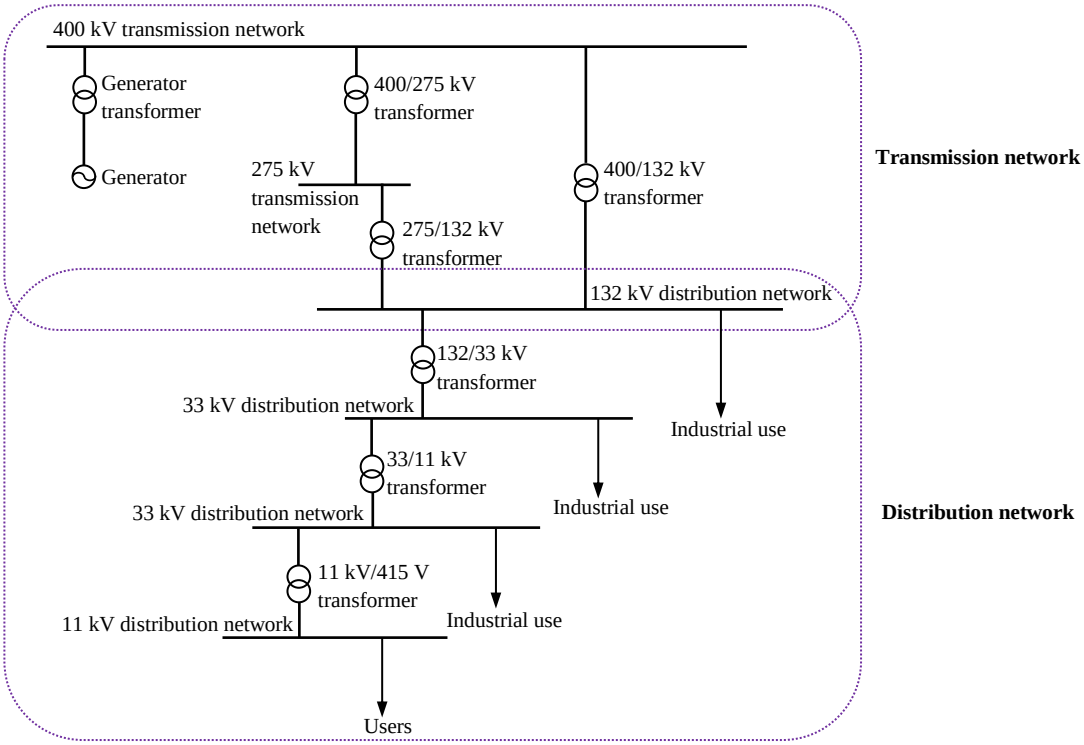

Figure 1-1: Schematic diagram of typical UK network [3].

All the NG transmission interbus transformers (400/275 kV, 400/132 kV and 275/132 kV) are auto (Y-a-d) connected, as the turn ratios between the HV side and LV side of the NG transmission transformers are lower than or close to 3:1, so autotransformers are more economical than two-winding transformers. In addition, 13 kV delta connected tertiary windings are broadly used in NG transmission interbus transformers.

In the National Grid database, a simple statistic shows that the number of 3-limb transformers is greater than 5-limb transformers. Taking 32 interbus transformers in the Southwest England NG Peninsula system as an example, 16 transformers are of the 3-limb core type and 8 transformers are of the 5-limb core type. For the other 8 transformers, it is difficult to ascertain their core types due to a lack of evidence.

Using the transformer data in the National Grid Database, Figure 1-2 displays the magnetising currents of the National Grid 400/275/13 kV 1000 MVA transformers manufactured before the 1990s and after the 1990s respectively. The statistics indicate that the transformers produced after the 1990s normally have lower magnetising currents (on average 0.013% *pu*) than the ones built before the 1990s (on average 0.053% *pu*). In addition, an imbalance is found in the three-phase magnetising currents from the same family, which could be caused by the unsymmetrical design of three-phase flux paths for three-phase transformers.

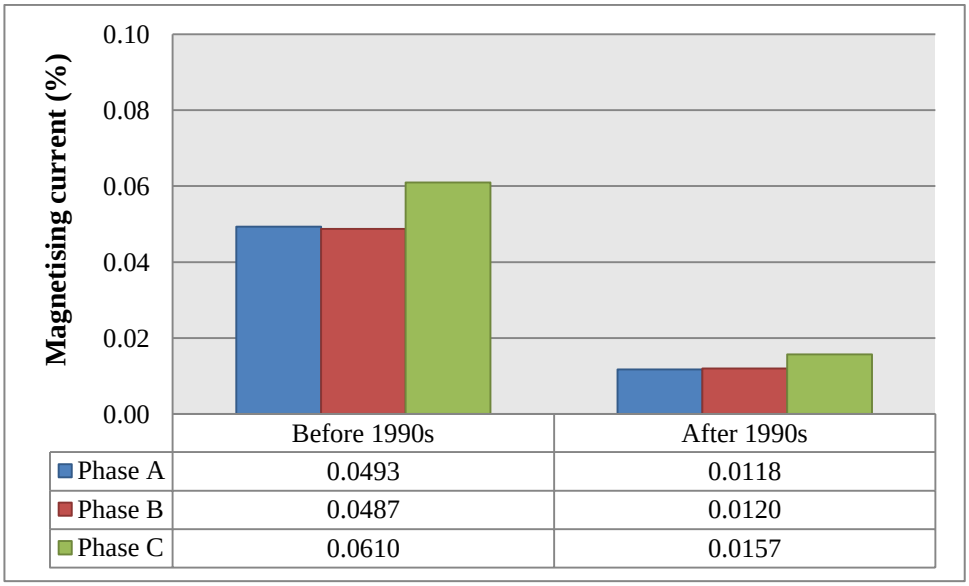

	Before 1990s	After 1990s
Phase A	0.0493	0.0118
Phase B	0.0487	0.0120
Phase C	0.0610	0.0157

Figure 1-2: Magnetising current for 400/275/13 kV 1000 MVA transformers manufactured before the 1990s and after the 1990s in National Grid system.

The reason why transformers have low magnetising currents under normal operation is that the core operating point is always limited below the knee point, which expects to retain the core linearity to avoid excessive harmonic currents and power losses. However, if a transformer suffers external interference, such as inrush current, ferroresonance or Geomagnetically Induced Current (GIC), the transformer core will work beyond the knee point, and the magnetising current will be severely distorted.

A brief description of the three power system transient phenomena, which involve the core characteristics and which are normally hidden in a normal 50 Hz operation, is given here. Firstly, inrush current is caused by the non-linear characteristics of transformer core. When a transformer is energized, the transformer core tends to enter the non-linear operation area due to the switching angle and the residual flux retained in the core since last switch-off, and hence an excessive magnetising current containing rich harmonics and great power losses will be produced [6]. The magnitude of the inrush current could be several times the rated current [7]. Secondly, ferroresonance refers to the non-linear resonance resulting from the saturated core inductances and the system capacitance during the opening switch operation. After system capacitance is cancelled with core inductance, the energy stored in the series capacitance leads to an overvoltage problem, which pushes the transformer core into the saturation area, and hence rich harmonics and excessive power losses are generated. The magnitude of the overvoltage could reach 1.5 times the nominal voltage [8]. Lastly, during solar storms, Geomagnetically Induced Current will be generated on the Earth's surface, which pushes the transformer core into the saturation area gradually [9]. In conclusion, transformers are vulnerable in these abnormal situations, so it is necessary to investigate these issues to provide a comprehensive protection for transformers.

1.1.3 Geomagnetically Induced Current

Generally, Geomagnetic Disturbance (GMD) is defined as a disturbance in the Earth's atmosphere caused by the interaction of the earth magnetic field and the space weather, mainly referred to as solar activity [10]. Normally, a solar activity's cycle is approximately 11 years. During the peak years of solar activity, large quantities of high energy particles are emitted from the sun, as shown in Figure 1-3, and reach the Earth in two or three days. Secondly, the plasmas in the magnetosphere and the ionosphere are charged by the high energy particles, so the movements of the plasmas become more dramatic, forming a circulating current in the magnetosphere and ionosphere. The circulating current in the atmosphere (magnetosphere and ionosphere) then induces a quasi-DC current with a frequency typically ranging from 0.01 Hz to 0.5 Hz [11] on the Earth's surface, which is called Geomagnetically Induced Current (GIC) [10, 12].

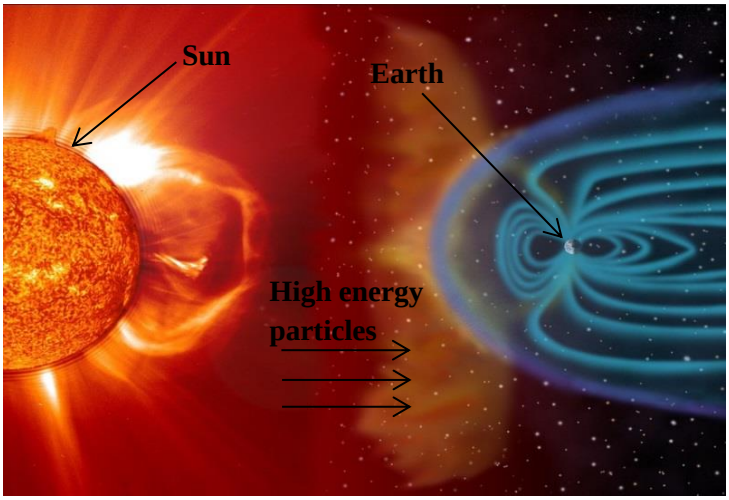

Figure 1-3: Effects of geomagnetic disturbances on Earth's surface magnetic field [10].

GIC has great effects on power systems [13, 14]. During GMD events, the quasi-DC current flows into the power system via the neutral points of two transformers. The neutral quasi-DC current tends to push the transformer core into the deep saturation area, which drives the magnetising currents to a higher magnitude containing greater harmonics. The excessive current and the deep saturated core lead to an increase in copper losses, core losses and reactive power consumption. Meanwhile, the excessive voltage drop across the transformer with the saturated core leads to low power delivery efficiency [14].

The abnormality of a transformer's operation during GMD events will also influence the other equipment in the power system, such as generators, relays and shunt capacitor banks. Generally speaking, generators are not exposed to GIC directly due to the D-Y winding connection for step-up transformers. However, the voltage drop and the excessive harmonics produced by the GIC effects in transmission systems could influence generators and result in excessive heating and stimulation of mechanical vibrations in generators [15]. During severe GIC events, abnormal relay tripping could be triggered by high peak currents or rich harmonics in the power system. Moreover, the overcurrent relays, which aim to protect the shunt capacitor banks, are susceptible to harmonic currents because capacitors show low impedance to harmonics [16].

For this reason, it is necessary to understand how GIC will impact transformers and power systems, so that precautions can be taken before equipment in power system is

damaged. This thesis mainly focuses on the impacts of Geomagnetically Induced Current on power transformers.

Solar activity also has negative effects on other man-made systems, such as communication systems and pipelines.

Firstly, the radiation produced by the solar storms causes the ionization of the ionosphere, which changes the radio wave propagation behaviour in the atmosphere [15]. In addition, the high energy particles generated during solar storms perturb the Earth's magnetic field, which results in disturbances to wireline facilities [15]. In 1847, Varley observed the telegraph line was interrupted by Earth's current in Great Britain [9].

Secondly, GIC can accelerate the corrosion of steel-made pipelines in that they contain high pressure liquid or gas. To prevent corrosion of the pipelines due to chemicals or other factors, the pipeline always has a protection coat. In case the coat is damaged for natural reasons, a negative potential is supplied along the pipeline to provide protection from corrosion. However, during a GMD event, this protection could be less effective, making the pipelines susceptible to corrosion and the reducing their service life [17]. For example, if a pipeline is exposed to a 0.5 V potential change (Equivalent to Kp=5, Kp is the GMD strength and will be introduced in Chapter 3) due to a GMD event, the corrosion rate will be 0.06 and 0.152 mm/year for GMD periods of 0.01 and 1 h respectively, both exceeding 0.025 mm/year which is generally considered as the acceptable corrosion rate [18].

1.1.4 Motivations

Currently, the research on GIC studies can be divided into two categories: experiments and simulations. Experiments can provide reliable results; however, due to the fact that only a limited number of transformers can be used in GIC tests and limited tests can be undertaken for each tested transformer, experimental measurements cannot be widely used in investigating GIC issues. In order to overcome the weakness of the measurements, the simulations, both for large scale power systems and for individual transformers, have become popular in the GIC investigation.

A laboratory test was undertaken by Matti Lahtinen in Toivila, Finland [13]. Two 400/120/21 kV transformers were set in parallel with an old rotating welding machine

connected between their neutral points to feed DC injection up to 200 A. 38 thermocouples and 16 optical fibre-base temperature sensors are inserted into one of the transformers to record the temperature data. In addition, Nobuo Takasu and Tetsuo Oshi compared the performances of the transformers with three different core types under AC+DC input in 1993 [19]. In the test, the transformers are shrunk to 1/20 of the original dimension, and the metallic tanks are not added to the transformers. On the one hand, these experiments can provide the test results for specific transformers under particular voltage supply, but the measurement results cannot be applied to the other transformers. Therefore, it is essential to undertake simulation work to investigate various types of transformers. On the other hand, the accuracy of the simulated results can be verified by comparing them with the measured results.

The large scale power system simulation applies the full-node linear resistance methods [20, 21], which simplifies the transformers, transmission lines and neutral grounds into linear resistances. In this way, the transient process is ignored to save computation time and improve simulation efficiency. However, the reactive power losses generated by a GIC event at each transformer need to be estimated by empirical equations that rely simply on the terminal DC voltage and the GIC level, where the empirical parameters remain to be tested and verified for all the occasions [22, 23]. In this way, this method can efficiently evaluate the GIC severities for transformers at different locations, which could help the operators analyse the GIC risks and plan for precautions. It is apparent that this method sacrifices the accuracy of simulation results because the transient characteristics of the equipment in power systems are completely ignored. The disadvantage is of course that the results are still a controversial issue for this method because the precision of the simulation relies heavily on the parameters used in the empirical equations. In addition, this method cannot distinguish the GIC's impacts on different types of transformers.

Taking the nonlinear characteristics into consideration, researchers develop various transformer models to conduct GIC transient simulations for individual transformers or small-scale power systems [24-26]. If the transformer saturation characteristics are properly described, the transient simulation will provide a better view on how the DC neutral input saturates the transformers. EMTP is one of the software platforms, which enables the transient simulation by using either internal or external transformer models.

EMTP or EMTDC is the suite of commercialised software [7, 27], which includes EMTP-RV, MT-EMTP, EMTP-ATP and PSCAD-EMTDC. EMTP-ATP (referred as ATP) is a kind of user-maintained software so it allows self-developed code to be added into the software package. There are three transformer models widely used in ATP: the BCTRAN model, the Saturable Transformer Component (STC) model and the Hybrid model. The Hybrid model is applicable in simulating GMD event because it considers both the core topology and the core non-linear saturation effects [28], although the simulation results cannot exactly match the measurement results.

Currently, there is no accurate model for the magnetic circuit of a transformer under high induction conditions, limiting the conclusions about the relationship between GIC and the level of damage a transformer may receive from a GIC. This inability appears to be general throughout the transformer industry and represents a significant gap in knowledge. This gap does not seem significant to transformer manufacturers, because during routine factory tests, the core of a transformer is operated below or around the maximum operational flux limits. For a utility, conservative assumptions about core saturation have therefore had to be adopted. Failure to accurately analyse these system events induced core saturation conditions leads either to excessive capital cost in increasing core dimensions, or potential failure in service due to the heating of the magnetic circuit and other steel parts in the transformers or reactors.

In conclusion, it is necessary to build a new model that enables the performance of transformer cores to be modelled in the high flux density region, by producing a viable algorithm to represent transformer magnetic circuits under deep saturation. Also, the model enables the identification of design features that must be considered when assessing the capability of a transformer to withstand over-excitation.

1.2 Objective of research

This project aims to investigate the GIC's impacts on transformers and power systems in transient. The work can be divided two steps. Firstly, the accuracy of the existing ATP models for simulating core half-cycle saturation effect will be verified. However, none of the existing models can accurately present the core saturation effect and key information. For example, the flux distribution and the magnetising current are unavailable in ATP, so it seems a new model is required for the GIC transient study. Secondly, a new transformer, which combines the electric circuit and magnetic circuit, is built for a better

understanding of transformer performance under AC and DC excitation because it is accessible to the flux distribution and magnetising current. By implementing this model, various transformer design features can be identified when assessing the transformer vulnerability to GIC. Furthermore, this model can be applied to investigate the impacts of the practical GIC injection and the load characteristics to the simulation results. Thirdly, a GIC study is conducted for part of the UK transmission system by using ATP, and the new model is expected to replace the ATP model in the future study. The specific objectives are listed as follows:

- Examination of the existing transient simulation capability
  - Understand the working principles of the existing ATP models and validate the models under AC+DC input. The simulation results are to be compared with the measurement results.
- Development and application of the new transformer model
  - Develop a new model, which incorporates the equivalent electric and magnetic circuits and takes the core saturation effect and the tank leakage flux paths into consideration. The model will be validated under AC+DC input by comparing it to the measurement results.
  - Understand the transient process before the transformer reaches the steady state. Analyse the flux distribution in the core and the tank corresponding to the magnetising current in the steady state, which makes it possible to evaluate the most vulnerable part in a transformer that suffers overheating problems.
  - Identify the designing features that need to be taken into account when assessing the capability of a transformer to withstand over-excitation, such as the various dimensions of the core and tank, the core type, the winding type (including a delta winding or not) and the winding impedance.
  - Investigate the performance of transformers under different practical time varying neutral injections.
  - Explore the impacts of the load characteristics on transformer operation state under neutral DC injection.
- GIC simulation for part of the UK transmission system.
  - Build part of the UK transmission system in ATP by using the existing ATP models. Give a case study to investigate the influences from the real GMD injection on the power system.

- In the future, the newly developed model is expected to be coded into ATP to conduct a power system level study for GIC.

1.3 Outline of the thesis

This thesis contains eight chapters which are briefly summarized below:

Chapter 1: Introduction

This chapter gives a general introduction of transformers and Geomagnetically Induced Current. The objectives and the scope of the research are also presented.

Chapter 2: Overview of Transformer Core and Winding

This chapter introduces the key components of transformers: the core and the winding. Firstly, the transformer core is described in terms of the core configuration, core steel and core losses. Secondly, the winding structures widely used in the UK transformers are discussed. Lastly, this chapter explains the transformer equivalent circuit.

Chapter 3: Review Literatures in Research Area of Geomagnetically Induced Current

This chapter provides an overview of Geomagnetically induced current from several aspects. First of all, it introduces how GIC is produced on the Earth's surface and the factors determining the GIC level. Following that, the GIC's impacts on power system networks together with the historical GIC events are given. Then the GIC mitigation devices are reviewed. Researchers have carried out GIC investigation through either experiments or simulations in recent years. This chapter conducts two categories of simulation methods, which are the non-linear model simulation for individual transformers and the equivalent full-node simplified resistance method for system level study, together with three experimental cases, aiding to validate the modelling accuracy of the transformer models.

Chapter 4: Development of Transformer Models for GIC Simulation Studies

This chapter firstly compares the results measured by Finnish Grid and the simulation results generated by three ATP models, which are the BCTRAN model, the STC model and the Hybrid model, to determine their suitability for GIC simulation. Secondly, a new

model that represents the equivalent electric and magnetic circuits of a transformer is developed based on material properties and physical dimension parameters. The model has an advantage that the leakage flux paths composed of the tank and oil gaps are adequately modelled. A 400 kV 5-limb transformer is given as an example to validate the model under AC+DC input. Many parameters interested such as the flux distribution, the current flow insides a delta connected winding and magnetising current can be extracted to aid the understanding.

Chapter 5: Sensitivity Study for New Model Parameters

This chapter conducts sensitivity studies on the structure of the transformer core, parameters of the tank-oil paths and winding impedance, since it is necessary to understand how sensitive each parameter used in the simulation impacts the results. The feature of the core structure looks into the cross-sectional area ratio between the yokes and limbs. The features that make up the tank-oil paths are the equivalent tank length, the tank area, the oil gap length and the oil gap area. The last part concentrates on the resistance and leakage inductance of the HV winding and the delta winding.

Chapter 6: Comparison of 3-limb and 5-limb Transformer under Neutral DC Offset

This chapter firstly introduces the newly developed 3-limb model and compares the simulation results of a 3-limb transformer and a 5-limb transformer under AC+DC input to prove the conventional concept that 5-limb transformers are more vulnerable to a neutral DC offset. Then the 3-limb transformer and 5-limb transformer are supplied by various levels of neutral DC offset to investigate the relationship between the induced current amplitude and the neutral DC offset level. Lastly, the 3-limb transformer is also simulated by the Hybrid model, and the simulation results are compared to those of the new model.

Chapter 7: Five-limb Transformer Modelling under Realistic GIC Waveforms

In this chapter, the GIC transient simulation studies are conducted on the 5-limb transformer, as 5-limb transformers are more susceptible to the neutral DC input than 3-limb transformers. This chapter starts with a study carried out to show the effect of tertiary delta-connected winding on time constant of saturation. It is followed by the

simulation of the 5-limb model under practical neutral time varying injection. Lastly, the 5-limb transformer simulation results with full load situation are also provided.

Chapter 8: Conclusion and Future Work

This chapter summarises the key findings in the research and gives recommendations for future research.

Chapter 2: Overview of Transformer Core and Winding

2.1 Overview

Proposed in 1831, transformers are based on Faraday's law of induction to transfer electrical energy among the electrical circuits operating at different voltage levels [29]. Nowadays, transformers are widely used for the transmission and distribution of electrical energy in power systems [30, 31]. Magnetic core and windings are the most important parts of a power transformer. Magnetic core, made of ferromagnetic steel with high magnetic permeability, enables electric energy to be transferred through electromagnetic induction and windings are made of insulated conductors which carry current. In this chapter, magnetic core and windings will be discussed separately from configurations, material and losses.

2.2 Transformer core

2.2.1 Core configuration

When transformers are classified by core configuration, there are mainly two types of transformers, shell type and core type, used in the industry. Shell type transformers are not widely manufactured and installed in the world, except North America and Japan [3]. ABB produces shell type transformers designed for high power rating and voltage usage (Unit rating up to 1300 MVA, Primary voltage up to 765 kV, single or three phases) [32]. Core type transformers are widely used in the UK and many other parts of the world. For this reason, this PhD research will mainly focus on core type transformers.

In terms of core type transformers, both three-phase transformers and three single-phase transformer banks are broadly applied in power systems. However, if both types are available, the industry prefers to use a three-phase transformer because the financial cost of a bank of three single-phase transformers is about 1.5 times that of a three-phase transformer for the same MVA [33]. In the NG transmission system in England and Wales, most of the transmission transformers are three-phase transformers. However, single-phase transformers are still important in power systems, as they can be used at the end of the distribution system in a rural area far from an urban area with low demand [34].

In addition, three single-phase transformer banks are used as generator transformers. This design is convenient for transportation (three single-phase transformer can be transported separately) and minimises the impact of faults [3].

There are two core forms for a three-phase transformer: 3-limb core and 5-limb core as displayed in Figure 2-1 (a) and (b). For a 3-limb core, the yoke cross-sectional area is often equal to that of the limb. Three-phase 3-limb core transformers are almost the unique arrangement in the UK transmission transformers because a 3-limb core saves the core material as well as reducing core losses. In the case of a 5-limb core, since the side limbs can provide valid flux paths, the cross-sectional area of the yokes can be reduced by about 50%, so the core height can also be reduced. For this reason, 5-limb cores are usually applied in generator transformers or large interbus transformers because the heights of 5-limb transformers are normally lower than the counterpart of 3-limb transformers. The lower height of a transformer will make transportation more convenient.

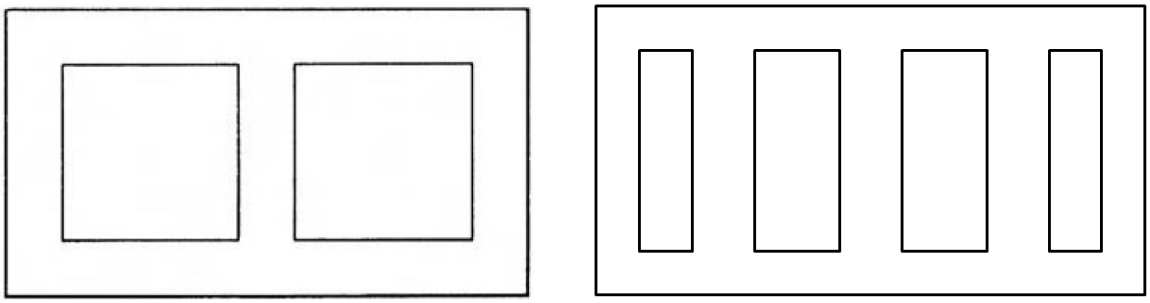

(a) **(b)**

Figure 2-1: Three-phase transformer core forms: (a) 3-limb (b) 5-limb.

Figure 2-2 (a), (b) and (c) displays three single-phase transformer core forms. For a single-phase transformer, the flux return paths must be provided. As shown in Figure 2-2 (a), both limbs are wound, and the cross-sectional area of the yoke equals that of the limbs, so the yoke is high for this core form. On the other hand, for the 3-limb core form as presented in Figure 2-2 (b), only the middle limb is wound by the windings and the two side limbs provide the flux return paths, so the height of the yoke is reduced. In terms of the cruciform as shown in Figure 2-2 (c), only the middle limb is wound, so the height of the yoke further decreases due to the four side limbs. The single-phase distribution transformers at the rural end always have both-wound 2-limb core, since it is not necessary to reduce the height of a distribution transformer.

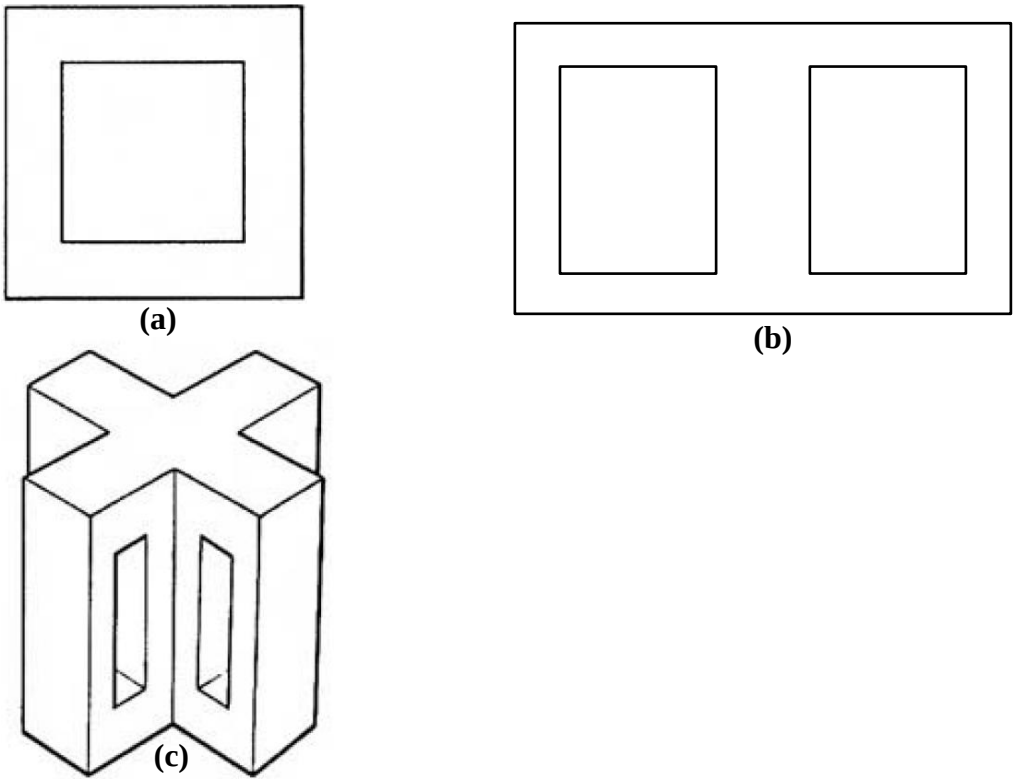

Figure 2-2: Single-phase transformer core forms: (a) 2-limb (b) 3-limb (c) cruciform.

2.2.2 Core steel

The magnetic core is made of electrical steel laminates with a high magnetic permeability, so that the magnetic flux produced by the transformer primary winding current is confined in the magnetic core and induces currents in the other windings.

Nowadays, the cores of power transformers are normally built with grain-oriented electric steels which include conventional grain-oriented steels (CGO) and high permeability grain-oriented steels (HGO). CGO and HGO were first produced in 1939 and 1965 respectively [3]. The manufacturing procedures of the CGO are different from those of the HGO. The grain growth of CGO and HGO are inhibited by MnS and AIN (aluminium nitride) respectively. In addition, one of the cold-rolling steps is eliminated by adding the melted aluminium and using AIN to produce HGO. Generally, HGO steels have a higher grain size, lower misalignment and lower power losses. The typical core losses under 50 Hz for CGO are 1.25 W/kg, while for HGO is 1 W/kg at 1.7 T. Normally, the average grain size of CGO and HGO are 5 mm and 10 mm in length respectively, which leads to the fact that CGO is widely used in the distribution transformers with

small size while HGO is applied in the transmission transformers with long limbs and yokes. CGO and HGO have different non-linear characteristics in the saturation region. That is why the material property is one of the key parameters for modelling GIC phenomena. The selection of the grain-oriented material is assessed by total ownership cost (TOC) which takes into account transformer capital cost, the cost of core losses and winding losses during its lifetime [35].

The magnetising characteristics of the core steel are normally described by B-H curves. Figure 2-3 shows a typical B-H curve for the CGO core steel M140-27S (in EN 10107 Classification-2005: Capital letter M for electrical steel; 140 is the number of 100 times the specified value of maximum specific total loss at 50 Hz 1.7 T; 27 represents 100 times of nominal thickness of the product in millimetres; S for conventional grain oriented products), which is also called 27M4 in BS 601 Classification (CGRO Grade is M4 in power loss and the thickness is 0.27 mm). Its knee point is about 1.75 T. Normally, transformer core operates in the high induction area below the knee point, for example, the generator transformer usually works at maximum flux density B_m of 1.70 T under nominal AC voltage Moreover, the transmission transformers work in a range from 1.60 T to 1.65 T, while distribution transformers work around 1.50 T due to large fluctuations of loads [3]. If the core operates beyond the knee point, the permeability of the core material will decrease rapidly, which will further result in serious distortion in the magnetising current. Meanwhile, the core losses grow significantly due to the high magnitude of flux densities.

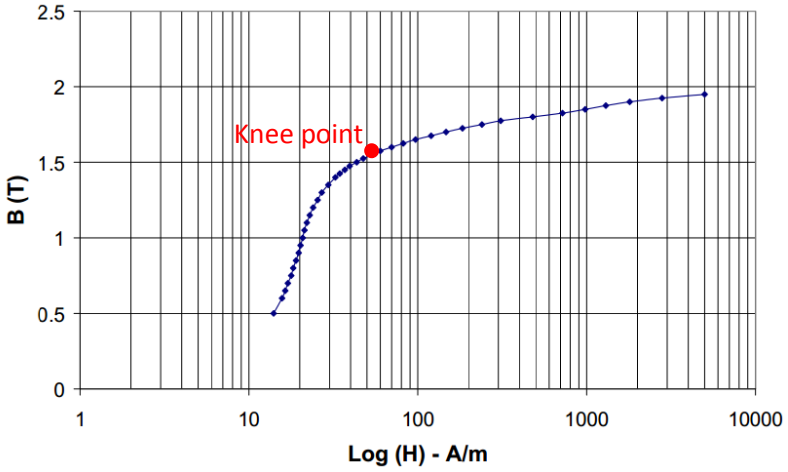

Figure 2-3: Typical B-H curve and knee point of core material M140-27S [36].

2.2.3 Core losses

Researchers have tried to find ways to reduce the core losses. The core losses of the modern grain-oriented material decrease to 0.4 W/kg nowadays from 15 W/kg at a very early stage [37]. As can be seen in Eq. 2.1, core losses consist of three parts: hysteresis loss, eddy current loss and anomalous loss.

$$P_{core} = P_{hysteresis} + P_{eddy} + P_{anomalous} \tag{2.1}$$

- **Hysteresis loss**

The ferromagnetic substance consists of many small regions of domains that are arranged in a random manner in a natural state, which means that the magnetic field is zero inside the material. When a Magnetic Motive Force (MMF) is provided externally, the dipoles will change their direction; however, some of them cannot change their direction immediately after the MMF is removed or reversed. This causes the angle of the magnetising current to lag to the magnetic field and explains how the hysteresis loop is generated. Figure 2-4 shows the B-H curve in the ferromagnetic substance when the AC input is provided. The area of the B-H loop represents the hysteresis loss.

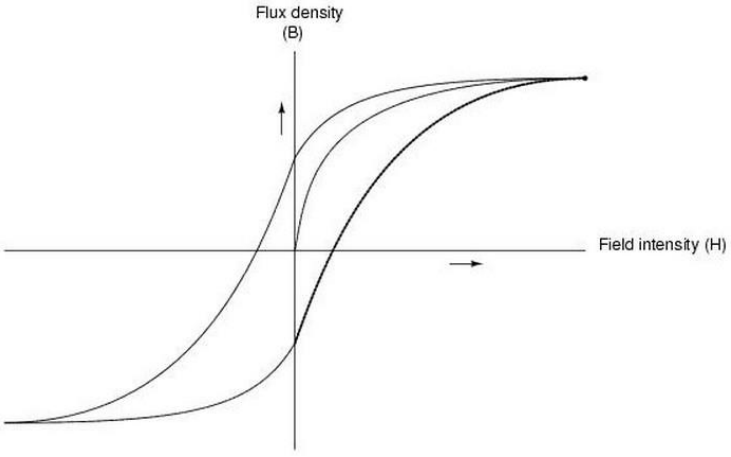

Figure 2-4: Hysteresis loop [38].

Eq. 2.2 shows the method to estimate the hysteresis loss.

$$P_{hysteresis} = k_h f B^n \tag{2.2}$$

where

$P_{hysteresis}$ Hysteresis loss (W/kg)

k_h	Constant relating to material characteristics
f	Frequency (Hz)
B	Peak AC flux density (T)

n is known as Steinmetz exponent always taken as 1.6 with low flux densities, but the constant changes with AC flux density.

- **Eddy current loss**

Eddy current loss is generated by the circulating current which is induced by the changing magnetic field in the metallic structures, including the transformer core, the tank and the windings. For this reason, transformer cores are laminated in order to decrease eddy current loss by reducing the lamination area as shown in Figure 2-5. Moreover, the core steel is expected to have high resistivity to reduce eddy current loss.

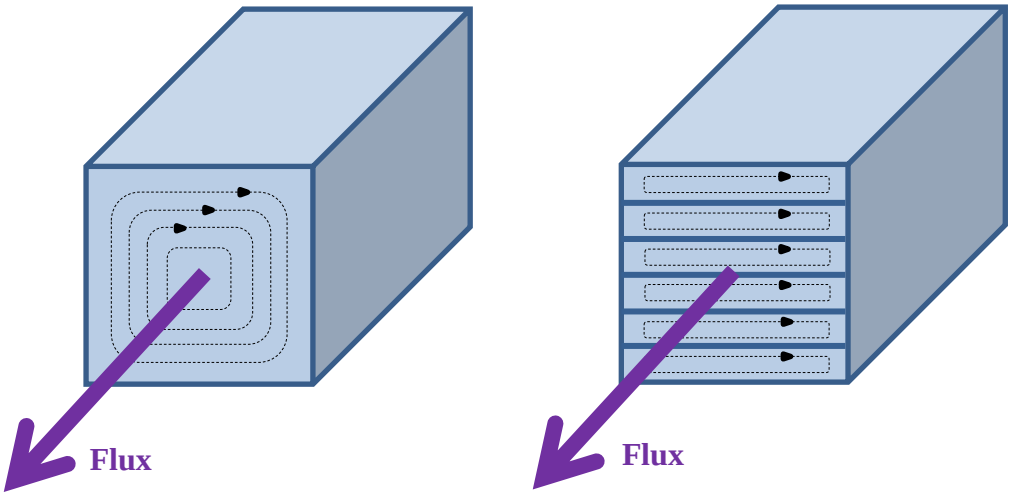

Figure 2-5: Schematic diagram of eddy current without lamination and with lamination.

Eq.2.3 shows the equation to estimate the eddy current loss.

$$P_{eddy} = \frac{\pi^2}{6\rho} d^2 f^2 B^2 \tag{2.3}$$

where

P_{eddy}	Eddy current loss (W/kg)
ρ	Steel lamination resistivity (Ω·m)

d	Thickness of laminations (m)
f	Frequency (Hz)
B	AC flux density magnitude (T)

For the purpose of reducing eddy current loss, transformer cores are laminated by joining insulated grain-oriented steels together [39, 40]. As can be seen in Figure 2-6, core laminations form a circular shape viewed from a cross-section. The core is usually built in a circular shape to better fit the windings and save space; the lamination can always fill up 93% to 95% of ideal circular space. The lamination steps of distribution transformers can be seven. However, for large generator transformers, the lamination steps will exceed eleven [3].

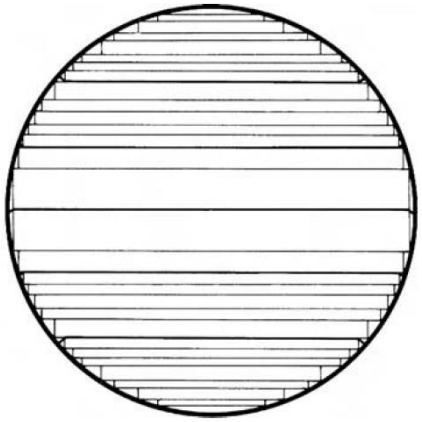

Figure 2-6: Transformer core lamination with 14 steps [3].

- **Anomalous loss**

Anomalous loss refers to the difference between the measured core losses and the calculated sum of the hysteresis loss and the eddy current loss. Anomalous loss could occupy up to 50% of the total core losses in a modern transformer. Anomalous loss is produced due to domain walls of grain-oriented steel [41]. A domain wall is a transition area between different domains in a piece of magnetic steel, and the power losses consumed in the domain walls are referred to as anomalous loss. A laser scribing technique can increase the number of domain walls and decrease the space between them, and the anomalous loss is thus reduced [3].

Anomalous loss can be calculated according to Eq. 2.4 [42], which is simplified as

$$P_{anomalous} = k_a f^{1.5} {B_p}^{1.5} \quad (2.4)$$

where

$P_{anomalous}$	Anomalous loss (W/kg)
k_a	Constant relating to material characteristics
f	Frequency (Hz)
B	Peak AC flux density (T)

2.3 Transformer winding

2.3.1 Winding type

Several types of winding commonly used nowadays are introduced in [43]. The Pancake shape winding is only used in shell form transformers, while the layer type winding, the helical type winding and the disc type winding are always used in core type transformers. The layer type windings are usually used in distribution transformers, while the helical type and the disc type are adopted for transmission transformers. The high voltage winding are usually the disc type, or otherwise the high voltage windings have to use a multi-layer method to ensure the axial height of the HV winding and the LV winding matching to each other.

2.3.2 Winding connection

For 3-phase transformers, there are mainly three types of winding arrangements: Star connection, Delta connection and Zig-Zag Interconnection arrangement. A two-winding transformer usually contains at least one delta winding to eliminate triplen harmonics. In the UK 400 kV and 275 kV grid systems, three-winding transformers with a tertiary delta winding are widely implemented. With a tertiary winding, the fault level on the LV side will be reduced. If the magnetising current contains high harmonics due to core saturation, the triplen harmonic currents can flow either in the tertiary winding or directly to the ground though the neutral point of Star connection [44]. In addition, for a two-winding transformer, the LV winding is always placed as the inner winding.

2.3.3 Winding material

Copper is mostly used as the material to build winding conductors due to its good conductivity as well as mechanical strength. Although aluminium is lighter and more

economical compared with copper, it needs a wider cross-section area to carry the same current. In addition, due to its low density, the mechanical strength is weaker than copper in high temperature region.

2.3.4 Winding losses

Owing to the current heating effect, the generation of power losses in windings, which are also referred to as copper losses, cannot be avoided. Copper losses are undesirable for transformer efficiency, so transformer designers try to confine them within an acceptable range [45]. There are several common ways to reduce copper losses.

- Increase conductivity of the winding conductor
- Reduce the number of winding turns
- Increase cross-sectional area of the conductor

2.4 Transformer equivalent circuit

The core and winding of a transformer can be simplified into an equivalent circuit for the convenience of analysis. The equivalent electric circuit of a two-winding transformer is shown in Figure 2-7. The transformer core, which is assumed to be a branch in parallel with the LV winding impedance and load impedance, is simplified as an equivalent resistance to represent core loss and an inductance for core inductance. The LV winding impedance and the load impedance are referred to the HV side.

According to Faraday's Law as shown in Eq. 2.5, the induced magnetic flux is linked to electromotive force on the core, which lays the foundation for a new model that will investigate transformer deep saturation performances, combining the equivalent electrical circuit and the core magnetic characteristics in this thesis.

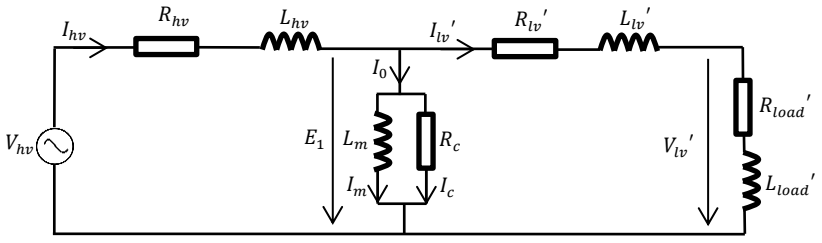

Figure 2-7: Equivalent circuit for two winding transformer.

where

V_{hv}	HV side terminal voltage (V)
$V_{lv}{}'$	LV side terminal voltage referred to HV side (V)
E_1	Electromotive force induced on HV side (V)
I_{hv}	HV winding current (A)
$I_{lv}{}'$	LV winding current referred to HV side (A)
I_m	Magnetising current (A)
I_c	Current supplying core loss (A)
I_0	No-load current (A)
R_{hv}	HV winding resistance (Ω)
L_{hv}	HV winding leakage inductance (mH)
$R_{lv}{}'$	LV winding resistance referred to HV side (Ω)
$L_{lv}{}'$	LV winding leakage inductance referred to HV side (mH)
R_c	Core resistance (Ω)
L_m	Core inductance (mH)

$$E = -N \cdot \frac{d\Phi}{dt} \tag{2.5}$$

where

E	Electromotive force (V)
N	Winding turn number
Φ	Flux (Wb)

Chapter 3: Review Literatures in Research Area of Geomagnetically Induced Current

3.1 GIC information

As introduced in Chapter 1, Geomagnetically Induced Current is formed on the Earth's surface due to complex space weather, such as solar activity, and it can interrupt the normal operation of power systems. Figure 3-1 explains the processes in which GIC is generated near the Earth's surface [46]. Firstly, the Coronal Mass Ejection (CME) is produced from the solar flare, and then the large quantities of high energy particles travel towards the Earth in typically 14 hours to 96 hours [47]. The charged particles interact with the Earth's magnetic field in the atmosphere and lead to a circulating current in the magnetosphere and the ionosphere. Secondly, the circulating current in the atmosphere further induces the electrical field on the Earth's surface which is controlled by Maxwell Equations and Earth condition parameters. Lastly, the induced electric field contributes to the formation of GIC flowing in the loop, consisting of the transmission lines, transformers and neutrals. The details for each step will be introduced in the following sections.

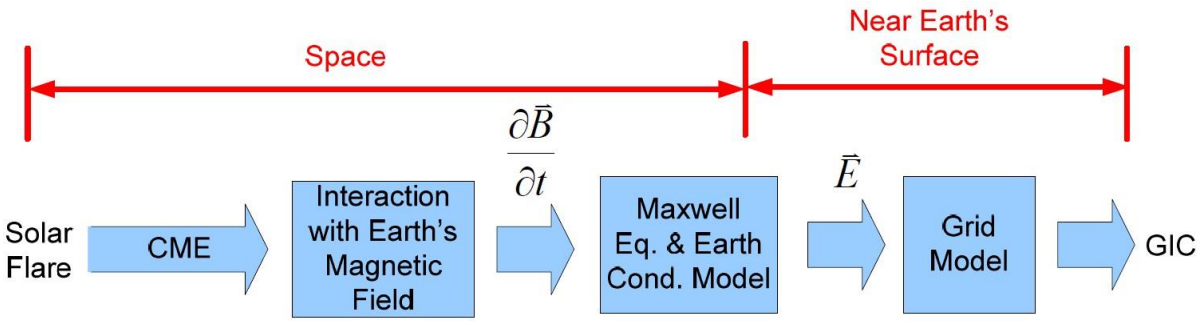

Figure 3-1: GIC generation process from Space to the surface of the Earth [46].

3.1.1 Solar activity cycle and strength

The space weather, including the conditions which vary over time in the solar system, such as solar wind, has an effect on the man-made systems on the Earth's surface [48]. The space weather changes due to the intensity of solar activity. Generally, each solar cycle lasts about 11 years [49].

Solar Cycle, which was firstly proposed by Samuel Heinrich Schwabe in 1843 [50], refers to the duration between the years that have minimum sunspot counts. Table 3-1 lists the duration and the strength of the solar cycles from Cycle 18 to Cycle 24. The cycle period ranges from 9.7 to 11.7 years. Each cycle starts and ends with the minimum Smoothed Sunspot Number (SSN), and the solar activity peak year (maximum SSN year) usually appears in 3-4 years after a cycle begins.

Table 3-1: List of solar cycles from Cycle 18 to Cycle 24 [49].

Cycle	Started	Finished	Duration (years)	Maximum (monthly Smoothed Sunspot Number (SSN))	Minimum (monthly SSN (at the end of cycle))	Spotless days (end of cycle)
Solar cycle 18	1944 January	1954 February	10.2	151.8 (May 1947)	3.4	446
Solar cycle 19	1954 February	1964 October	10.5	201.3 (Mar 1958)	9.6	227
Solar cycle 20	1964 October	1976 May	11.7	110.6 (Nov 1968)	12.2	272
Solar cycle 21	1976 May	1986 March	10.3	164.5 (Dec 1979)	12.3	273
Solar cycle 22	1986 March	1996 June	9.7	158.5 (Jul 1989)	8.0	309
Solar cycle 23	1996 June	2008 January	11.7	120.8 (Mar 2000)	1.7	821
Solar cycle 24	2008 January					

For the purpose of monitoring and scaling the solar activity strength, observatories around the world measure the Earth's horizontal magnetic field every three hours, and the average values are obtained from the measured data from observatories worldwide. *Kp* index is applied to quantify the magnetic field in the geomagnetic storm forecast and alert system [51]. Normally, *Kp* index scales the geomagnetic intensity from 0 (less than 5 nT) to 9 (more than 500 nT) [51]. The higher value represents the stronger geomagnetic storm

and consequently there is a higher risk of power networks suffering more severe damage. A geomagnetic storm will occur when *Kp* index equals or exceeds 5, and *Kp*=7 means a strong storm. Table 3-2 shows the relative geomagnetic disturbance scale for specific *Kp* index and the average number of days for each *Kp* index in one solar cycle. In each cycle, a total of 64 days with *Kp* index equals or exceeds 8, which can have a potentially significant impact on man-made systems, such as power system networks.

Table 3-2: Scale of geomagnetic disturbance, relevant *Kp* index and average days for each scale at each solar cycle.

Scale	Physical measure	Average frequency
G5 (extreme)	K_p=9	4 days/cycle
G4 (severe)	K_p=8	60 days/cycle
G3 (strong)	K_p=7	130 days/cycle
G2 (moderate)	K_p=6	360 days/cycle
G1 (minor)	K_p=5	900 days/cycle

A recent solar activity with the *Kp* index of 8 occurred on 18th March, 22nd June and 23rd June in 2015 according to the data provided by the US National Oceanic and Atmospheric Administration. In 2018, the *Kp* index reaches 6 on 18th March and 20th April. Historically, the most severe GIC event happened in Quebec, Canada in 1989 (peak year in Cycle 22) [52-54]. During the GIC event, the *Kp* value reached 9 on 13th March and 14th March, which is the highest level in the scale [55].

Figure 3-2 shows the number of events and the *Kp* index recorded by the National Oceanic and Atmospheric Administration's Space Environmental Service Centre (SESC) in the US and the Ministry of Energy, Mines and Resources (EMR) in Canada on March 13, 1989 [52]. The X-axis represents the North American Eastern Standard Time hour (EST, UTC-5), and the left Y-axis and the right Y-axis are the number of events and the *Kp* index respectively. In addition, it can be observed that the *Kp* index remained over 6 for the whole day. Even worse, the *Kp* index exceeds 8 for 11 hours. At 9 pm North

American Eastern Standard Time (EST, UTC-5), the power system experienced over 50 events that include Static VAR Compensator tripping, transformer breakdowns and relay fault operations.

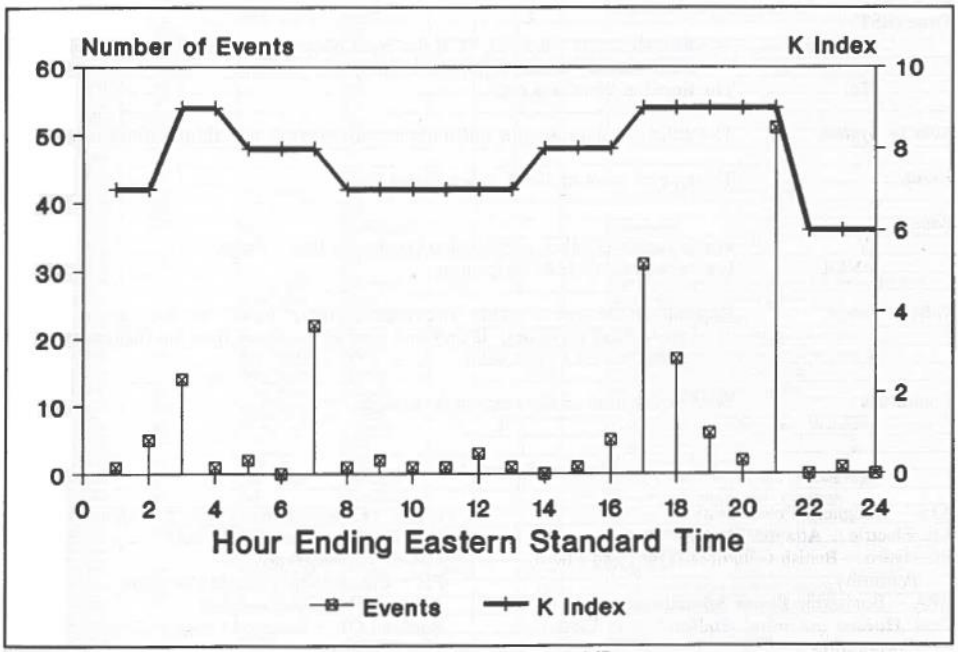

Figure 3-2: Number of power system events and *Kp* index on March 13, 1989 [52].

3.1.2 Induced electric field on earth

During solar storms, high energy particles are emitted to the Earth. The moving particles interact with the magnetic field in the Earth's atmosphere, and then an aurora current will be produced above the Earth [15]. Following that, the aurora current further contributes to the changes in electric field on the Earth's surface [56].

A classic method was proposed by McNish. The electric field induced on the Earth's surface is derived as in Eq. 3.1 [57].

$$\boldsymbol{E} = -\frac{\partial \boldsymbol{A}_{aurora}}{\partial t} \tag{3.1}$$

where

$\boldsymbol{A}_{aurora}$	Vector potential of aurora-zone current (A)
$\boldsymbol{E}$	Induced electric field on Earth's surface (V/km)

3.1.3 GIC on earth

The electric field will further produce a voltage drop between the adjacent transformers. As shown in Figure 3-3, GIC flows into the power system via the transformer neutral points [15]. The *YNd* transformer on the left side is connected with the *YNa* autotransformer on the right side by the transmission lines, so that GIC can flow in a loop consisting of the transformer neutrals, the transformer windings and the transmission lines. In addition, the grounded autotransformer is connected to the rest of the network, so that GIC can flow into the networks operating at lower voltage levels. It is necessary to mention that the delta winding of the *YNd* transformer is inaccessible for DC current after the system reaches a steady state.

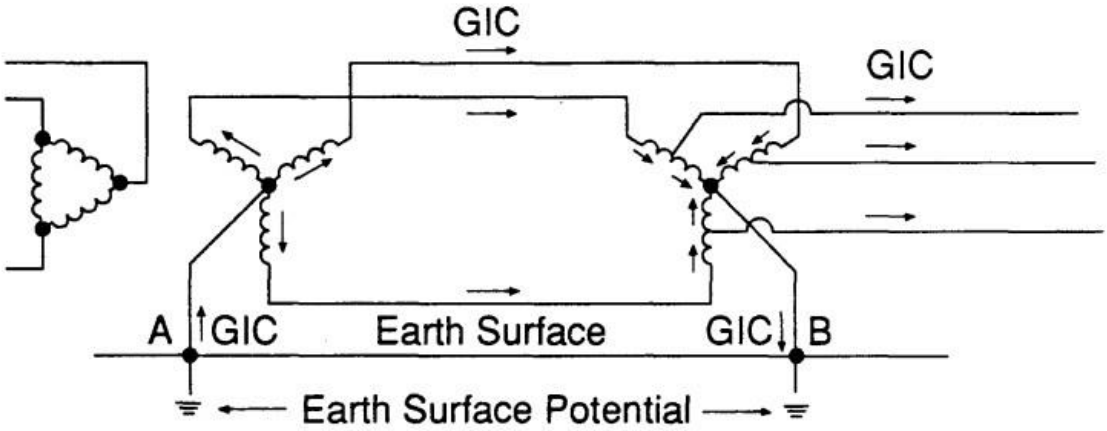

Figure 3-3: GIC flow in power system network [15].

As shown in Figure 3-4, the DC flux induced by the continuous DC injection will gradually lift the flux density up and push the core into the saturation area beyond the knee point [58]. Consequently, the magnetising current is significantly distorted in the half cycle where the flux density exceeds the knee point.

Once the Earth's electric field induced by the aurora current is estimated according to practical cases, the voltage drop between the adjacent transformers can be calculated as in Eq. 3.2.

$$\Delta V = \vec{E} \cdot \vec{l} \tag{3.2}$$

where

ΔV	Voltage drop between substations (V)
$\vec{E}$	Induced electric field on Earth (V/km)
$\vec{l}$	Distance between transformers (km)

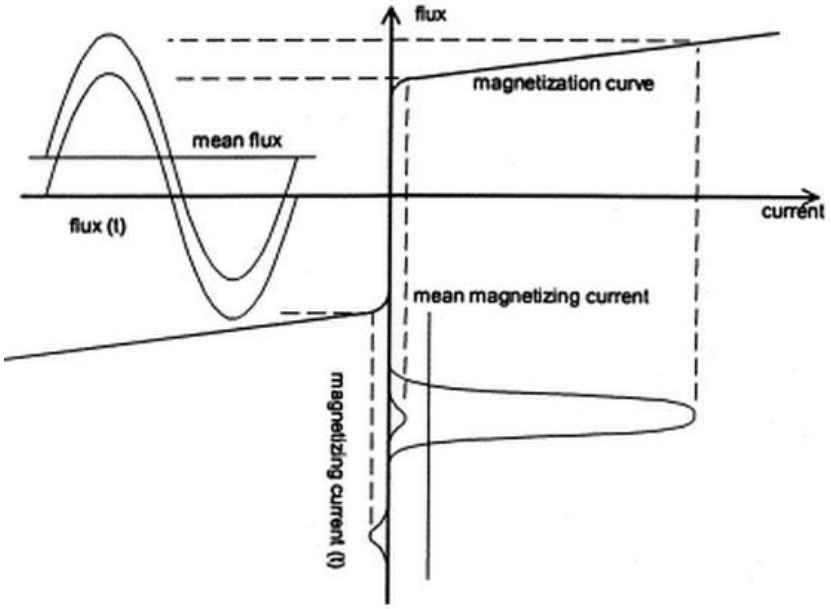

Figure 3-4: Magnetising current due to flux saturation [58].

3.2 Factors impact on GIC magnitude

The magnitudes of GIC can be affected by two categories of factors, which are geophysical factors and engineering factors [16, 44, 46]. As indicated in Figure 3-5, in terms of the geophysical factors, the GIC level is subject to the strength of GMD event, latitude of substations, soil resistivity and coastal effect. In terms of the engineering factors, the GIC level is associated with the power system direction, the distance between substations, electrical resistance and transformer designs including core and windings.

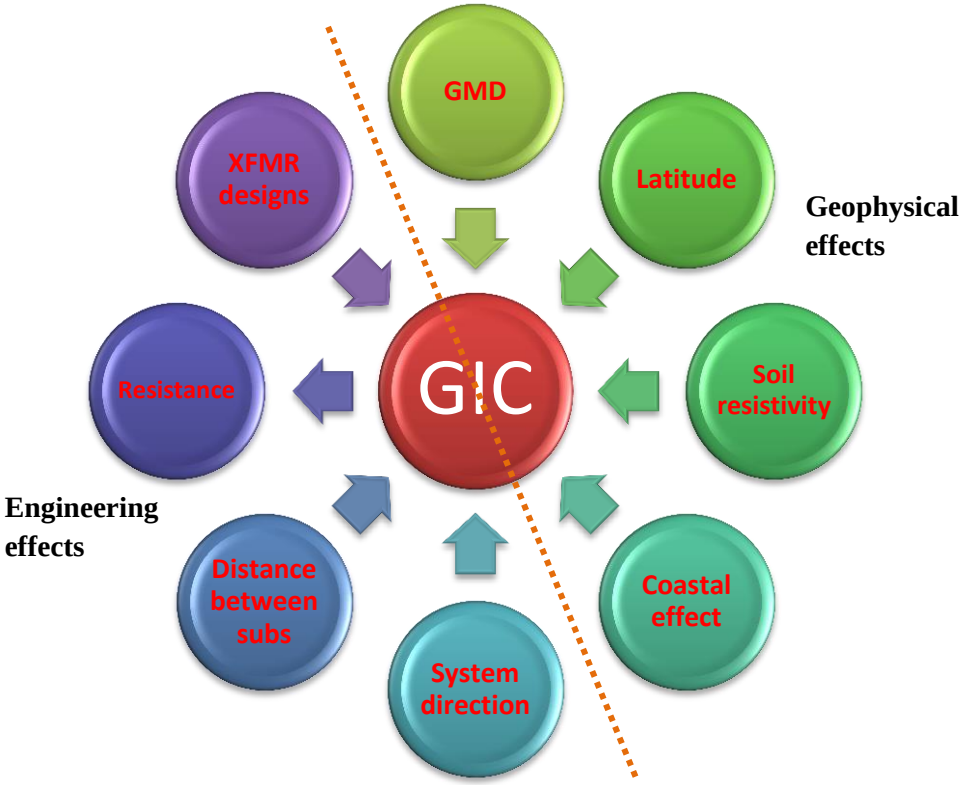

Figure 3-5: Factors affecting GIC level.

Geophysical factors:

- Geomagnetic disturbance strength and duration. Obviously, the stronger and the longer the GMD event is, the higher GIC and the more severe damage to the transformers and the power system will result.

- Latitude of position. Normally, the GIC tends to occur in the Aurora zone with latitude of 55 degrees to 70 degrees. The situation in the northern hemisphere is more severe than that in the southern hemisphere because of the igneous rock with high earth resistivity in the northern hemisphere.

- Local soil conductivity. Igneous rock with higher resistivity contributes to a higher voltage drop between the neutral points of two transformers.

- Coastal effect. The GIC flowing into the ocean meets the land with higher resistivity, causing charges to accumulate in the boundary area, leading to a higher susceptibility to GIC in coastal areas [59].

Engineering factors:

- Power system network direction. The power system networks in eastward or westward directions are more susceptible to GIC than the systems in northward or southward directions due to the Aurora electrojets in the ionosphere. The aurora electrojets are generated near the geomagnetic poles at an altitude over 100 km in eastward or westward directions [60], so currents induced at the Earth's surface tend to have higher magnitudes in eastward or westward directions during GMD events.

- The length of the transmission line [61]. The GIC can be calculated by Eq. 3.3 when the total DC resistances of the two transformers are represented by R_T including the winding resistance and the neutral resistance, and the per unit length resistance of the transmission line is represented by r. E and l are the electric field on the Earth's surface and the transmission line length respectively. If the total transformer resistance R_T is comparable to the transmission line resistance $r \cdot l$, it is clear that GIC will be higher with a longer transmission line length.

$$GIC = \frac{\vec{E} \cdot \vec{l}}{r \cdot l + R_T} \tag{3.3}$$

- Electrical resistance. Clearly, a higher resistivity of the transmission lines and a higher transformer resistance (both winding resistance and neutral resistance) will contribute to a lower GIC magnitude according to Eq. 3.3. In addition, high voltage transmission lines tend to have a lower resistivity because the conductors have to be strong enough to carry high currents. This explains that the high voltage systems are easily affected by GIC.

- Transformer designs. The transformer with delta winding will slow down the transformer saturation rate, but the power losses produced by the delta winding will thus increase. In addition, 5-limb transformers can be more easily saturated by the DC injection than 3-limb transformers [62]. The impacts of the transformer designs on GIC risks will be discussed based on the simulation results in this thesis.

3.3 GIC's impacts to power system network

The GMD's impact on the power system network was recognized in the early 1940s [63]. Since the quasi DC voltage varies on the ground, currents can flow into the neutral points of transformers, pushing the operating point above the knee point of the B-H curve and leading to the half-cycle saturation of the core. The high magnetising current and the harmonics contained in the winding current will contribute to the unnecessary tripping of the relays. Vitally, GIC will lead to a significant increase in the losses of active power and reactive power of transformers [64].

The active power losses in a transformer can be divided into two categories: copper losses and core losses. Copper losses, in the primary winding at least, will have a growth due to the excessive excitation currents produced by the saturated core during GMD events. In addition, extra eddy current loss is generated by large stray flux due to the DC offset injection. Core losses, also referred to as iron losses, can be further divided into hysteresis loss, eddy current loss and anomalous loss [65]. During a GMD event, huge core losses are produced by the excessive fundamental and DC flux. For example, the core loss measurements on a single-sheet sample of 3% grain-oriented electrical steel M85-23 show that the core losses are 1.1 W/kg under 1.6 T AC fundamental flux with a 0.24 T DC flux offset, while the core losses are 0.8 W/kg under 1.6 T AC fundamental flux [66]. Outside the core, large quantities of active power losses are also dissipated in tank [26]. Transformer tanks are normally made of stainless steel that has low permeability and is not laminated, so the current induced by the stray flux will produce unexpected active power losses. The large active power consumption will cause hotspot problems which could accelerate the aging process of transformers. As recorded in a GMD event on 10^{th} May 1992, a 60 A DC neutral current (20 A per phase) was observed in a transformer operated by Allegheny Energy, and the peak tank temperature was 173 degrees Celsius, which was 120 degrees Celsius higher than the temperature before the GMD event. The high temperature could cause aging issues of transformer insulation and unacceptable levels of dissolved gases in oil.

Excessive reactive power losses will lead to a large voltage drop in the system. For this reason, large Static VAR Compensators (SVCs) or capacitor banks need to be installed in the system [9]. However, SVCs are sensitive to the high 2^{nd} harmonics produced by core saturation [67]. There could be a resonance in the impedance of the

Thyristor-controlled reactor (TCR) at 2nd harmonic, which causes a voltage distortion in TCR. During GMD events, large quantities of 2nd harmonics will be produced due to core saturation, which tends to cause the abnormal operation of SVCs in the system [15]. According to National Grid Electricity Ten Year Statement, a total of 31 SVCs has been installed in National Grid Electricity Transmission (NGET) network. For this reason, it is necessary to assess the GIC susceptibility of the SVCs in the NG network.

In addition, [26] gave the risk assessment for different types of transformers under different levels of GIC input as displayed in Table 3-3. The GIC risk is defined as level of transformer losses and excessive temperature.

Table 3-3: Risks of GIC in different transformer structures [26].

Transformer structure type	GIC current (Amps per phase)				
	5	10	25	50	100
3-limb no core bolts in limbs or yokes	None	Low	Low	Low	Medium
3-limb with core bolts in limbs and yokes	Low	Low	Low	Low	Medium
5-limb no core bolts in limbs or yokes	Low	Low	Low	Medium	High
5-limb with core bolts in limbs and yokes	Low	Medium	Medium	Medium	High
3-phase bank single-phase, no core bolts in limbs or yokes	Low	Low	Medium	Medium	High
3 phase bank single-phase, with core bolts in limbs and yokes	Low	Medium	High	High	High

5-limb transformers and single-phase transformers are more vulnerable to GIC compared with 3-limb transformers. The return limbs of the 5-limb transformer core and the single-phase transformer core can provide low reluctance zero-sequence flux paths, so the cores are more likely to be pushed into the saturation area. This statement will be further verified by the results simulated by the new model developed in this thesis. In addition, the bolts in limbs or yokes will increase the GIC risk of a transformer because the bolts are made of non-ferromagnetic material with low permeability, and thus the high flux density near the bolts will produce excessive heat. As for the effect on the leakage

flux path, a higher magnitude flux density appearing in the area near bolts, would encourage further flux to leak out from the side of the core. Therefore, it may be necessary to model into details, such as whether having bolts or not in the core structure. This is also true for simulating the details of magnetic shield of tank, if sensitivity studies need to be done.

3.4 GIC historical events

Figure 3-6 shows the year and location of severe GIC events that have happened in the world since 1940. Obviously, the majority of the countries impacted by GMD events are located in high latitude areas, in both the Northern Hemisphere and the Southern Hemisphere. The area most likely to be affected by GIC includes North America (Canada, US) and Northern Europe (Sweden, UK).

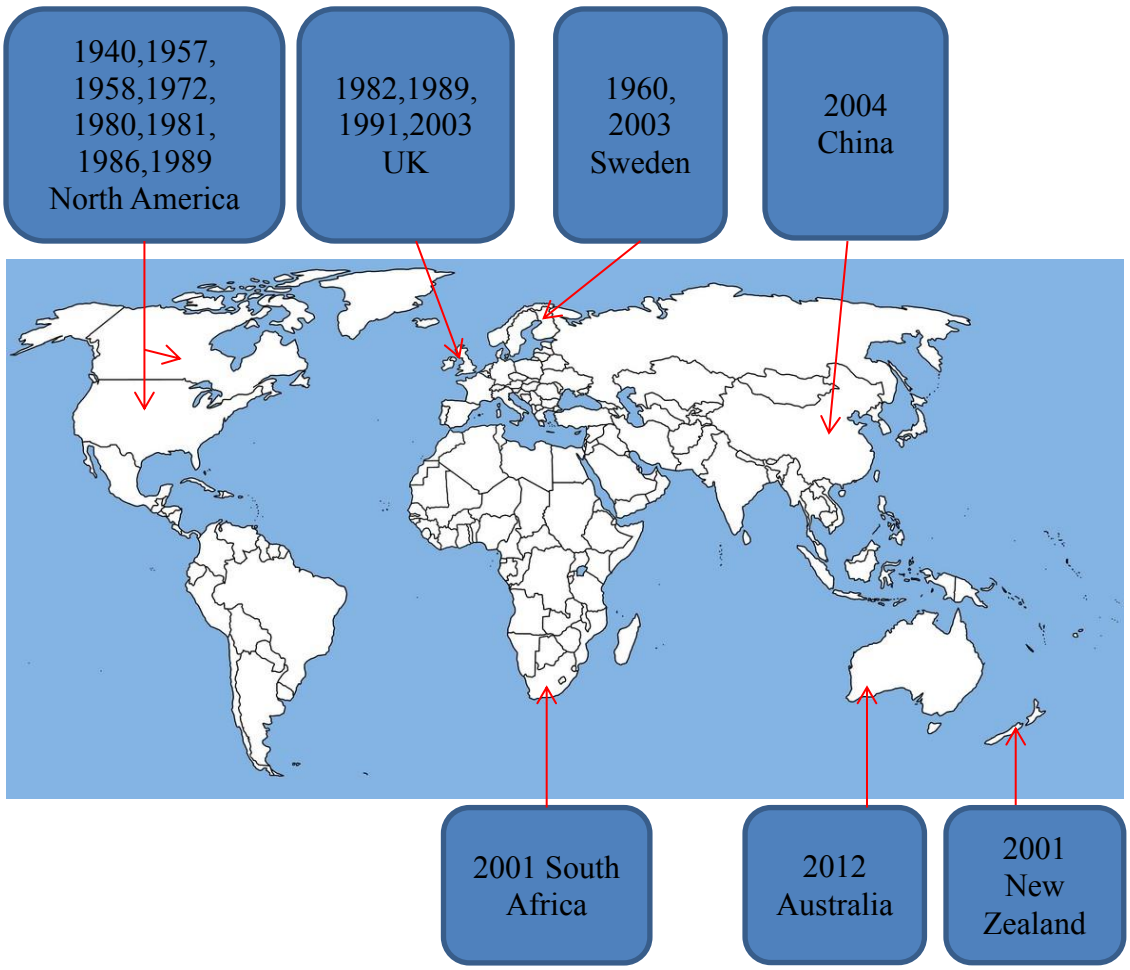

Figure 3-6: GIC historical events around the world.

- North America

Table 3-4 displays the major GIC events in North America, which is the area with the most frequent GIC events in the world.

Table 3-4: Historical GIC events in North America.

Year	Location	Description
1940	Philadelphia Electric Company system	Reactive power swings of 20% and voltage dips Two transformers broke down [68]
	Central Maine Power Co. and Ontario Hydro system	Several transformers tripped in these networks A Total of 10 transformers tripped in North America [69]
1957	Jamestown, North Dakota	A 230 kV circuit breaker tripped by rich 3rd harmonics produced by transformer core saturation [68]
1958	Toronto, Ontario	Two generator transformers at Port Arthur and Raynor Generating Station tripped, which caused a temporary network blackout in Toronto. [70]
1972	Minneapolis and Newfoundland and Labrador	Three transformers tripped by relays [69]
	Northwest US and Light Company	A capacitor tripped by high neutral current [69]
	Minnesota and Manitoba	Report an under-voltage breaker operation [69]
1980	St. James Bay, Canada	A 735 kV transformer tripped [71]
	Winnipeg, Manitoba and Minneapolis	749-km 500 kV transmission line were tripped by mal-operations of protection system [68]
1981	St. James Bay, Canada	A 735 kV transformer tripped again [71]
1986	Winnipeg, Manitoba and Minneapolis	749-km 500 kV transmission line were tripped by mal-operation of protection system again [68]
1989	Quebec	SVCs and transformers failed. Excessive voltage drop caused network blackout [52, 72]

In March 1989, the most severe GIC disaster in the history of humanity happened in Quebec Canada [72]. During this geomagnetic disturbance, seven SVCs in the La Grande network tripped within 59 seconds as a result of excessive harmonics at the very beginning of the disturbance [52]. Due to a lack of SVCs, further transmission network problems in La Grande were caused, such as large voltage drop and frequency fluctuation.

All the five transmission networks in La Grande area eventually tripped. Therefore, the system of the La Grande area was totally separated out of the Quebec network, which caused the voltage and frequency to fluctuate within the Quebec power network. A total of 9400 MW of the generation collapsed in the Quebec region. Two single-phase transformers in La Grande were destroyed. On 14th March, the Meadow Brook 500/138 kV power transformer was removed from the network because of the over-heating problem. After the event, only 430 MW of Quebec's customers continued to be provided with power. It took approximately 9 hours for 83% (17,500 MW) of the network to recover from the collapse. Six million people were affected by this electrical tripping, and a total of 6 billion dollars was lost during this event.

- United Kingdom

The United Kingdom lies between geomagnetic latitude 53 degree to 62 degree in the Northern Hemisphere, meaning that the northern part of the UK is exposed to high strength GMD [73]. Table 3-5 lists the historical GIC events in the UK.

Table 3-5: Historical GIC events in UK.

Year	Location	Description
1982	South Scotland	Voltage dip in the Scottish grid [73]
1989	Norwich, Pembroke and Indian Queen	Neutral currents varying from +5 A to -2 A were recorded by National Grid Company. Two identical 400/275 kV transformers failed at Norwich Main and Indian Queen and Dissolved Gas Analysis (DGA) alert was triggered for both transformers Voltage dips of 5% on the 400 and 275 kV network Transformer saturation led to high even order harmonics [74]
1991	Harker	High harmonics were measured in a transformer [75]
2003	Strathaven	GIC measuring equipment recorded 42 A at the earth neutral of a single-phase transformer in an eastwards system Transformer heating and voltage dips were found at a manageable level [76]

- Rest of the world

Not only in North America and the United Kingdom, but also some other countries suffered geomagnetic disturbances, such as Sweden, New Zealand, South Africa, China and Australia, as listed in Table 3-6.

Sweden is located in Northern Europe with high latitude, and its power system network has been seriously impacted by GIC [77].

Some countries located in middle-low latitude regions, such as China, Australia and South Africa have increased interest in the possible impacts of space weather to the power grid, although the GIC risks in these countries are not as severe as high-latitude countries.

Table 3-6: Historical GIC events in the rest of the world.

Year	Location	Description
1960	Sweden	30 circuit breakers tripped the 400-220-130 kV network [77]
2003	Sweden	Neutral current with a magnitude of 330 A was detected in one generator transformer [78] A blackout lasted 20-50 min due to a tripping of a 130 kV line
2001	New Zealand	A transformer at the Halfway Bush Substation tipped [78]
2001	South Africa	The neutral DC current with a magnitude of 6 A induced a high 6^{th} harmonic current with a magnitude of 13 A. Seven transformers were permanently damaged due to internal heating [79]
2004	Liaoning, China	The system neutral currents reached 47.2 A and 75.5 A [80]
2012	Australia	Current maxima of 4-5 amps were observed equivalent to geomagnetic field level of 0.06-0.07 V/km [81]

3.5 Mitigation of GIC

GIC has a negative effect on the power system, so it is necessary to block it from the power system. The ideal mitigation devices are considered to be low impedance to AC currents and high impedance to DC currents simultaneously. This section mainly

discusses two categories of GIC mitigation methods, which are passive type blocking devices and active type blocking devices [82, 83].

In terms of the passive type, the mitigation resistances or capacitances are installed either in transmission lines or at the neutral leads of transformers. Inserting blocking capacitors in transmission lines is a mature GIC mitigation technology, but it is not suitable for autotransformers which are widely used in the UK transmission system. When a geomagnetic disturbance happens, GIC tends to flow in both series winding and common winding in the auto-transformers. If the blocking devices are installed in the transmission line, only one side of the GIC can be blocked. In addition, adding a blocking capacitor in transmission lines could lead to an increase in system susceptibility to sub-synchronous resonance which is caused by the match between the electric resonance of power network and the mechanical resonance in the shaft of large generators [83].

Neutral series capacitors [84, 85] or neutral series resistances are considered a reliable choice for autotransformers. Neutral series capacitors can be considered as the elements open-circuited to quasi-DC current and short-circuited to neutral AC current, so the capacitors can totally block out the DC components in the neutral current [86]. However, its disadvantage is that it will weaken the relay's ability to detect fault current because the neutral capacitor could change the characteristics of the fault current and neutral current [87]. In addition, the neutral capacitor has the potential to cause ferroresonant problems. The neutral series resistances are also a kind of mature GIC technology, and they are less dependent on the network configuration. However, the disadvantage of adding resistors at neutral is that the installation of the blocking device should take the geographical factors, such as soil resistance, into account to give reasonable values of the resistance. The linear resistance added at the neutral could lead to a poor neutral quality because it impacts on the flow of the unbalance AC current at neutral. Lastly, the insert of the resistance will lead to a larger power loss at neutral point if the system is not balanced. For these reasons, it seems a good choice to apply the neutral series capacitors rather than the neutral series resistors.

For the active type, two kinds of blocking methods are mainly applied. Firstly, a DC current generator can be installed at the neutral leads in order to compensate the GIC from the ground [83, 88]. The other active method is to add an open delta auxiliary winding next to the core as shown in Figure 3-7 [89]. The auxiliary winding is fed by a

DC source to cancel the core flux accumulation caused by the GIC [15]. The advantage of the active type mitigation methods is that it has the least impact on the power network ground system. However, the active devices are more expensive and complex. An accurate GIC detection technique is necessary, but at this stage, it is still difficult to precisely control the active mitigation devices. Therefore, neutral DC injection cannot be totally eliminated. In conclusion, the active devices are not mature enough to be widely promoted in the industry at the current time.

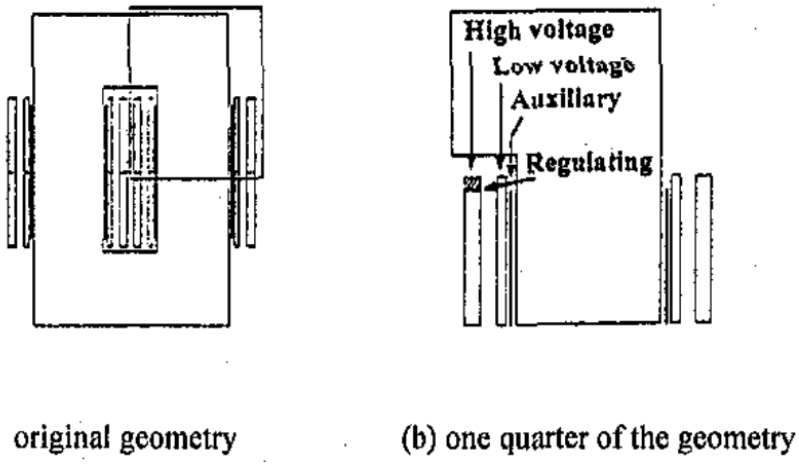

Figure 3-7: Single-phase transformer schematic with auxiliary winding [89].

The advantages and the disadvantages of the GIC mitigation methods are summarised in Table 3-7.

Table 3-7: Advantages and Disadvantages of GIC mitigation devices.

Mitigation method	Advantage/ Disadvantage
Blocking capacitors in transmission line	Advantage: • Mature GIC mitigation method Disadvantage: • Unsuitable to auto-transformers
Neutral series capacitor	Advantage: • Open-circuit to DC current, short-circuit to AC current Disadvantage: • Weaken the relays' ability to detect fault current • Potential to cause ferroresonant problems

Neutral series resistance	Advantage: • Mature GIC mitigation method • Less dependent on the network configuration Disadvantage: • Need to take soil resistance into consideration • Lead to poor neutral quality • Large neutral loss if the system is not balanced
Active type: neutral DC current generator/ Delta auxiliary winding	Advantage: • Least impact on the power network ground system Disadvantage: • More expensive • Accurate GIC detection technique is required

3.6 GIC experimental research

Experiments are vital to understand the impacts of GIC on power transformers. This section discusses three GIC experiments designed by the Japanese, Canadian and Finnish researchers. Firstly, the test arrangements will be introduced in detail. Then the key findings of each case will be displayed accompanied by a discussion of the advantages and the disadvantages of the tests. Lastly, the experiments with the most transformer parameters and the detailed measurement results will be applied to the transformer model verification under GMD events in this thesis.

- **Test 1**

The Japanese researchers Nobuo Takasu and Tetsuo Oshi conducted tests on small-scale models in 1993 [19], in order to evaluate the GIC's impacts on the transformers with different types of cores. As shown in Figure 3-8, the neutral points of the two models were connected with a DC power supply. In the experiment, Model #1 and Model #2, connected in parallel to the AC power supply, applied three small-scale core models of a single-phase three-limb core, a 3-phase three-limb core and a 3-phase five-limb core. The core models were produced with a scale of 1:20, and the original 1 GVA transformers correspond to 7.5 kVA. The small scale models used the grain-oriented silicon steel plate with T joint structure. However, these transformer models are built without a tank, which

is considered as a disadvantage of the test, as the leakage flux paths under the core saturation status were not provided.

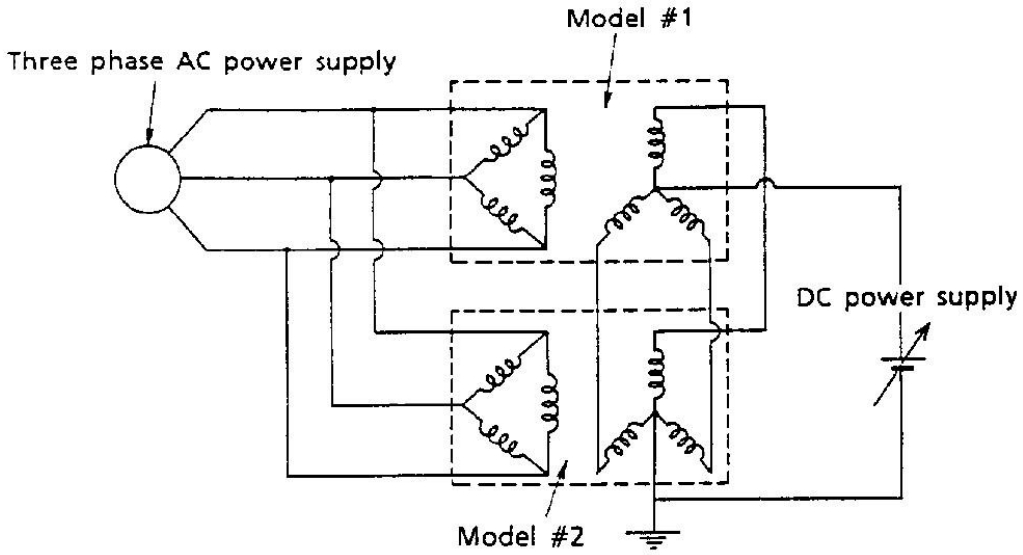

Figure 3-8: Experimental setup for Japanese neutral DC offset test [19].

When the DC current was provided to the single-phase three-limb transformer with the magnitude of 35 A per phase, the input line voltage on the secondary side and the phase current on the primary AC side are shown in Figure 3-9. The figure indicates that the peak of the half-cycle saturation current reached 70 A. The waveform also contains a negative part as marked in the dotted line box, but the value is unavailable in the paper.

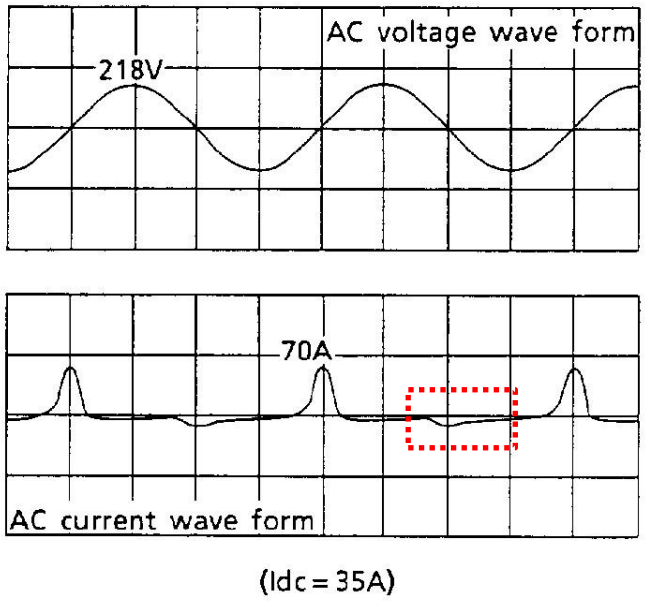

Figure 3-9: Input AC voltage and phase current in single-phase three-limb core [19].

Figure 3-10 shows the peak phase currents measured from the single-phase three-limb core model, the 3-phase three-limb core model and the 3-phase five-limb core transformer under various levels of DC current injection up to 35 A per phase. On the one hand, the results reveal that the single-phase three-limb core model is more vulnerable to neutral DC injection than the three-phase five-limb model. On the other hand, it is not surprising to find that the peak AC primary winding current of the 3-phase three-limb model keeps steady, regardless of the increase in the neutral DC injection because the small-scale model is constructed without a metallic tank, which leads to a lack of zero-sequence flux return paths. In reality, three-limb transformers are not completely immune to GIC because the tank can provide valid flux return paths when the core is saturated [90].

To conclude, the results in this set of measurements will not be applied in verification of the newly developed model in this thesis due to neglecting the tank effect and a lack of the transformer parameters required for simulation, such as nominal voltage, core size and open circuit/short circuit test report. However, as a pioneering GIC experimental research, it provides the firm foundation for GIC experiments by future researchers.

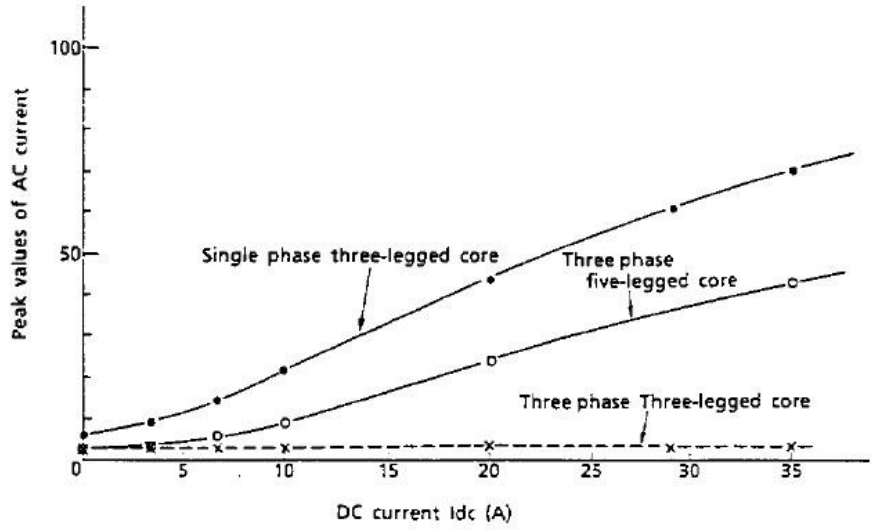

Figure 3-10: Peak phase current against DC input in different types of transformers [19].

- **Test 2**

Canadian researchers did measurements on two 735 kV (one 370 MVA and another 550 MVA) single-phase autotransformers under DC excitation in Quebec [91]. The 370 MVA transformer is a two-limb wound single-phase autotransformer with a HV winding of 1425 turns and a TV winding of 42 turns. The 550 MVA transformer is a four-limb

single-phase autotransformer with a HV winding of 1050 turns and a TV winding of 31 turns. The experimental setup is shown in Figure 3-11. 735 kV AC input was provided on the primary side, and the DC current was provided by a diode bridge and an AC voltage source ranging from 0 V to 55 V from the TV windings.

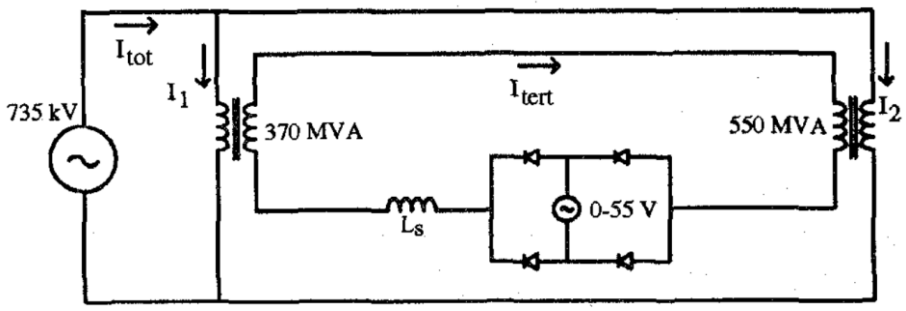

Figure 3-11: Experimental setup for Canadian neutral DC offset test [91].

The measured peak primary winding currents for both these two autotransformers under a DC injection up to 75 A per phase are shown in Figure 3-12. Under the same DC injection current, the 550 MVA transformer experienced a larger peak current than the 370 MVA autotransformer. The peak value of AC current increases approximately linearly with the DC current provided. When the DC current injection reached 75 A per phase, the peak AC current of the 550 MVA transformer approached 600 A.

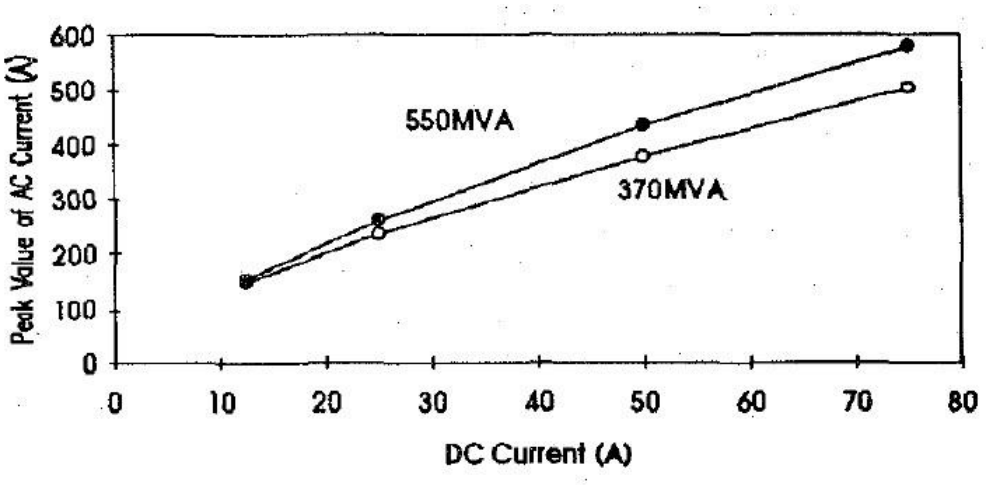

Figure 3-12: Autotransformers peak AC current against neutral DC current [91]

The power losses were also provided in [91] as displayed in Table 3-8. The total losses were measured at the end of the AC power source, and the resistance losses were calculated from the phase AC current, the HV winding resistance and the TV winding resistance. The method was introduced in [92] to calculate the winding stray losses by

setting the apparent resistance of 8 Ω and the exponent of 1.5. The total losses measured at the AC source rise linearly with the DC injection. As shown in Table 3-8, the winding losses (sum of the resistive losses and the winding stray losses) have a higher increasing rate than the core losses (the rest of the total losses except for the winding losses). However, the maximum core temperature rises is limited to 13℃, which is lower than the temperature rise under 1.95 T AC flux.

Table 3-8: Power losses with different levels of DC current injection [44].

I_{dc} (A)	Total losses (kW)	Resistive losses (kW)	Windings stray losses (kW)
12.5	330	1	2.3
25	380	3.1	7
50	473	10.3	22
75	571	20.4	41

This paper provides limited information about the tested transformers, and detailed current waves are not provided. Thus, the newly developed transformer model for GIC simulations will not be verified by this measurement. However, the information discussed above, such as the peak AC current and the active power losses, helps us understand GIC's impacts on single-phase transformers. The peak AC current and the total active power losses are useful for verifying whether the results simulated by the new model are within the reasonable range.

- **Test 3**

In 2002, another laboratory test was undertaken by Matti Lahtinen and Jarmo Elovaara in Toivila, Finland [13]. A new type of transformer was used in the Finland grid, so a new transformer of this type was installed in parallel with another old transformer to take a GIC test. As seen in Figure 3-13, an old welding rotating machine is connected between the HV side neutral points of the old transformer T1 and the new transformer T2 to supply a DC injection. Both ends of the DC supply are grounded with a shunt capacitance to provide the neutral for AC unbalance currents. There is a total of 38 thermocouples and 16 optical fibre-based temperature sensors installed in the windings

and the core structures of T2 for investigating the hotspot problems produced by the DC injection.

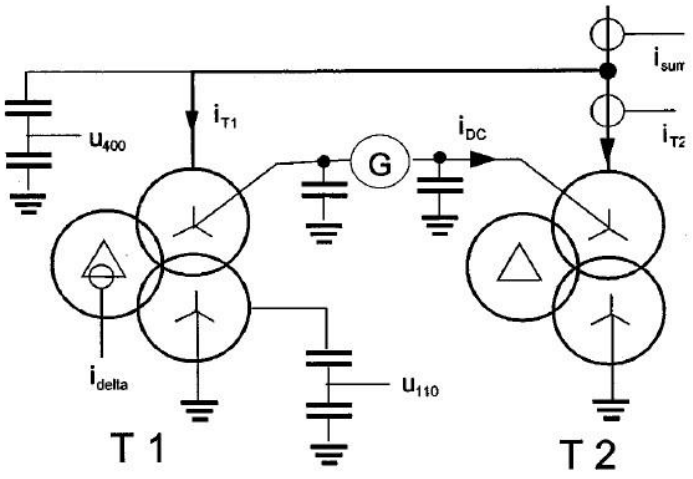

Figure 3-13: Experimental setup for Finnish neutral DC offset test [13].

The transformer parameters are given as follows, so it is possible to compare the measured results with the simulation results calculated by the new model developed in this thesis and the ATP existing models.

Main parameters of two transformers:
Core type: 3-phase 5-limb
Rated voltages: 410 ±6*1.33%/120/21 kV
Rated power 400/400/125 MVA
Short circuit impedance: HV/MV: 19.7%, HV/LV: 40.4%, MV/LV: 65.6%
Winding turns: HV/MV/LV, 766/224/68
Air core inductance: HV/MV/LV, 496/24.9/7.1 mH
No-load losses: T1:170 kW, T2: 100 kW
No-load apparent power: T1: 500 kVA, T2: 120 kVA

In the test, the input DC current increased step by step to the maximum of 66.7 A/phase as shown in Figure 3-14. With the increase in the neutral DC current, the sum of apparent power losses also grew step by step. When the input DC current reached 66.7 A/phase, the sum of the apparent power consumption would be about 115 MVA.

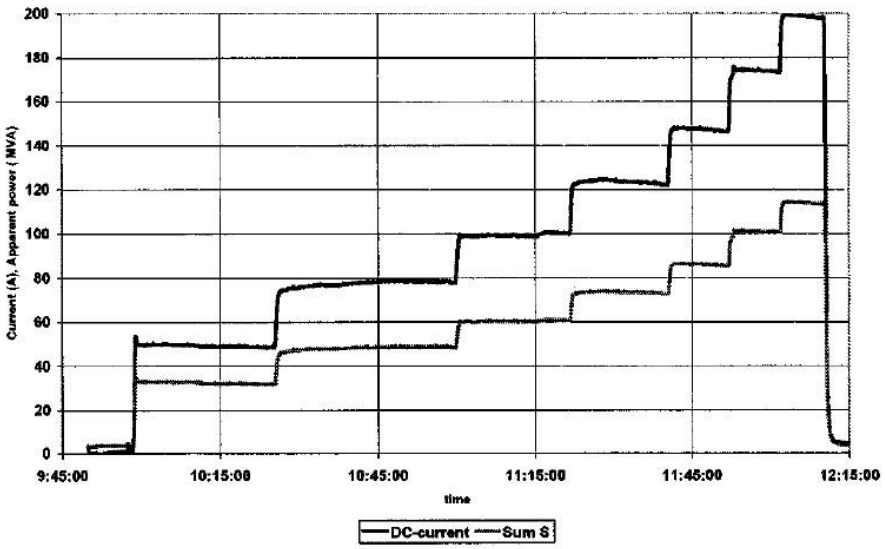

Figure 3-14: Three-phase neutral DC current input (upper curve) and sum of apparent power (lower curve) of both transformers against time [13].

Figure 3-15 provides the HV winding currents of T2 in the steady state when the neutral DC current is 66.7 A per phase. It should be noted that the provided HV winding currents contain the DC components because the DC current injection was provided at the neutral of the HV winding. It can be observed that the HV current for the middle phase is lower than those of the other two phases, which is partly due to the different zero-sequence reluctance for the middle limb. The waveforms are vital for the verification of the models in ATP and the new models in Chapter 4.

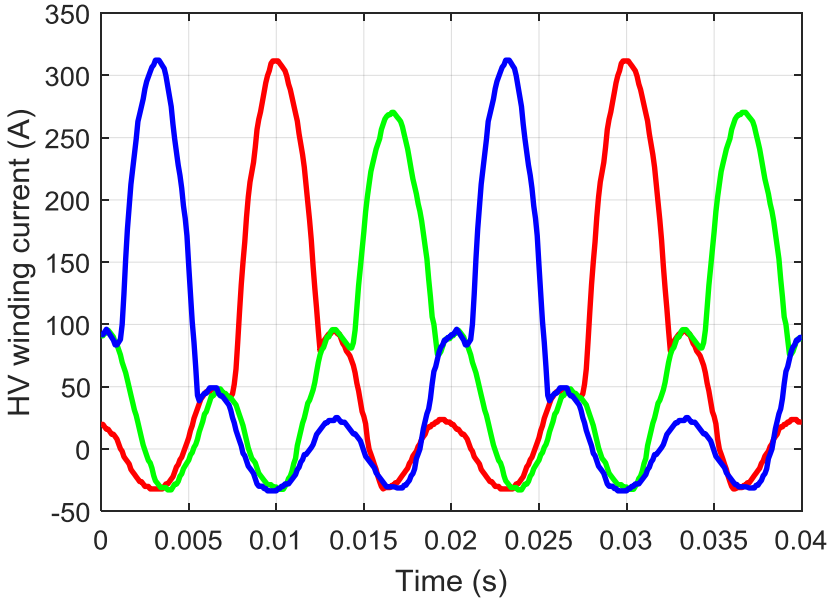

Figure 3-15: HV winding currents of T2 in steady state under 200 A neutral DC current.

In terms of the temperature rise inside the transformer, the peak temperature at the top yoke clamp reached 130℃ under a 66.7 A per phase neutral DC current, while the ambient temperature was only -2℃. The temperature at the bottom yoke clamp had the most significant growth with about 110 K. The time constant of the temperature growth at the bottom yoke clamp was about 10 min. Figure 3-16 shows the temperature rise curve measured by the thermocouples inserted at the flitch plate near the limb under the step-increasing DC input. This curve will help temperature rise equations under various core losses to be obtained in future work.

Figure 3-16: Temperature rise at flitch plate under the step-up DC injection.

Overall, the detailed transformer parameters were provided in the paper, so the transformers measured in the paper can be simulated under AC+DC input. The HV winding current waveforms provided in this paper could be applied to validate the simulation accuracy of the newly developed model and the ATP existing models. In addition, the temperature rise curve will be applied in the simulation for the core temperature in future work.

3.7 GIC simulation research

There are two types of GIC simulation studies depending on the scale of the power system to be simulated. At the level of individual transformer modelling, detailed transformer model is proposed in order to understand how a transformer itself can be affected by GIC in terms of flux distribution in core, tank and structure components. On the other hand, the large scale power system GIC simulation aims to calculate the DC current flow by simplifying power network components into resistances, and evaluate

transformer reactive power consumption according to the empirical equations. The purpose of the large-scale DC current flow calculation is to provide precautions of GIC risks for power systems.

The advantage of individual transformer transient modelling is that the simulation results will be more accurate since the transient process of the transformer core and other key factors are considered, such as core saturation characteristics, core topology and flux leakage effect. However, transient simulation is time consuming, so it is only suitable for individual transformers or small-scale system investigations. If the accuracy is guaranteed, the advantages of transient simulations are the capabilities to provide detailed case studies, where all the winding currents and flux distribution could be provided, so that it allows researchers to assess the over current or over heating risks of transformers during GMD events.

However, the transient GIC study for a large-scale power system is not widely applied because it is time-consuming and complex. For this reason, many GIC studies for a large transmission system simplify the transformers and transmission lines into constant resistances to calculate the GIC flows in the network. Based on the DC current, the reactive power consumption can be evaluated by the empirical equations, and the power system stability will be assessed.

3.7.1 Individual transformer simulation by transformer models

- **Model 1: Single-phase transformer**

A low frequency single-phase transformer model was built by W. Chandrasena, and P. G. McLaren [93]. The schematic diagram of the transformer model is displayed in Figure 3-17.

The equivalent magnetic circuit is shown in Figure 3-17 (b). Φ_1, Φ_2 and Φ_5 represent the fluxes inside the core, and Φ_3 and Φ_4 are the leakage fluxes. First of all, the limb flux density is calculated by the electromagnetic force added on the core. Secondly, the flux distribution needs to be calculated by the equivalent magnetic circuit shown in Figure 3-17 (b). The reluctance in the equivalent circuit should be updated for each simulation cycle according to the B-H curve. The model considered the hysteresis characteristics to represent the half cycle saturation effect instead of the piece-wise linear B-H

characteristics, which could be important for transformer GIC simulation. The model was validated by the open circuit test of a single-phase 3 kVA, 2.3 kV distribution transformer provided with different levels of AC voltage.

The model was only verified under pure AC input, so verification of the model under a DC offset is still required. However, the model still provides the idea to build a new model based on the electric circuit and magnetic circuit.

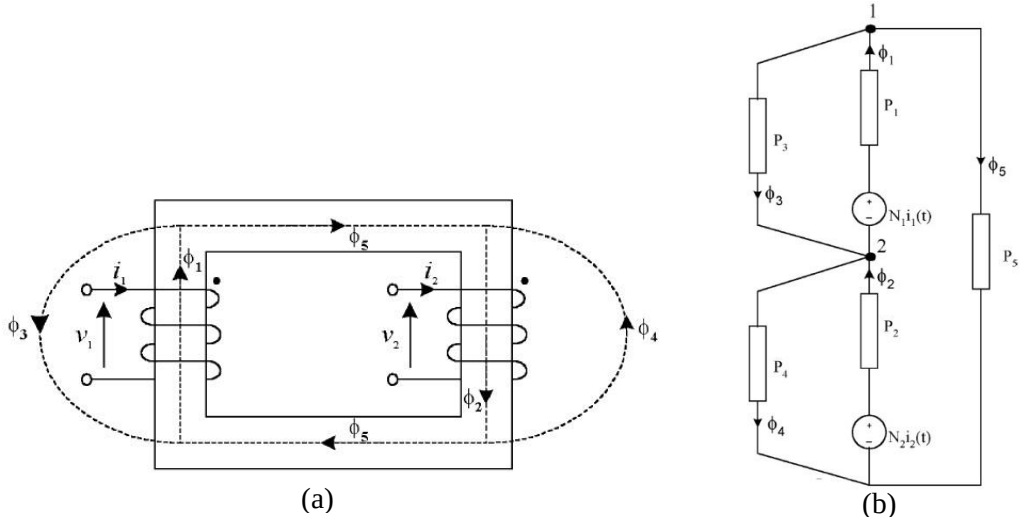

(a) (b)

Figure 3-17: (a) Single-phase two legged transformer model (b) Equivalent circuit of magnetic core model [93].

- **Model 2: Three-phase transformer**

The transformer models for the single-phase transformer and three-phase transformers were developed by Philip R. Price [26]. Figure 3-18 shows the schematic diagram of the model of a 3-limb *YNd* transformer. The transformer model consists of the magnetic circuit and the electric circuit. For the electric circuit, the AC sources, the DC source, the resistance, the mature inductance and the self-inductance are represented by $[V_{AN}, V_{BN}, V_{CN}]$, V_{GIC} , $[R]$,$[M]$ and $[L]$ respectively. In terms of the magnetic circuit, $[k]$ and $[\Phi]$ are the reluctance and flux at each magnetic path. Specifically, k_4 and k_6 are two series terms representing the reluctance of the tank shunt path in parallel with the core, which represent the flux leakage paths on the middle limb. k_5 is the reluctance of zero sequence path found from the zero sequence impedance test. The equivalent electrical circuit and the magnetic circuit are linked by the flux and the phase magnetising current as described in Eq. 3.4.

$$[N][i] = [k][\Phi] \tag{3.4}$$

where

$[N]$	Turn number
$[i]$	Phase magnetising current (A)
[k]	Reluctance (A/Wb)
$[\Phi]$	Flux (Wb)

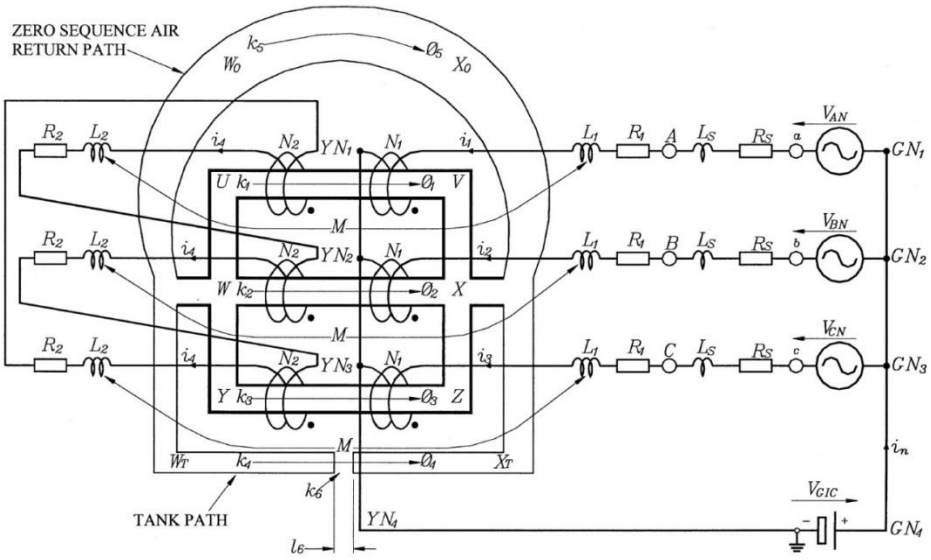

Figure 3-18: Three-limb *YNd* connected transformer model with zero sequence path and leakage flux path [26].

According to the equivalent electric circuit, Eq. 3.5 can be obtained.

$$[V] = -[N]\left[\frac{d\phi}{dt}\right] + [L]\left[\frac{di}{dt}\right] + [R][i] \tag{3.5}$$

where

$[V]$	Input voltage (V)
$[L]$	Winding inductance (mH)
$[R]$	Winding resistance (Ω)

Figure 3-19 shows the simulation case in which 50 A per phase DC current is injected into the 800 MVA generator transformer bank, which is working at nominal voltage. The 3-phase HV winding current is displayed in Figure 3-19, as well as the delta winding current referred to the HV side, after the core is fully saturated and the system reaches the steady state. It can be observed that the frequency of the delta winding current is 150 Hz, which proves that high triplen harmonics are contained in the delta winding.

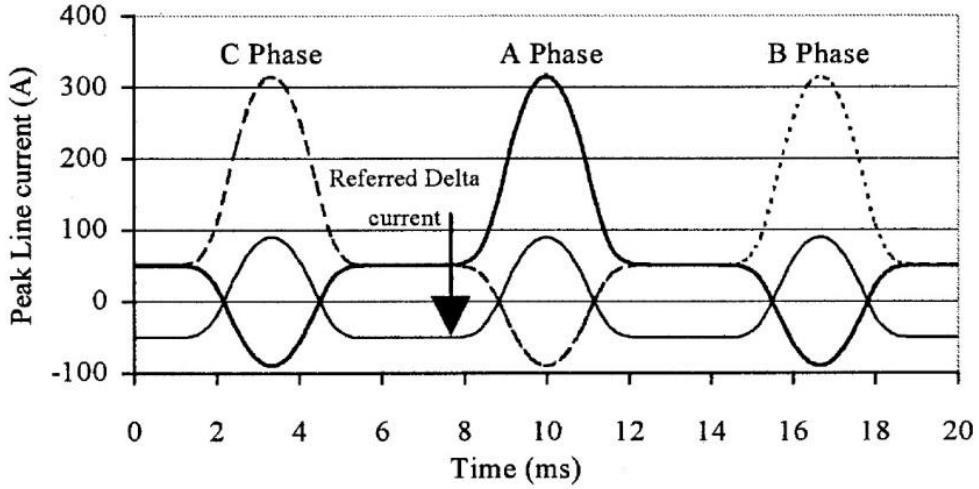

Figure 3-19: Three-phase primary current under AC+DC input [26].

This research also presented the experimental results on a single-phase transformer energized with only a 12 V DC source to determine the transformer's response to DC current. Figure 3-20 displays the line current of the single-phase transformer under the DC injected, when the core residual flux stays at 75% saturation status. The line current increases swiftly to a steady state and lasts until about 40 s. During this period, DC current flows in the HV winding and the LV delta-connected winding, so the current value is equal to the DC voltage divided by the sum of the HV winding resistance and the LV winding resistance. After the core reaches the full saturation state, the peak line current will stabilise at 66.7 A/phase. The experiment in this research emphasises the advantages of the delta winding in improving a transformer ability to defend against GIC.

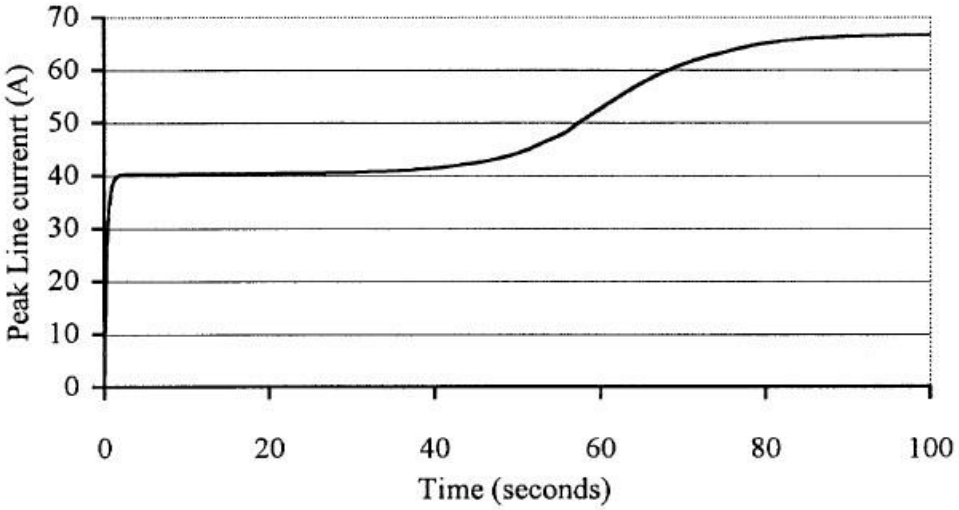

Figure 3-20: Single-phase transformer banks with only DC current injection with 75% residual flux [26].

- **Model 3, 4, 5: ATP models**

EMTP or EMTDC is a kind of commercialised software [7, 27]. There are many EMTP type programs, e.g. EMTP-RV, MT-EMTP, EMTP-ATP and PSCAD-EMTDC. ATP is a kind of user-maintained software so it allows self-developed codes to be added into the software package. Normally, ATP, which can apply a graphical, mouse-driven, dynamic tool called ATPDraw to pre-process the graphical files and convert them to the codes to be further processed, is used to solve transient problems. Three ATP models, the BCTRAN model, the STC model and the Hybrid model are widely used.

- BCTRAN transformer model

The BCTRAN transformer model can represent single-phase/three-phase transformers with 2 windings or 3 windings. The BCTRAN model considers the self-inductance of phase and the phase to phase coupling by mutual-inductance. In the transient calculation, the model is implemented based on Eq. 3.6 [94].

$$[V] = [R][i] + L\left[\frac{di}{dt}\right] \tag{3.6}$$

The BCTRAN model, which requires the short circuit test and the open circuit test results to be able to calculate the impedance and admittance matrices, has acceptable performance in simulating transformers under a frequency less than 1 kHz [95]. It has been widely used in transformer energisation studies, and the frequency of the

transformer energisation ferroresonance typically ranges from 0.1 Hz to 1 kHz [96, 97]. The model cannot provide the selections of different core types. In the recent ATPDraw version, the user can add the AC non-linear inductance characteristics (automatically adding magnetising inductances to the lower terminal) in the BCTRAN model by checking the option Auto-add nonlinearities. Alternatively, delta-connected non-linear inductances can be added by the user in the lowest voltage terminal. As shown in Figure 3-21, the purpose of adding the delta-connected inductances is to calculate the flux-linkage or to set the initial values to carry out AC transient studies. However, the neutral DC current cannot flow into the delta-connected magnetising inductance at the lowest terminal, so the half-cycle saturation effect cannot be observed by using this model. In summary, the BCTRAN cannot be applied in GIC simulation because it adds the non-linear magnetising characteristics at the lowest voltage terminals.

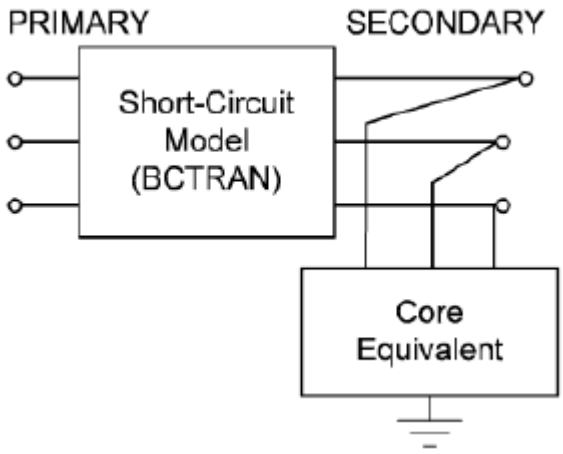

Figure 3-21: Schematic diagram for BCTRAN transformer model added with delta connected core representation [95].

- **Saturable Transformer Component (STC)**

Figure 3-22 displays the equivalent circuit of the single-phase N winding STC model which simplifies the transformer as equivalent to a T-type circuit while the transformer is open-circuited. The STC model consists of the matrices for the winding resistance, winding leakage inductance and core impedance. The core saturation characteristics are described by nonlinear core magnetising inductances, L_m, and the core loss is represented by core magnetising resistances, R_m, connected in parallel with L_m [27, 95]. The inductances L_m are set by the user according to the relationship between the flux linkage

and the current generating the linkage. In addition, the winding inductances ($L_1\ L_2 \ldots L_n$) of the transformer need to be calculated from the transformer test report by the user.

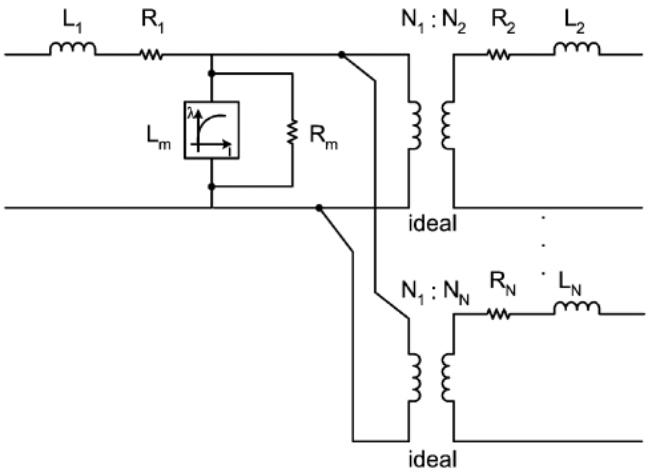

Figure 3-22: Single-phase equivalent circuit for Saturable Transformer Component [95].

The model can be used to simulate not only the single-phase but also the three-phase transformers. The zero-sequence reluctances are added in the three-phase model in order to take the three-phase flux coupling effects into consideration. The user can choose to check the option called 3-leg core, and then a 3-leg transformer can be simulated after the reluctance of the zero-sequence air-return flux path is provided by the user. If the option is not checked, the transformer is assumed to be 5-leg core type or 3-leg shell type by default. Although the model will have different non-linear inductances for 3-limb and 5-limb transformers, the reluctances for three phases are considered the same. Actually, for 3-limb transformers the reluctances for Phase A and Phase C are the same due to geometric symmetry, whereas Phase A and Phase B will be different, especially when the core reaches the saturation area during GMD events. The difference between Phase A and Phase B reluctances is even larger for 5-limb transformers.

- **Hybrid transformer model**

The Hybrid model can be applied to investigate ferroresonance, inrush current and other nonlinear problems of transformers [98, 99]. As displayed in Figure 3-23, the Hybrid model consists of four matrices, which are the electrical circuit matrix for core model, the inverse inductance matrix for leakage representation, the matrix expressing the capacitive coupling and the matrix for modelling frequency dependent resistance [100].

The Hybrid model takes the transformer saturation effects into consideration by adding both the core non-linear characteristics and the transformer core topology [28, 101]. The core design, which is described by the length ratio and cross-sectional area ratios between the limb and the yoke, is required for parameter settings. The core model is converted into an equivalent electrical circuit via duality transformation, in which meshes in the magnetic circuit are transformed to nodes in the electrical dual: reluctances are replaced by inductances; sources of magneto motive force are replaced by current sources [102]. The core non-linear characteristics (as known as *V-i* curve) are represented by Eq. 3.7, where parameters a and b can be obtained by the open circuit test results under 100% of the nominal voltage and 110% of the nominal voltage.

$$V = \frac{i}{a + bi} \tag{3.7}$$

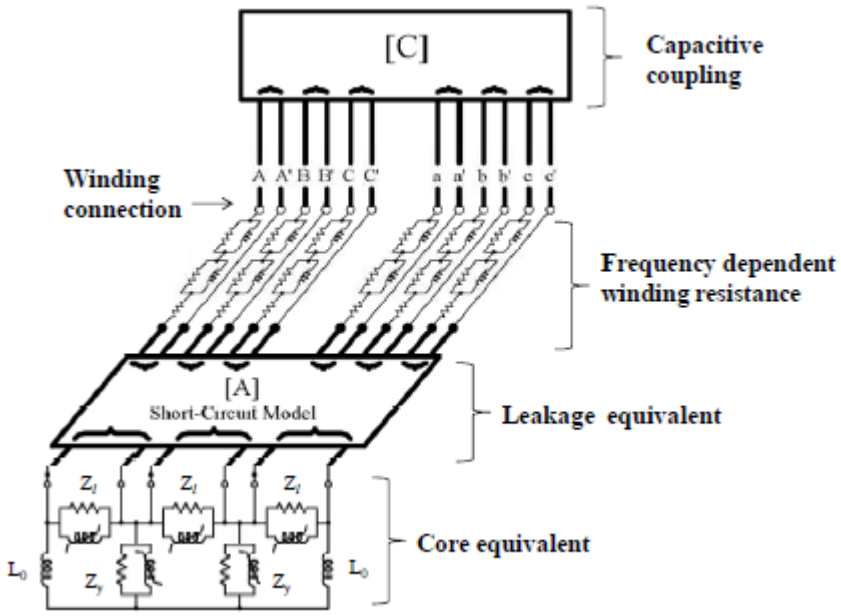

Figure 3-23: Schematic diagram for Hybrid model [100].

However, the Hybrid model also has limitations. The zero-sequence flux paths for Phase A and Phase C limbs of a 3-limb transformer are presented as an equivalent inductance *L* in the core equivalent circuit, while Phase B limb leakage flux path is not represented [100]. For a 5-limb transformer, the equivalent inductance *L* represents the outer legs, which is a saturable core section, and the tank-air zero-sequence flux leakage paths are neglected. In fact, the zero-sequence flux leakage paths are important when

large DC flux and harmonic flux exist in the core, which will be demonstrated by the new model in Section 5.3.

In summary, Table 3-9 lists the advantages and disadvantages of the transformer models, especially on the accuracy in simulating GIC.

Table 3-9: Advantages and disadvantages of ATP models.

Transformer model	Advantages and disadvantages
BCTRAN [95]	Advantages: • Phase to phase coupling considered. • Accurate for frequency under 1 kHz. • Fewer transformer parameters required Disadvantages: • The model does not consider the core topology. • DC neutral bias cannot be recognized. • The model cannot provide the results of flux distribution in the core, magnetising current and delta winding current.
STC [95]	Advantages: • Core saturation and hysteresis effects modelled by a non-linear inductance L_m on the HV side. Disadvantages: • Manual input of the core non-linear curve and winding resistances are required. • The model does not consider the core topology. • Inaccurate representation of zero-sequence reluctances. • The model cannot provide the results of flux distribution in the core, magnetising current and delta winding current.
Hybrid Transformer [100, 102]	Advantages: • The core is presented by a nonlinear duality-based topological method. Disadvantages: • Flux leakage paths via tank for 5-limb transformers are neglected. • The model cannot provide the results of flux distribution in the core, magnetising current and delta winding current.

3.7.2 GIC flow simulation

The study [21] simulates the GIC flow in a 20-bus EHV 500/345 kV system. The topological structure of this part of the network is displayed in Figure 3-24. The methodology of the test is to simplify all the transformers, the transmission lines and the other electric components in the system into equivalent resistances and calculate the DC current flows. Basically, it requires the values of resistances obtained from the substation, transmission lines and transformer data. The delta winding resistances are not considered as GIC paths in this study because they cannot provide DC current paths in the steady state.

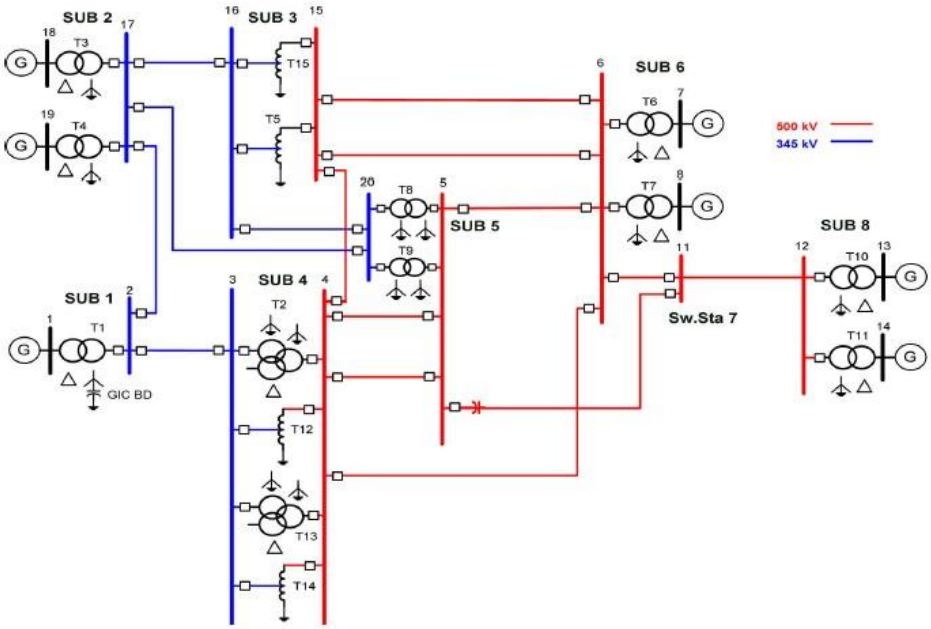

Figure 3-24: Power system network diagram for GIC simulation [21].

The magnitude of the DC voltage is determined by the electric field and the distance between the adjacent substations with transmission line connected as Eq. 3.8. Since the Earth's surface is a sphere, the distances in northward and in eastward directions need be calculated as shown in Appendix I, once the longitudes and the latitudes of the substation are given. The electric field is assumed with the magnitude of 1.414 V/km in a southwest to northeast direction, and the electric field can also be decomposed into the magnitude in a northward and eastward direction. Two methods are proposed to provide GMD-induced electric field: adding voltage sources at the neutrals or connecting voltage sources in series with transmission line. The former method is only suitable for a uniform electric field, and the latter method can handle both uniform and non-uniform electric field [103].

This study adds the DC voltage input in series with transmission lines, and the voltage input at each substation can be obtained as shown in Table 3-10.

$$\Delta V = \overrightarrow{E_N} \cdot \overrightarrow{l_N} + \overrightarrow{E_E} \cdot \overrightarrow{l_E} \tag{3.8}$$

where

E_N, E_E	Electric field in Northward and Eastward (V/km)
l_N, l_E	Distance between buses in Northward and Eastward (km)
ΔV	DC voltage (V)

Table 3-10: Bus bar voltage for north-south direction and east-west direction [21].

Substation	Bus	Northward electric field (volts)	Eastward electric field (volts)
1	2	-12.39	-190.04
2	17	25.05	-41.01
3	15	30.09	-24.39
3	16	29.37	-22.99
4	3	20.04	-125.10
4	4	20.33	-125.97
5	5	-29.01	-7.26
5	20	-29.04	-6.13
6	6	-7.16	44.32
7	11	60.57	-40.47
8	12	7.11	15.67

After the network is simulated by the model, Table 3-11 provides GIC at Sub 1 to Sub 8 after summarising all phases for all transformers at each site. Then the total GIC can be calculated as the scalar sum of the northward GIC and the eastward GIC.

Table 3-11: GIC current at each substation for Northward direction and Eastward direction [21].

Substation name	Northward GIC (Amps)	Eastward GIC (Amps)
Sub 1	0.00	0.00
Sub 2	115.63	-189.29
Sub 3	139.85	-109.49
Sub 4	19.98	-124.58
Sub 5	-279.08	-65.46
Sub 6	-57.29	354.52
Sub 7	0.00	0.00
Sub 8	60.90	134.30

A larger scale system was simulated by Thomas J. Overbye in [23]. This paper gave an example simulation of the North America Eastern Interconnected model with 62000 buses. The simulation method is similar to that in [21]. The resistances for regular transformers and autotransformers are referred to HV side by Eq. 3.9 and Eq. 3.10 respectively, when the turn ratio is a_t.

$$R = R_{HighSide} + {a_t}^2 R_{LowSide} \tag{3.9}$$

$$R = R_{Series} + (a_t - 1)^2 R_{Common} \tag{3.10}$$

Firstly, the voltage between two buses can be calculated as

$$\Delta V = \overrightarrow{E_N} \cdot \overrightarrow{l_N} + \overrightarrow{E_E} \cdot \overrightarrow{l_E} \tag{3.11}$$

where

E_N, E_E	Electric field in Northward and Eastward (V/km)
l_N, l_E	Distance between buses in Northward and Eastward (km)
ΔV	DC voltage (V)

Then GIC can be indicated as Eq. 3.12.

$$[V] = [G]^{-1}[I] \tag{3.12}$$

where

$[G]^{-1}$	Inverse matrix of bus admittance matrix (Ω^{-1})
$[I]$	GIC matrix (A)

When the uniform northeast to southwest electric field is added on the power system network, the GIC flows in an Eastward direction and Northward direction can be achieved as Figure 3-25. The yellow arrows present the GIC flows in the power system.

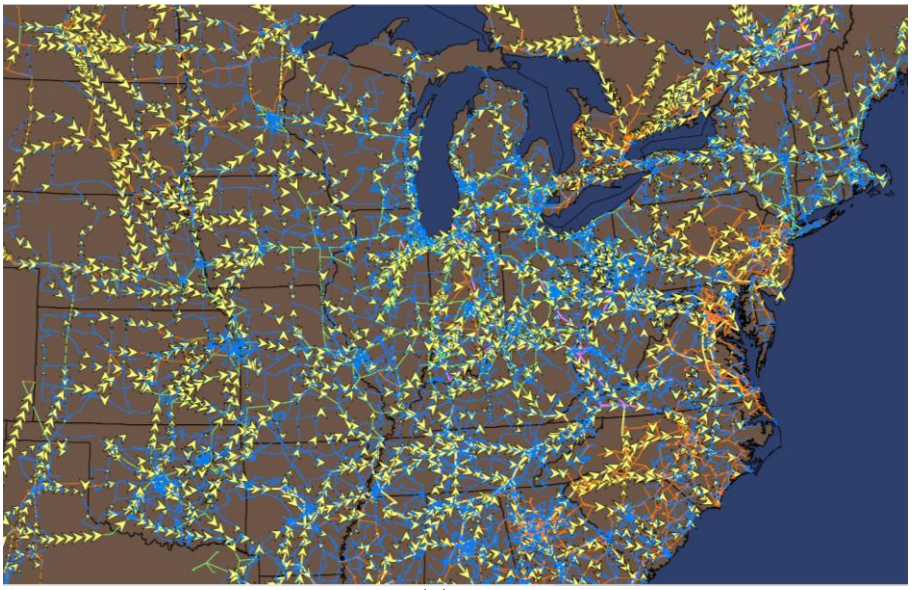

(a)

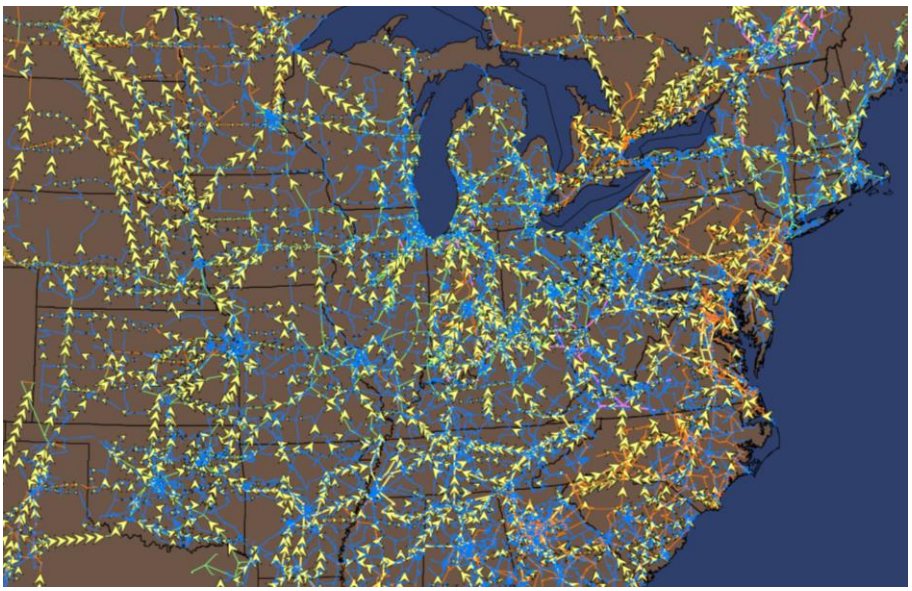

(b)

Figure 3-25: (a) GIC flows in the power system with east- west electric field. (b) GIC flows in the power system with north- south electric field [23].

In summary, similar simulation methodologies are applied in the two studies introduced above in Section 3.7.2. The GIC studies for large transmission networks always simplify the transformers and transmission lines into constant resistances to calculate the GIC flows in the network more efficiently.

Following that, a linear relationship can be found between GIC flows and reactive power absorbed by transformers [78, 104-106]. The reactive power losses caused by GIC can be derived by Eq.3.13.

$$Q_{loss} = V_{pu} \cdot k_{loss} \cdot I_{GIC} \tag{3.13}$$

where Q_{loss} is the transformer reactive power losses associated with GIC in MVar, V_{kV} is the terminal voltage in *pu*, k_{loss} is a constant associated with transformer core type in MVar/A and I_{GIC} is three-phase neutral GIC.

According to the calculation for a 200 MVA 230/115 kV 3-phase 3-limb transformer and a 750 MVA 525/303 kV 3-phase 5-limb transformer in [105], the k is 0.29 and 0.66 respectively.

Although this method is capable of calculating the GIC flows and the transformer reactive power consumption in a vast system in a speedy way, the results may not be accurate as compared with those of transient studies because they do not account for the nonlinear characteristics of the transformers and the differences in core structures.

3.8 Summary

This chapter firstly introduces GIC comprehensively from several aspects, which include how GIC is induced on the ground, factors affecting the GIC magnitude, GIC's impacts on power systems and GIC mitigation technologies.

In the history of humanity, GIC has had great impacts on man-made systems. The most severe GIC disaster happened in Quebec, Canada in 1989. During this event, seven SVCs and two single-phase transformers tripped on the La Grande network. A total of 9400 MW of the generation collapsed in the Quebec region. After the event, only 430 MW of the Quebec load isolated to specific generation stations continued to be provided with power. It took approximately 9 hours for 83% (17500 MW) of the network to

recover from the collapse. Six million people were affected by this electrical tripping, and a total of 6 billion dollars was lost during this event.

For this reason, researchers have carried out large quantities of experimental measurements and computation simulations in recent years.

Researchers in Japan, Canada and Finland conducted tests on either small-scale transformer models or real transformers. Although it is difficult to generalize the measurement results to assess the GIC risks of the other transformers, the measurement results can be applied to validate the accuracy of GIC modelling.

In terms of GIC modelling, researchers mainly focus on two types of models, i.e. the individual transformer model in transient simulation for accurately representing core saturation characteristics and core topology, and the large-scale power system simulation for DC current flow in order to provide precautions of GIC risks for power systems.

Chapter 4: Development of Transformer Models for GIC Simulation Studies

4.1 Introduction

In this chapter, three ATP transformer models, which are the BCTRAN model, the STC model and the Hybrid model, are firstly studied to determine their suitability for GIC simulation modelling; The individual ATP transformer models are subjected to AC+DC input, and the HV winding currents simulated are compared to those measured by Finnish Grid.

Secondly, a MATLAB model that represents the equivalent electric and magnetic circuits of transformer is developed based on material properties and physical dimension parameters. The model has an advantage that the leakage flux paths composed of the tank and oil gaps are adequately modelled. The newly developed model is also subject to AC+DC input. The parameters interested, such as flux distribution, the current flow inside a delta connected winding and magnetising current, can be extracted to aid the understanding.

4.2 Individual ATP transformer models

In this section, the ATP models will be studied under AC+DC input and the simulation results will be compared with the Finnish Grid measurements.

4.2.1 ATP simulation circuit

GIC flows into the power system via the transformer neutral points. Figure 4-1 shows the circuit diagram for simulating the GIC's impact on an individual transformer in ATP. A DC voltage source is added at the neutral point, and an AC nominal voltage source is connected to the HV side. The LV side and the TV side are open-circuited. The thick solid lines in the circuit correspond to the three-phase circuit. A voltage probe and a current probe are inserted on the HV side circuit to record the voltage and current data. ATP cannot provide other data except for the line currents and voltages, so limiting information about the transformer's internal condition, such as flux distribution and current inside the delta-connected windings, can be obtained from the simulation.

In the ATP simulation, instead to provide the DC injection between the neutral points of two parallel connected transformers as the experimental setup in Finnish Grid, DC source can be applied between the neutral of the ATP transformer model and the ground, and the grounding quality will not be affected due to the connection of the ideal DC source.

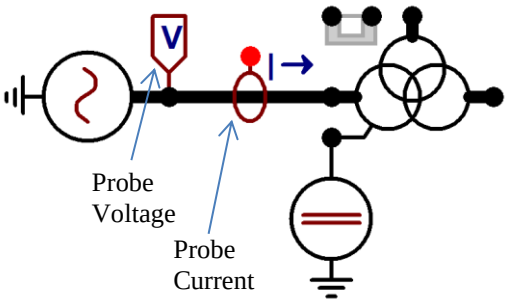

Figure 4-1: Circuit diagram for individual transformer AC+DC simulation.

The current and the voltage results are obtained by the Probe Current and the Probe Voltage respectively as noted in Figure 4-1. Figure 4-2 shows the tool called 'Harmonics' to calculate the frequency spectrum of a signal which can be either a current or a voltage. Point A is a node that receives a current/voltage input signal. Point B and Point C provide the magnitudes and the phase shifts of the harmonics up to 26th, while Point D provides the DC magnitude. It is worth noting that this tool is only valid for a single-phase signal; thus three-phase signals require 3 pieces of this tool to calculate the results.

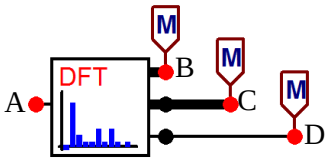

Figure 4-2: Power system analysis tool 'Harmonics'.

4.2.2 Transformer parameter setting

Table 4-1 shows the parameters required for the BCTRAN model, the STC model and the Hybrid model. The models will be tested under AC+DC input in this section to assess their feasibility for use in GIC simulation.

Table 4-1: Required parameters for three widely used ATP transformer models.

	BCTRAN	STC	Hybrid
Rated voltage and power rating	✓	✓	✓
Winding connection type	✓	✓	✓
Winding resistance	Software calculating from SC test report	User calculating from SC test report	Software calculating from SC test report
Leakage reactance			
Core resistance	Software calculating from OC test report	User calculating from OC test report	Software calculating from OC test report
Non-linear characteristic			
Core topology	×	✓	✓
Physical dimension	×	×	✓

✓ stands for required input and × for non-required input, OC for open-circuited test, SC for short-circuited test

The Finnish test did not provide the open circuit and short circuit test report or the core non-linear characteristics which are necessary as the setup parameters of the ATP models. For this reason, a 400/132/13 kV UK transmission transformer will be simulated and compared to the measurement results. Although the transformer simulated in ATP is not exactly the same as that measured in the Finnish test, the two transformers have some common points.

- Primary voltage of 400 kV
- 5-limb core
- With a delta-connected tertiary winding

For these reasons, the magnitude of the measured waveforms and the simulated waveforms are not necessarily equal, but at least similar to each other. In addition, the current waveforms of the results should have similar features.

The transformer data were extracted from the test reports for all the 400/132/13 kV 5-limb transformers operated in the south west of England Peninsula power network and

the average values are calculated. This section provides transformer information including:

a. Transformer basic information (required by BCTRAN, STC and Hybrid model)
b. Transformer short circuit test report (required by BCTRAN and Hybrid model)
   Winding resistance and leakage inductance calculated from the test report (required by the STC model)
c. Transformer open circuit test report (required by BCTRAN and Hybrid model)
   Core non-linear saturation curve (required by STC model)
d. Core size and tank dimensions (required by Hybrid model)

The input interfaces of these models are displayed in Appendix II.

a. Transformer basic information

Table 4-2: Transformer basic information to be applied in simulation.

Voltage	400/132/13 kV
Power rating	240/240/60 MVA
Winding connection	*Y-a-d*
Core type	5-limb

b. Winding resistance and leakage inductance

The average values of the short circuit test reports are calculated and shown in Table 4-3. The user needs to fill in the short circuit test report into the BCTRAN model and the Hybrid model. The models will calculate the winding resistance and leakage inductance automatically.

In terms of the STC model, the user needs to offer the winding resistance and reactance. The test reports provide the winding resistances. The resistances of the common winding, the series winding and the tertiary winding are 0.1553 Ω, 0.9046 Ω and 3.683 Ω respectively referred to the HV side. However, the leakage inductance needs to be calculated from the short circuit test report. The calculation steps of the winding leakage inductance based on the test report are shown in Appendix III.

Table 4-3: Average short circuit test report data for 5-limb transformers in Southwest UK transmission system.

	Impedance (%)	Power (MVA)	Losses (kW)
Primary-secondary	19.75	240	868.0
Primary-tertiary	13.36	60	147.2
Secondary-tertiary	7.77	60	144.5

c. Core nonlinear characteristics

The average values of the open circuit test reports are calculated and shown in Table 4-4. The BCTRAN model and the Hybrid model use the open circuit test report to express the AC non-linear characteristics of the core, while the STC model needs the B-H non-linear characteristics provided by the users. Figure 4-3 shows the B-H curve of M140-27S core steel, which is applied in the simulation of the STC model.

Table 4-4: Average open circuit test report data for 5-limb transformers in Southwest UK transmission system.

Voltage (%)	Losses (kW)	I_{av} (%)
90	91.70	0.066
100	110.53	0.156
110	181.20	0.640

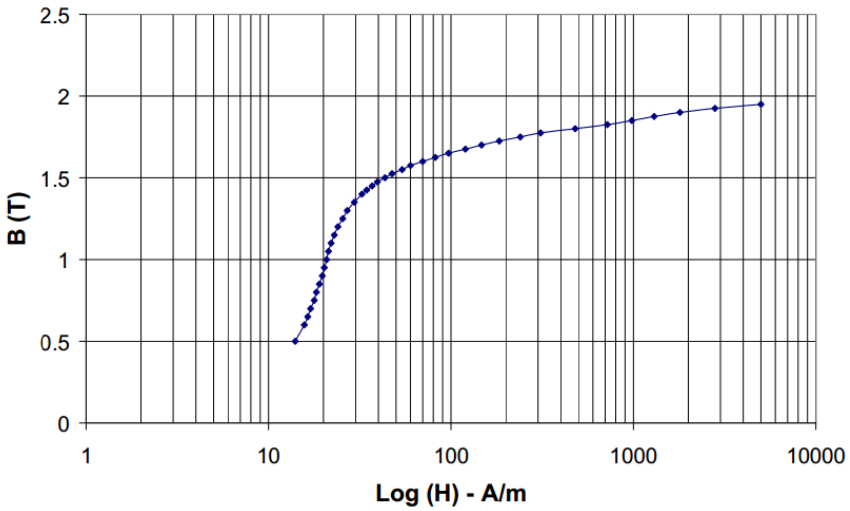

Figure 4-3: B-H curve of M140-27S Steel [36].

d. Core and tank dimensions

The Hybrid model needs the ratios of the core dimension. Table 4-5 shows the ratios of the core length and cross-sectional area of a 400 kV 5-limb transformer. The nameplate of each part of the core and the dimensions are also displayed in Figure 4-4. The length ratios (*l2/l1*, and *l3/l1*) for a 400 kV 240 MVA 5-limb transformer are believed to be similar to those of a 400 kV 1000 MVA 5-limb transformer because of insulation clearance is more dominated by voltage level rather than power rating. In addition, the default area ratio for a 5-limb core is usually around 50%-60%. Therefore, the dimension ratios shown in Table 4-5 are reasonable and will be applied in the Hybrid model.

Table 4-5: Core length and cross-sectional area ratio of a 400 kV UK transformer.

Main yoke length/ Main limb length (***l2/l1***)	0.921
Side yoke length/ Main limb length (***l3/l1***)	0.591
Main yoke area/ Main limb area (***A2/A1***)	0.603
Side yoke area/ Main limb area (***A3/A1***)	0.603

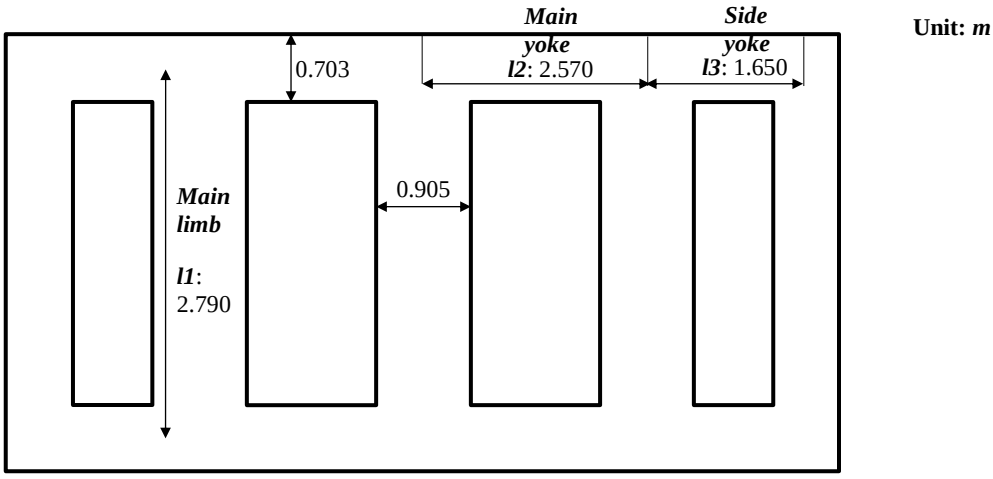

Figure 4-4: Core dimension of 400 kV 1000 MVA transformer.

4.2.3 Verification of models

In this section, the 400 kV transformer is simulated under AC+DC input by the BCTRAN model, the STC model and the Hybrid model respectively, and the simulation results are compared with the measurement results.

a. HV winding current analysis

Figure 4-5 shows the comparisons of the steady-state HV winding current waveforms between the measurement results and the simulation results generated by the BCTRAN model, the STC model and the Hybrid transformer model under nominal AC input plus 200 A neutral DC input.

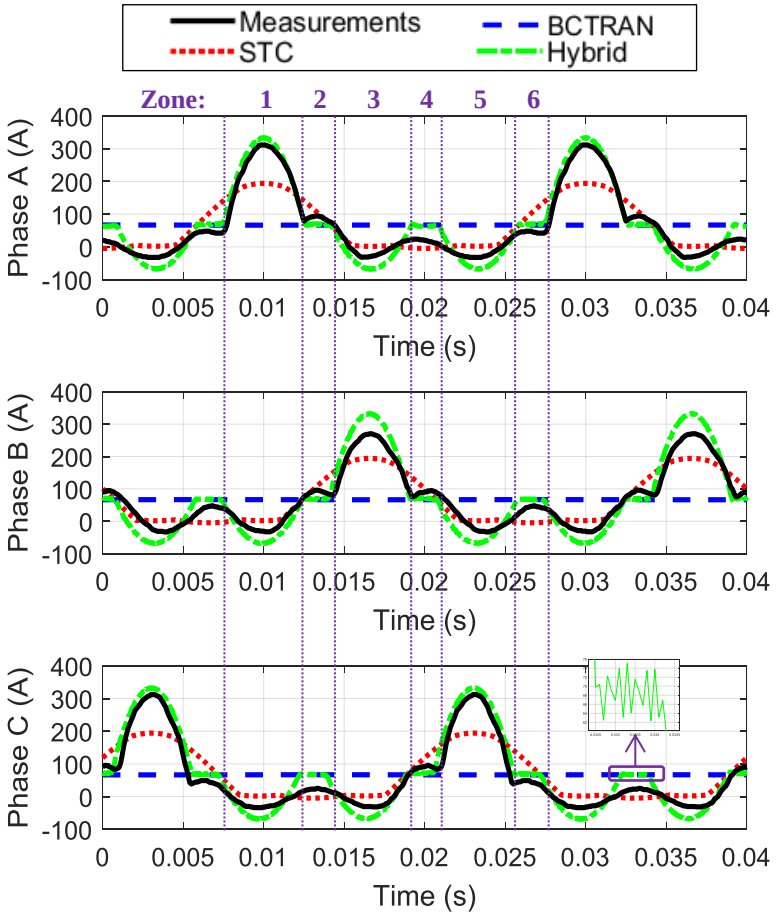

Figure 4-5: Comparison of HV currents between measurements and ATP models simulation results.

The measurements show that the current waveforms of the three phases share a similar pattern, but with a fixed phase angle shift. The peak currents of Phase A and Phase C are almost identical due to geometric symmetry, whereas the peak current of Phase B is noticeably lower, arising from the higher reluctance of Phase B flux.

As can be seen from Figure 4-5, one period of the measured current waveforms can be divided into 6 zones. In Zone 1, Phase A HV winding current experiences a peak, which is caused by the flux in Phase A limb approaching its peak. The two troughs of Phase A currents in Zone 3 and Zone 5 are produced due to the circulating delta winding current.

The same reasoning goes for the peaks and troughs in Phase B and Phase C. In Zone 2 and 4, relatively smaller current peaks are observed in the three phases, arising from the peaks of the flux in the corresponding yoke and tank leakage path. In Zone 6, the minor peaks in the three-phase current are mostly determined by the delta winding current. More detailed current waveform and flux distribution analyses are to be presented in the new model simulation part in Section 4.3 because the ATP cannot provide the flux distribution.

Compared to the measured current waveforms, the waveforms generated by the BCTRAN model are prominent with a constant DC magnitude; however, they do have unnoticeable AC components which are equal to the magnetising currents under AC only. This model cannot represent the core saturation caused by neutral DC offset, so it is ruled out as a suitable model to simulate GMD events.

The waveforms from the STC model have lower peak values; for example, the peak value of Phase A simulated by STC is 117.4 A lower than the measured result. In addition, the three-phase waveforms from STC are identical, with 120 degree phase shift. Furthermore, the STC results only have two featured zones, which are mainly caused by the inaccurate representation of the core non-linear characteristics in the deep saturation region. The *B-H* nonlinear characteristics are required to implement the STC model. For this simulation, the *B-H* curve provided is up to 1.98 T.

Overall, the current waveforms from the Hybrid model are closest to the measurement results. However, the Hybrid model still cannot differentiate Phase B from Phase A/C. In addition, in Zone 2, 4 and 6, the HV winding currents from the Hybrid model only contain DC components, which shows that the Hybrid model fails to capture the features of localized core saturation. Moreover, a part of the Hybrid model simulation results cannot be converged as shown by the inset on Phase C current waveform in Figure 4-5.

b. HV winding current frequency spectrum

It is accepted that the harmonics' magnitude and phase could influence the time domain signal's waveform significantly; hence it is necessary to compare the harmonic contents of the simulated and measured results.

The frequency spectrum of HV winding currents from the measurements and ATP models is displayed in Figure 4-6 for Phase A and Phase B. Comparisons for Phase C

results are not presented because of their close identity with Phase A results. In general, Phase A 3rd harmonic has a much higher magnitude than its Phase B counterpart.

The results of BCTRAN are not displayed because of its unsuitability in simulating GMD events.

For Phase A current, as shown in Figure 4-6 (a), the harmonics magnitudes from the STC model are generally lower than the measured results, and this coincides with its poor representation of the core non-linear characteristics in the deep saturation region. On the other hand, the Hybrid model generates harmonics that are closer to the measured results, except for the 3rd harmonic which is much lower than the measurement. In terms of phase shifts of Phase A harmonics, as shown in Figure 4-6 (b), the STC model and the Hybrid model have similar results as the measurements, except for the 3rd and the 4th harmonics.

For Phase B currents, the STC harmonics are generally smaller than the measurement results, and the Hybrid model harmonics are generally closer to the measurements, except for the 2nd harmonic as shown in Figure 4-6 (c). In terms of phase shifts of Phase B harmonics, both the STC and the Hybrid model results are similar to the measurement results, except for the 3rd and 4th harmonics as shown in Figure 4-6 (d).

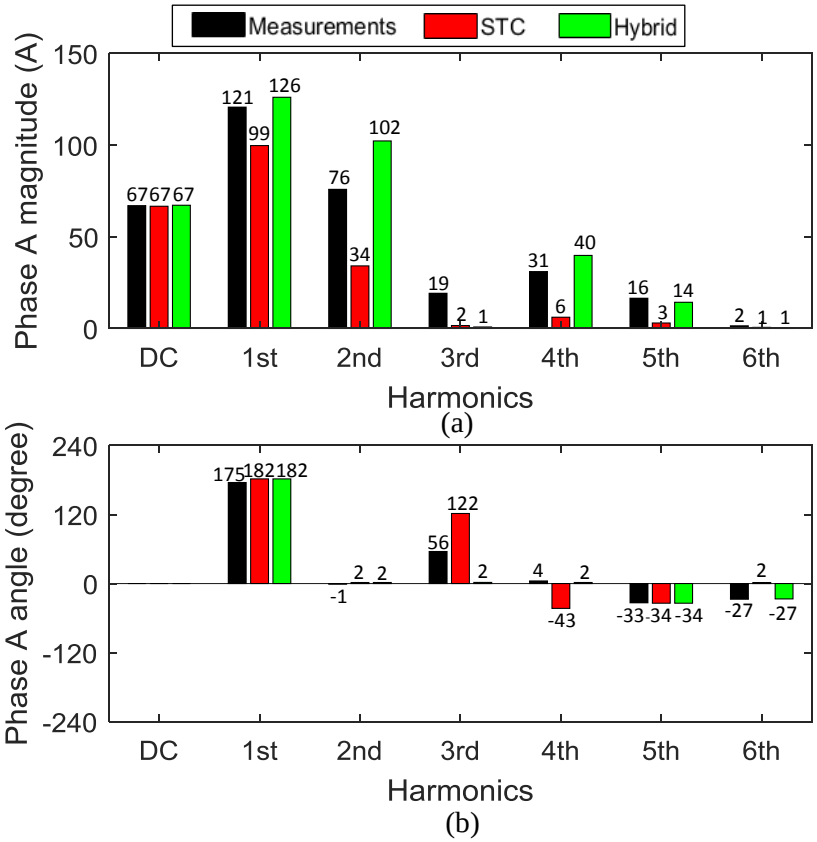

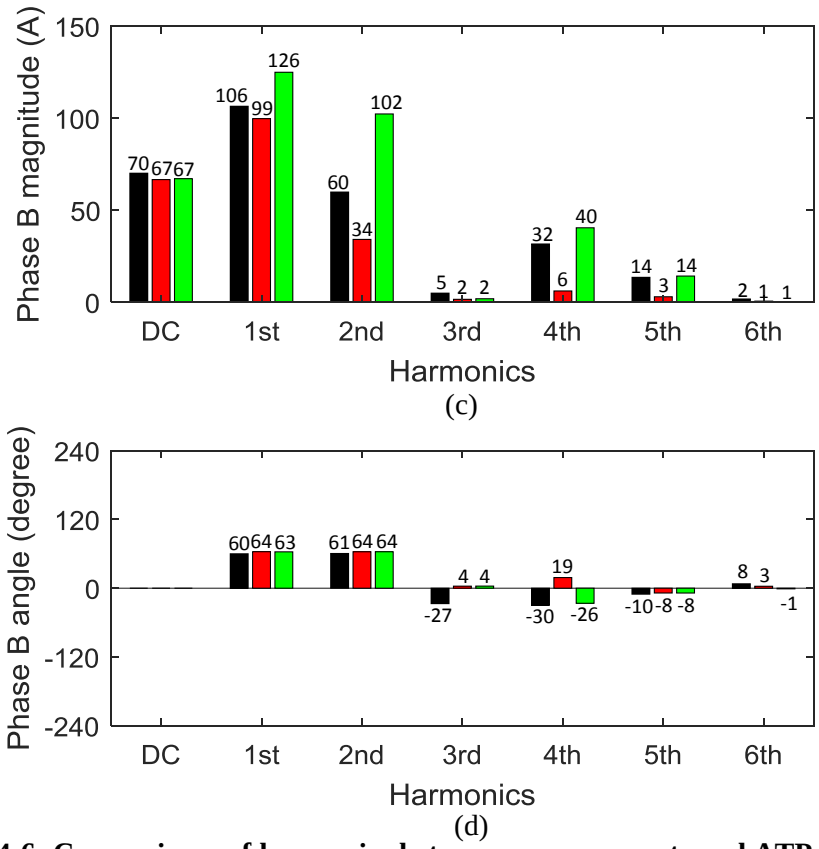

Figure 4-6: Comparisons of harmonics between measurements and ATP models simulation results (a) Phase A magnitude (b) Phase A phase angle (c) Phase B magnitude (d) Phase B phase angle.

Comparing Phase A and Phase B harmonics from the measurements, one can see the distinct difference that Phase A 3rd harmonic magnitude is much higher than that of Phase B. This is because Phase A zero-sequence flux can go through side limb more easily. More detailed analyses on the 3rd harmonic difference are shown in Section 4.3. However, both the STC model and the Hybrid model fail to show the difference.

Note that the results of the delta winding current and the magnetic flux distribution cannot be obtained from the ATP models. Therefore, no further information can be achieved from ATP simulation; the detailed analysis from the view of flux distribution will be obtained in Section 4.3.

4.2.4 Summary

Based on the simulation results discussed above, the Hybrid model has the best performance in simulating GMD events among the ATP models. The Hybrid model takes the transformer saturation effects into consideration by adding both the core non-linear characteristics and the transformer core topology. However, the tank-air zero-sequence

flux leakage paths are neglected for 5-limb transformers. In addition, the Hybrid model fails to capture the peaks and the troughs of the current waveforms. Lastly, the ATP models cannot provide the magnetising current, delta winding current and flux distribution results, which are believed useful for us to build a better understanding of the transformer's behaviour under GIC. In the next section, a MATLAB model using the parameters of physical dimensions and magnetic materials of the core will be developed to help build the understanding.

4.3 Development of new transformer model: methodology and verification

This section introduces a new time-domain transformer model composed of the equivalent electric circuit and magnetic circuit.

In terms of the equivalent electric circuit, winding resistance and leakage reactance can be calculated from the transformer short circuit test report. Based on Ohm's Law and Faraday's law, the phase limb flux is calculated and given as the input to the equivalent magnetic circuit.

The magnetic circuit is composed of the transformer core and the leakage flux paths which include the tank and oil gaps. The flux distribution and the magnetising current are calculated in each calculation step with the input of the phase limb flux from the equivalent electric circuit. The magnetising current obtained from the magnetic circuit is fed to the equivalent electric circuit in the next calculation step as the input. The limb residual flux needs to be assumed correctly to enable the flux densities and currents to reach the AC steady state quickly.

An example of a 400 kV 5-limb transformer is simulated under AC+DC input with the LV side and the TV side open-circuited. The simulation results under AC+DC input are compared with industrial GIC measurements on the 5-limb transformers. The waveforms of the currents and the flux densities are analysed in transient and in steady state.

4.3.1 Overview of 5-limb model

A new model is coded in MATLAB and composed of the equivalent electric circuit and the equivalent magnetic circuit. Figure 4-7 shows the schematic diagram of the

electric circuit and the core of a 400 kV 5-limb transformer as an example. The black lines represent the electric circuit on the HV side, while the blue lines and the red lines are the parts on the LV side and TV side respectively. The voltage source V_{AC} is connected on the HV side, and the LV side and the TV side are open-circuited. In the new model, the transformer parameters are all referred to the HV side. The DC voltage input is provided at the transformer neutral point because GIC is caused by the quasi-DC electric field on the Earth's surface.

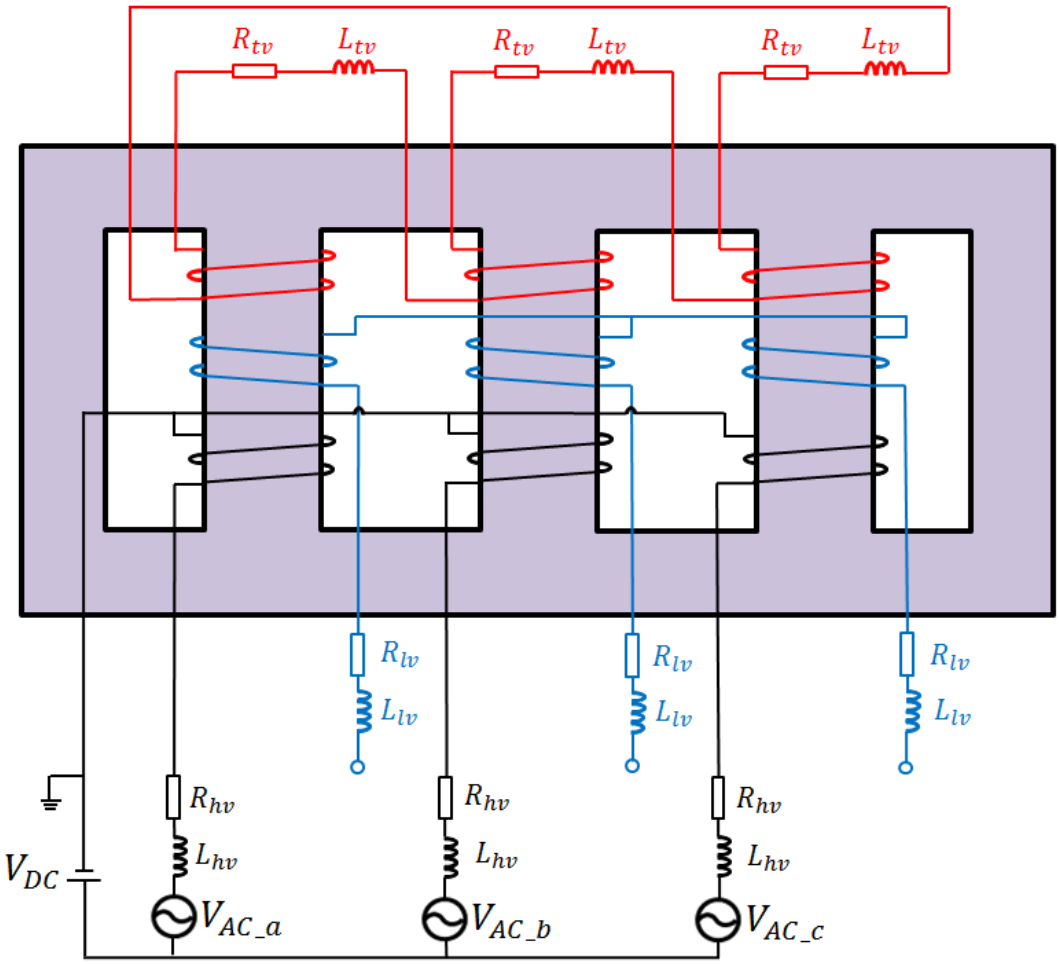

Figure 4-7: New model including equivalent electrical circuit and core for a 400 kV 5-limb *YNyd* transformer.

where

L_{hv}	HV winding inductance (mH)
L'_{lv}	LV winding inductance referred to HV side (mH)
L'_{tv}	TV winding inductance referred to HV side (mH)
R_{hv}	HV winding resistance (Ω)

R'_{lv}	LV winding resistance referred to HV side (Ω)
R'_{tv}	TV winding resistance referred to HV side (Ω)
$[V_{AC}]$	AC voltage matrix, $[V_{AC\_a};V_{AC\_b};V_{AC\_c}]$(V)
V_{DC}	DC voltage source (V)

4.3.1.1 Equivalent electric circuit

The equivalent electric circuit is built based on the classic transformer equivalent model as introduced in Section 2.4. The equivalent electric circuit requires the parameters of winding resistance and leakage inductance calculated from the transformer short circuit test report, so that the new model can calculate the electromotive force added on the core as Eq. 4.1.

$$[E_1] = [V_{hv}] - [I_{hv}]R_{hv} - L_{hv}\frac{d[I_{hv}]}{dt} \tag{4.1}$$

where

$[E_1]$	Electromotive force matrix, $[E_{1a};E_{1b};E_{1c}]$(V)
$[I_{hv}]$	HV winding current matrix, $[I_{hv\_a};I_{hv\_b};I_{hv\_c}]$ (A)
R_{hv}	HV winding resistance (Ω)
L_{hv}	HV winding inductance (mH)
$[V_{hv}]$	HV winding voltage source (V)

Then the phase limb flux density, which is applied as the input of the equivalent magnetic circuit, can be calculated as Eq. 4.2.

$$[B_{limb}] = [\Phi_{limb}]/A_{limb} = -\frac{1}{N \cdot A_{limb}} \cdot \int [E_1]dt \tag{4.2}$$

where

A_{limb}	Cross-sectional area matrix of main limbs (m^2)
$[B_{limb}]$	Magnetic flux density matrix for limbs, $[B_a;B_b;B_c]$(T)
N	HV winding turn number
$[\Phi_{limb}]$	Magnetic flux matrix for limbs $[\Phi_a;\Phi_b;\Phi_c]$ (Wb)

The flux density distribution $[B]$ and the phase magnetising current $[I_m]$ will be calculated according to the equivalent magnetic circuit to be introduced in Section 4.3.1.2.

After calculating the TV winding current according to Eq. 4.3, the HV winding current can be obtained as the sum of the magnetising current as shown in Eq. 4.4.

$$E_{1a} + E_{1b} + E_{1c} = 3 \cdot \left(I'_{tv} \cdot R'_{tv} + L'_{tv} \frac{dI'_{tv}}{dt} \right) \tag{4.3}$$

$$[I_{hv}] = [I_m] + [I'_{tv}] \tag{4.4}$$

where

$[I_m]$ Magnetising current matrix, $[I_{ma}; I_{mb}; I_{mc}]$ (A)

$[I'_{tv}]$ TV winding current matrix, $[I'_{tv\_a}; I'_{tv\_b}; I'_{tv\_c}]$ (A)

L'_{tv} TV winding inductance referred to HV side (mH)

R'_{tv} TV winding resistance referred to HV side (Ω)

The HV winding current $[I_{hv}]$ will be fed back to Eq. 4.1 for the calculation for the next time step.

It is worth mentioning that the initial residual flux in main limbs needs to be set properly as Eq. 4.5, or the model requires a long time to cancel the residual flux and return to normal operation state.

$$[B_{limb(0)}] = -\frac{1}{N \cdot A_{limb}} \cdot \int [V_{AC(0)}] dt \tag{4.5}$$

where

$[B_{limb(0)}]$ Initial magnetic flux density matrix for limbs $[B_{a(0)}; B_{b(0)}; B_{c(0)}]$ (T)

$[V_{AC(0)}]$ Initial AC voltage matrix $[V_{AC\_a(0)}; V_{AC\_b(0)}; V_{AC\_c(0)}]$ (V)

For example, if the AC voltage source of Phase A is a sinusoidal wave as shown in Eq. 4.6, the limb flux density of Phase A can be calculated as Eq. 4.7.

$$V_{AC\_a} = V_{AC\_peak} \cdot \sin(2\pi f t) \tag{4.6}$$

$$B_{a(0)} = \frac{V_{AC\_peak}}{2\pi \cdot A_{limb} \cdot N \cdot f} \cdot \cos(2\pi f t) = \frac{V_{AC\_rms}}{4.44 \cdot A_{limb} \cdot N \cdot f} \tag{4.7}$$

where

f	Frequency (Hz)
V_{AC_rms}	RMS value of AC voltage input (V)
V_{AC_peak}	Peak value of AC voltage input (V)

4.3.1.2 Equivalent magnetic circuit

Figure 4-8 shows the schematic diagram of the 5-limb transformer core which contains the leakage flux paths consisting of the insulation oil gaps and the tank. There is a total of 5 leakage paths, including 2 paths of the side limbs. The labels in Figure 4-8 represent the flux densities at various locations of the core. The default directions of flux flows are defined as the blue arrows for the convenience of understanding the equations.

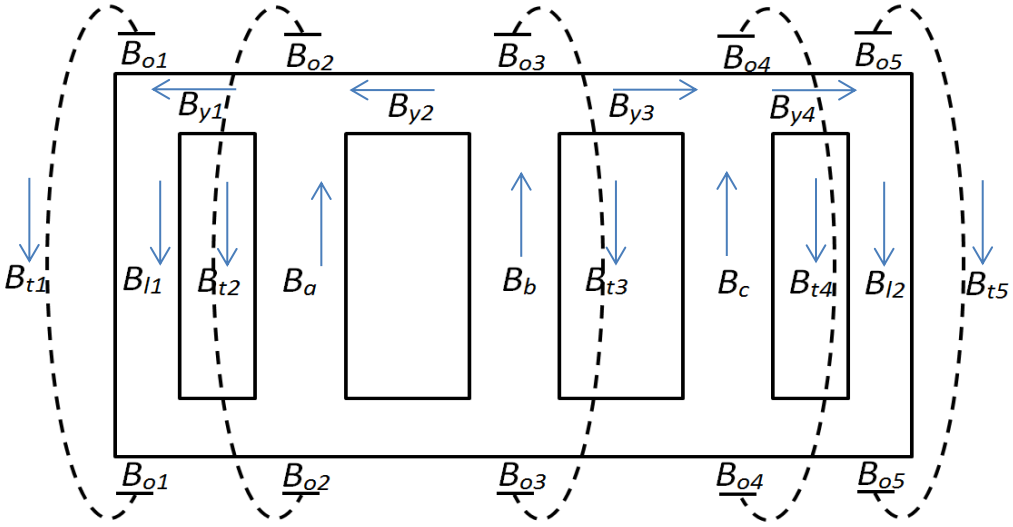

Figure 4-8: Schematic diagram of 5-limb transformer core including oil gaps and tank flux paths.

There are several assumptions made to the core model.

- The limb and yoke flux is assumed to be evenly distributed.
- The leakage flux is assumed to leak out of the core limbs to the oil gaps to the tank.
- The equivalent oil gap length is equal to the shortest distance between the core and the tank, while the oil gap area is set to be the cross-sectional area of the limbs.
- The equivalent length of the tank paths is assumed to be the sum of the tank width and the tank height. The cross-sectional area of the tank path is

calculated as the perimeter of the top/bottom of the tank multiplied by the thickness of the tank.

- No magnetic shield is used on the tank.

The flux distribution and the phase magnetising current will be calculated in the equivalent magnetic circuit according to Kirchhoff's Magneto Motive Force Law and Ampere's Law.

- Equations based on Kirchhoff's Magneto Motive Force Law

At each cross area of the limbs and the yokes, the flux entering into the node is equal to the flux leaving from the node as described in Eq. 4.8 - Eq. 4.12. In addition, the flux in the tank is equivalent to the flux in the oil gap for each leakage path as expressed in Eq. 4.13.

$$B_{y1} \cdot A_{y1} = B_{l1} \cdot A_{l1} + B_{o1} \cdot A_{o1} \tag{4.8}$$

$$B_a \cdot A_a + B_{y2} \cdot A_{y2} = B_{y1} \cdot A_{y1} + B_{o2} \cdot A_{o2} \tag{4.9}$$

$$B_b \cdot A_b = B_{y2} \cdot A_{y2} + B_{y3} \cdot A_{y3} + B_{o3} \cdot A_{o3} \tag{4.10}$$

$$B_c \cdot A_c + B_{y3} \cdot A_{y3} = B_{y4} \cdot A_{y4} + B_{o4} \cdot A_{o4} \tag{4.11}$$

$$B_{y4} \cdot A_{y4} = B_{l2} \cdot A_{l2} + B_{o5} \cdot A_{o5} \tag{4.12}$$

$$B_{ok} \cdot A_{ok} = B_{tk} \cdot A_{tk} \quad where\ k = 1, 2, 3, 4, 5 \tag{4.13}$$

where

$[A]$ Cross-sectional area matrix for all structural parts (m^2)

$[B]$ Flux density matrix for all structural parts (T)

- Equations based on Ampere's Law

The integral form of the Ampere's circuital law is a line integral of the magnetic field around each closed loop. Since the magnetic field is assumed to be evenly distributed at each part of the core, tank and oil gaps, one equation can be obtained for each magnetic circuit closed loop as displayed in Eq. 4.14 – Eq. 4.19. For example, Eq. 4.15 is obtained from the closed loop as marked as the red lines in Figure 4-9.

$$-H_{l1} \cdot l_{l1} + 2H_{o1} \cdot l_{o1} + H_{t1} \cdot l_{t1} = 0 \quad (4.14)$$

$$-H_{l1} \cdot l_{l1} - 2H_{y1} \cdot l_{y1} + 2H_{o2} \cdot l_{o2} + H_{t2} \cdot l_{t2} = 0 \quad (4.15)$$

$$-H_{l1} \cdot l_{l1} - 2H_{y1} \cdot l_{y1} - 2H_{y2} \cdot l_{y2} + 2H_{o3} \cdot l_{o3} + H_{t3} \cdot l_{t3} = 0 \quad (4.16)$$

$$-H_{l1} \cdot l_{l1} - 2H_{y1} \cdot l_{y1} - 2H_{y2} \cdot l_{y2} + 2H_{y3} \cdot l_{y3} + 2H_{o4} \cdot l_{o4} + H_{t4} \cdot l_{t4} = 0 \quad (4.17)$$

$$-H_{l1} \cdot l_{l1} - 2H_{y1} \cdot l_{y1} - 2H_{y2} \cdot l_{y2} + 2H_{y3} \cdot l_{y3} + 2H_{y4} \cdot l_{y4} + H_{l2} \cdot l_{l2} = 0 \quad (4.18)$$

$$-H_{l2} \cdot l_{l2} + 2H_{o5} \cdot l_{o5} + H_{t5} \cdot l_{t5} = 0 \quad (4.19)$$

where

$[H]$ Magnetic field intensities for all structural parts (A/m)

$[l]$ Structural length (m)

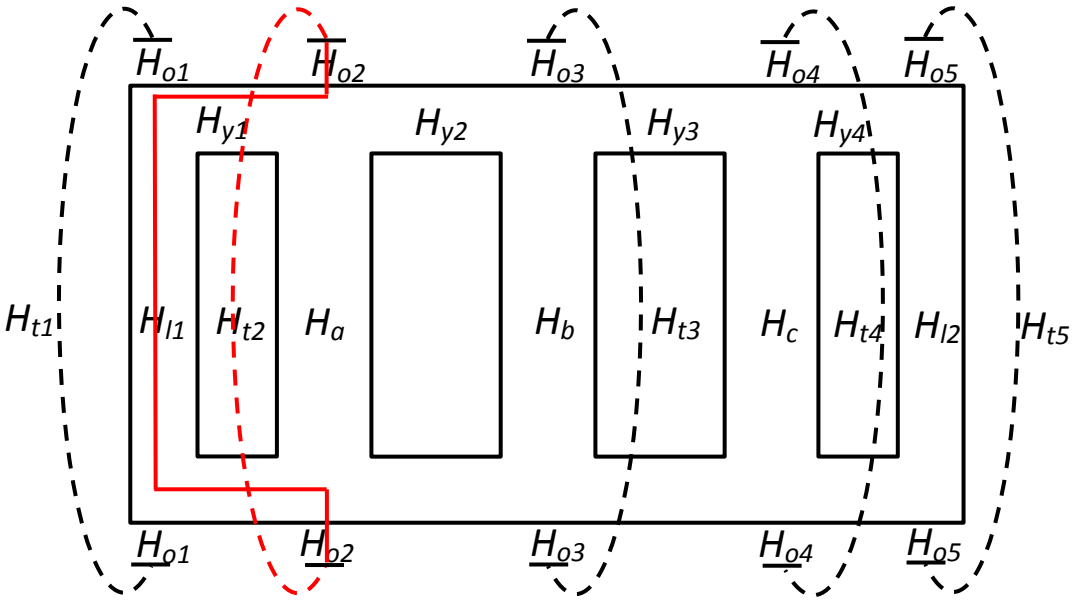

Figure 4-9: Schematic diagram of 5-limb transformer core including oil gaps and tank flux paths.

- B-H curves

The B-H curves of the transformer core, the tank and the oil gap are described by Eq. 4.20 – Eq. 4.22 [107]. The B-H curves are drawn in Figure 4-10 for core material M140-27S, the ferromagnetic mild steel tank material and the insulation material which has the same permeability as vacuum. It can be seen that the B-H curve of the core material has a

much higher permeability μ than that of the tank material in the liner region. When the flux density exceeds the knee point, the permeability of the core material drops dramatically to a very low level.

$$H_{core} = 20 \cdot B_{core} + (6.5 \times 10^{-5}) \cdot B^{27}_{core} \tag{4.20}$$

$$H_{tank} = 2250 \cdot B_{tank} + 0.25 \cdot B^{17}_{tank} \tag{4.21}$$

$$H_{oil} = 7.94 \times 10^{5} \cdot B_{oil} \tag{4.22}$$

where

$[B]$ Flux densities for core tank and oil (T)

$[H]$ Magnetic field intensities for core tank and oil (A/m)

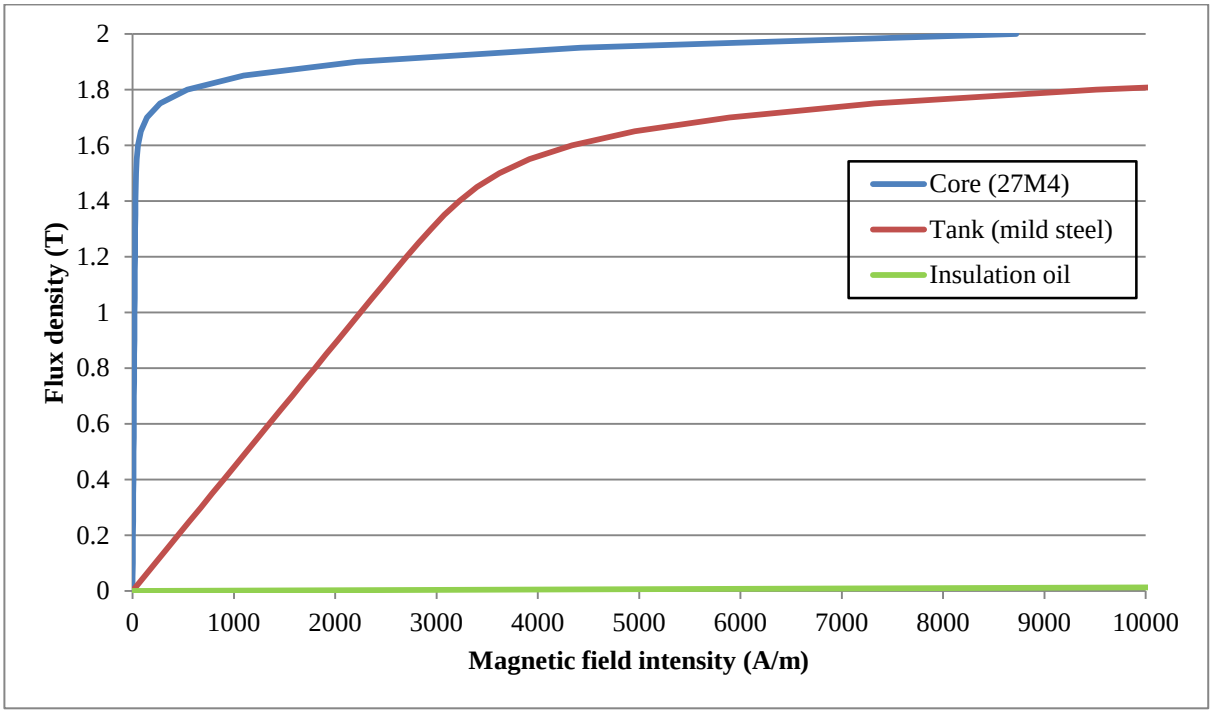

Figure 4-10: B-H curves of core material, tank material and insulation oil.

Combined with all the equations explained above (Eq. 4.8 – Eq. 4.22), once the three-phase limb flux densities (B_a, B_b, B_c) are given as the input to the equivalent magnetic circuit, the flux distribution in the core, tank and oil gaps ($[B]$, $[H]$) can be calculated.

The Magneto Motive Force (MMF) can be derived as Eq. 4.23 according to Hopkinson's law or Rowland's law. Then the phase magnetising currents are obtained from the MMF as shown in Eq. 4.24 – Eq. 4.26.

$$MMF = \oint H \cdot l = \oint \Phi \cdot \mathcal{R} = N \cdot I \tag{4.23}$$

$$I_{ma} = (H_a \cdot l_a + 2H_{o2} \cdot l_{o2} + H_{t2} \cdot l_{t2})/N \tag{4.24}$$

$$I_{mb} = (H_b \cdot l_b + 2H_{o3} \cdot l_{o3} + H_{t3} \cdot l_{t3})/N \tag{4.25}$$

$$I_{mc} = (H_c \cdot l_c + 2H_{o4} \cdot l_{o4} + H_{t4} \cdot l_{t4})/N \tag{4.26}$$

where

MMF	Phase magnetomotive force (A)
$\mathcal{R}$	Reluctance (H^{-1})
$[I_{ma}\ I_{mb}\ I_{mc}]$	Phase magnetising current (A)

Since it is hard to derive the inverse functions of the B-H curves, the iterative method applied in the calculation of the magnetic circuit is the Bisection method with a relative error tolerance of 0.0001%. The bisection method in mathematics is a root-finding method that repeatedly bisects an interval and then redefines a subinterval in which a root must lie for further processing [108].

Figure 4-11 shows the flow chart of the calculation steps of the equivalent magnetic circuit for one time instant. First of all, the equivalent magnetic circuit receives the main limbs flux densities from the equivalent electric circuit. The initial upper limit value B_{l1_max} and lower limit value B_{l1_min} for the left side limb flux are assumed far beyond the practical flux densities, say 10 T and -10 T. The average value B_{l1_ave} of the upper limit B_{l1_max} and the lower limit B_{l1_min} keeps updating in every loop.

The flux densities and the magnetic field intensities can be derived from Eq. 4.8- Eq. 4.18 and Eq. 4.20- Eq. 4.22 when B_{l1} equals B_{l1_max}, B_{l1_min} and B_{l1_ave} respectively. Based on Eq. 4.19, the deviation y_{max}, y_{ave} and y_{min} can be written as Eq. 4.27- Eq. 4.29. As shown in Figure 4-11, the check condition is '$y_{max} \cdot y_{ave} < 0$'. If the check condition is satisfied, the correct value of B_{l1} is located between B_{l1_max} and B_{l1_ave}, and thus B_{l1_ave} will be assigned to B_{l1_min}, while B_{l1_max} remains the same. Otherwise, B_{l1_ave} will be assigned to B_{l1_max}, while B_{l1_min} remains the same. In the next loop, B_{l1_ave} will be calculated again based on the updated B_{l1_max} and the updated B_{l1_min}.

$$y_{max} = -H_{l2\_max} \cdot l_{l2} + 2 \cdot H_{o5\_max} \cdot l_{o5} + H_{t5\_max} \cdot l_{t5} \quad (4.27)$$

$$y_{ave} = -H_{l2\_ave} \cdot l_{l2} + 2 \cdot H_{o5\_ave} \cdot l_{o5} + H_{t5\_ave} \cdot l_{t5} \quad (4.28)$$

$$y_{min} = -H_{l2\_min} \cdot l_{l2} + 2 \cdot H_{o5\_min} \cdot l_{o5} + H_{t5\_min} \cdot l_{t5} \quad (4.29)$$

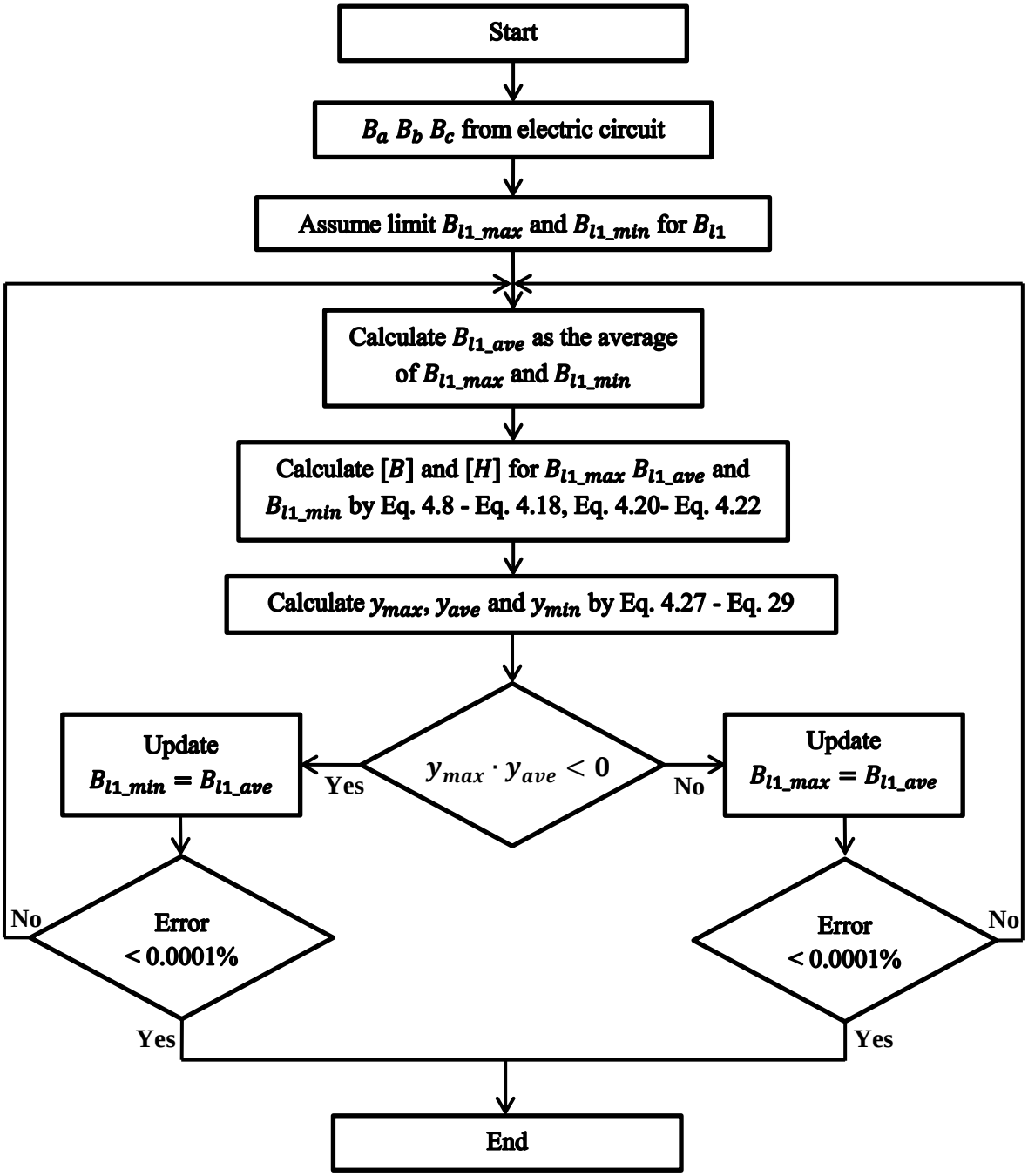

Figure 4-11: Flow chart of equivalent magnetic circuit calculation by using bisection method

After a few tens of the calculation loops, the upper limit and the lower limit will keep being updated and approach each other. Finally, the difference between them will be lower than 0.0001% of the final flux density.

Overall, after the limb flux densities are provided, the magnetic circuit can obtain the phase magnetising currents and feed them back to the equivalent electric circuit.

4.3.2 Transformer parameter setting

In this section, the model is validated under AC+DC input by the five-limb transformer used in the Finnish measurement as an example [13]. However, neither the winding resistance nor the dimension of the tank and the core are given in the paper. The validation aims to show the major characteristics and similarities rather than specific details.

Table 4-6 shows the fundamental information of the 5-limb transformer applied in the simulation. The winding resistance is not provided in the paper [13], so the parameters of a 400 kV UK transmission transformer are used in the simulation.

Table 4-6: Transformer basic information to be applied in simulation.

Voltage	400/120/21 kV
Winding connection	*Y-y-d*
Core type	5-limb
Winding resistance (HV/TV referred to HV side)	1.060/ 3.683 Ω
Leakage inductance (HV/TV referred to HV side)	496/ 2706 mH

According to the assumptions of the equivalent magnetic circuit, Table 4-7 provides the equivalent length and the equivalent cross-sectional area of the tank paths and the oil gaps calculated from the tank and the core physical size as shown in Figure 4-12. It is necessary to note that the width of the tank is 2 m since it cannot be displayed in a 2D figure.

Table 4-7: Transformer dimensions of the 5-limb transformer applied in the equivalent magnetic circuit.

Main limb length/ side limb length (m)	2.79/2.79
Main yoke length/ side yoke length (m)	2.57/1.65
Oil gap length for main limbs/ side limbs (m)	0.223/0.1
Tank path length (m)	5.94
Main limb cross-sectional area (m^2)	0.6438
Side limb/ main yoke/ side yoke cross-sectional area (m^2)	0.3884
Oil gap area for main limbs/ side limbs (m^2)	0.6438/0.3884
Tank path cross-sectional area (m^2)	0.2268

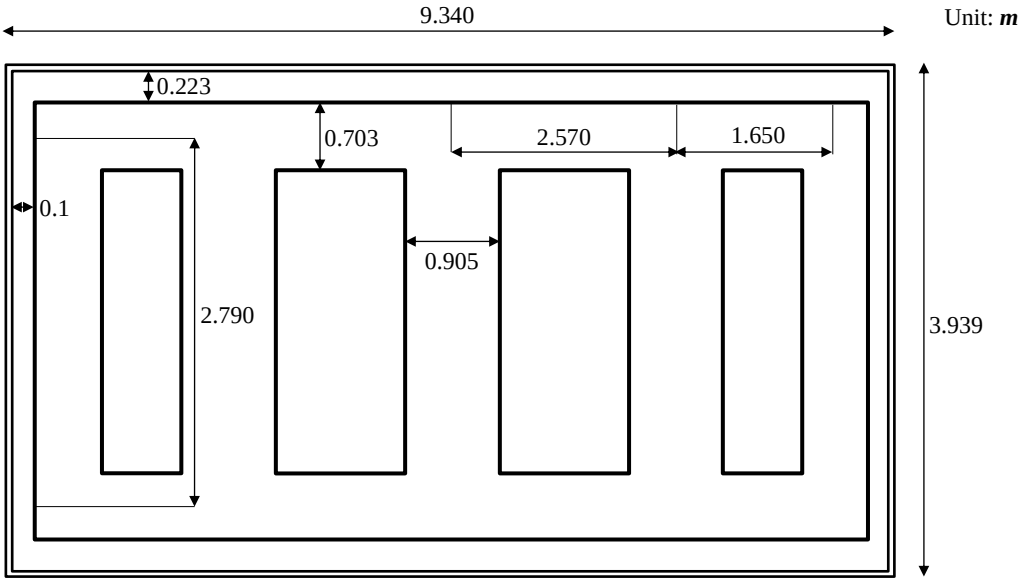

Figure 4-12: Structural dimension of 5-limb core and tank.

In [26], the flux leakage path for a 3-limb core was simulated as a tank path in series with an adjustable air gap. The adjustable air gap is also commonly used in Finite Element magnetic simulation to represent core joint in order to achieve the same open circuit test results. For a 5-limb core, each limb has its own air gap representation, as Phase B is situated at the middle limb, its leakage path could be different from those of Phase A and Phase C, to match simulation to measurement results, Phase B oil gap area

was increased to 1.7 times of its original value in Section 4.3.3 whist tank path cross section area and length are kept same for all three phases. This change (1.7 times) was made by trial and error.

To match simulation to measurement results of delta winding currents, one more parameter change was also made for three phase tertiary winding leakage reactance in Section 4.3.3. The TV winding leakage inductance is reduced to 1/5 of its original value, which was determined by trial and error.

The justification of parameter adjustment above is an area for future work. Moreover, the sensitivity study in Chapter 5 is designed to show the impacts of each parameter on the simulation results.

4.3.3 Simulation results under nominal AC+ 200 A DC input

In this section, AC+DC voltage input will be provided to the new model. The simulation results will be compared to the measurement results of a 400 kV 5-limb transformer from Finnish Grid. For fair comparison, the DC voltage is provided with the magnitude of 70.7 V, so that the final steady state DC current in the HV winding stabilises at 66.7 A per phase.

4.3.3.1 Current waveforms in whole duration

Figure 4-13 (a), (b) and (c) shows the HV winding current, the magnetising current and the TV delta winding current of Phase A referred to the HV side. Within 30 s, the currents finally reach a steady state. The peak of the HV winding current in the steady state is 328.5 A because the core is fully saturated by the DC neutral input. The peak-to-peak of TV winding current is much lower than that of the HV winding current and the magnetising current.

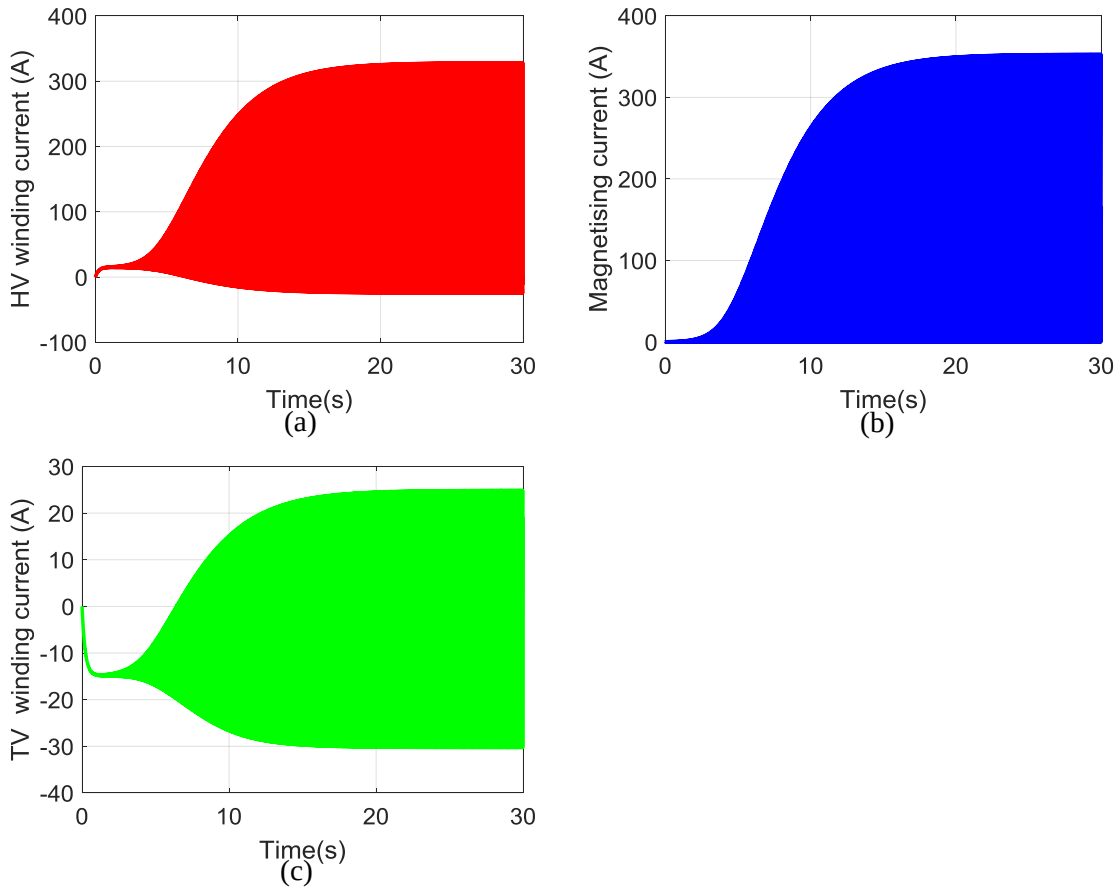

Figure 4-13: Phase A HV current I_{hv_a} (b) Phase A magnetising current I_{ma} (c) Delta (TV) winding current I_{tv_a} over 30 s.

The DC current magnitudes are calculated by frequency spectrum in transient. Figure 4-14 shows the DC components in the HV winding current, magnetising current and TV winding current over 30 s. The DC component in the delta winding current is reversed to give a clearer comparison to the other DC current waveforms. The current curves are divided into four stages.

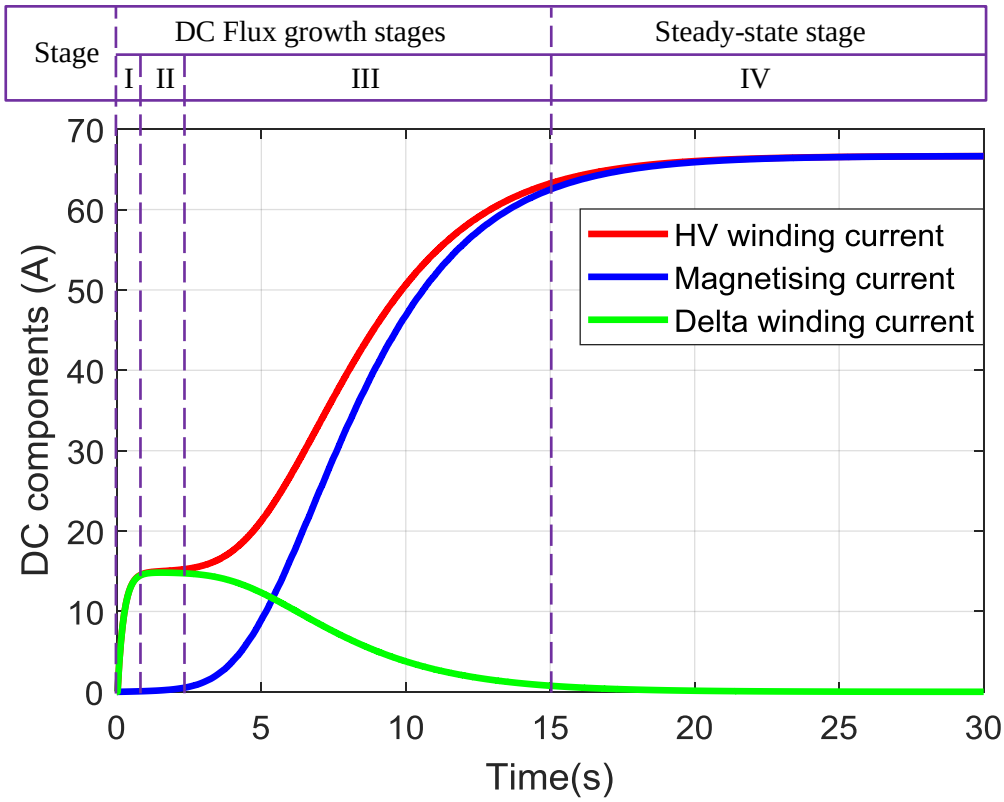

Figure 4-14: DC Components in HV winding current, magnetising current and delta winding current over 30 s.

- **Stage I:**

Stage I is a step response period caused by the winding resistance and the leakage inductance. As can be seen in Figure 4-15, in the first 40 cycles or so, the AC magnitudes in the magnetising current are close to the open circuit current. Meanwhile, the HV winding current waveform is composed of AC and DC currents, and the DC current starts to be built in the delta winding. In Stage I, the core is still operating in the linear area. Figure 4-16 displays the equivalent DC circuit for the transformer. The core impedance behaves as an open circuit branch to DC current, so the DC currents only rise in the HV winding and the delta winding in this stage. The increasing rate of the DC current is determined by the inductances of the HV winding and the delta winding. The impact of the winding inductance will be further discussed in Chapter 5.

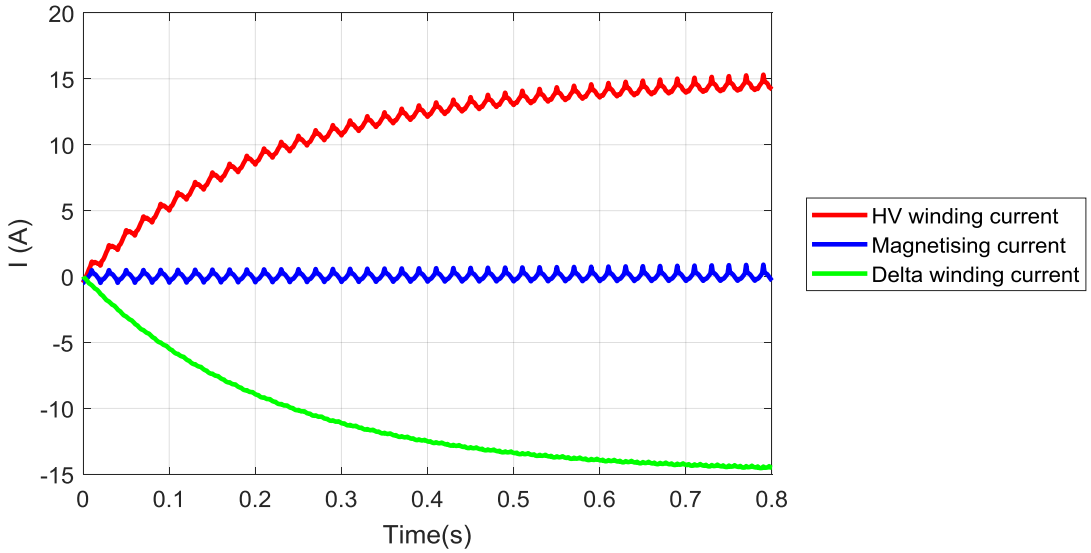

Figure 4-15: HV winding current, magnetising current and delta winding current in Stage I.

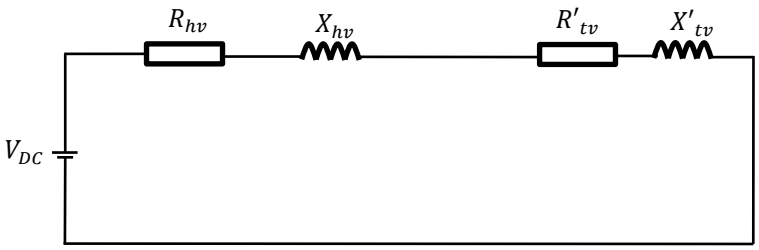

Figure 4-16: Simplified single-phase DC equivalent circuit in Stage I and Stage II.

- **Stage II:**

Stage II is the pseudo flat stage after the step response stage. As can be observed from Figure 4-17, the AC current magnitudes of the HV winding current and the magnetising current grow slowly, and the DC current in the HV winding current is stable. In terms of the delta winding current, it contains very low AC components while the DC components keep steady. According to the equivalent DC circuit in stage II as shown in Figure 4-16, the DC currents in the HV winding and the delta winding can be calculated by Eq. 4.30. This steady DC magnitude in this stage is determined by the HV winding resistance and the delta winding resistance. The continuous DC electromotive force added on the core leads to the DC flux accumulating in the core and gradually pushes the core into saturation area, which can explain the reason why the AC current magnitudes of the HV winding current and the magnetising current increase as observed in Figure 4-17.

$$I_{dc\_II} = \frac{V_{DC}}{R_{hv} + R'_{tv}} = \frac{70.67\ V}{(1.06 + 3.68)\ \Omega} = 14.90\ A \tag{4.30}$$

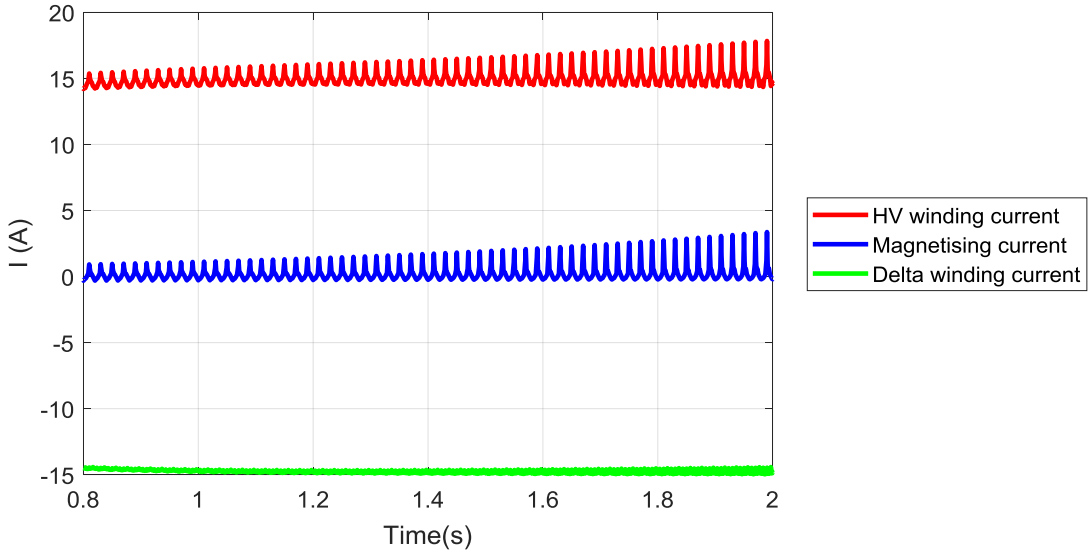

Figure 4-17: HV winding current, magnetising current and delta winding current in Stage II.

- **Stage III:**

As can be seen in Figure 4-18, the AC magnetising current and the AC HV winding current show a rapid increase in Stage III due to the core saturation effect. Large quantities of harmonics are produced in the HV winding current, magnetising current and delta winding current. On the one hand, the DC components in the magnetising current rise and gradually approach that in the HV winding current. On the other hand, the DC components in the delta winding slowly decrease to zero. The DC flux produced in the limbs becomes higher in this stage, so that it has to leak out of the core to the tank via the oil gaps. In addition, the saturation of the core leads to its high reluctance and thus low core impedance, so that the part of the HV winding DC current flows in the core branch becomes higher as shown in Figure 4-19. The core resistance is so large compared to winding impedance that the core resistance branch is neglected in the equivalent circuit. When the currents approach the final steady state, their increasing rates will become slower.

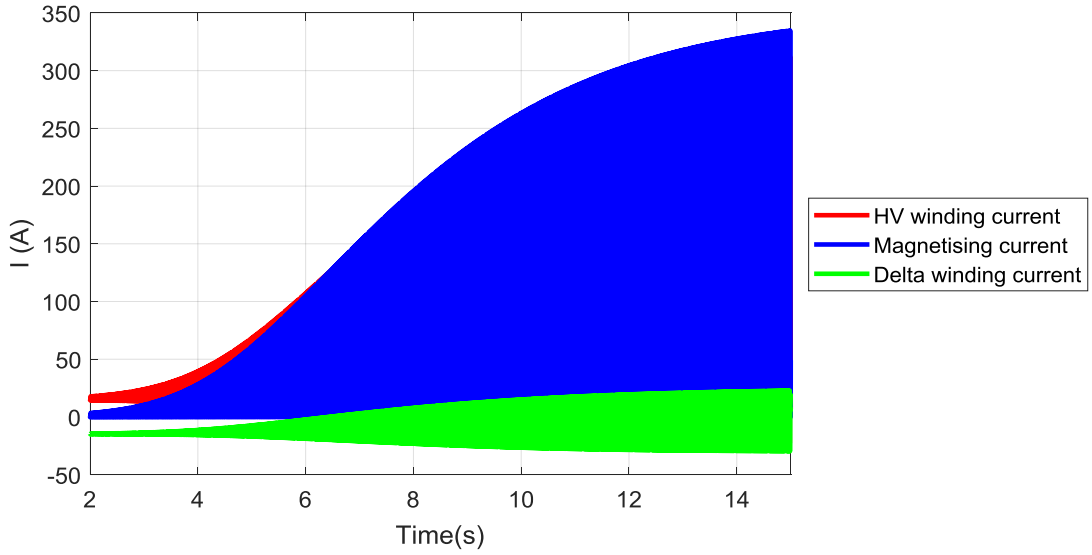

Figure 4-18: HV winding current, magnetising current and delta winding current in Stage III.

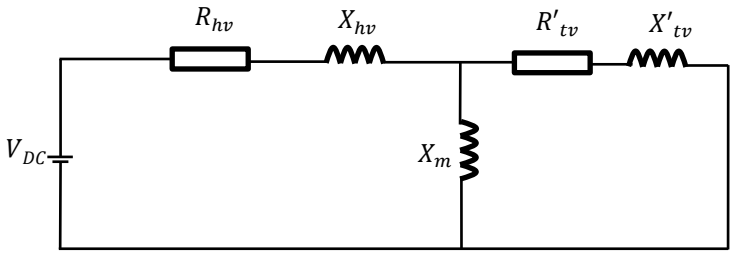

Figure 4-19: Simplified single-phase DC equivalent circuit in Stage III.

- **Stage IV:**

In Stage IV, Figure 4-20 illustrates that both AC and DC components in the currents reach the steady state. The delta winding current contains high-magnitude harmonics. However, no DC current exists in the delta winding anymore because the core branch will provide a short-circuit path for DC current after the core reaches a deep saturation state as can be seen in Figure 4-21. The final steady current can be calculated as Eq. 4.31.

$$I_{dc\_IV} = \frac{V_{DC}}{R_{hv}} = \frac{70.67\ V}{1.06\ \Omega} = 66.67\ A \tag{4.31}$$

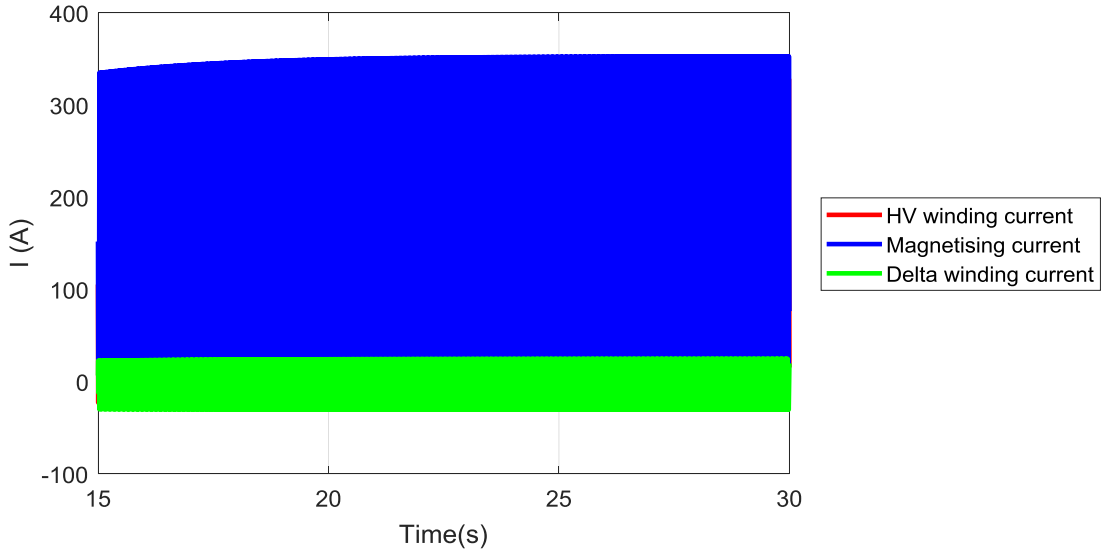

Figure 4-20: HV winding current, magnetising current and delta winding current in Stage IV.

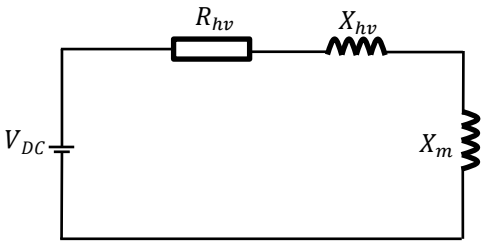

Figure 4-21: Simplified single-phase DC equivalent circuit in Stage IV.

4.3.3.2 Verification in steady state

Finnish Grid paper [13] provides 2 cycles of the HV winding current and delta winding current waveforms in the steady state. In this section, the simulated results will be compared with the measured results both under 200 A neutral DC current injections.

The optimization is to expand the Phase B oil gap cross-sectional area to 1.7 times its original value and to reduce the TV winding leakage inductance to 1/5 its original value. Figure 4-22 shows the comparison between the simulation results with the original parameters and the measurement results. It reveals that the peak of Phase B HV winding current simulated by the new model is slightly lower than the measurement results. In addition, the troughs in the three-phase HV winding currents cannot fit the measurement

results. Therefore, the optimisation of the input parameters as stated above is required to obtain more accurate simulation results.

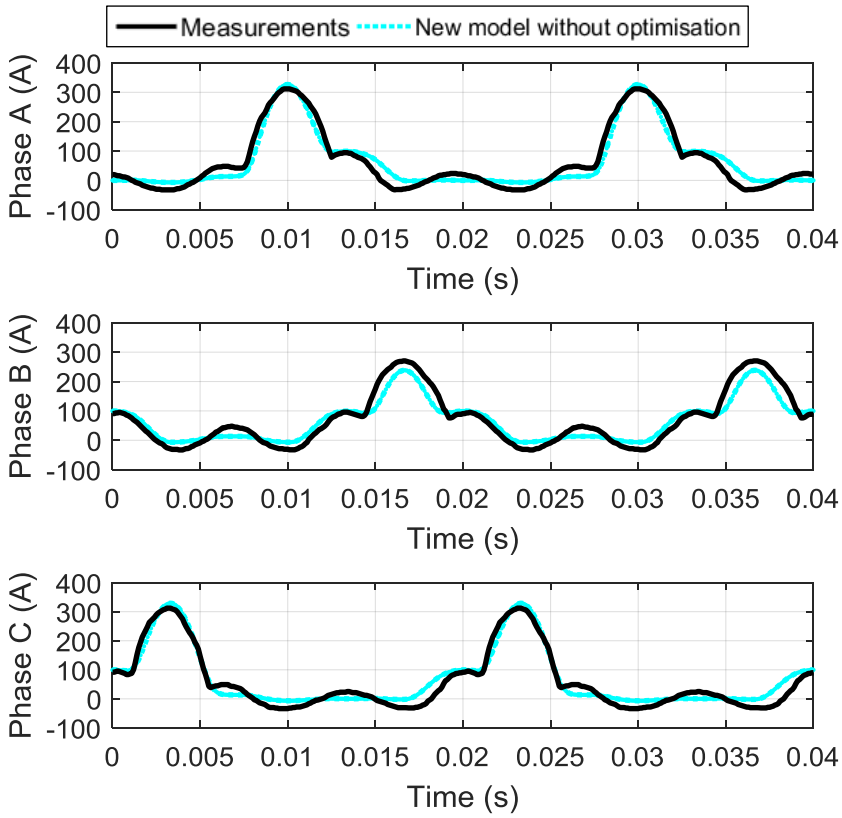

Figure 4-22: Comparison of HV currents between measurements and new model simulation results without optimisation.

- **HV winding current waveform**

After the optimisation, the simulated HV winding current waveforms from the new model match well with the measured results as shown in Figure 4-23. The waveform of Phase A current and Phase C current are symmetrical because the reluctances for Phase A and Phase C are the same due to geometric symmetry, whereas Phase A and Phase B will be different, especially when the core reaches the deep saturation area during GMD events. Therefore, both the measured and the simulated results illustrate that Phase B current has relatively lower peaks compared to those of Phase A.

There are minor differences in the waveforms of HV winding currents between measurement results and those produced by the new model. The difference is likely to be controlled by the composition of harmonics hence the frequency spectra are analysed.

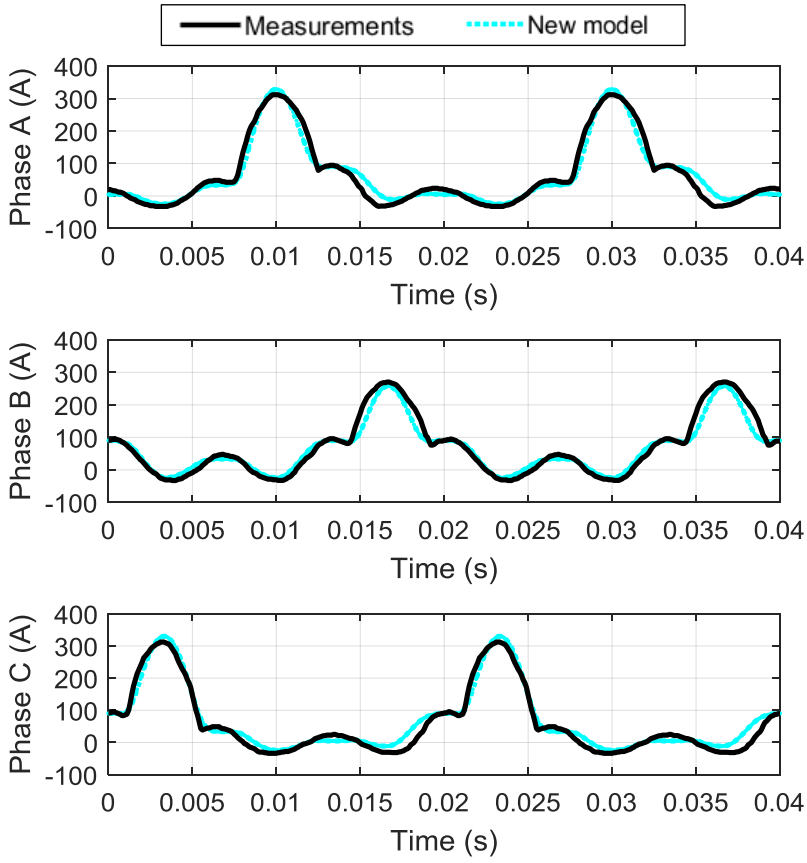

Figure 4-23: Comparison of HV currents between measurements and new model simulation results.

- **HV current frequency spectrum**

Figure 4-24 shows the comparative frequency spectra results between Phase A and Phase B HV winding current, both in magnitude as well as in phase angle. Comparisons for Phase C results are not presented because of their close identity with Phase A results. For Phase A and Phase B HV winding currents, the fundamental frequency component is the largest, followed by the 2nd harmonics and the 4th harmonics. The Phase A fundamental frequency component produced by the new model is 7% lower than the measured one, and Phase B is 16% lower.

Phase A current has a significant amount of 3rd harmonic, whist Phase B has an insignificant amount. The Phase A 3rd harmonic component produced by the new model is 58% higher than the measured one, which may result in the waveform difference between the simulated and measured Phase A current in Figure 4-23, whilst close matches can be found for Phase B current waveforms.

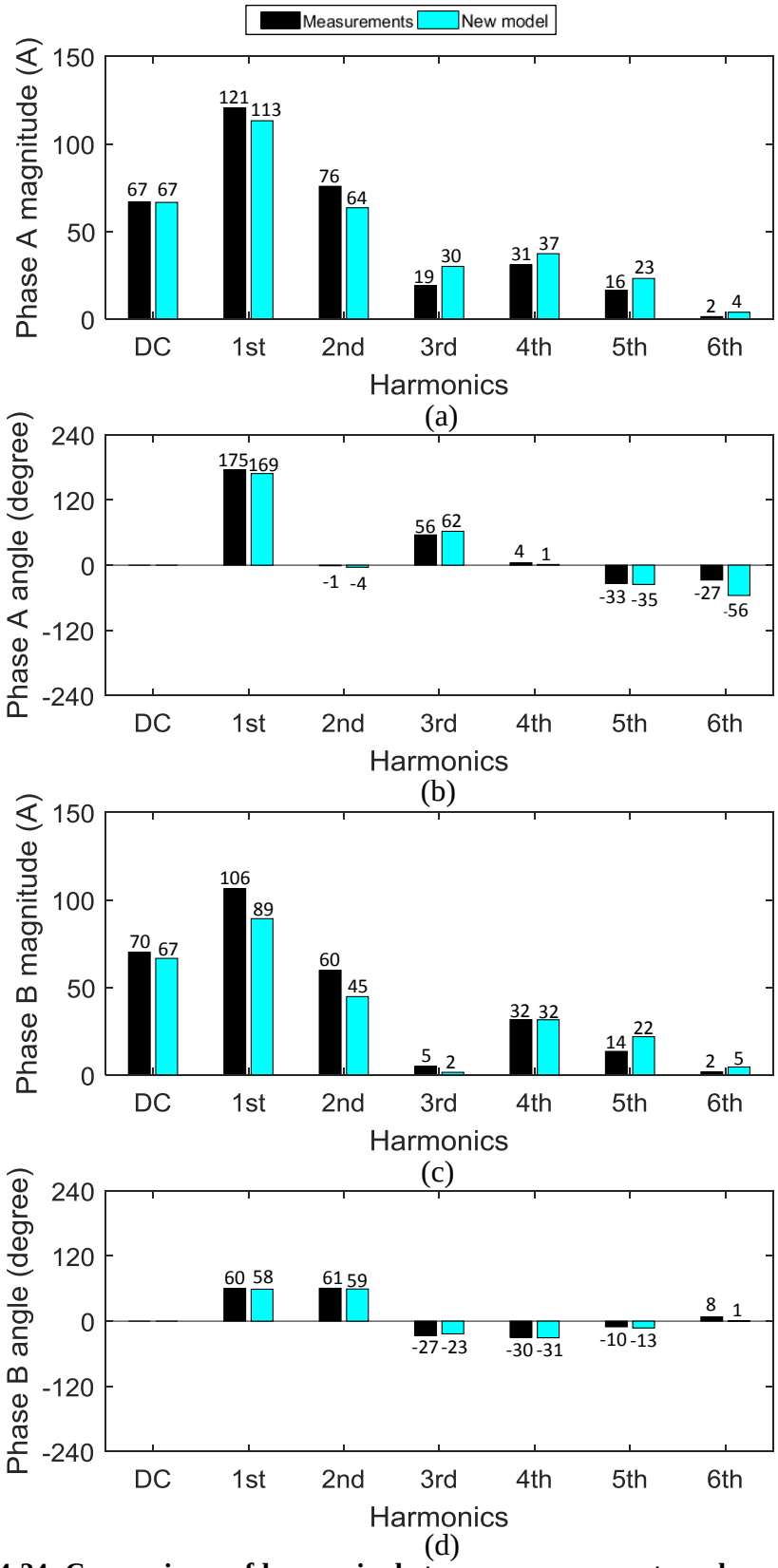

Figure 4-24: Comparisons of harmonics between measurements and new model simulation results (a) Phase A magnitude (b) Phase A phase angle (c) Phase B magnitude (d) Phase B phase angle.

- **Delta winding waveform**

Figure 4-25 shows the delta winding current referred to the HV side in the steady state. The simulated TV winding current waveforms from the new model are similar to the measured results as shown in Figure 4-25. The trough magnitudes of the measured and the simulated results are very close. In terms of the peaks, the magnitudes of the three peaks of the simulated results in one period are different from those of the measured results. The measured results show three peaks with approximately identical magnitudes; however, the simulated results show that the peak produced by Phase B saturation is lower than the other two peaks. The difference between the simulated and the measured results should be further analysed by comparing the frequency spectra of those waveforms, and carry out sensitivity study on the core and tank B-H curves.

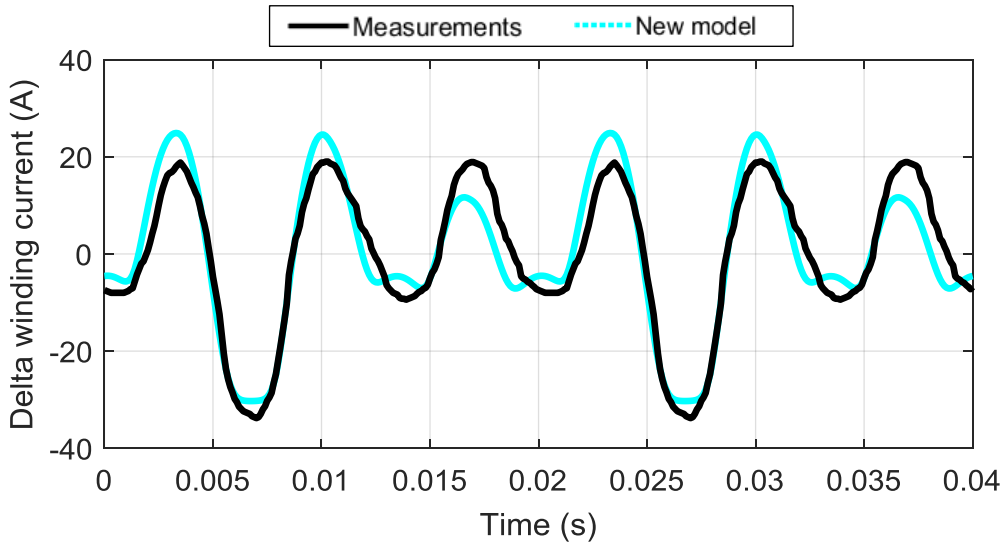

Figure 4-25: Comparison of Delta winding currents between measurements and new model simulation results.

4.3.3.3 Flux density analysis

The model can provide flux distribution during the whole simulation period. Figure 4-26 (a), (b) and (c) displays Phase A and Phase B HV winding currents, magnetising currents and three-phase delta winding currents in a steady state, and the peaks and troughs of the HV winding currents are explained by the delta winding current and the flux distribution as shown in Figure 4-26 (c), (d) and (e). The names of the limbs and the yokes are displayed in Figure 4-8 and Figure 4-9.

As can be seen from Figure 4-26 (a), Phase A winding current has 4 peaks and 2 troughs in the 6 zones of a period as indicated in Figure 4-26. It is worth noting that the magnetising current is less than 1 A when the core is not saturated, and the differences between the HV winding current and the magnetising current are caused by the induced delta winding current as shown in Figure 4-26 (c). The delta winding current is mainly dominated by 3rd harmonic (18.0 A) but also fundamental current, 2nd and 4th harmonics produced by the imbalanced magnetising current due to the core topology. Peak 3, Peak 4, Trough 1 and Trough 2 are all due to the delta winding current. Peak 1 is mainly produced by the value of Phase A limb flux B_a reaching its peak. Peak 2 is produced by the peaks of flux densities in the left side yoke B_{y1} and the tank path B_{t2}, which are the only two paths for Phase A flux as the left main yoke flux B_{y2} is crossing zero.

Similarly, Phase B HV winding current has 4 peaks and 2 troughs as displayed in Figure 4-26 (b). Peak 1 is produced by the saturation of the right main yoke B_{y3} and the tank path B_{t3}, which are the only two paths for phase B flux as the left main yoke flux B_{y2} equals zero. Peak 2 is generated by the consequential saturation peak of Phase B limb B_b. Peak 3 is produced by the flux peaks of the left main yoke B_{y2} and the tank path B_{t3}, which are the only two magnetic paths for Phase B as the right main yoke flux B_{y3} is crossing zero. Peak 4, Trough 1 and Trough 2 are due to delta winding current.

The main limbs are half-cycle saturated by the DC injection in a steady state. However, compared to the main limbs, the main yokes and the side yokes are more likely to produce large extra core losses, because the main yoke flux densities (B_{y2}, B_{y3}) and the side yoke flux densities (B_{y1}, B_{y4}) exceed 1.60 T for 52% and 65% of the time respectively in a single period (0.02 s), which could lead to overheating problems in the transformer core. In the meantime, the limb flux densities B_a/B_c and B_b exceed 1.60 T for 33% and 30% of a single period. The flux density at the tank path B_{t2}/B_{t3} also has high magnitude; thus the overheating for the tank would be more severe due to the tank material nature of non-orientation.

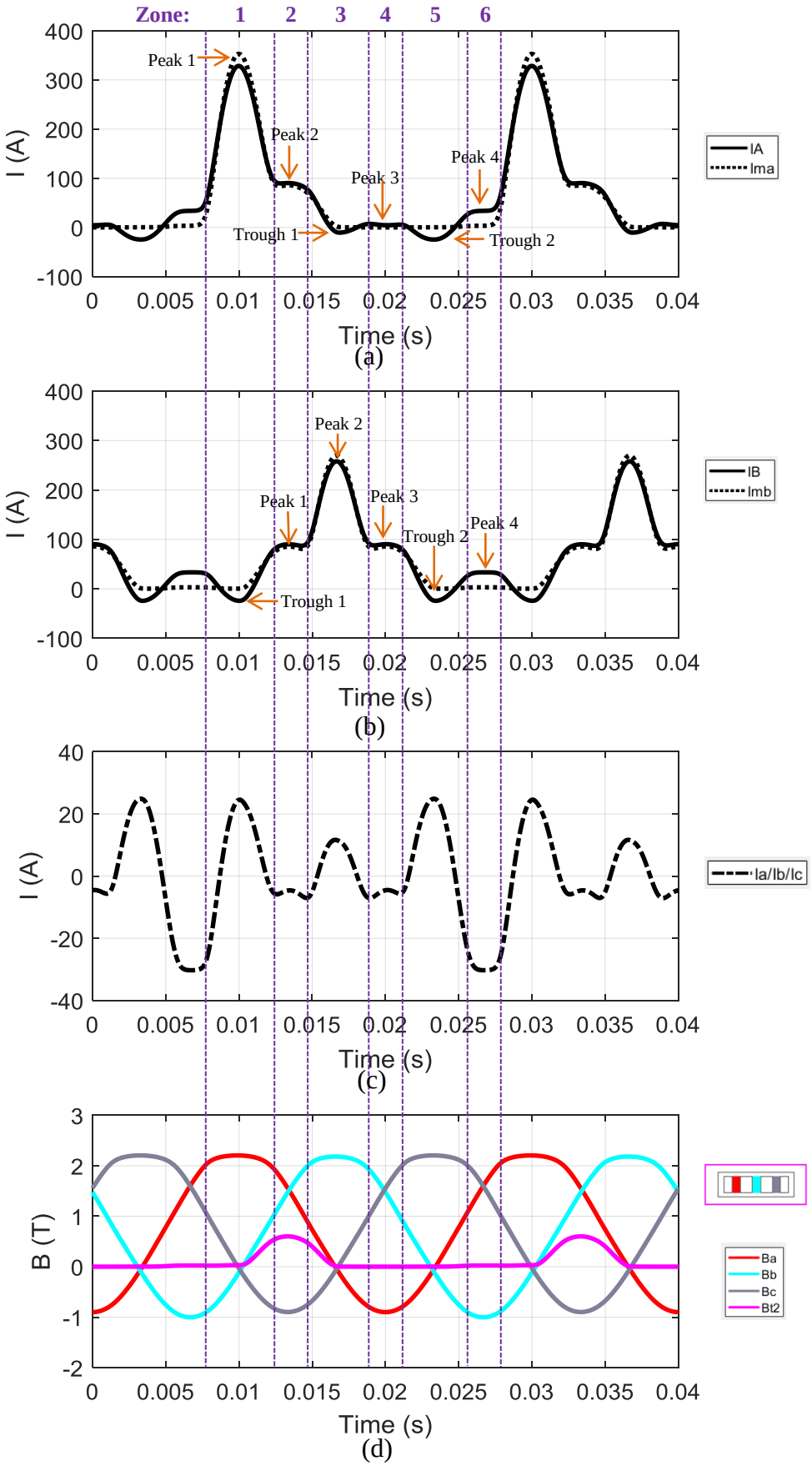
Zone: 1 2 3 4 5 6
Peak 1
Peak 2
Peak 3
Peak 4
Trough 1
Trough 2
I (A)
Time (s)
IA
Ima
(a)
IB
Imb
(b)
Ia/Ib/Ic
(c)
B (T)
Ba
Bb
Bc
Bt2
(d)

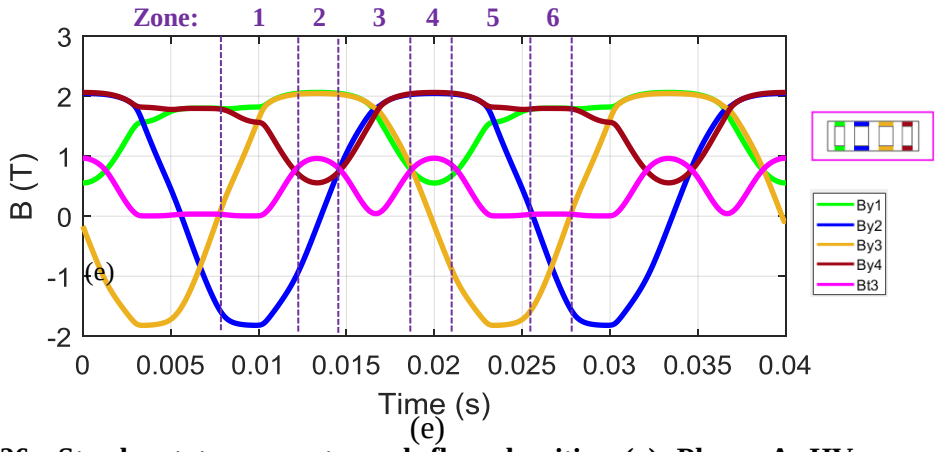

(e)

Figure 4-26: Steady state currents and flux densities (a) Phase A HV current I_A, magnetising current I_{ma} (b) Phase B HV current I_B, magnetising current I_{mb} (c) Delta (TV) winding current I_a, I_b, I_c (d) flux densities of limbs and tank (e) flux densities of yokes and tank.

4.3.3.4 Voltage drop

DC offset has potential to cause a significant voltage drop added on transformer core. Figure 4-27 displays the Phase B voltage waveforms added on transformer core with and without the DC offset respectively. Obviously, the voltage on the core is significantly distorted when the DC offset is provided. The RMS calculation results reveal that the voltage on the core has a 4% reduction after the DC offset is added (222 kV with DC offset against 231 kV without DC offset).

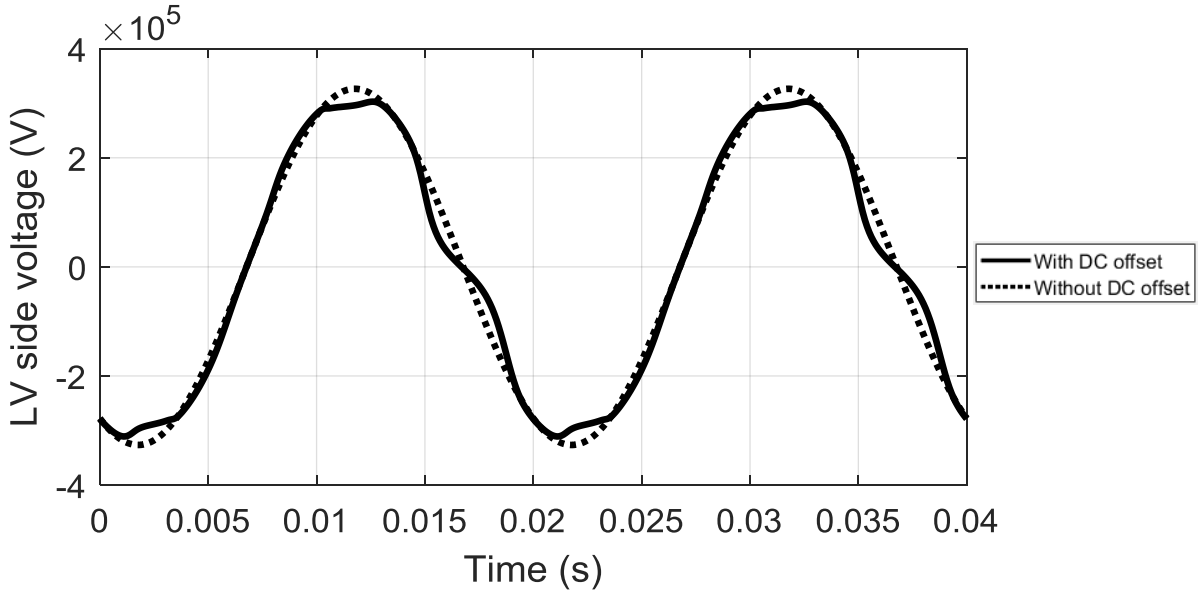

Figure 4-27: Comparison of Phase B electromotive force with and without DC offset.

4.3.4 Summary

Section 4.3 introduces a new transformer model composed of an equivalent electric circuit and an equivalent magnetic circuit, which contains the flux leakage paths through the oil gaps and the tank walls for all the limbs. Therefore, this model enables transient simulations of the winding currents, the magnetising currents and the flux distribution in the core and through the leakage flux paths. When the nominal AC input and 200 A neutral DC current is provided to the new model, the simulated results are compared with the measured results from a real transformer GIC test. The simulated HV winding current and delta winding current waveforms from the new model match well with the measured results. After the core reaches a steady state, the flux density values in the main yokes and the side yokes can remain at high magnitudes for a long time in a period. Therefore, the risks of having excessive core losses and unacceptable temperature rise in the transformer core can be further assessed by the new model in future work.

This chapter introduces and validates the ATP models and the new model under AC+DC input. The new model shows a greater ability to capture the features of current waveforms and is able to provide detailed information, such as the magnetising current, delta winding current and flux distribution. In Chapter 5, the sensitivity studies will be conducted under AC+DC input for transformer design features, such as the core cross-sectional area, leakage paths dimensions and winding impedance.

Chapter 5: Sensitivity Study for New Model Parameters

5.1 Introduction

In Chapter 4 Section 4.3, some of the parameters used in simulation were adjusted to match the simulation results with the measurement results, i.e. the oil gap cross-sectional area for Phase B leakage path was expanded to 1.7 times its original value, and the TV winding leakage inductance was reduced to 1/5 its original value for all three phases. These modifications have little physical meaning, but to match the simulation results with the measurement results, hence it is necessary to understand how sensitive each parameter used in the simulation impacts the results. In addition, the parameters of the transformers required for simulation are sometimes missing, so it is necessary to find out whether the parameters can be replaced by typical values.

In this chapter, the sensitivity study will mainly focus on core topology, flux leakage paths and transformer winding impedance as follows:

- Core topology
  - Cross-sectional area ratio between yokes and limbs
- Leakage paths
  - Simulation without tank-oil gap leakage paths
  - Equivalent tank path length
  - Equivalent tank path area
  - Equivalent oil gap length
  - Equivalent oil gap area
- Winding impedance
  - HV winding resistance
  - TV winding resistance
  - HV winding leakage inductance
  - TV winding leakage inductance

The steady state results are presented by Phase B HV winding current, the delta winding current and the flux distribution. The results for Phase B are emphasized, since Phase B current is more sensitive to the change in parameters as mentioned above.

Meanwhile, the saturation process is quantified by the DC components in Phase B HV winding current and Phase B limb flux density and the 2nd harmonic contained in Phase B HV winding current. The reasons why these values are recorded are explained as follows:

- The DC components in HV winding currents are the GIC flows between the substations within a power system network.
- The DC offset flux leads to an excessive core loss.
- The 2nd harmonic in the HV winding current has great impacts on relay operations. Moreover, the magnitude of the 2nd current is higher than any other harmonics in HV winding currents.

5.2 Core topology

5.2.1 Cross-sectional area ratio

The purpose of five-limb core configuration is to ease transformer transportation by reducing its height, and the design principle is that the sum of the main yoke and the side yoke cross-sectional area should be close to the main limb cross-sectional area to contain the flux from the limbs. Normally, the main yoke cross-sectional area could be half a limb. Generally, if the transformer height is allowed for transport, it is unnecessary to reduce the main yoke cross-sectional area to half the limb area, say the area ratio of 60% was used for some UK transmission transformers.

In this section, different yoke cross-sectional areas will be simulated in order to assess their performance under GIC input. The sum of the main yoke and side yoke cross-sectional area is larger than or at least equal to the main limb cross-sectional area to guarantee that the yokes are unsaturated under nominal AC input.

Figure 5-1 (a) and (b) shows Phase B HV winding current and the delta winding current in the steady state simulated by the transformers with different yoke cross-sectional area. To assist the analysis of the current waveforms, the flux densities in Phase B limb, the left main yoke, left side yoke and Phase B tank path are displayed in Figure 5-2 (a) and (b). The insets of the peaks of the flux densities are added in Figure 5-2 to show

the waveform differences more clearly. With regard to the legend of Figure 5-1, the main yoke and the side yoke cross-sectional area are presented as proportionate to the main limb cross-sectional area. For example, '60%--50%' means that the main yoke area and the side yoke area are equal to 60% and 50% of the main limb area respectively.

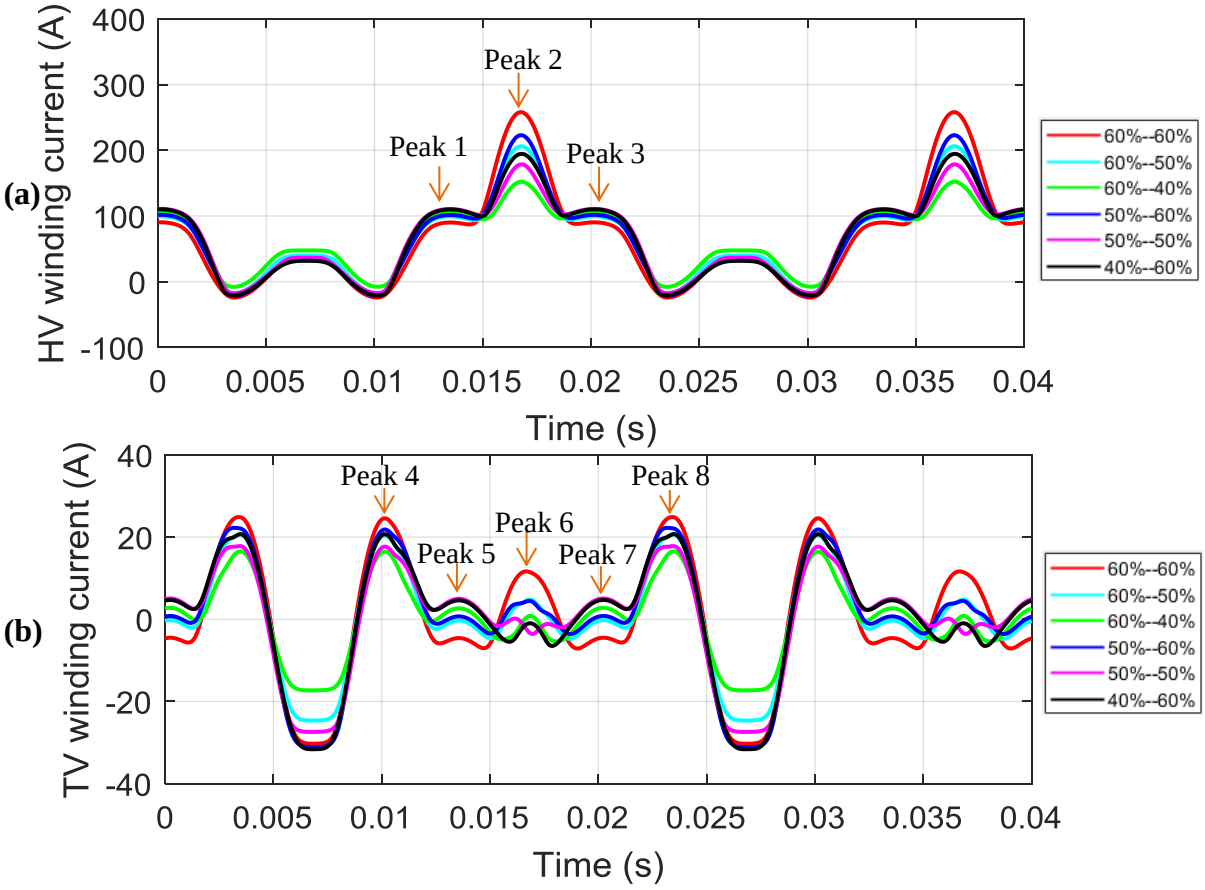

Figure 5-1: (a) Phase B HV winding current (b) Delta winding current in steady state when simulating with different yoke cross-sectional area ratio.

As shown in Figure 5-1 (a), it is clear that the transformer with a '60%--60%' area proportion has the highest peak HV winding current.

Comparing the simulation results of the transformers with the '60%--60%', '50%--60%' and the '40%--60%' area proportion, a higher main yoke cross-sectional area results in a higher HV winding current and magnetising current. It is clear that the transformer with the '60%--60%' ratio allows the greatest peak flux ϕ_{y2} in the main yokes, as shown in Figure 5-2 (a), and it causes the greatest main limb flux density B_b. Meanwhile, the peak flux density in the Phase B tank path decreases with the increase in the main yoke area because the flux from Phase B limb tends to pass via the main yokes

more when its area expands. The higher the peak limb flux density is, the greater the phase magnetising current will be. Finally, a higher peak magnetising current and thus the peak HV winding current are obtained with a larger main yoke cross-sectional area.

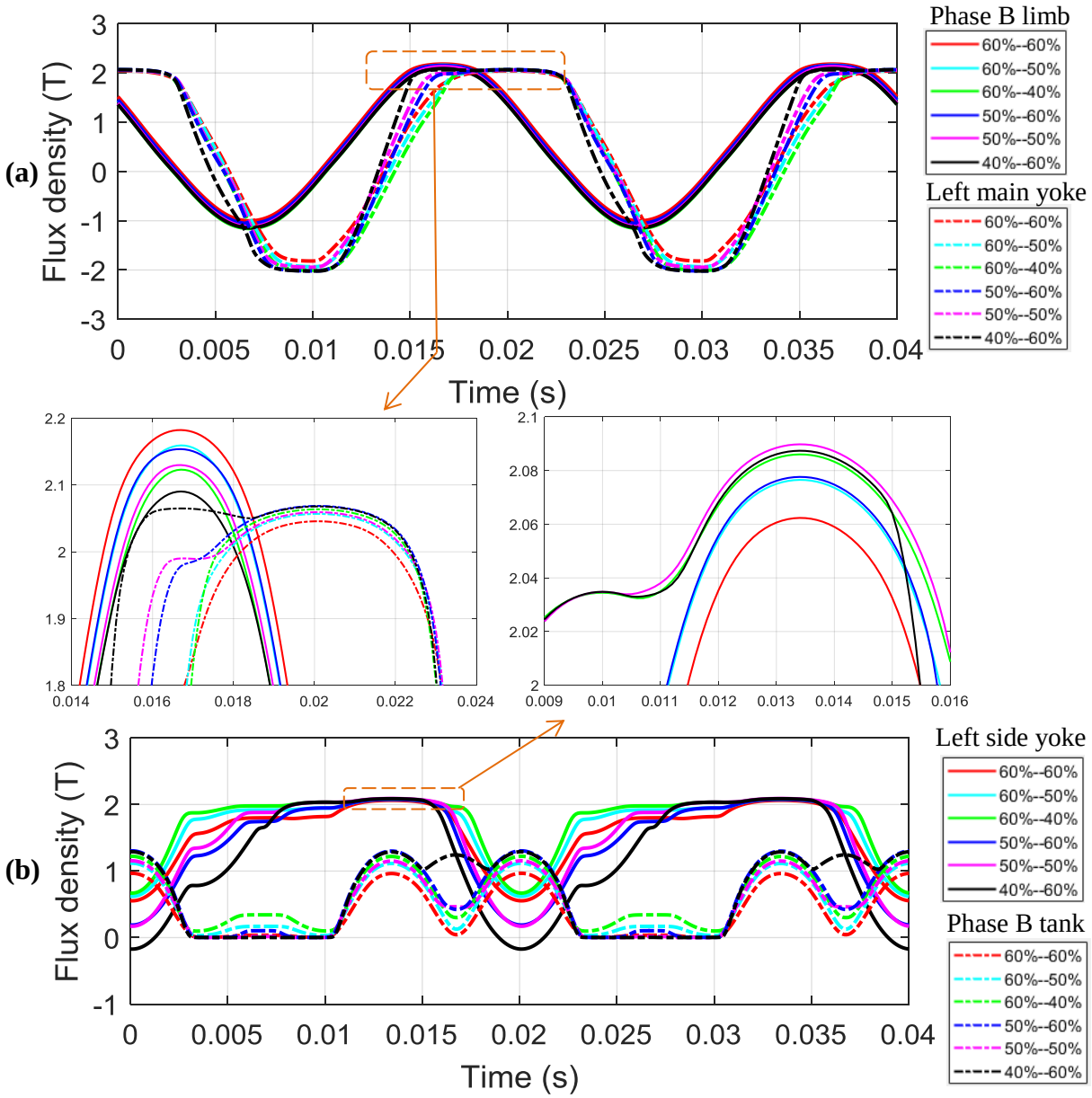

Figure 5-2: (a) Phase B limb flux density and left main yoke flux density (b) Left side yoke flux density and Phase B tank flux density in steady state when simulating with different yoke cross-sectional area ratio.

Comparing the simulation results of the transformers with the '60%--60%', '60%--50%' and the '60%--40%' area proportion, the lowest peak Phase B HV winding current is obtained from the transformer with '60%--40%' area proportion. The lower the side yoke area, the higher the zero-sequence reluctance in the side yoke. Thus higher flux leaks to the tank paths, as illustrated by Figure 5-2 (b), which also shows that the peak

side yoke flux ϕ_{y1} and the peak main limb flux density B_b are the lowest for the transformer with the '60%--40%' area proportion. Overall, the pattern with the '60%--40%' area proportion has the lowest HV winding current in the steady state under the AC+DC input.

Figure 5-3 (a), (b) and (c) displays the DC components and the 2nd harmonic in Phase B HV winding current and the DC limb flux density calculated by frequency spectra.

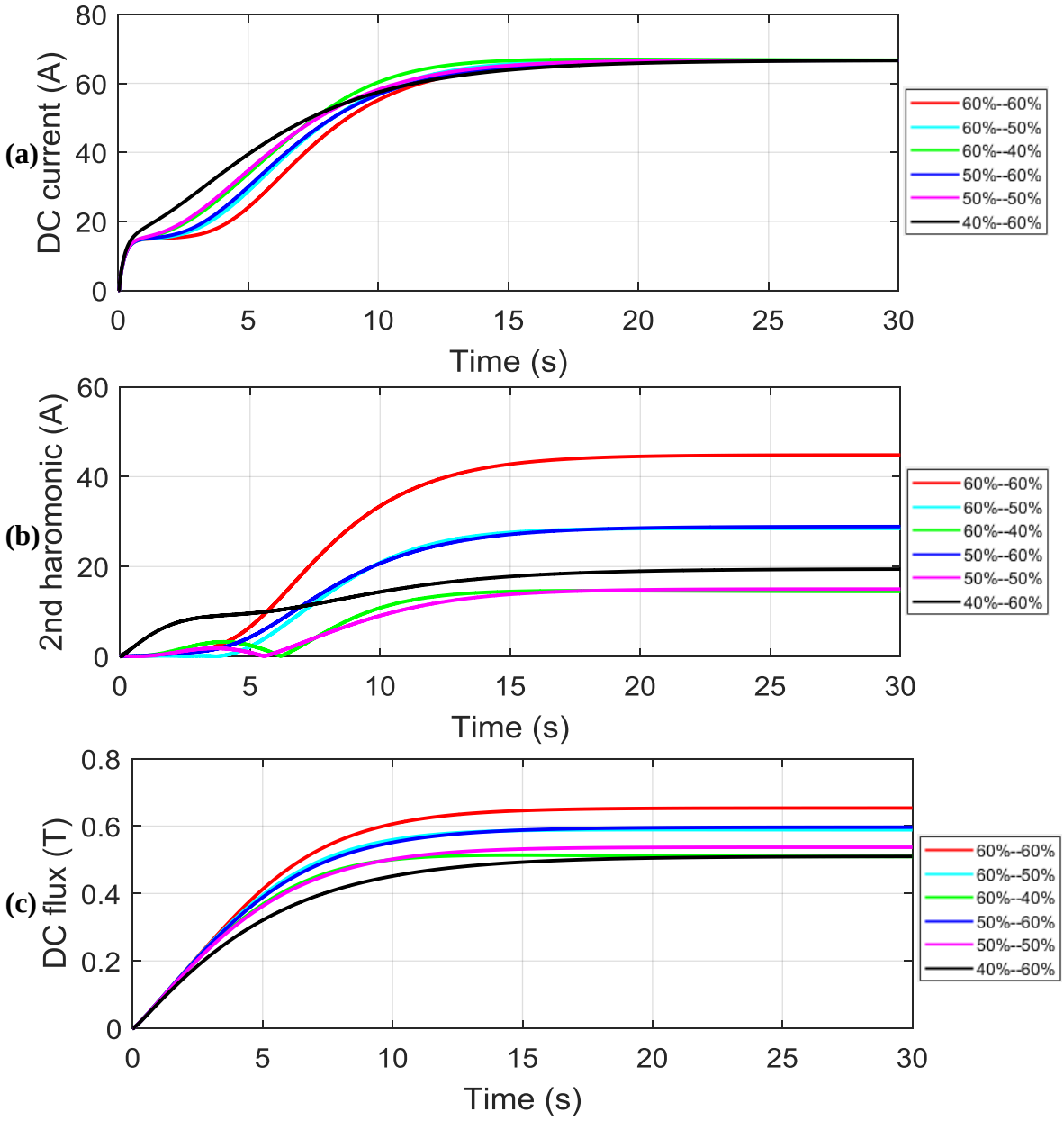

Figure 5-3: (a) DC components in Phase B HV winding current (b) 2nd harmonic in Phase B HV winding current (c) DC flux density in Phase B limb when simulating with different yoke cross-sectional area ratio.

It is clear that both the DC components and the 2nd harmonic of the HV winding current simulated by the transformer with the '40%--60%' ratio increase faster than any other cases. In addition, the 2nd harmonic current of the transformer with the '60%--60%' area proportion finally stabilised at 44.8 A which is significantly higher than those in other cases. Moreover, the DC limb flux density in the transformer with the '60%--60%' ratio is 0.65 T, so it has potential to cause higher core losses in the limbs. The increasing rates of the flux densities are relatively close in the early simulation stage.

Taking into consideration all the factors, the transformer with the '60%--40%' area proportion has the best performance under GIC because of its low peak steady state currents, low saturation speed and low DC flux density in the limbs.

5.3 Leakage paths

The leakage paths of the limb fluxes in the model are composed of the tank and oil gaps in series. Generally, the leakage path reluctance will become larger if the tank path length and the oil gap length increase, or the tank path and oil gap areas decrease. The ranges of the parameters are assumed as an arbitrary wide range to show clear impacts of each parameter to the simulation results. In reality, the leakage path especially the penetration depth into the tank wall can only be determined by a detailed finite element study.

5.3.1 Simulation for effects of tank

As discussed in Chapter 4, the ATP models cannot properly consider the tank effects for 5-limb transformers, which may mean that inaccurate or even misleading results are generated. To prove this point, the 5-limb transformer with all the other same parameters but excluding the flux tank paths, will be simulated in this section to illustrate the effect of the tank under GIC.

Figure 5-4 shows the comparisons of the HV winding currents obtained for the transformer without tank and the measurement results from Finnish Grid. The simulation results are obviously different from the measured results, in magnitude as well as in waveform. Without the tank to provide the second path for the flux, the GIC flux needs to be contained within the core side yokes and the magnitudes of the peak HV winding currents change. This difference in waveforms illustrates that the tank is vital for the GIC modelling.

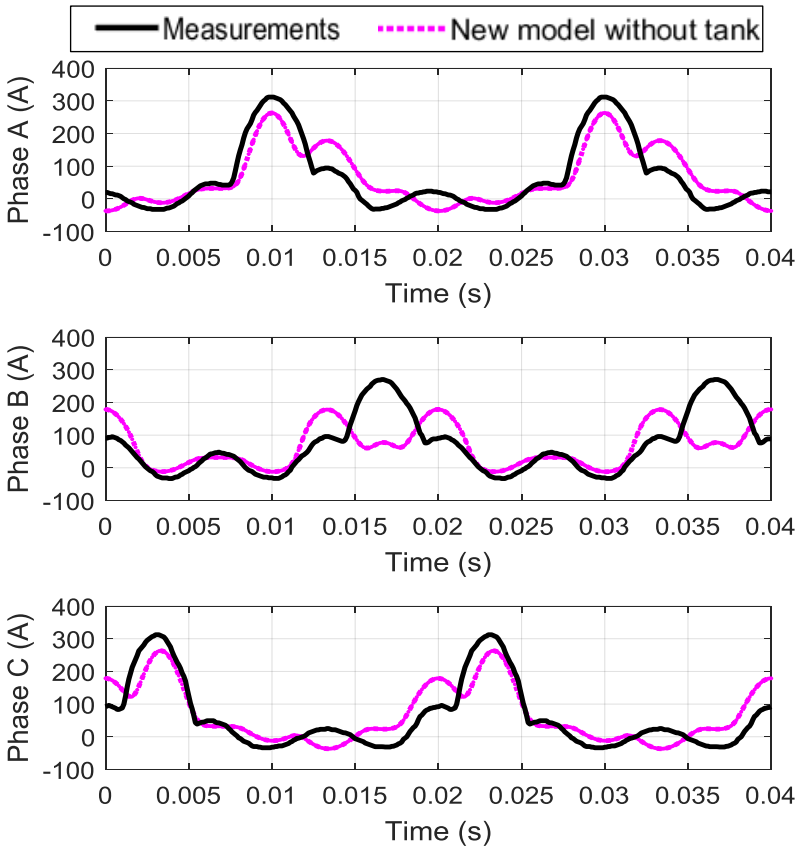

Figure 5-4: Comparison of HV currents between measurements and new model without tank simulation results.

Figure 5-5 (a) shows the difference in flux distributions in parts of the core for the transformer simulated with tank and without tank respectively. The flux distribution data helps in the analysis of the different Phase A and Phase B magnetising current waveforms for the transformer with a tank and the transformer without a tank as shown in Figure 5-5 (b) and (c).

As illustrated in Figure 5-5 (b), Peak 1 of Phase A magnetising current simulated by the transformer without a tank is 77.9 A lower than that of the transformer with a tank because the peak flux at Phase A limb for the transformer without a tank is 0.02 T lower than that of the transformer with a tank. The lower Phase A limb flux peak of the transformer without a tank is caused by neglecting Phase A leakage tank paths, which prohibits the flux from leaking to the tank, thereby increasing the reluctance. In the meantime, Peak 2 of Phase A magnetising current for the transformer without a tank is 129.2 A higher than that for the transformer with a tank. Peak 2 is caused by the saturation of the side yoke, and the side yoke peak flux for the transformer without a tank is 0.04 T higher than that for the transformer with a tank. This is caused by the leakage flux produced in Phase B being forced to enter the side yokes due to the lack of the tank

leakage path, which increases the flux density value at side yokes and thus leads to a higher Peak 2 magnitude for Phase A magnetising current.

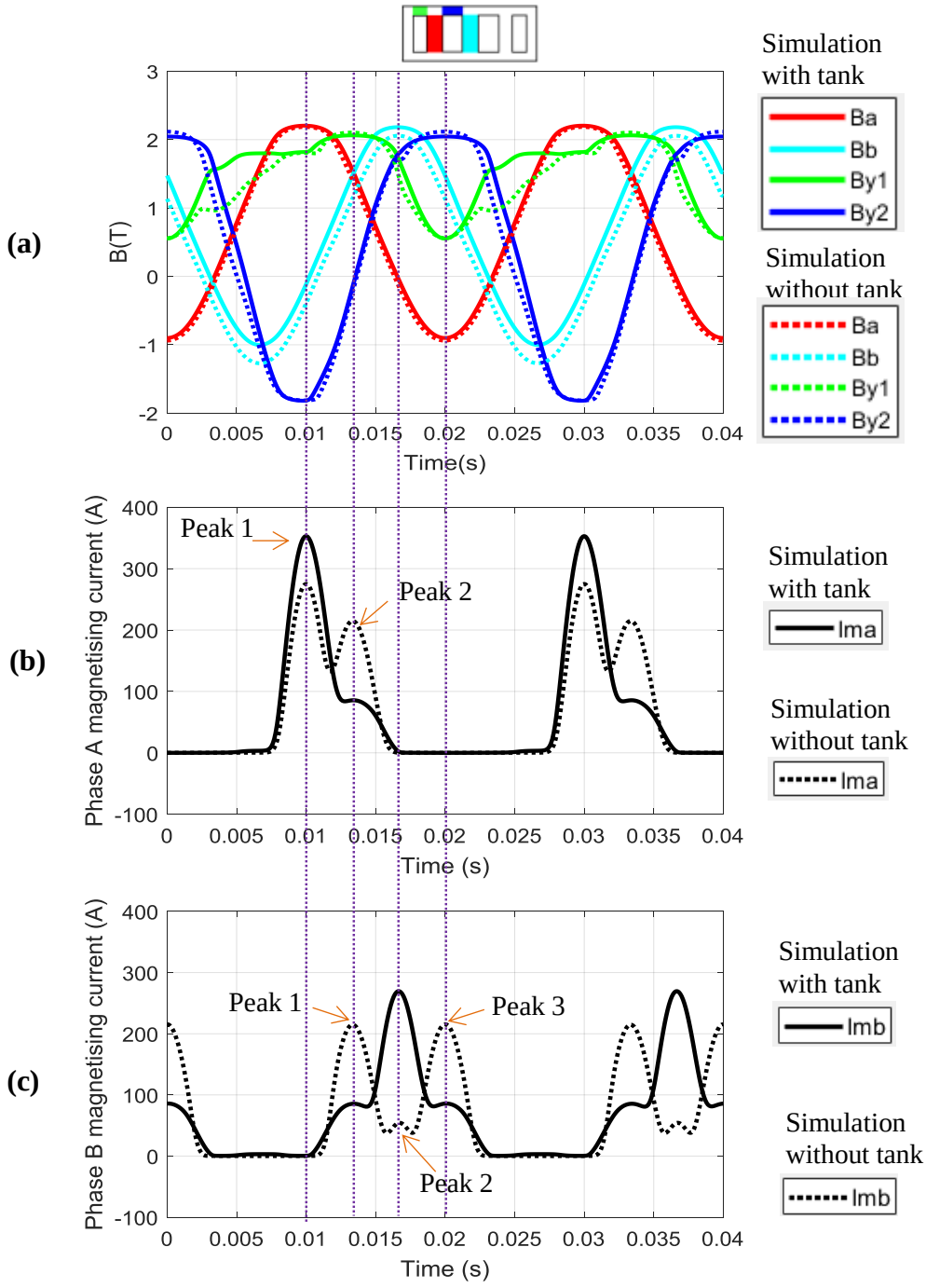

Figure 5-5: Comparisons of simulation results with and without tank (a) flux distribution (b) Phase A magnetising current (c) Phase B magnetising current.

Figure 5-5 (c) illustrates that the tank leakage paths have more pronounced impacts on Phase B magnetising current, where Peak 2 of the magnetising current for the transformer without tank is 215.2 A lower than that for the transformer with a tank. For the

transformer without tank, the only valid zero-sequence flux paths are the side yokes, but they are relatively far to be accessed by Phase B flux, so the zero-sequence reluctance for Phase B is higher when the tank paths are not available. As can be seen from Figure 5-5 (a), Phase B limb peak flux density is 0.13 T lower than the case of the transformer with a tank, which explains why the middle peak of Phase B magnetising current becomes lower when Phase B limb flux reaches the peak. Similarly, the increases in the two side current peaks, Peak 1 and Peak 3, are due to higher magnetic densities in the side limbs.

Therefore, the tank influences the flux distribution and the current results significantly. It is necessary to take into account the tank leakage paths when modelling GIC; and this is also the key reason why we believe the current ATP models may not be suitable for GIC studies.

5.3.2 Equivalent tank path length

As described in Section 4.3, the equivalent tank length is assumed as the sum of the tank width and the tank height. This assumption is reasonable, or at least approaches the real tank path length. Therefore, the sensitivity study in this section will apply a relatively narrow range from 50% to 150% of the original length to see how sensitive this parameter influences the flux distribution and winding currents.

Figure 5-6 (a) and (b) illustrate that subtle differences are found in the simulation results of Phase B HV winding current and Phase B limb flux density in the steady state. For the transformer with 150% tank path length, the peak of Phase B HV winding current is 253.4 A, slightly lower than 262.8 A simulated by the transformer with 50% tank path length. It seems that the tank path length does not have to be absolutely accurate for GIC simulation.

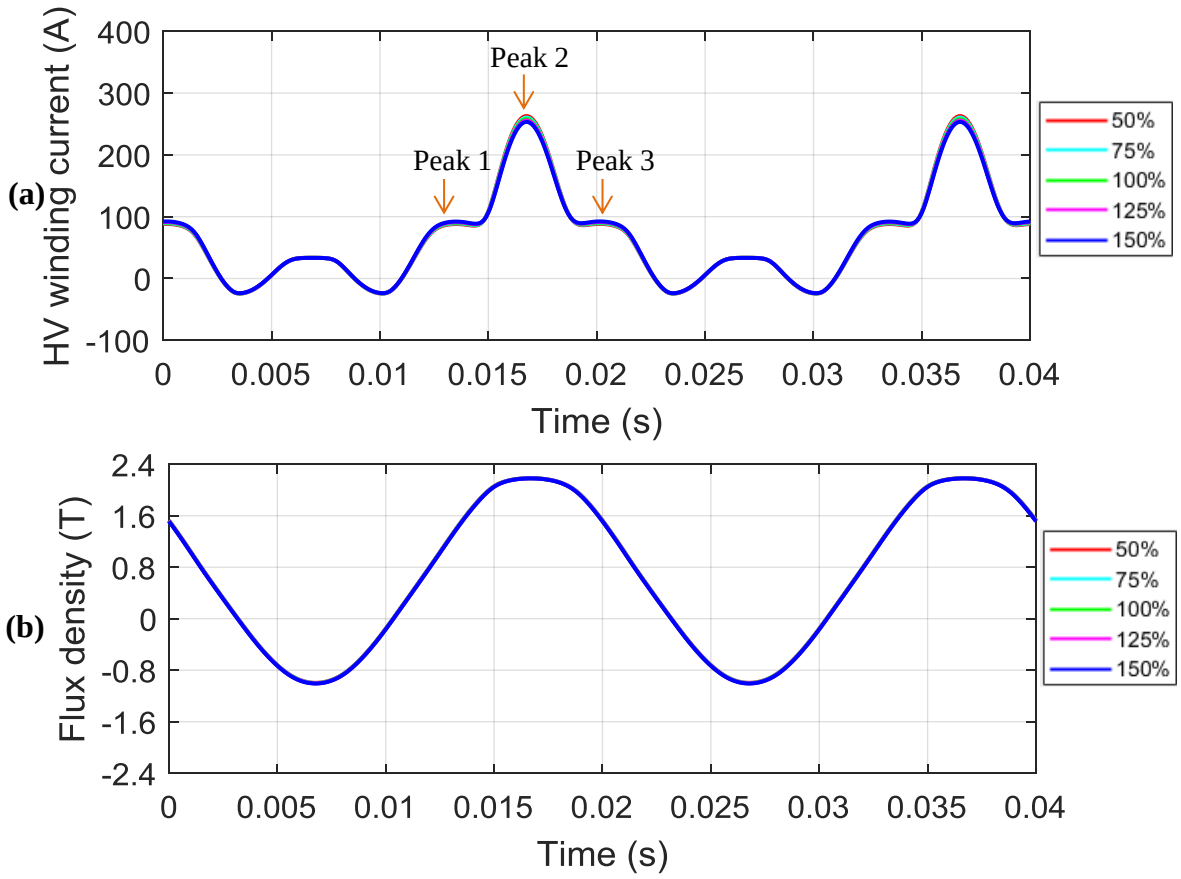

Figure 5-6: (a) Phase B HV winding current (b) Phase B limb flux density in steady state when simulating with different tank path length.

5.3.3 Equivalent tank path area

As described in Section 4.3, the area of the tank path is calculated as the perimeter of the top/bottom of the tank multiplied by the thickness of the tank. However, the effective tank area could be lower due to the uneven distribution of the flux in the tank. In addition, the accuracy of the tank path area calculation is largely dependent on the thickness of the tank. Hence, it is necessary to conduct the GIC sensitivity study for the equivalent tank area.

- **Steady state results**

Figure 5-7 (a) illustrates that visible difference can be found in Phase B HV winding current waveforms with various tank areas. When the tank area decreases to 33% of the assumed value, Peak 2 of Phase B HV winding current will decrease to 223.3 A which is much lower than 258.0 A simulated in the case of the 100% tank area, since the peak Phase B limb flux density is the lowest with 33% tank area as shown in the inset for

Figure 5-8 (a). On the other hand, Peak 2 magnitude is not sensitive to the growth of the tank area over 75% its original value. When the tank area expands to 150% its original value, Peak 2 magnitude only increases to 261.2 A.

Peak 1 and Peak 3 are formed because the flux densities of the side yokes reach their peaks. The tank leakage paths will be less accessible by the leakage flux when the equivalent tank area is assumed to be smaller. Therefore, the stray flux is restrained in the core, and hence the side yoke flux density will apparently increase as shown in the inset of Figure 5-8 (b). Finally, it will lead to higher Peak 1 and Peak 3 magnitudes.

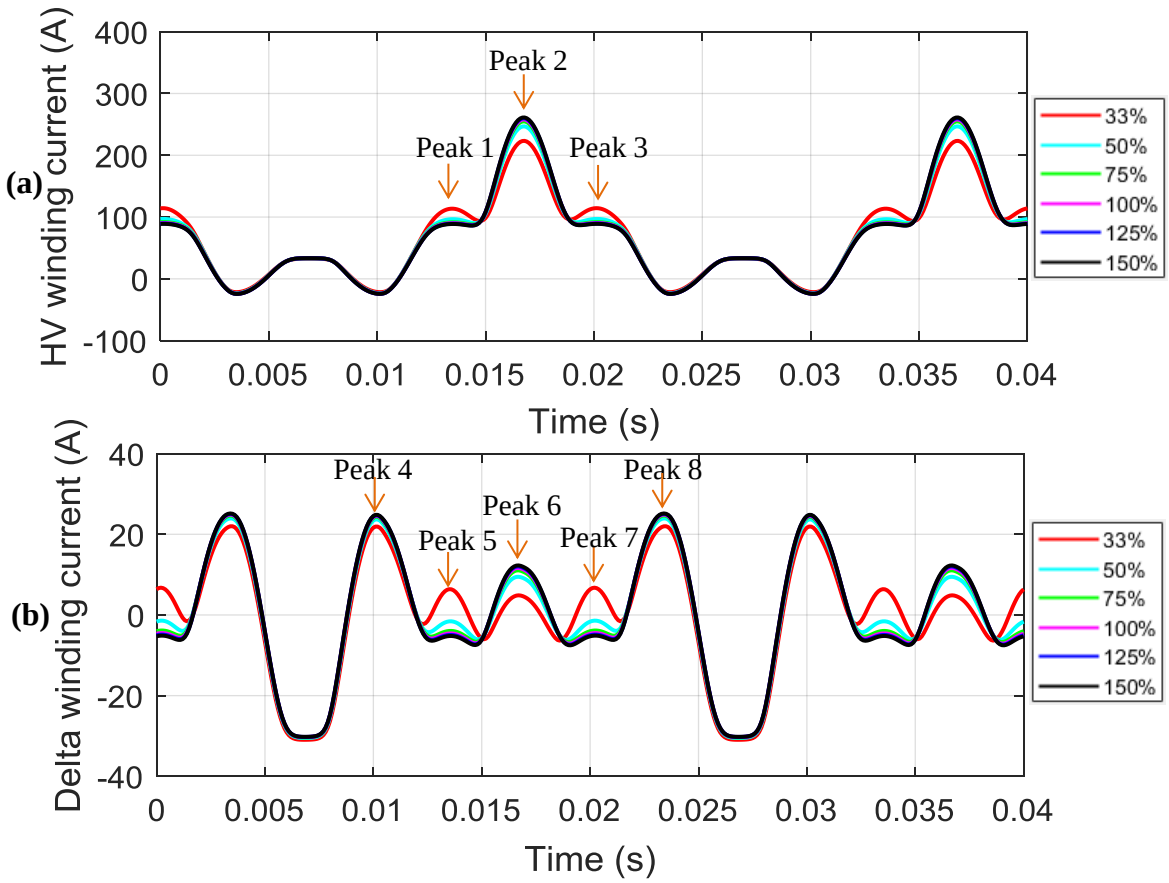

Figure 5-7: (a) Phase B HV winding current (b) Delta winding current in steady state when simulating with different tank path area.

Figure 5-7 (b) illuminates that Peak 5, Peak 6 and Peak 7 are more sensitive to the change in the tank area. Peak 5 and Peak 7 are caused by the saturation of the side yokes as displayed in the inset of Figure 5-8 (b). The reduction of the equivalent tank area leads to an increase in the tank leakage path reluctance and thus a decrease in the amount of the flux leaking out to the tank. Consequently, the peak flux densities in the side yokes

increase when Peak 5 and Peak 7 occur, and hence higher peak magnetising currents are found, which is also reflected in the higher Peak 5 and Peak 7 in the delta winding current. As for Peak 6, a lower equivalent tank area results in a smaller peak Phase B limb flux density, which further leads to a lower Peak 2 in Phase B magnetising current and thus a lower magnitude Peak 6 in the delta winding current. However, it is noticeable that the delta winding current shows an invisible difference when the tank area is over 75% its original value.

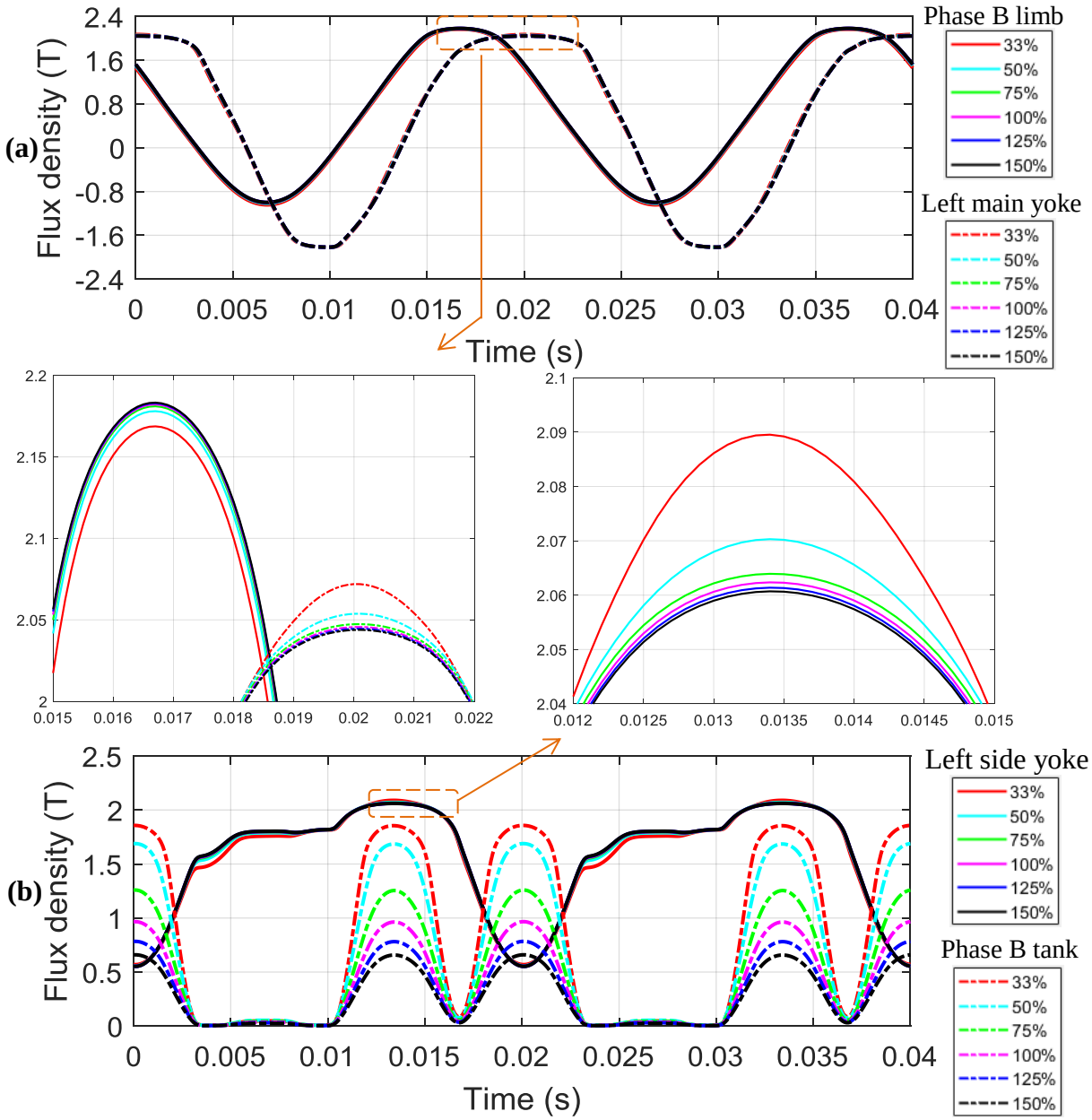

Figure 5-8: (a) Phase B limb flux density and left main yoke flux density (b) Left side yoke flux density and Phase B tank flux density in steady state when simulating with different tank path area.

- **Frequency spectrum in the whole simulation duration**

Figure 5-9 (a), (b) and (c) shows the frequency spectrum results of the DC components and 2nd harmonic in the HV winding current and the DC flux density in Phase B limb with different equivalent tank path area.

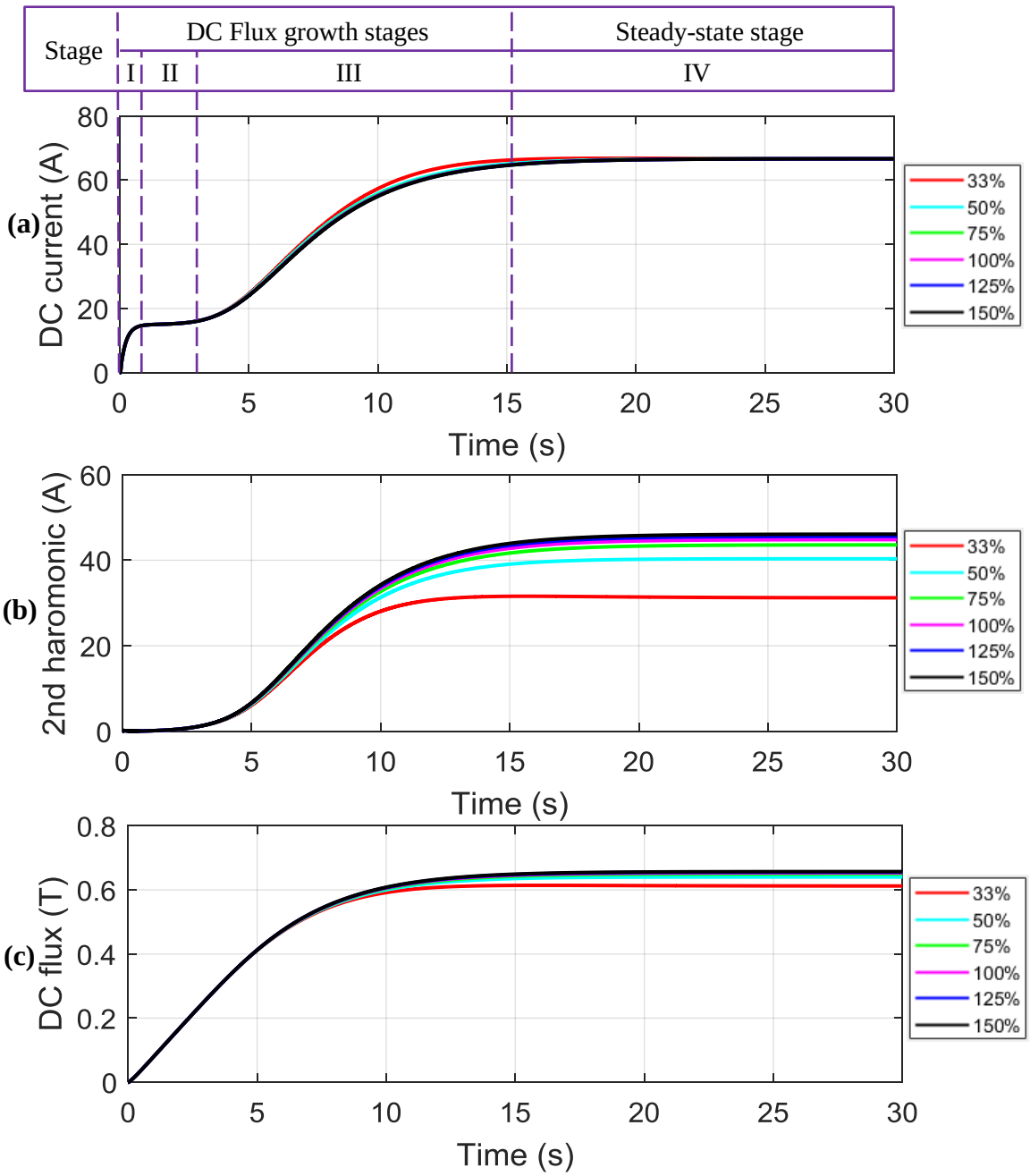

Figure 5-9: (a) DC components in Phase B HV winding current (b) 2nd harmonic in Phase B HV winding current (c) DC flux density in Phase B limb when simulating with different tank path area.

Figure 5-9 (a) illuminates that the tank area slightly influences the DC current increase in Stage III. However, Figure 5-9 (b) indicates that, the HV winding current with

33% tank area, contains only 31.2 A 2nd harmonic in the steady state which is much lower than 44.8 A simulated in the case of the 100% tank area. As displayed in Figure 5-9 (c), the lower the equivalent tank area, the smaller DC flux in Phase B limb in the steady state, but the tank area does not impact on the DC flux increasing rate at the early stage.

The simulation results prove that it is vital to correctly set the tank area in the GIC study. However, it is difficult to determine the exact tank area without using the finite element study. Generally, the model can obtain reasonable simulation results with the initial setting of the equivalent tank area.

In terms of the transformer technical design, the reduction in the equivalent tank area will cut down the peak HV winding current and the 2nd harmonic in the HV winding current which have the potential to trigger the relays in power system networks. On the other hand, the reduction in the tank area leads to higher flux density in the tank, which can potentially increase eddy current loss in the tank and finally results in more severe hotspot problems.

5.3.4 Equivalent oil gap length

In Section 4.3, the oil gap lengths are set as 0.22 m and 0.1 m for the main limb leakage and the side limb leakage path respectively. This section will conduct the sensitivity study for the oil gap length ranging from 50% to 150% its original values. In an extreme case, the equivalent oil gap between the transformer core and the tank could be 2 mm to 5 mm in a 240 MVA transformer [26, 90]. For this reason, the simulation results for the case with 2 mm oil gap are also provided and compared to those of the other cases.

- **Steady state results**

Figure 5-10 (a) indicates that the lower the oil gap length is, the higher the peak HV winding current will be. Apparently, if the oil gap length decreases, the flux leaks out of the core and enters the tank more easily. On the one hand, the peak flux density in the main yokes and the side yokes decrease as seen in the insets of Figure 5-11 (a) and (b). Furthermore, the lower reluctance of the leakage paths results in higher main limb flux density and tank path flux density. When the oil gap becomes 2 mm, Peak 2 reaches 363.8 A which is noticeably higher than 258.0 A for the original oil gap length.

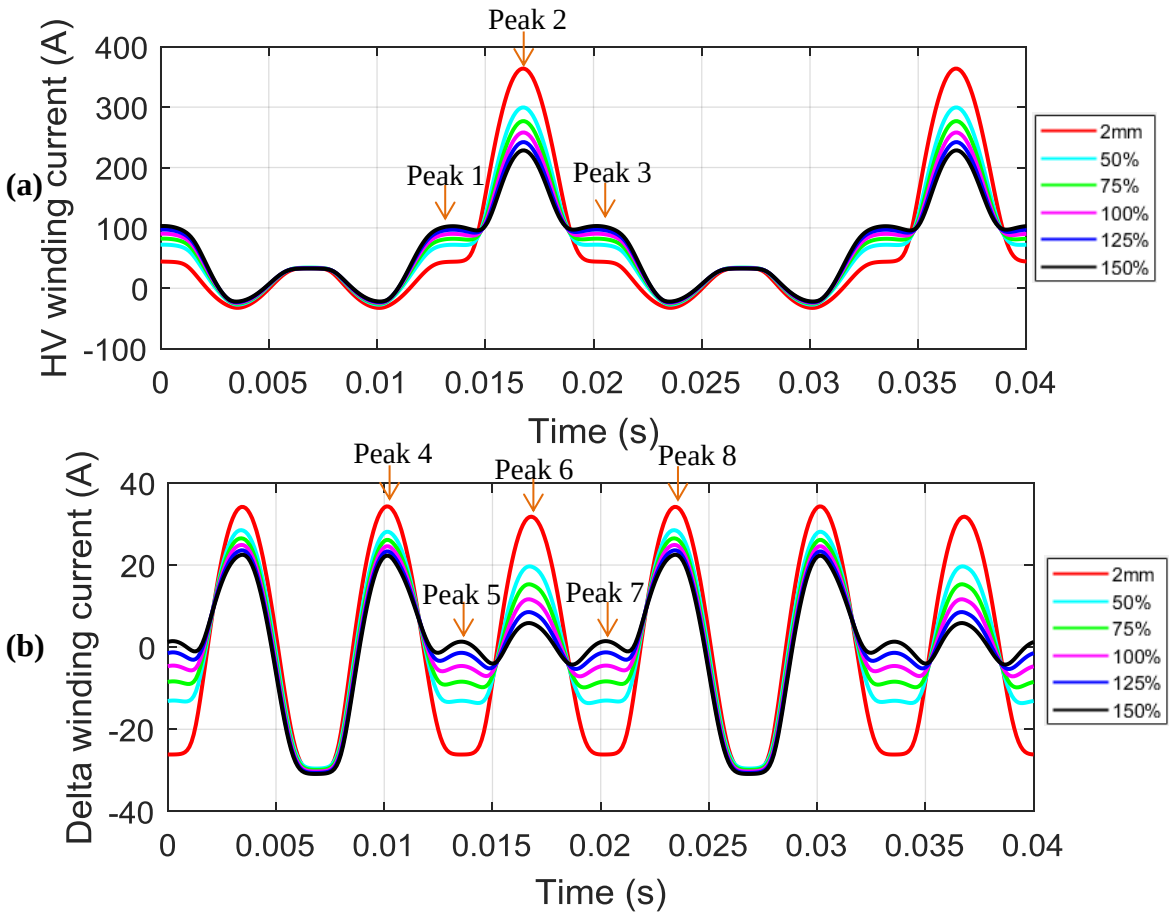

Figure 5-10: (a) Phase B HV winding current (b) Delta winding current in steady state when simulating with different oil gap length.

Figure 5-10 (b) illustrates that the delta winding current is very sensitive to the change in the oil gap length. Peak 5 or Peak 7 are caused by the saturation of the side yokes, and the side yoke flux density decreases if the oil gap length decreases as shown in Figure 5-11 (b). This is because a larger amount of flux tends to pass via the tank leakage paths rather than the side yokes with a smaller oil gap length. As for Peak 6, a narrower oil gap leads to a higher Phase B limb flux density as shown in the inset of Figure 5-11 (a), which results in a greater magnitude of Phase B magnetising current and thus a higher magnitude of Peak 6 reflecting in the delta winding. Peak 4 and Peak 8 are caused by the saturation of Phase A limb and Phase C limb, and the explanation for Peak 6 also goes for explaining the difference in the magnitudes of Peak 4 and Peak 8.

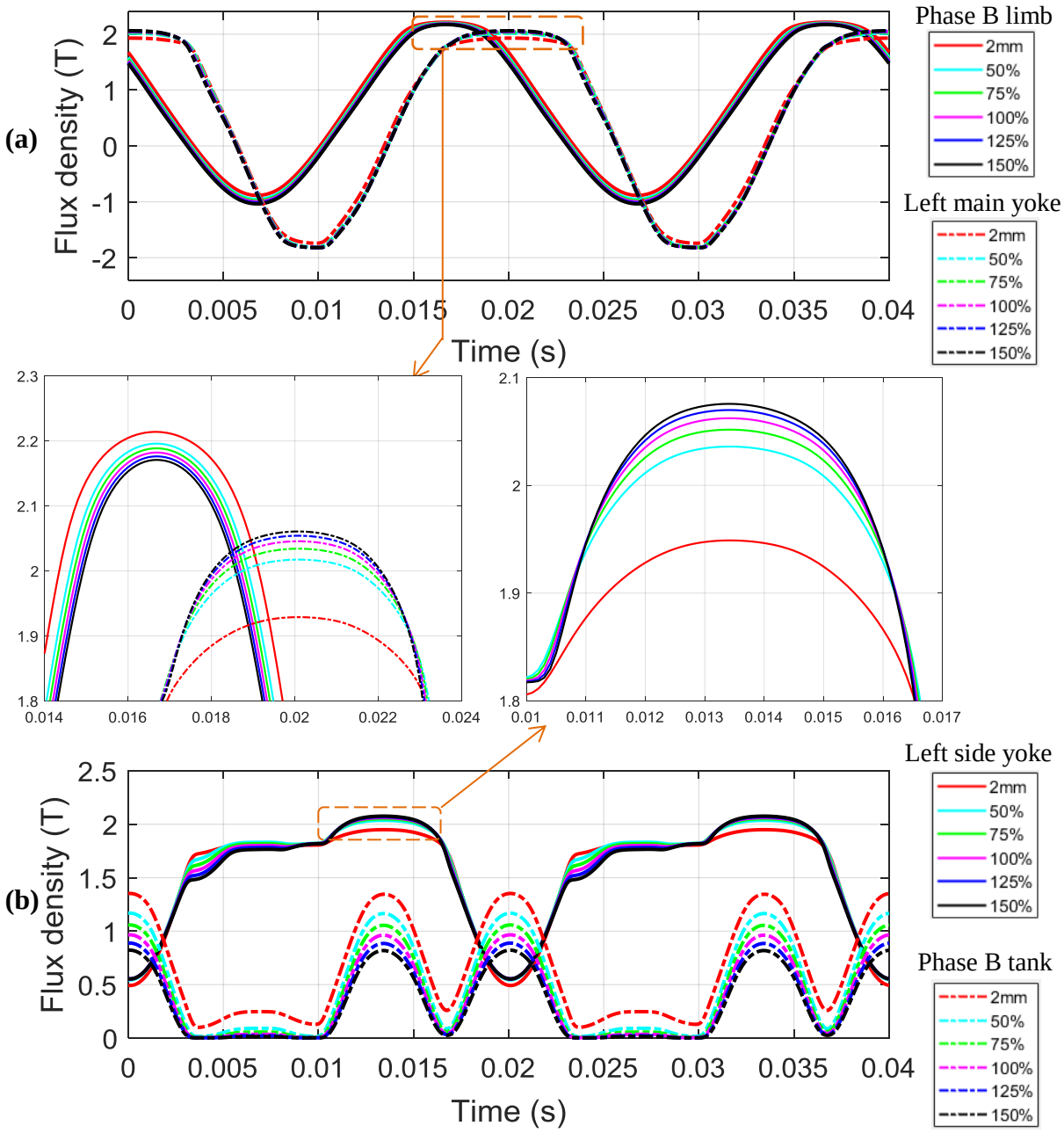

Figure 5-11: (a) Phase B limb flux density and left main yoke flux density (b) Left side yoke flux density and Phase B tank flux density in steady state when simulating with different oil gap length.

- **Frequency spectrum in the whole simulation duration**

As can be seen in Figure 5-12 (a), the oil gap length only impacts on the DC components of Phase B HV winding current in Stage III. It takes 15.9 s for the DC components to reach 95% of the steady state value with 2 mm oil gaps. Compared to 13.1 s with 100% oil gaps, the saturation time has a mild extension with 2 mm oil gaps.

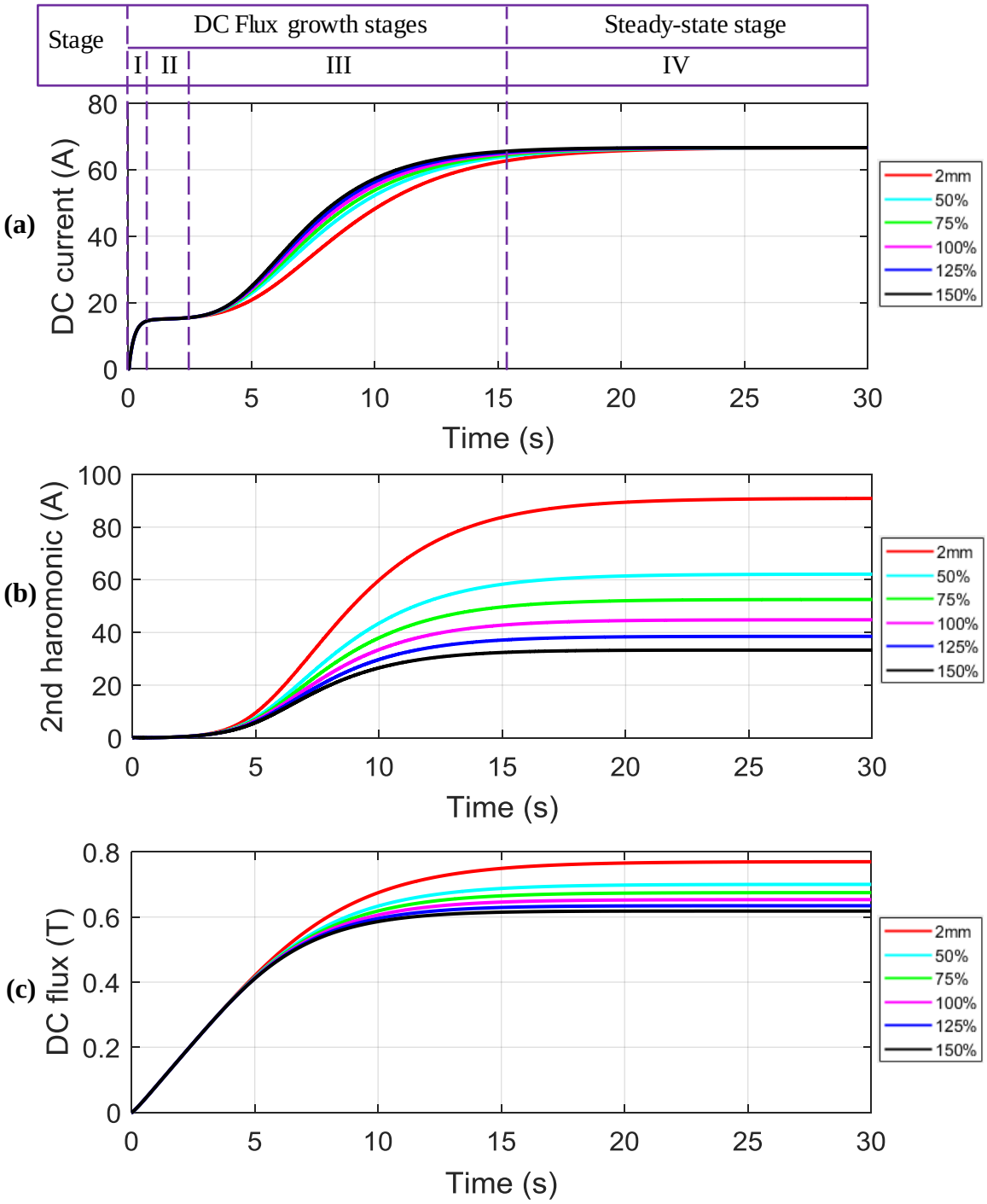

Figure 5-12: (a) DC components in Phase B HV winding current (b) 2nd harmonic in Phase B HV winding current (c) DC flux density in Phase B limb when simulating with different oil gap length.

However, Figure 5-12 (b) shows that the 2nd harmonic in Phase B HV winding current rises dramatically after 5 s simulated for the case with 2 mm oil gaps. In the steady state, the magnitude reaches 90.9 A which is over twice that of 44.8 A with 100% oil gaps.

In addition, Figure 5-12 (c) demonstrates that higher DC flux in the limbs is obtained with narrower oil gaps, and hence the core losses in the limbs will significantly increase.

In summary, the reduction in the oil gap will lead to the higher peak and 2nd harmonic in the HV winding current and the higher peak flux densities in the tank and the limbs, although it saves the tank material and the insulation oil, and slightly extends the saturation time. If conditions permit, the designer should leave a reasonable gap between the tank and the core to mitigate the GIC threat to transformers.

5.3.5 Equivalent oil gap area

In Section 4.3, the equivalent area of Phase B oil gap is expanded to 1.7 times that of Phase A and Phase C to match the measurement results better. It is considered reasonable to expand the Phase B oil gap cross-sectional area, as Phase B is the middle limb and it is accessible to a larger area of the top tank. In order to investigate the impacts of various oil gap areas on the AC+DC simulation results, this section presents the comparisons of the simulation results with different oil gap areas ranging from 50% to 170% of the original value.

- **Steady state results**

Figure 5-13 (a) indicates that accurately setting an oil gap area is vital to achieving the accurate HV winding current under AC+DC input. When the oil gap area decreases to 50% of its original value, the peak of Phase B HV winding current will decrease to 206.3 A, much lower than 258.0 A with 100% oil gap area. The smaller oil gap area means the greater leakage path reluctance; hence the peak Phase B limb flux density is the lowest with 50% oil gap area as shown in the inset of Figure 5-14 (a). Meanwhile, Peak 1 and Peak 3 in Phase B HV winding current have an increase of 28.4 A compared to the case with 100% oil gap area because of its higher side yoke flux density as shown in Figure 5-14 (b).

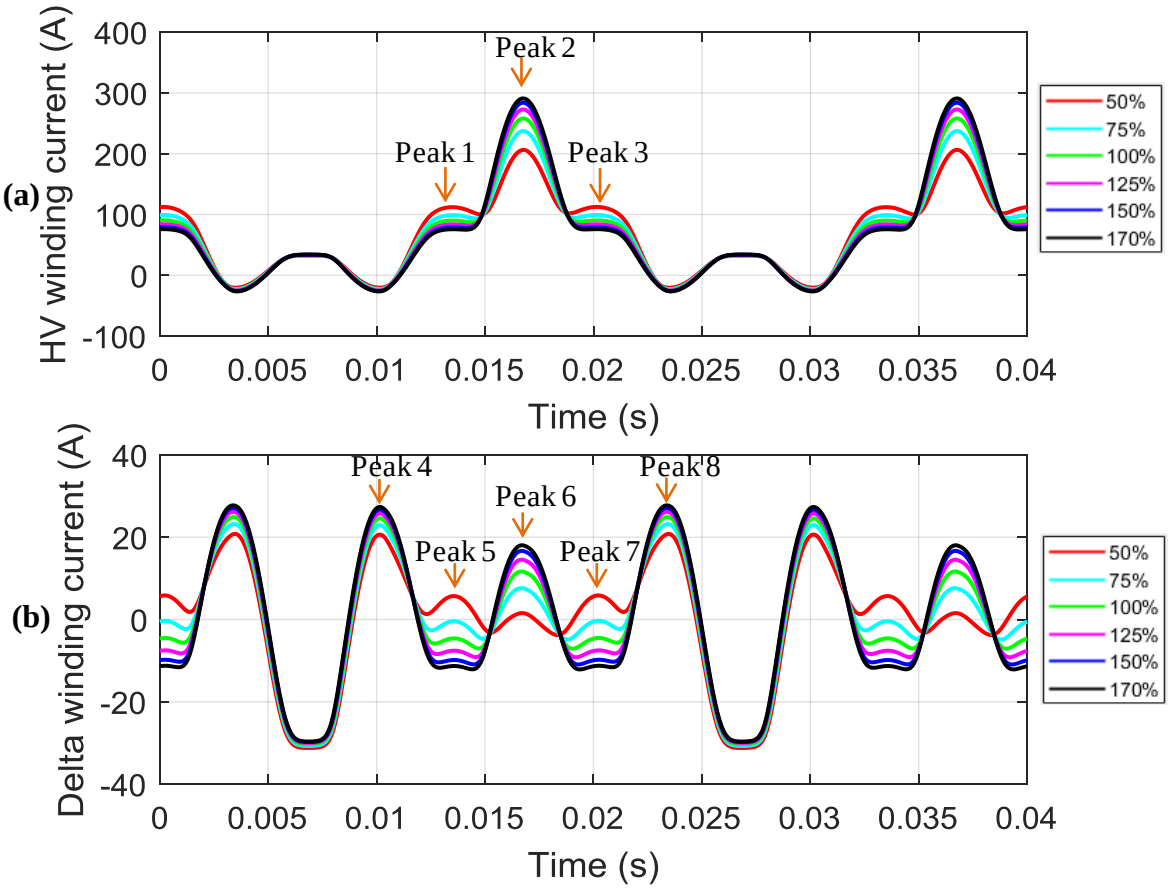

Figure 5-13: (a) Phase B HV winding current (b) Delta winding current in steady state when simulating with different oil gap area.

The increase in the oil gap area is equivalent to shorten the oil gap because both of them make the leakage paths reluctances lower. Therefore, the reasons for the difference of Peak 4, 5, 6, 7, 8 with various oil gap length in Section 5.3.4 can also be applied in this section.

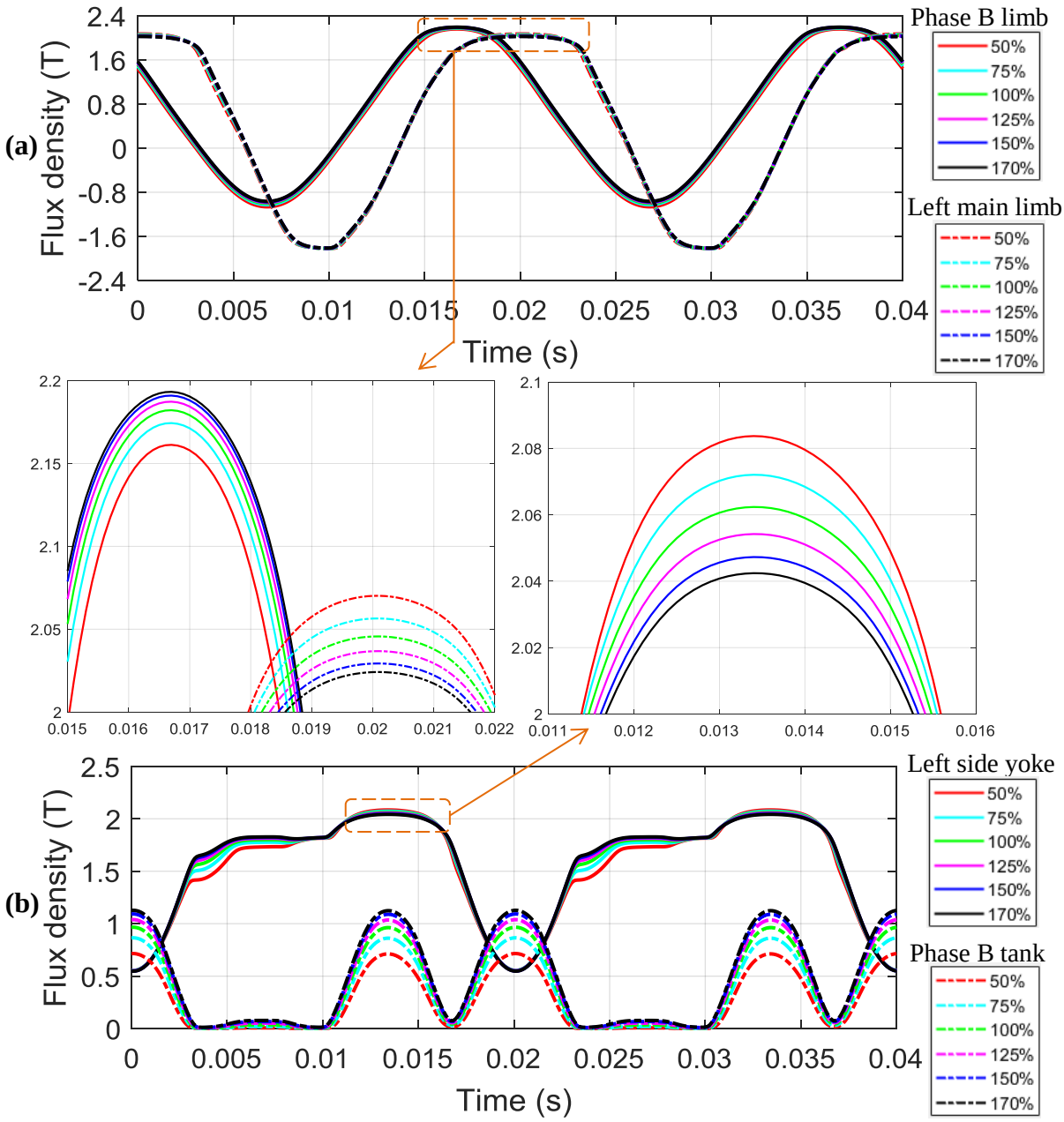

Figure 5-14: (a) Phase B limb flux density and left main yoke flux density (b) Left side yoke flux density and Phase B tank flux density in steady state when simulating with different oil gap area.

- **Frequency spectrum in the whole simulation duration**

An increase in the oil gap area has similar impacts on the currents and the flux densities in the core and the tank as a reduction of the oil gap length, since both of them decrease the leakage path reluctance.

As can be seen in Figure 5-15 (a), the increase in the oil gap cross-sectional area slows down the DC components growth in the HV winding current in Stage III. Figure 5-15 (b) indicates that the transformer with the higher oil gap area will produce larger quantities of 2nd harmonic in the HV winding current. The magnitude of the 2nd harmonic in Phase B HV winding current with 50% oil gap area rises dramatically after 5 s until reaching the steady state with a magnitude of 25.2 A, just over half of 44.8 A simulated with 100% oil gap area. Meanwhile, the 2nd harmonic magnitude is 58.5 A with 170% oil gap area. In addition, Figure 5-15 (c) demonstrates that the higher DC flux is induced in the limbs with the higher oil gap area.

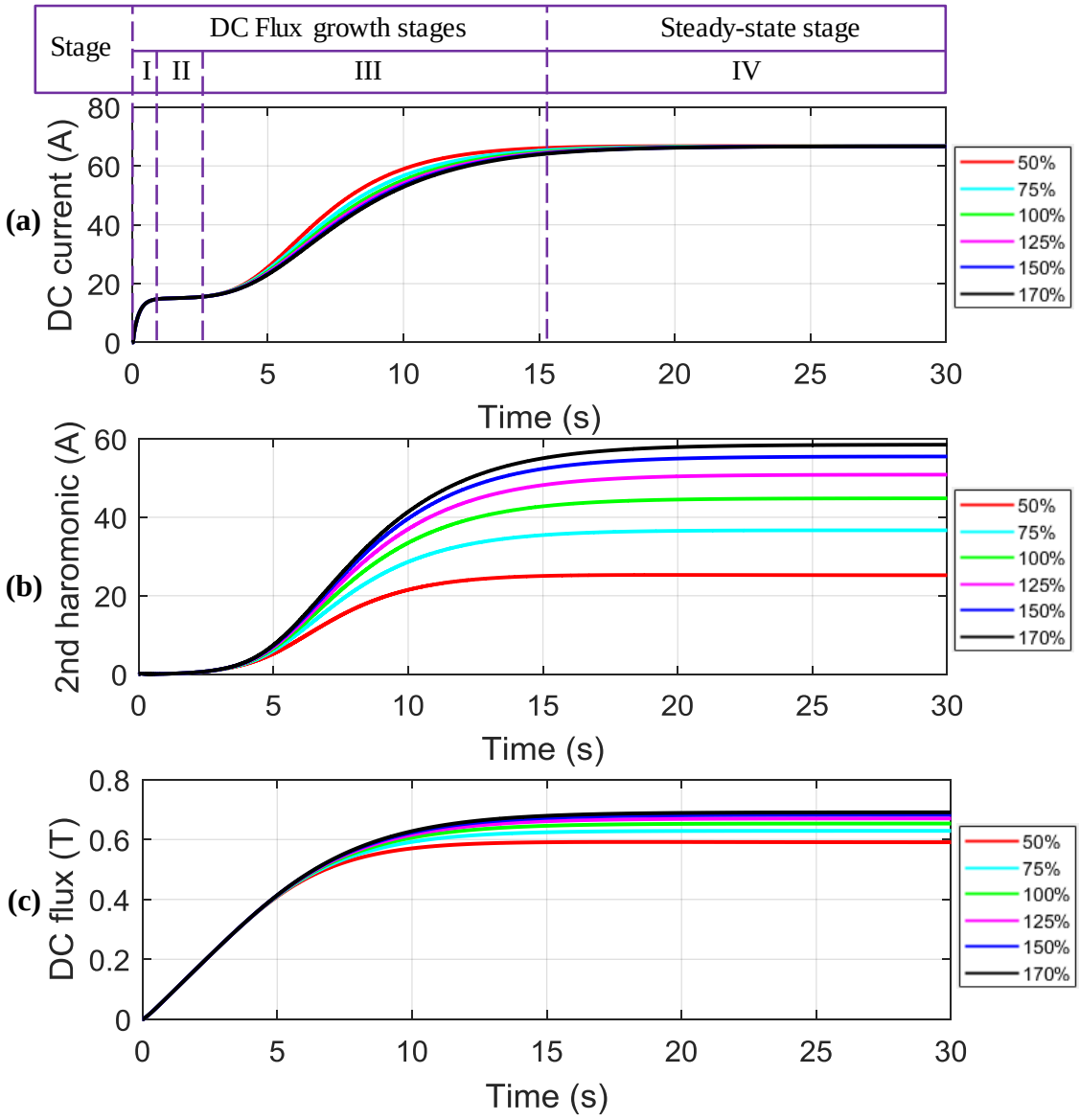

Figure 5-15: (a) DC components in Phase B HV winding current (b) 2nd harmonic in Phase B HV winding current (c) DC flux density in Phase B limb when simulating with different oil gap area.

The sensitivity study in this section shows the importance of correctly setting the oil gap area to obtain accurate simulation results. However, the oil gap area is difficult to calculate from the physical dimension. The values assumed in the simulation show great ability to match the measured results. Therefore, the assumptions for the oil gap area can be applied when simulating the other transformers.

Compared with the tank length and tank area, the simulation results are more sensitive to the parameter setting of the oil gap length and oil gap area.

5.4 Sensitivity study for winding impedance

Transformer impedance helps to limit the fault current, i.e. the leakage reactance of a 240 MVA transformer is usually designed as around 20%. In addition, winding resistance is desired to be much smaller in order to minimise load loss in a transformer.

This section will conduct the sensitivity study for the HV winding impedance and the TV winding impedance by artificially altering the leakage inductance and winding resistance. The flux paths in the main insulation clearance between windings and between the tertiary winding and the core are represented by the winding leakage inductances of the electrical circuit; such an approximation may be questionable without carrying out a detailed finite element field calculation. In this sense, sensitivity studies on leakage inductances of the windings are more relative to the effects of flux paths in main insulation clearance when the core is saturated. The ranges of the winding impedance are assumed as an arbitrary wide range to show clear impacts of each parameter on the simulation results more clearly. For real transformers, the parameters will be restrained in a narrow range.

5.4.1 HV winding resistance

The HV winding resistance of the simulated transformer is 1.060 Ω referred to the 400 kV side. In this section, the model is simulated with different HV winding resistances ranging from 0.636 Ω to 1.908 Ω while the other parameters remain the same. Since GIC is caused by the electric field on the Earth's surface, the DC neutral voltage remains the same in this section, but the steady state DC currents are various due to the different HV winding resistances.

- Steady state results

Figure 5-16 (a) provides Phase B HV winding current in the steady state. Apparently, the peak HV winding current is the highest (400.9 A) when the HV winding resistance is 0.636 Ω. Normally, the transformer designer expects to decrease the winding resistance to reduce copper losses for normal operating conditions. However, if the transformer suffers a GIC, the current induced by the core saturation is comparable to the full-load current (346 A). Therefore, a low HV winding resistance could result in a high copper loss when the transformer suffers GMD events. As can be observed from Figure 5-16 (b), the lower the HV winding resistance is, the greater delta winding current will be.

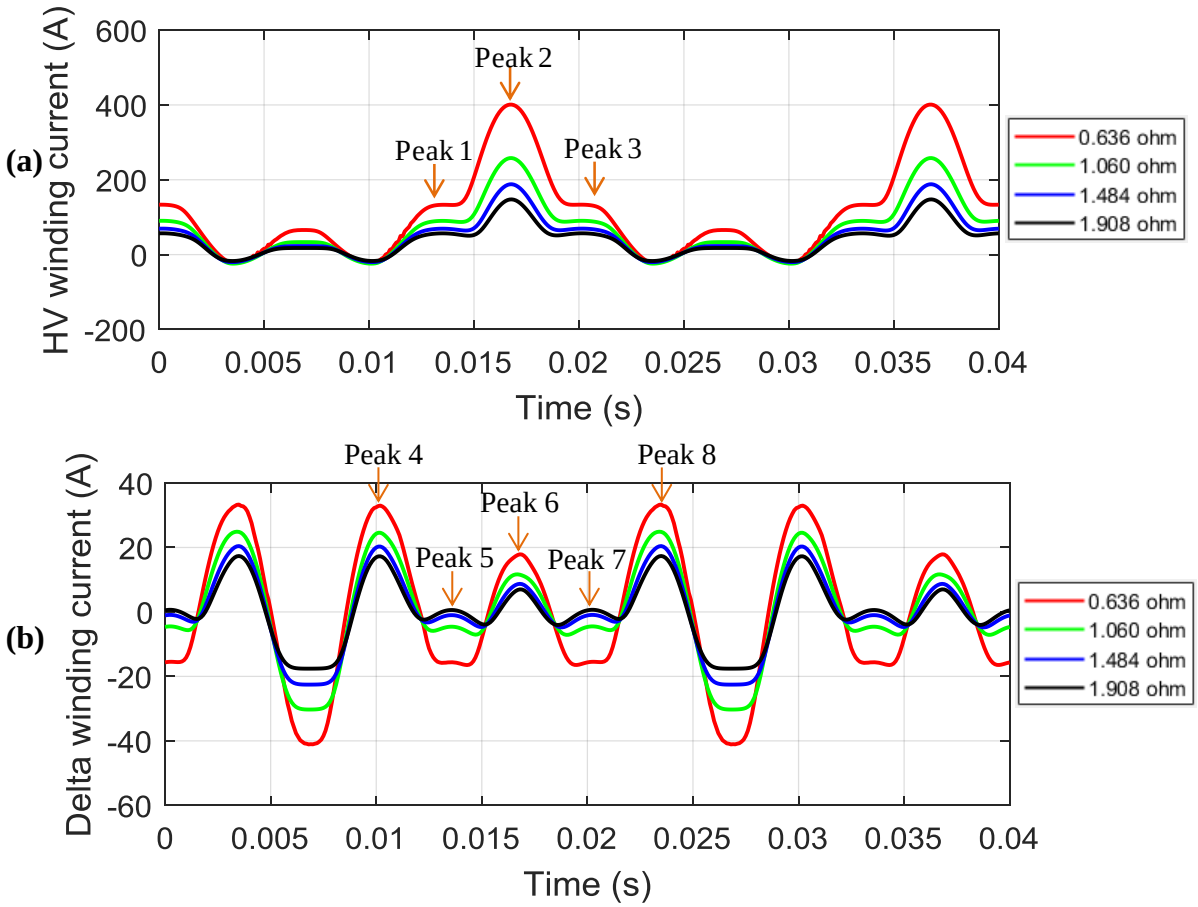

Figure 5-16: (a) Phase B HV winding current (b) Delta winding current in steady state when simulating with different HV winding resistance.

Figure 5-17 (a) and (b) indicate that the lower HV winding resistance will cause a comprehensively higher peak flux density in the limbs, the yokes and the tank. In brief, a higher HV winding resistance helps to defend against GIC according to the steady state results.

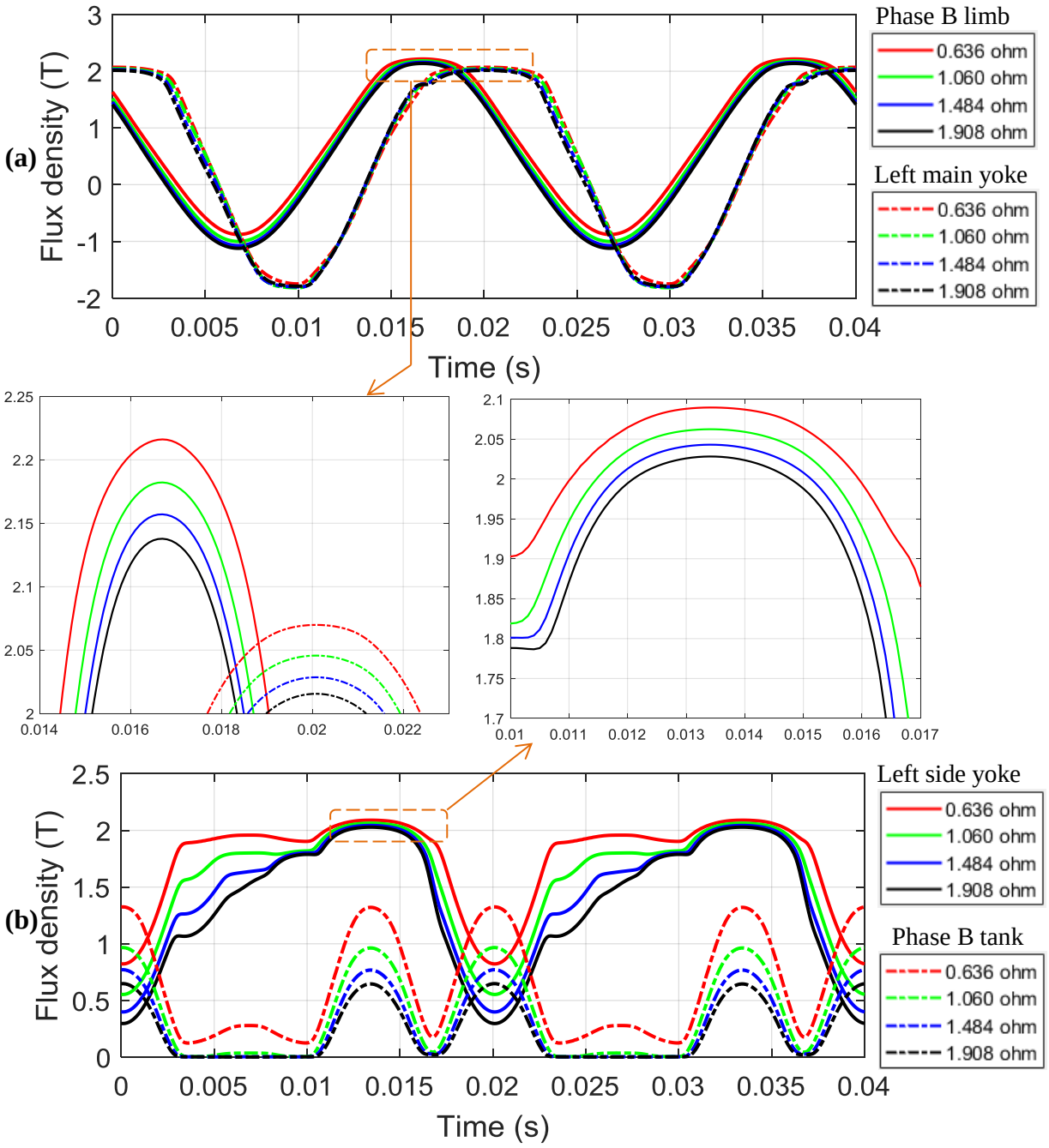

Figure 5-17: (a) Phase B limb flux density and left main yoke flux density (b) Left side yoke flux density and Phase B tank flux density in steady state when simulating with different HV winding resistance.

- **Frequency spectrum in the whole simulation duration**

Apparently, a smaller HV winding resistance contributes to a higher DC current in the steady state when the DC voltage input remains the same as shown in Figure 5-18 (a). Following that, the higher DC current means that the core is more seriously saturated, and hence the higher 2nd harmonic magnitude in the HV current and DC flux in the main

limbs as demonstrated in Figure 5-18 (b) and (c). Figure 5-18 (a) also illustrates that a lower HV winding resistance leads to a higher HV winding current in Stage II. Meanwhile, the core DC electromotive force added on the core is higher with a smaller HV winding resistance, accelerating the DC flux accumulation rate as shown in Figure 5-18 (c). Consequently, the DC flux has the fastest growth rate when the HV winding resistance is 0.636 Ω. In summary, the reduction in the HV winding resistance will lead to a faster saturation rate and a more serious saturation state in transient.

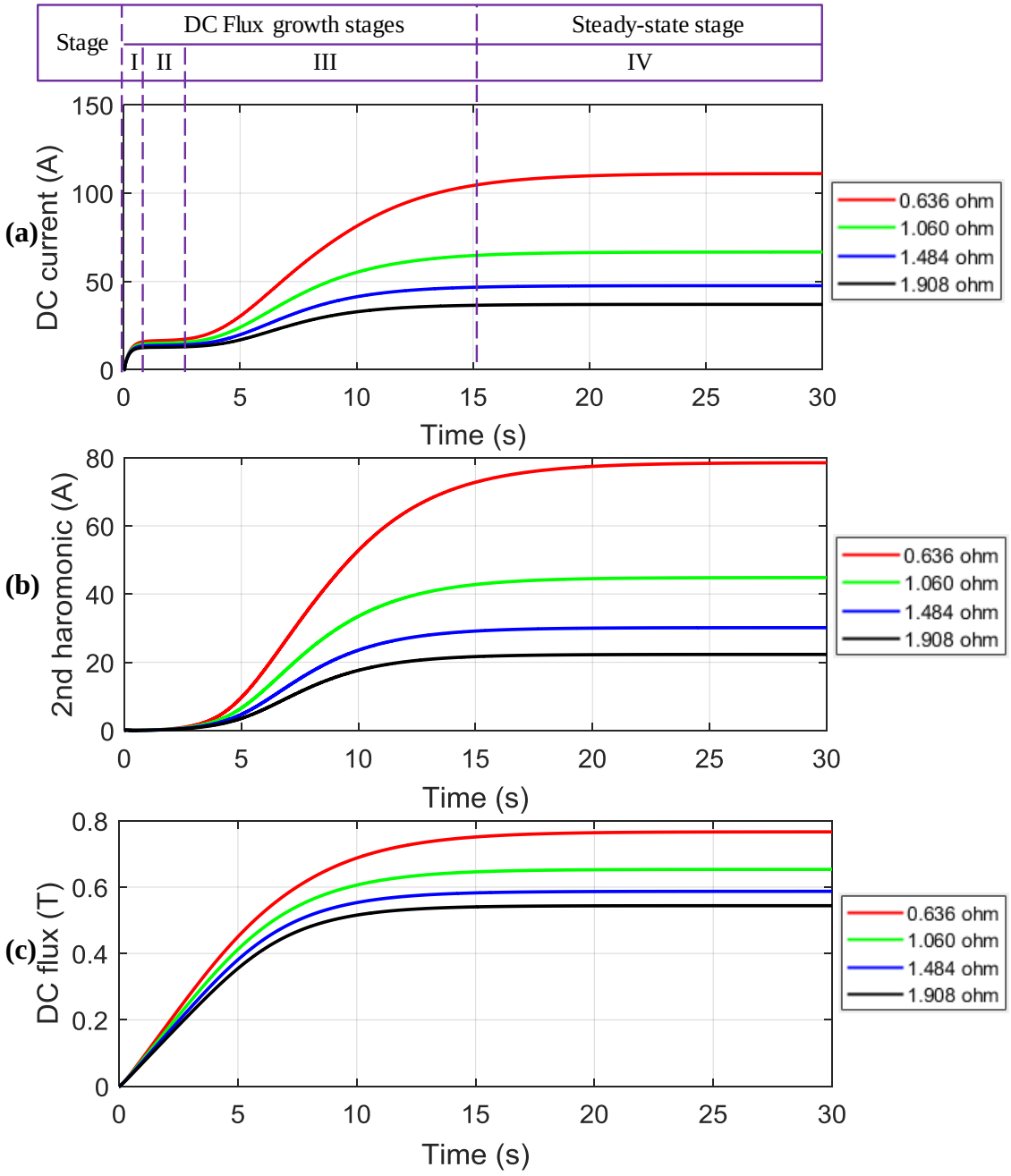

Figure 5-18: (a) DC components in Phase B HV winding current (b) 2nd harmonic in Phase B HV winding current (c) DC flux density in Phase B limb when simulating with different HV winding resistance.

5.4.2 TV winding resistance

Originally, the delta winding resistance is 3.683 Ω referred to the HV side. To investigate its influence on the GIC simulation results, the delta winding resistance is modified equivalently from 2.210 Ω to 6.629 Ω.

- Steady state results

Figure 5-19 (a) and (b) show Phase B HV winding current and delta winding current in the steady state. The comparisons prove that the change in the delta winding resistance will not impact the steady state results. There are no DC components in the delta winding current in the steady state. Meanwhile, the DC voltage supply and the HV winding resistance remain the same, so the steady state HV winding DC current will equal 66.7 A. Finally, the transformer core will reach an identical saturation state in spite of the different delta winding resistances, which leads to a consistent magnetising current. In addition, the delta winding resistance only influences the DC components in the delta winding current; therefore, it will not affect the delta winding waveform in the steady state which only contains AC components as displayed in Figure 5-19 (b). As a result, the waveforms of the HV winding current also remain the same as shown in Figure 5-19 (a).

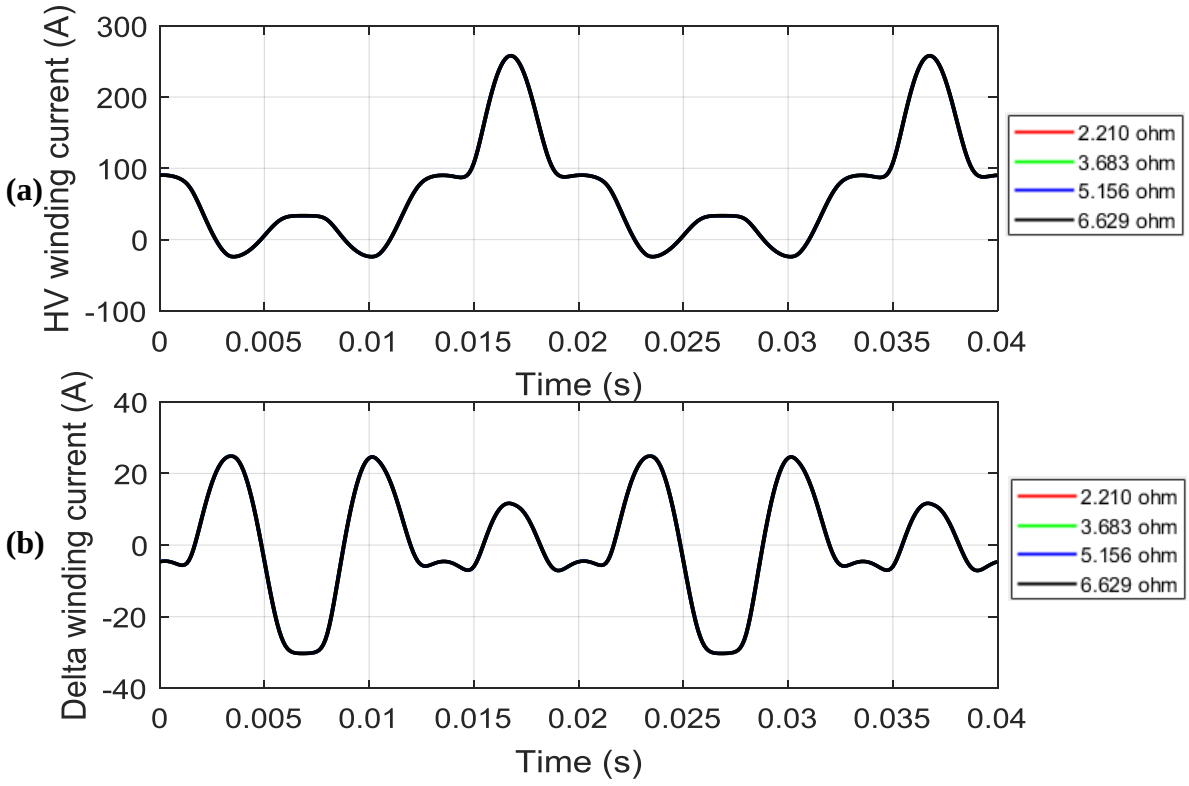

Figure 5-19: (a) Phase B HV winding current (b) Delta winding current in steady state when simulating with different TV winding resistance.

- **Frequency spectrum in the whole simulation duration**

Figure 5-20 (a), (b) and (c), which display the DC components and the 2nd harmonic in Phase B HV winding current and the DC flux in Phase B main limb, illustrate that the TV winding resistance can determine the transformer saturation process.

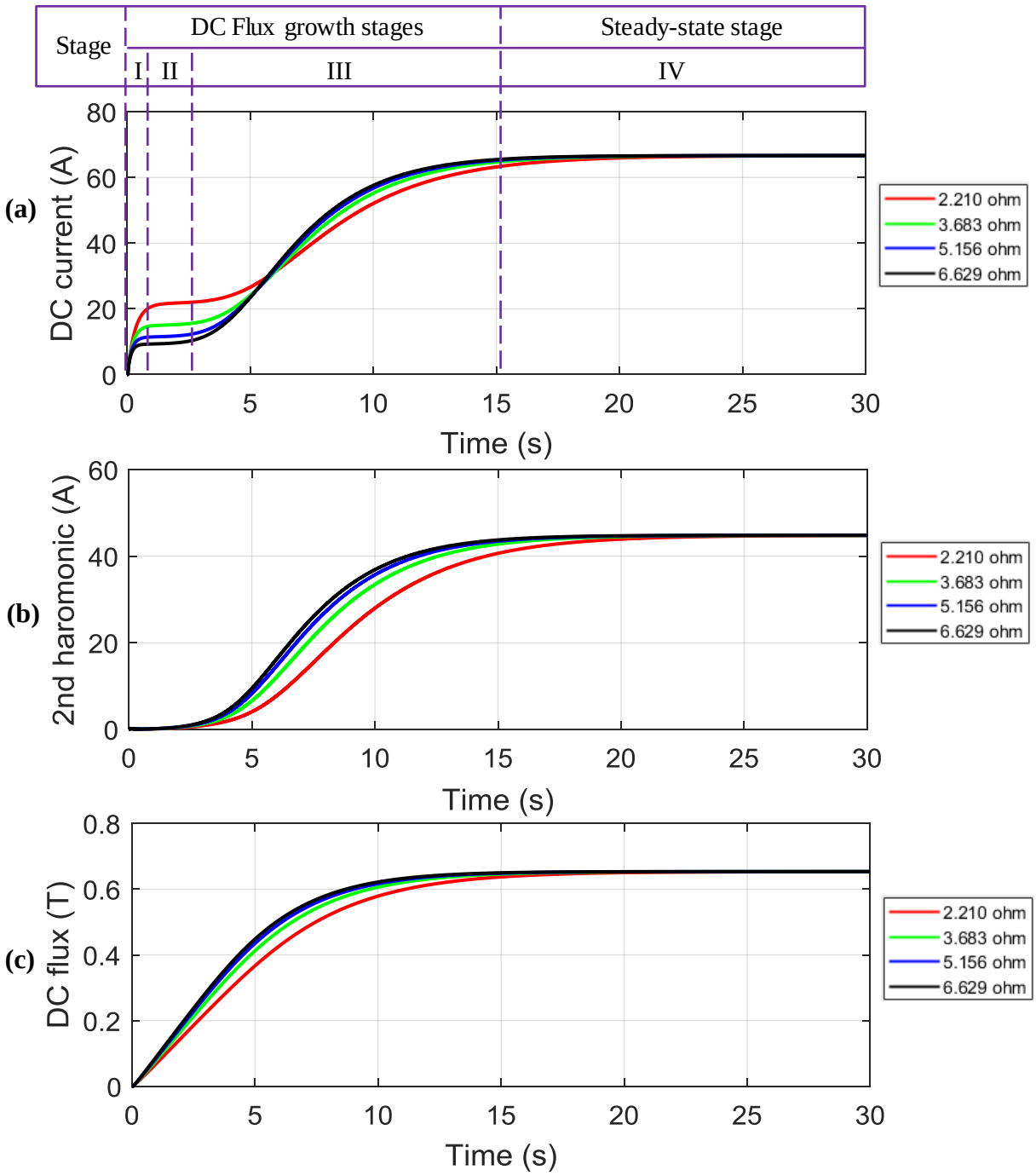

Figure 5-20: (a) DC components in Phase B HV winding current (b) 2nd harmonic in Phase B HV winding current (c) DC flux density in Phase B limb when simulating with different TV winding resistance.

As can be seen in Figure 5-20 (a), different DC current magnitudes can be observed in Stage II. As explained in Section 4.3, the DC current in Stage II is determined by both the HV winding resistance and the delta winding resistance. While the HV winding resistance remains the same, the lower the delta winding resistance is, the higher DC current Stage II will be. Meanwhile, the DC electromotive force on the core is lower with the smaller delta winding resistance, which contributes to the lower saturation rate as shown in Figure 5-20 (b) and (c). Figure 5-20 (a) shows that the DC current spends 15.1 s reaching 95% of its steady state value when the delta winding resistance is 2.210 Ω. However, it only requires 12.5 s in the case of 6.629 Ω. However, the delta winding resistance is not associated with the steady state values of the currents and the flux densities. Overall, reducing the delta winding resistance can delay the saturation process and has no impacts on the steady state results.

5.4.3 HV winding leakage inductance

Normally, the transformer impedance of a 240 MVA transformer is an isolated value around 20% between the HV and LV winding to limit the short circuit current. In this section, the HV winding inductance is set at 99 mH, 298 mH and 496 mH respectively to determine the impacts of the HV winding inductance on the GIC simulation results.

- Steady state results

Figure 5-21 (a) indicates that the peak HV winding current increases with the reduction in the HV winding inductance. Apparently, the lower HV winding inductance is, the higher magnitude of the HV winding current (seen from Figure 5-21 (a)) and the limb flux density (seen from Figure 5-21 (c)) will be. In addition, Figure 5-21 (b) shows that the HV winding leakage inductance influences the delta winding current peaks, especially for Peak 4 and Peak 8 caused by the saturation of Phase A limb and Phase C limb. Generally, the simulation results with 298 mH and 496 mH HV winding inductance are similar in the steady state.

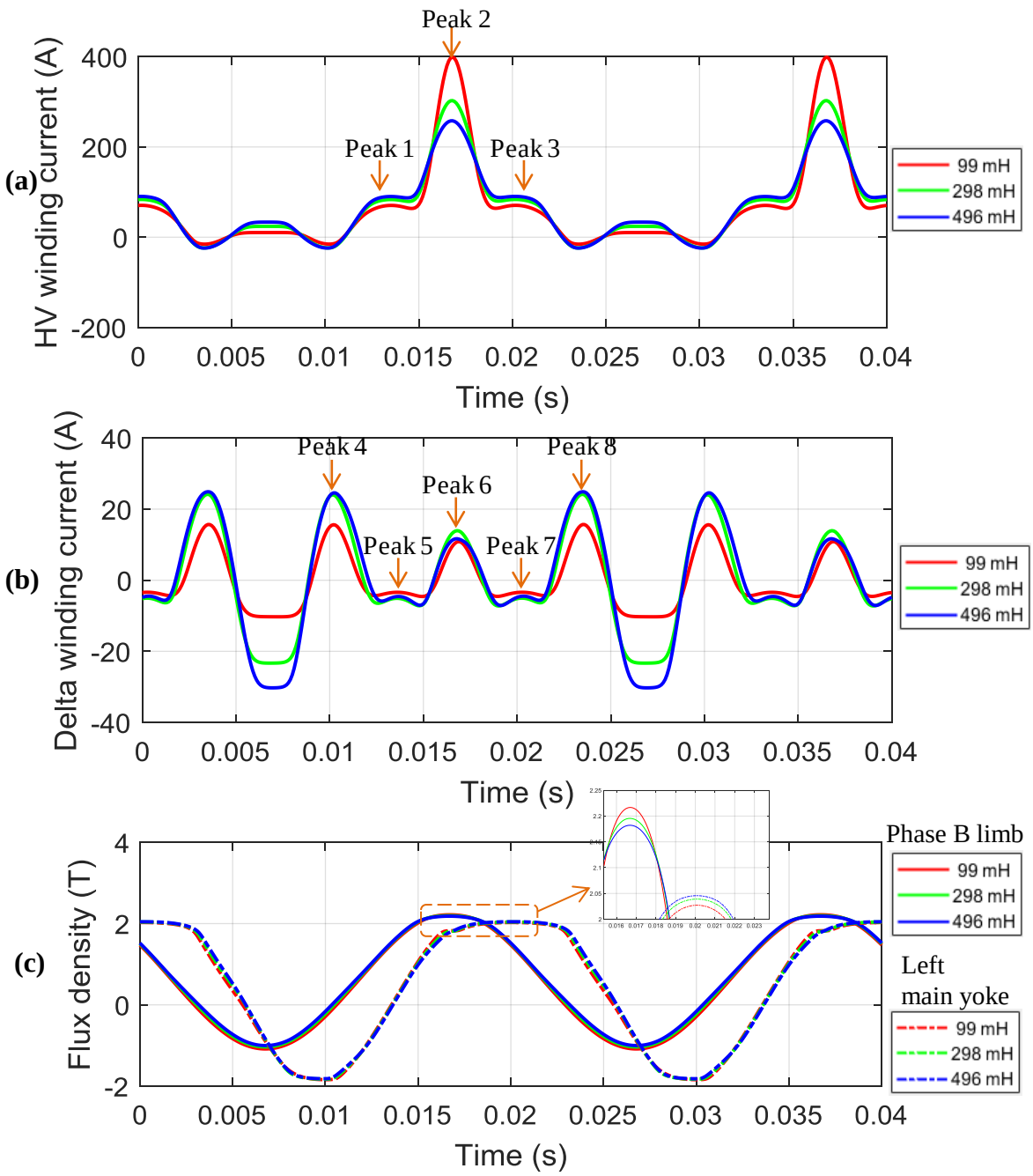

Figure 5-21: (a) Phase B HV winding current (b) delta winding current (c) Phase B limb flux density and left main limb flux density in steady state when simulating with different HV winding inductance.

- **Frequency spectrum in the whole simulation duration**

As described before, the transformer saturation rates in Stage II are mainly determined by the electromotive force on the core, which is mainly decided by the winding resistances. Consequently, the simulation results did not show any obvious

difference in Stage II for both the current and the flux frequency spectrum results as can be observed from Figure 5-22 (a), (b) and (c).

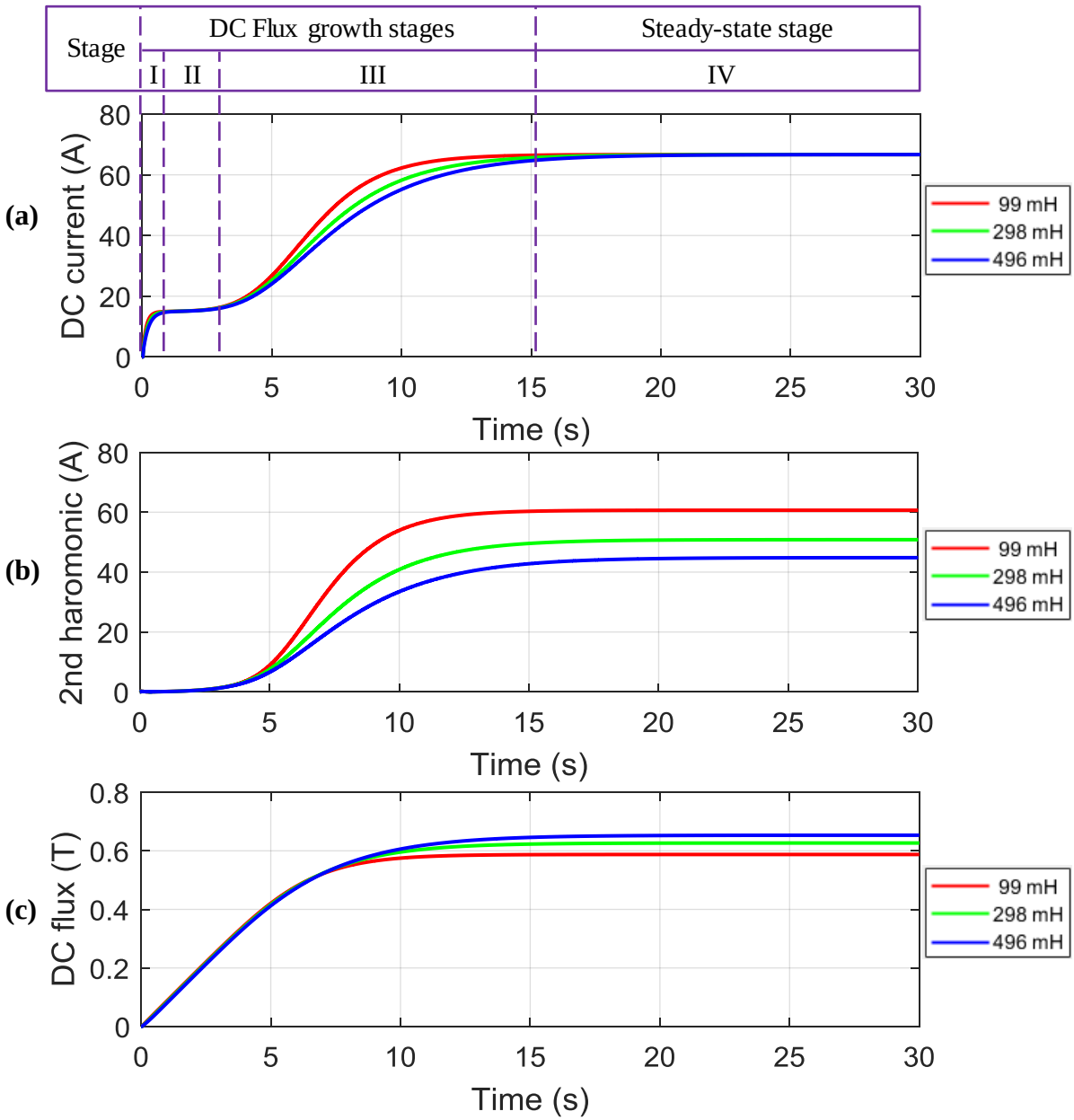

Figure 5-22: (a) DC components in Phase B HV winding current (b) 2nd harmonic in Phase B HV winding current (c) DC flux density in Phase B limb when simulating with different HV winding inductance.

However, Figure 5-22 (a) demonstrates that the DC current has a higher growth rate in Stage III with a lower HV leakage inductance. Moreover, the 2nd harmonic in the HV winding current has the greatest increasing rate and steady state magnitude when the HV leakage inductance is 99 mH. However, it is interesting to note that the DC flux density in

Phase B limb is the lowest with 99 mH HV winding inductance, as seen from Figure 5-22 (c), while the peak Phase B limb flux density is the highest shown in Figure 5-21 (c) because the highest harmonic flux is contained in the main limb.

To conclude, the reduction in HV leakage inductance will lead to a higher magnitude and 2nd harmonic current of the HV winding current, but there is no evidence to show that the saturation rate of the transformer limbs is related to HV winding inductance in Stage I and Stage II.

5.4.4 TV winding leakage inductance

In this section, the leakage inductance of the TV side is assumed as 541 mH, 1624mH and 2706 mH respectively, afterwards referred to 400 kV side, for which a sensitivity study for GIC is conducted.

- Steady state results

Figure 5-23 (a) illustrates that the change in the TV winding inductance will not severely impact the peaks of the HV winding current. The peaks of the HV winding current are generated by the peaks of the magnetising current, which is determined by the peaks of the main limb flux density. As can be observed in Figure 5-23 (c), the limb flux densities with different TV winding inductances are almost identical, so the close peak magnetising current and the peak HV winding current will be achieved. However, the troughs of the HV winding current, which are mainly caused by the delta winding current, become deeper with lower TV winding inductance because the amplitude of the delta winding current is larger as shown in Figure 5-23 (b). To conclude, the TV winding inductance mainly impacts on the troughs of the HV winding current and the full waveform of the delta winding current in the steady state.

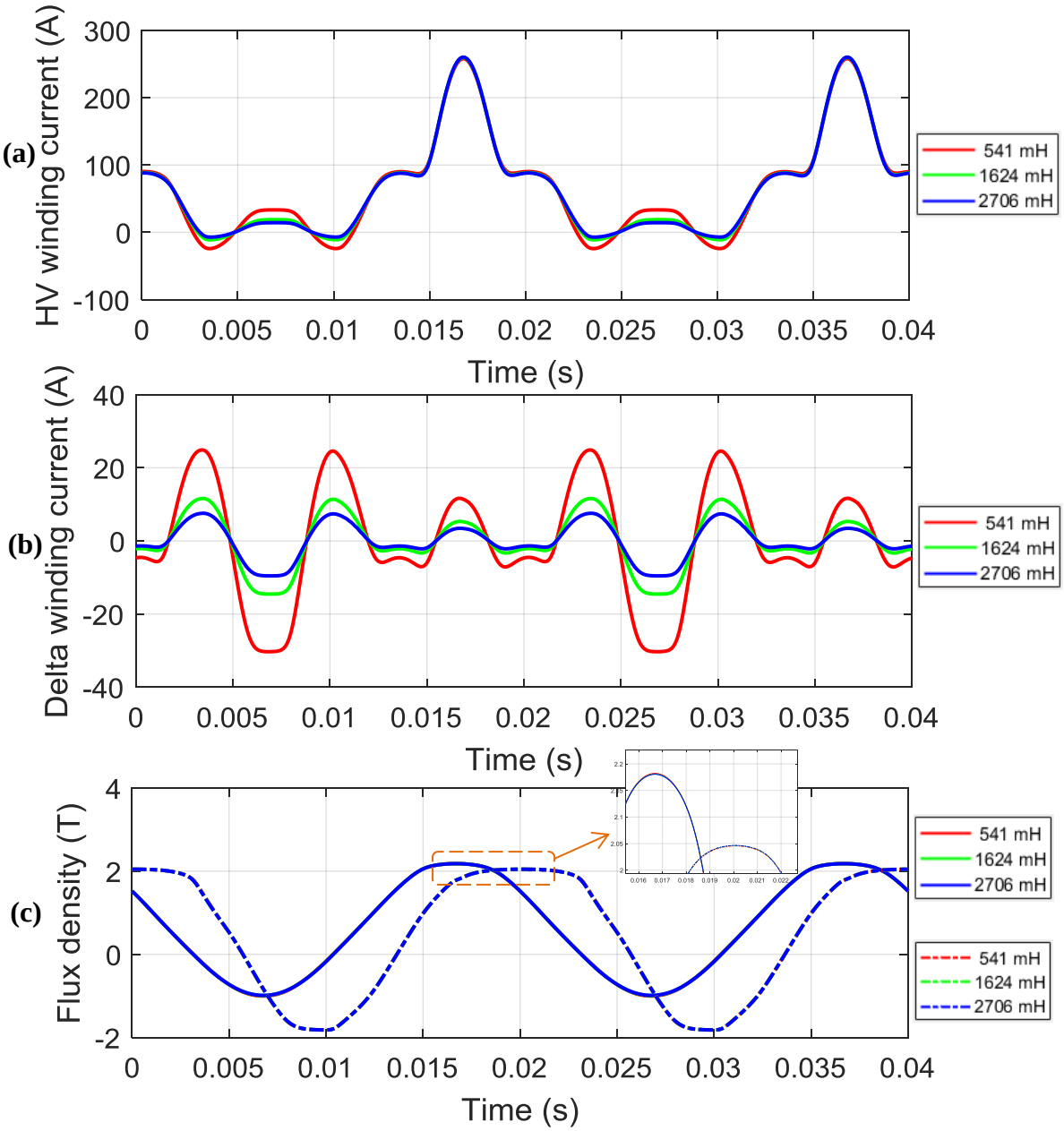

Figure 5-23: (a) Phase B HV winding current (b) delta winding current (c) Phase B limb flux density and left main limb flux density in steady state when simulating with different TV winding inductance.

- **Frequency spectrum in the whole simulation duration**

Figure 5-24 (a) indicates that the TV winding inductance only impacts the DC components in the HV winding current in Stage I. As discussed before, Stage I is the step response stage for building up the DC current, which is determined by the winding inductance. Thus the lower TV winding leakage inductance means that the DC current reaches the steady state value in Stage II earlier. However, the faster increasing rate in

Stage I does not impact the overall core saturation process as shown in Figure 5-24 (c). The waveforms of the DC flux density in Phase B limb almost overlap, proving that the TV winding leakage inductance has limited impacts on the core saturation process. In terms of the 2nd harmonic in the HV winding current, the waveform simulated in the case with 541 mH TV winding inductance increases the fastest and finally reaches the highest steady state magnitude. The additional 2nd harmonic current is produced in the delta winding due to the low TV winding inductance.

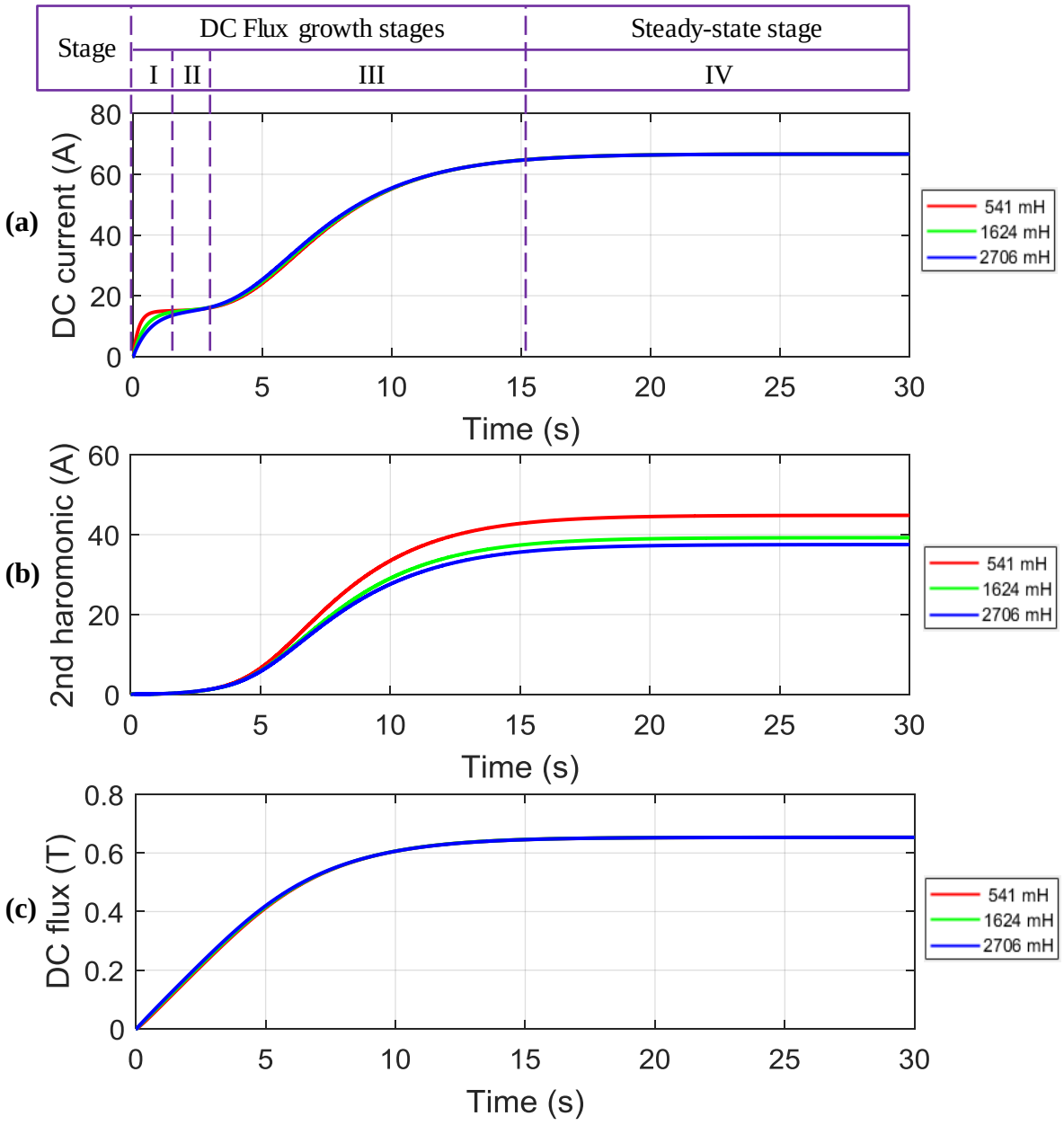

Figure 5-24: (a) DC components in Phase B HV winding current (b) 2nd harmonic in Phase B HV winding current (c) DC flux density in Phase B limb when simulating with different TV winding inductance.

Overall, the main threat to the reduction in TV winding leakage inductance comes from the increasing harmonics in delta winding and is thus the part induced in the HV side.

5.5 Summary

In this chapter, sensitivity studies for parameters of the magnetic circuit including yoke/limb cross-sectional area ratio, and the flux leakage paths are conducted. For electric circuit, an arbitrary range of winding impedance was also used to show their impacts, although it is clearly understood by the author that the electrical circuit can be designed to confine the actual value of winding resistance and leakage inductance within a precise range.

Section 5.2 and Section 5.3 discuss sensitivity studies for the transformer yoke/limb cross-sectional area ratio and the tank-oil leakage path parameter setting under GIC input. The yoke/limb cross-sectional area ratio and the leakage paths setting significantly impact the simulation in the steady state. The risk level for the factors in Section 5.2 and 5.3 are shown in Table 5-1. The change of each factor is from 50% to 150% of the original value with a step of 25%. There are arbitrary 5 classes to assess how each factor impacts on the transformer susceptibility to GIC, and the upper limit and the lower limit of each class are defined by the percentage of the change in the peak of Phase B HV winding current (I_B) as given in Table 5-1. In conclusion, the cross-sectional ratio of the yokes and the length and the area of the oil gaps need to be noted in the simulation and when determining the transformer design, since the HV winding current magnitude is significantly impacted by these factors.

Section 5.4 introduces the impact of the winding impedance on the GIC simulation results, the change of each factor is arbitrarily set as from 20% to 180% of the original value with a step of 40%, and the winding impedance's impact on the steady state current magnitude as well as the saturation rate, was studied. To conclude, the HV winding resistance will significantly influence the steady state results and the transformer core saturation rate because it changes the steady state DC current injection. The change in the TV winding resistance will not impact on the steady state results, but the lower TV winding current will lead to a faster core saturation rate.

Table 5-1: Severities of core and tank dimensions affecting GIC simulation results.

Factor		Minor (<1%)	Moderate (1%-5%)	Strong (5%-10%)	Severe (10%-20%)	Extreme (>20%)
Yoke/limb cross-sectional area ratio	Main yoke				✓	
	Side yoke					✓
Tank path length		✓				
Tank path area			✓			
Oil gap length				✓		
Oil gap area				✓		

Chapter 6: Comparison of 3-limb and 5-limb Transformer under Neutral DC Offset

6.1 Introduction

This chapter introduces the comparison of the 3-limb transformer and 5-limb transformer under a neutral DC offset. Normally, 5-limb transformers are more vulnerable to GIC than 3-limb transformers. 3-limb transformers are conventionally considered as the immune type to defend against GIC. However, it is doubtful because 3-limb transformers could suffer severe damage during GMD events according to a recent study [26, 90], especially for transformers with narrow gaps between the core and the tank.

In this chapter, the newly developed 3-limb transformer model will be introduced first. Secondly, an artificial 3-limb transformer is provided with AC+DC input and the simulation results are compared with those simulated by the 5-limb model. Thirdly, different magnitudes of the DC input are injected to the 3-limb and 5-limb transformer to assess their vulnerabilities based on the current and flux density results. Lastly, the 3-limb transformer is also simulated by the Hybrid model, and the simulation results are compared to those of the new model.

6.2 Overview of 3-limb model

The newly developed 3-limb model is also composed of the equivalent electric circuit and magnetic circuit. The electric circuit of the 3-limb model is exactly the same as that of the 5-limb model. The calculation steps of the electric circuit are explained in the 5-limb model referred to in Section 4.3.1. This section introduces the equivalent magnetic circuit of the 3-limb model.

6.2.1 Equivalent magnetic circuit

The various core structures of the 3-limb core inevitably cause different algorithms to be applied in the magnetic circuit. As can be observed from Figure 6-1, the 3-limb core model only contains 3 leakage paths, one path for each limb. Eq. 6.1 to Eq. 6.6, which are

based on Kirchhoff's Magneto Motive Force Law and Ampere's Law, can obtain the flux density ($[B]$) and magnetic field intensity values ($[H]$) at each part of the core, tank and oil gaps, after the magnetic model receives the limb flux density data from the equivalent electric circuit. After the magnetising currents are calculated by Eq. 6.7 to Eq. 6.9, the values are given to the equivalent electric circuit.

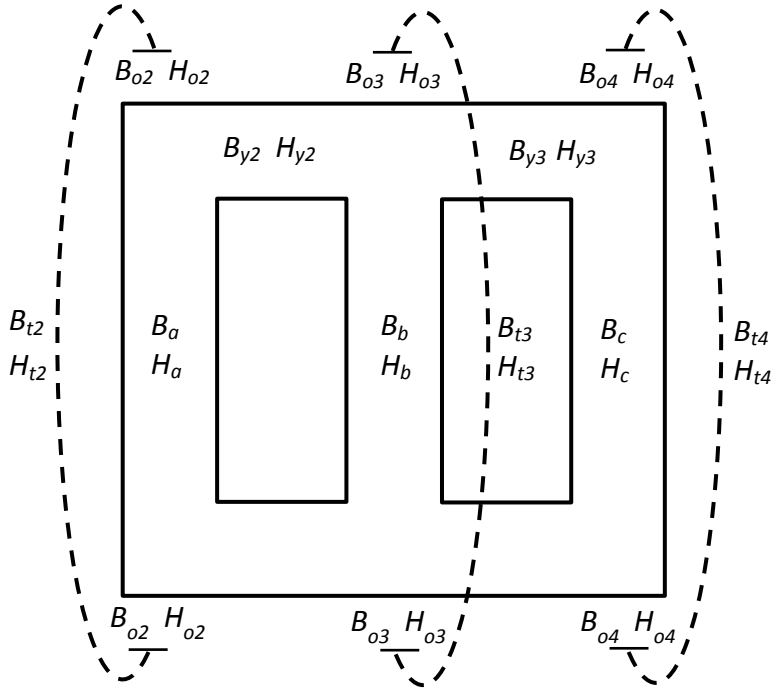

Figure 6-1: Schematic diagram of 3-limb transformer core including oil gaps and tank flux paths.

$$B_{tn} \cdot A_{tn} = B_{on} \cdot A_{on} \tag{6.1}$$

$$B_a \cdot A_a + B_{y2} \cdot A_{y2} = B_{o2} \cdot A_{o2} \tag{6.2}$$

$$B_b \cdot A_b = B_{y2} \cdot A_{y2} + B_{y3} \cdot A_{y3} + B_{o3} \cdot A_{o3} \tag{6.3}$$

$$B_c \cdot A_c + B_{y3} \cdot A_{y3} = B_{o4} \cdot A_{o4} \tag{6.4}$$

$$2 \cdot H_{o2} \cdot l_{o2} + H_{t2} \cdot l_{t2} + 2 \cdot H_{y2} \cdot l_{y2} = 2 \cdot H_{o3} \cdot l_{o3} + H_{t3} \cdot l_{t3} \tag{6.5}$$

$$2 \cdot H_{y2} \cdot l_{y2} + 2 \cdot H_{o2} \cdot l_{o2} + H_{t2} \cdot l_{t2} = 2 \cdot H_{y3} \cdot l_{y3} + 2 \cdot H_{o4} \cdot l_{o4} + H_{t4} \cdot l_{t4} \tag{6.6}$$

$$MMF_A = H_a \cdot l_a + 2 \cdot H_{o2} \cdot l_{o2} + H_{t2} \cdot l_{t2} = N \cdot I_{ma} \tag{6.7}$$

$$MMF_B = H_b \cdot l_b + 2 \cdot H_{o3} \cdot l_{o3} + H_{t3} \cdot l_{t3} = N \cdot I_{mb} \tag{6.8}$$

$$MMF_C = H_c \cdot l_c + 2 \cdot H_{o4} \cdot l_{o4} + H_{t4} \cdot l_{t4} = N \cdot I_{mc} \tag{6.9}$$

where n=2, 3, 4

$[A]$	Cross-sectional area matrix for all structural parts (m^2)
$[B]$	Flux density matrix for all structural parts (T)
$[H]$	Magnetic field intensities for all structural parts (A/m)
$[I_m]$	Phase magnetising current (A)
$[MMF]$	Phase magnetomotive force (A)
N	Turn number in HV side
$[l]$	Structural length (m)

6.2.2 Transformer parameter setting

For the purpose of comparing the simulation results for 3-limb transformers and 5-limb transformers, an artificial 3-limb transformer is assumed in this section, whose parameters are based on the 5-limb transformer applied in the simulation of Section 4.3. The parameters of the electric circuit of the 3-limb transformer are displayed in Table 6-1, whose values are the same as those of the 5-limb transformer.

Table 6-1: Transformer basic information applied in simulation for 3-limb transformer.

Voltage	400/120/21 kV
Winding connection	*Y-y-d*
Core type	3-limb
Winding resistance (HV/TV referred to HV side)	1.060/ 3.683 Ω
Leakage inductance (HV/TV referred to HV side)	496/ 2706 mH

The key difference between a 5-limb transformer and a 3-limb transformer is the core dimensions. In this section, the artificial 3-limb transformer core is assumed according to the dimension of the 5-limb core. As seen from Figure 6-2, the length and the cross-sectional area of the 3-limb core main limb is the same as those of the 5-limb core, while the yoke length of the 3-limb core is assumed to equal the main yoke length of the 5-limb transformer. Meanwhile, the yoke cross-sectional area equals the limb cross-sectional area. The distance between the top yoke and the top tank is 0.223 m which is identical to that of the 5-limb transformer. The equivalent area and length of the oil gaps are the same

as those of the 5-limb core. Therefore, the tank size is redefined as shown in Figure 6-2. It is necessary to mention that the distance between the side limb and the side tank is 0.933 m, which is much greater than the value in the 5-limb model because extra space is required for accommodating the winding of the outer limbs. Table 6-2 provides the length and the cross-sectional area of the flux paths in the core, in the insulation oil and in the tank.

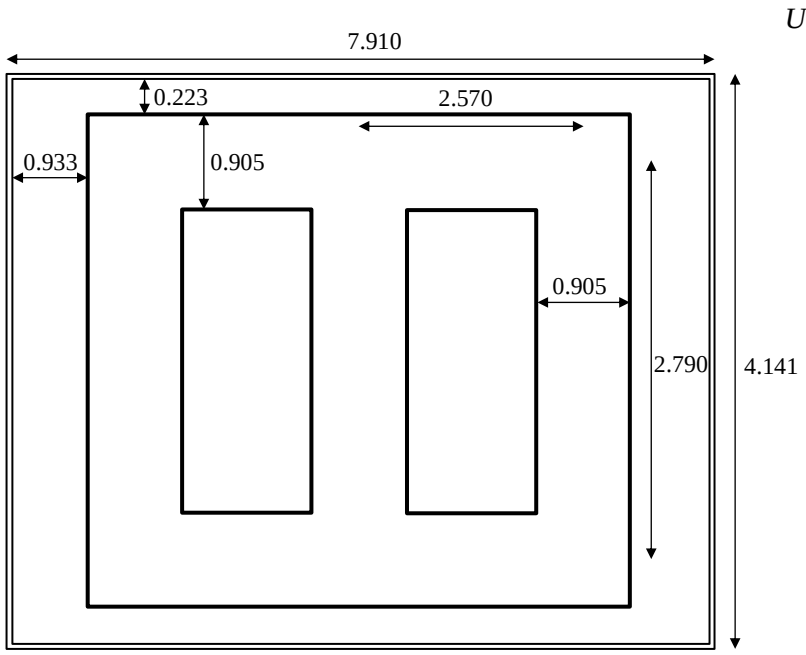

Figure 6-2: Schematic diagram of 3-limb transformer core including oil gaps and tank flux paths.

Table 6-2: Tank and core size of the artificial 400 kV 3-limb transformer.

Limb length (m)	2.790
Yoke length (m)	2.570
Oil gap length (m)	0.223
Tank path length (m)	6.141
Limb cross-section area (m^2)	0.6438
Yoke cross-section area (m^2)	0.6438
Oil gap cross-sectional area (m^2)	0.6438
Tank path cross-sectional area(m^2)	0.1982

6.3 Simulation under AC+DC input

6.3.1 Current waveforms over whole duration

In this section, a DC voltage source of 70.7 V is also provided to the 3-limb transformer in order to guarantee the steady state neutral DC current is 200 A. In other words, both the 3-limb and 5-limb transformers experience the same strength GMD phenomenon.

Figure 6-3 (a)-(f) shows the comparison of the current results simulated by the 3-limb transformer and 5-limb transformer under a 200 A DC neutral input. Both simulations show that 30 s simulation duration is significant as both of the currents finally reach the steady state. Obviously, the currents of the 5-limb transformer contain much greater harmonics than those of the 3-limb transformer. For example, the peak-to-peak amplitudes of Phase A HV winding current for the 3-limb transformer and 5-limb transformer are 5.1 A and 353.2 A respectively.

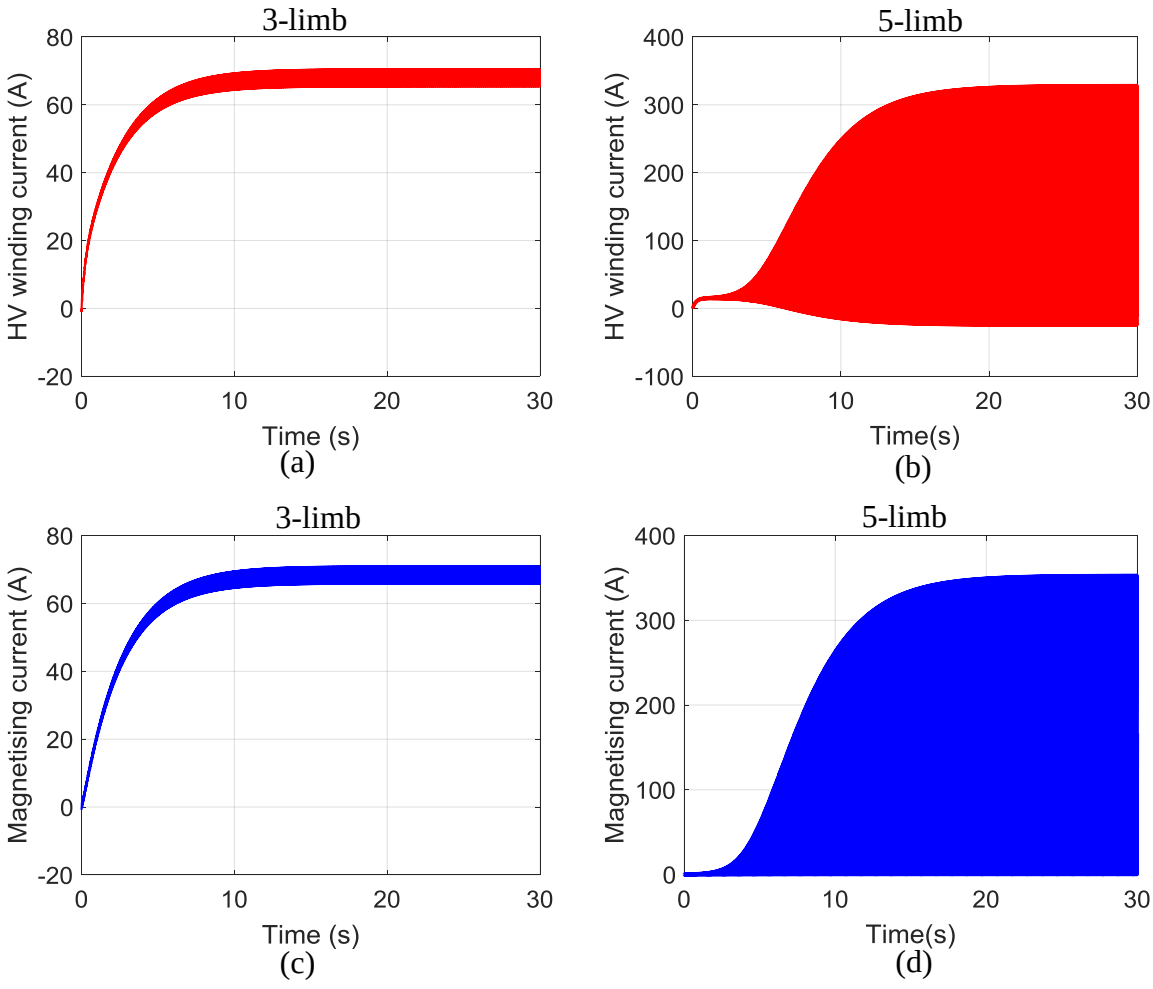

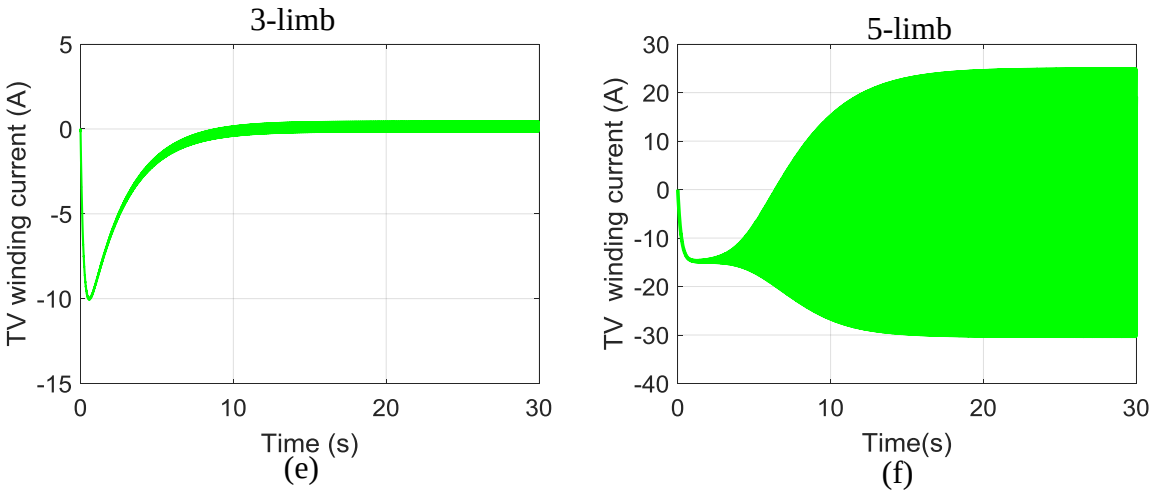

Figure 6-3: Phase A (a) HV current I_{hv_a} for 3-limb transformer (b) HV current I_{hv_a} for 5-limb transformer (c) magnetising current I_{ma} for 3-limb transformer (d) magnetising current I_{ma} for 5-limb transformer (e) Delta (TV) winding current I_{tv_a} of 3-limb transformer (f) Delta (TV) winding current I_{tv_a} of 5-limb transformer over 30 s.

Regarding the waveforms obtained by the 3-limb transformer, the currents of the 3-limb transformer mainly contain the DC components and low AC components. The peak-to-peak amplitudes of the HV winding current, magnetising current and delta winding current in the steady state are 5.1 A, 5.1 A and 0.6 A respectively.

As observed in Figure 6-4 (a) and (b), unlike the simulation results of the 5-limb transformer, the DC components waveforms of the 3-limb transformer only contain three stages. The waveforms of the 3-limb transformer do not contain the pseudo flat stage as those of the 5-limb transformer. It can be observed that the magnetising current of the 3-limb transformer increases dramatically, while the magnetising current of the 5-limb transformer starts to rise quickly in Stage III. In addition, the DC components in the HV winding current of the 3-limb transformer increase faster than that of the 5-limb transformer.

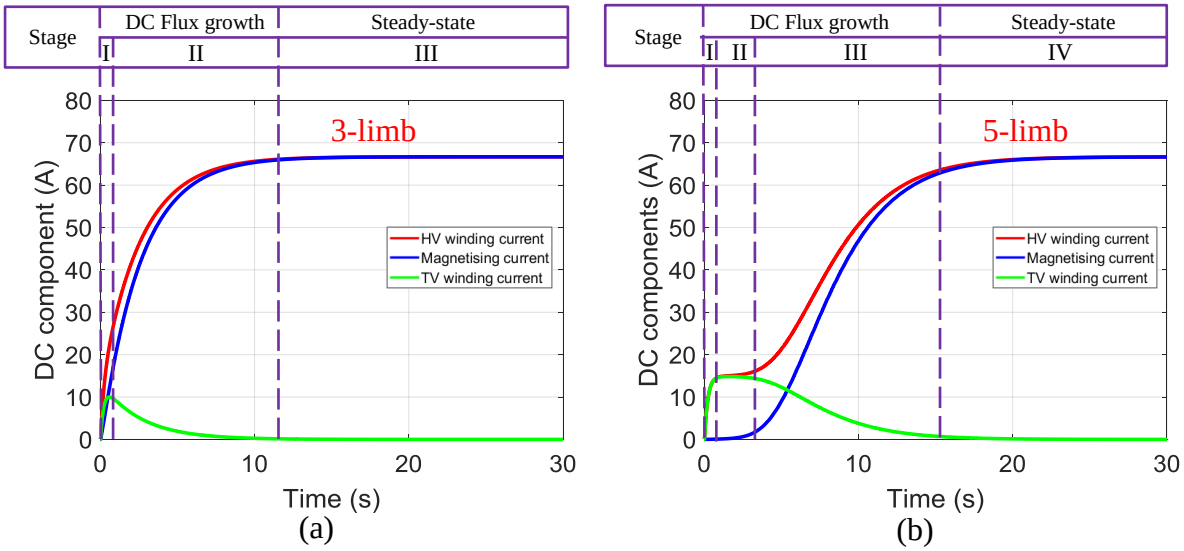

Figure 6-4: DC Components in Phase A HV winding current, magnetising current and delta winding current in 30 s for (a) 3-limb transformer (b) 5-limb transformer.

The 3 stages for the current waveforms of the 3-limb transformer are discussed as follows:

- **Stage I:**

Stage I is the step response period caused by the winding resistance and the leakage inductance. Low AC components are contained in the HV winding current and the magnetising current, while the delta winding current does not contain AC components. In this stage, the core still works in the linear area.

The DC components keep rising steadily in the HV winding and the delta winding in this stage. Unlike the 5-limb model simulation results, the DC current in the magnetising current increases instantaneously after the DC voltage is provided. Since no side yokes can provide DC flux paths for the 3-limb transformer, the DC flux leaks to the oil gaps and the tank with high zero-sequence reluctance. Therefore, DC components in the magnetising current increases instantly, after the DC voltage is provided.

- **Stage II:**

In Stage II, the DC components in the HV winding current and in the magnetising current keep increasing, but the DC components in the delta winding start to decrease. The core is pushed into the saturation area gradually, which leads to lower core

impedance, so that the part of the HV winding DC current flowing into the core branch becomes higher while the part flowing into the delta winding branch becomes lower, as shown in Figure 6-5. Finally, the DC components in the delta winding current will drop to zero gradually. There is no 'pseudo flat' stage in the HV winding current of the waveform simulated by the 3-limb transformer because the DC components in the delta winding current begin to decrease at the very early stage. Generally, this stage performs in a similar way to Stage III in the 5-limb transformer waveform as shown in Figure 6-4 (b).

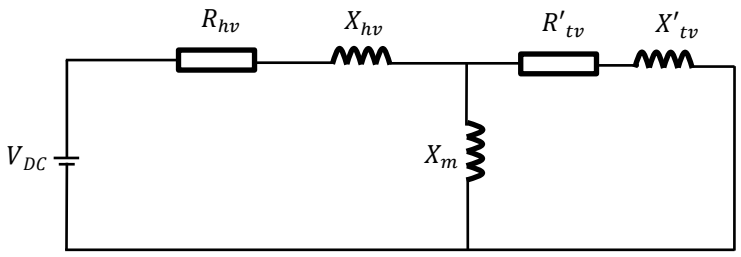

Figure 6-5: Simplified single-phase DC equivalent circuit in Stage II.

- **Stage III:**

In Stage III, both AC and DC components in the currents reach the steady state. The HV winding current, magnetising current and delta winding current contain lower level harmonics compared with the results simulated by the 5-limb model. Similar to the 5-limb transformer results, the DC components only exist in the HV winding current and the magnetising current due to the low core impedance to the DC components in the steady state.

6.3.2 Steady state results

- Current waveforms

In Stage III, the HV winding currents of the 3-limb transformer finally reach the steady state. Figure 6-6 (a) and (b) shows the 2 cycles of the three-phase HV winding currents of the 3-limb transformer and 5-limb transformer respectively in the steady state. The peak-to-peak amplitude of Phase A HV winding current of the 3-limb transformer is 5.1 A which is much lower than 353.2 A of the 5-limb transformer. For this reason, the widely accepted opinion that 5-limb transformers are more vulnerable to GIC than 3-limb transformers is reasonable [90]. When the 3-limb transformer simulation results are

considered, the peak-to-peak amplitude of Phase B HV winding current is 4.5 A which is slightly lower than 5.1 A the Phase A value. The imbalance of the currents is caused by the different flux paths for Phase A limb flux and Phase B limb flux.

However, 3-limb transformers are immune to GIC as shown in the experiments in [19, 109], since the 3-limb transformers measured in these tests are the small-scale transformer model without tank or the distribution transformers with low zero sequence impedance. [26] mentioned that for 240 MVA 3-limb transformers in the UK transmission network, the oil gap can be as low as 2-5 mm, which will lead to low reluctances of the leakage paths and hence high induced current.

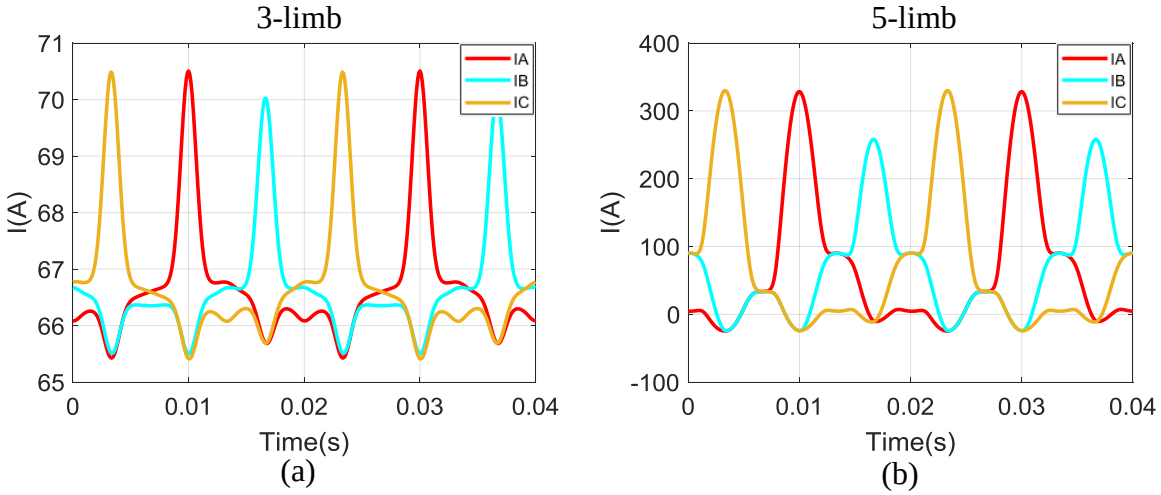

Figure 6-6: Three-phase HV winding current in steady state (a) 3-limb transformer (b) 5-limb transformer.

- Currents frequency spectrum

Figure 6-7 (a) and (b) illustrates the harmonics in Phase A HV winding current, magnetising current and delta winding current of the 3-limb transformer and 5-limb transformer respectively. The harmonics produced by the 3-limb transformer are significantly lower than those of the 5-limb transformer. In addition, the delta winding current of the 3-limb transformer only contains 3^{rd} and 6^{th} harmonics, while the delta winding current of the 5-limb transformer also includes all the other order harmonics except the 5^{th} harmonic. This is caused by the fact that the side limbs of the 5-limb core contribute to an imbalance in the three-phase magnetising current, and the delta winding helps to hold the imbalance current.

Specifically for the 3-limb transformer results, Figure 6-7 (a) does not show the full magnitude of the DC components for the purpose of displaying the magnitude of the other harmonics more clearly. The delta winding current only contains 3rd harmonic and 6th harmonic, and so the magnitudes of 3rd and 6th harmonics in the HV winding current are reduced compared to those in the magnetising current. Consequently, the delta winding helps to hold the triplen harmonics, thus reducing the part flowing into the rest of the power network.

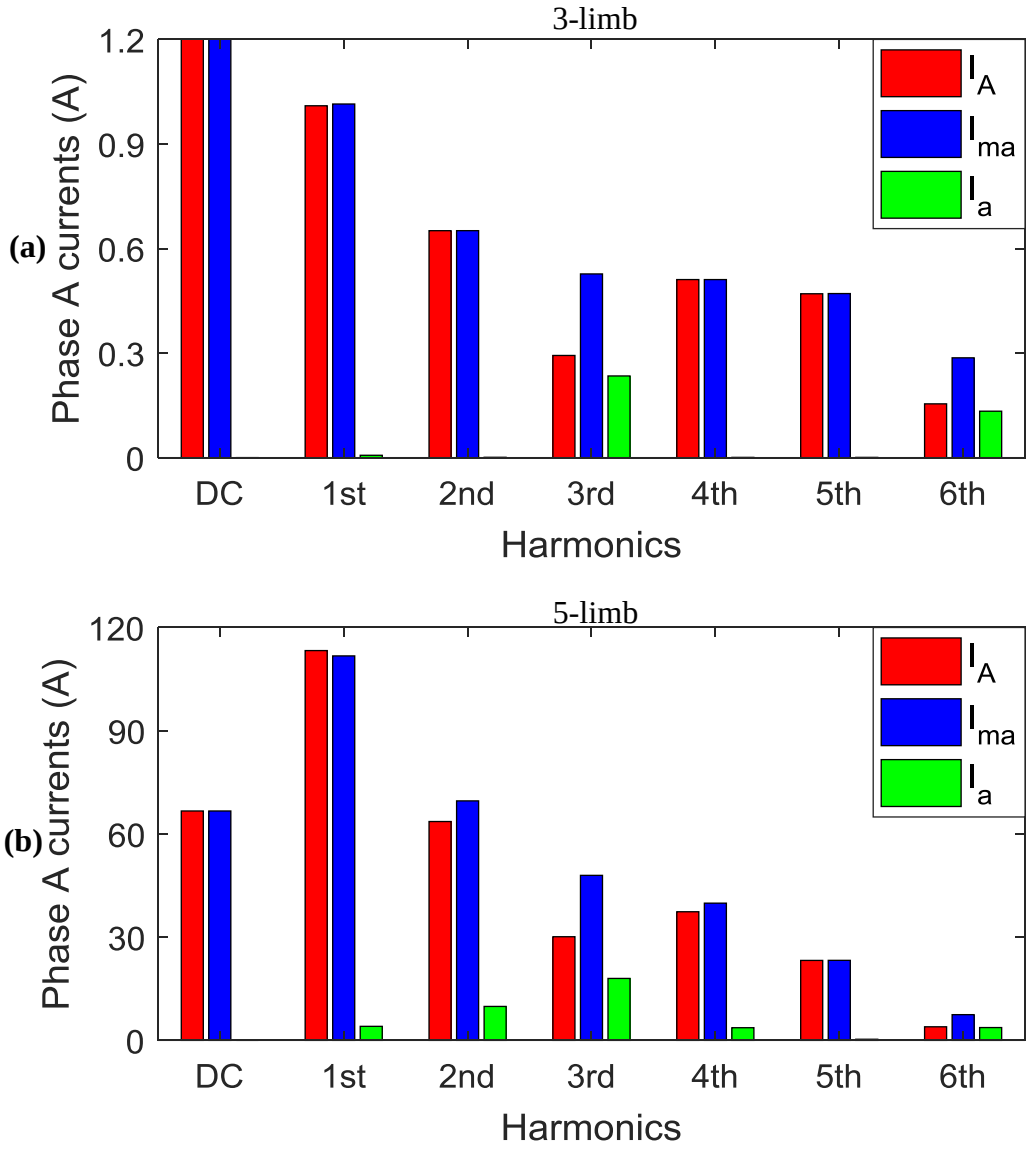

Figure 6-7: Frequency spectrum of Phase A HV winding current, magnetising current and delta winding current in steady state (a) 3-limb transformer (b) 5-limb transformer.

- Flux density analysis

Figure 6-8 (a) and (c) display Phase A HV winding currents, magnetising currents and delta winding current of the 3-limb transformer in the steady state. The peaks and the troughs of the HV winding currents can be explained by the delta winding current and the flux distribution as shown in Figure 6-8 (c) (e) and (g). The nameplates of the limbs and the yokes are displayed in Figure 6-1. Figure 6-8 (b), (d), (f) and (h) are the simulation results of the 5-limb transformer, which has been discussed in Section 4.3. The purpose of displaying the 5-limb transformer simulation results is to give a comparison between the results of 3-limb and 5-limb transformer. Generally speaking, the flux densities in the 3-limb core are lower than those in the 5-limb core.

Regarding the 3-limb transformer simulation results, Figure 6-8 (a) indicates that there is a peak and two troughs in each cycle of Phase A HV winding current. The peak magnetising current is higher than the peak HV winding current because the delta winding will hold part of the triplen order harmonics, so that the harmonics produced in the HV side decreases. Peak 1 of Phase A HV winding current occurs when Phase A limb flux density B_a reaches its peak. The peak Phase A limb flux density B_a is 1.87 T, which is much lower than 2.20 T simulated by the 5-limb model. It is worth noting that the waveforms of B_{y2} and B_{y3} are still in perfect sinusoidal shape, because the zero-sequence flux paths for the 3-limb transformer are the oil gaps and the tank. Two troughs in Phase A HV winding current are produced by the coupling of the delta winding current, when Phase B and Phase C magnetising currents reach their peaks respectively. Trough 1 is generated by the saturation of Phase C limb, and Trough 2 is produced by the saturation of Phase B limb.

Figure 6-9 displays the frequency spectrum results of the flux densities of the 3-limb transformer and 5-limb transformer. Since the HV winding current is seriously distorted for the 5-limb transformer, harmonic flux in the limbs and the other parts of the core will inevitably ensue. Other than the 5-limb transformer, the 3-limb transformer produces little high order harmonic flux. In addition, the DC flux densities in the main limbs of the 5-limb transformer (B_a and B_b) are higher than those of the 3-limb transformer, which also indicates that the 5-limb transformer is more seriously saturated than the 3-limb transformer. In terms of the DC flux densities in the yokes, part of the DC flux in the Phase B limb enters the side yokes (B_{y1} and B_{y4}), which also causes a much higher DC

flux in the yokes for the 5-limb transformer than the 3-limb transformer. The side yokes are important DC flux paths for the 5-limb transformer core, so it is not surprising that the DC flux density in the side yoke reaches 1.57 T.

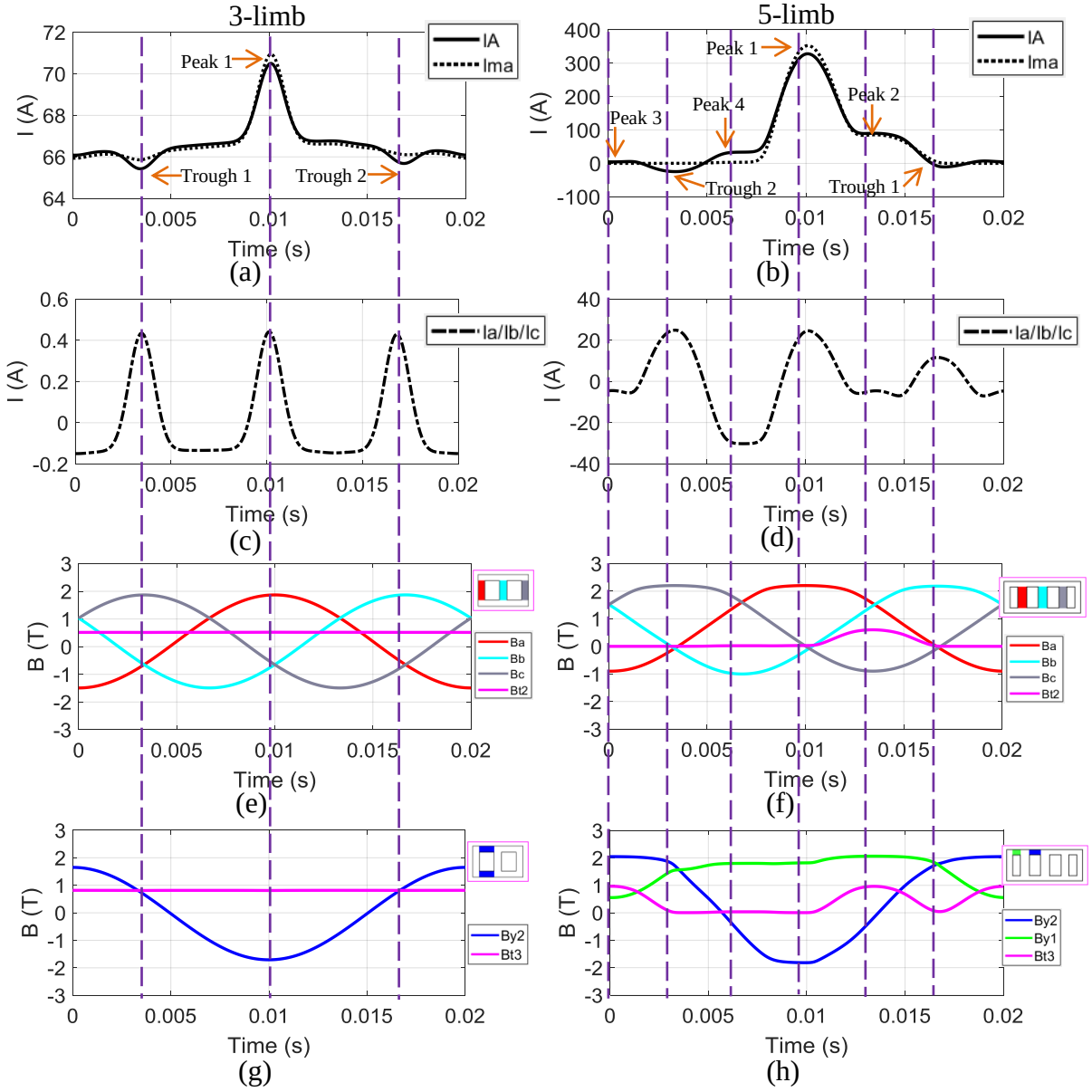

Figure 6-8: Steady-state winding current and flux densities (a) Phase A HV winding current I_{hv_a}, magnetising current I_{ma} of 3-limb transformer (b) Phase A HV winding current I_{hv_a}, magnetising current I_{ma} of 5-limb transformer (c) Delta (TV) winding current I_{tv_a}, I_{tv_b}, I_{tv_c} of 3-limb transformer (d) Delta (TV) winding current I_{tv_a}, I_{tv_b}, I_{tv_c} of 5-limb transformer (e) flux densities of limbs and tank of 3-limb transformer (f) flux densities of limbs and tank of 5-limb transformer (g) flux densities of yokes and tank of 3-limb transformer (h) flux densities of yokes and tank of 5-limb transformer.

The flux leaking to the tank is totally different in the 3-limb transformer and the 5-limb transformer. In the 3-limb transformer, the flux in the tank only contains the DC

components, while the tank flux of the 5-limb transformer also contains large quantities of harmonics because of the harmonic flux produced in the core. In addition, the DC flux density in the tank of the 3-limb transformer is actually higher than that of the 5-limb transformer because the tank-oil gap is the only path of the leakage zero-sequence flux for the 3-limb transformer. On one hand, the hotspot problems in the limbs and tank of a 3-limb transformer cannot be neglected. On the other hand, the 5-limb core may suffer a more severe hotspot problem than the 3-limb core under the same neutral DC input. As recorded in a GMD event on 10th May 1992, a 60 A DC neutral current (20 A per phase) was observed in a transformer operated by Allegheny Energy, and the peak tank temperature was 173 degrees Celsius, which was 120 degrees Celsius higher than the temperature before the GMD event (although the core type is unknown) [78].

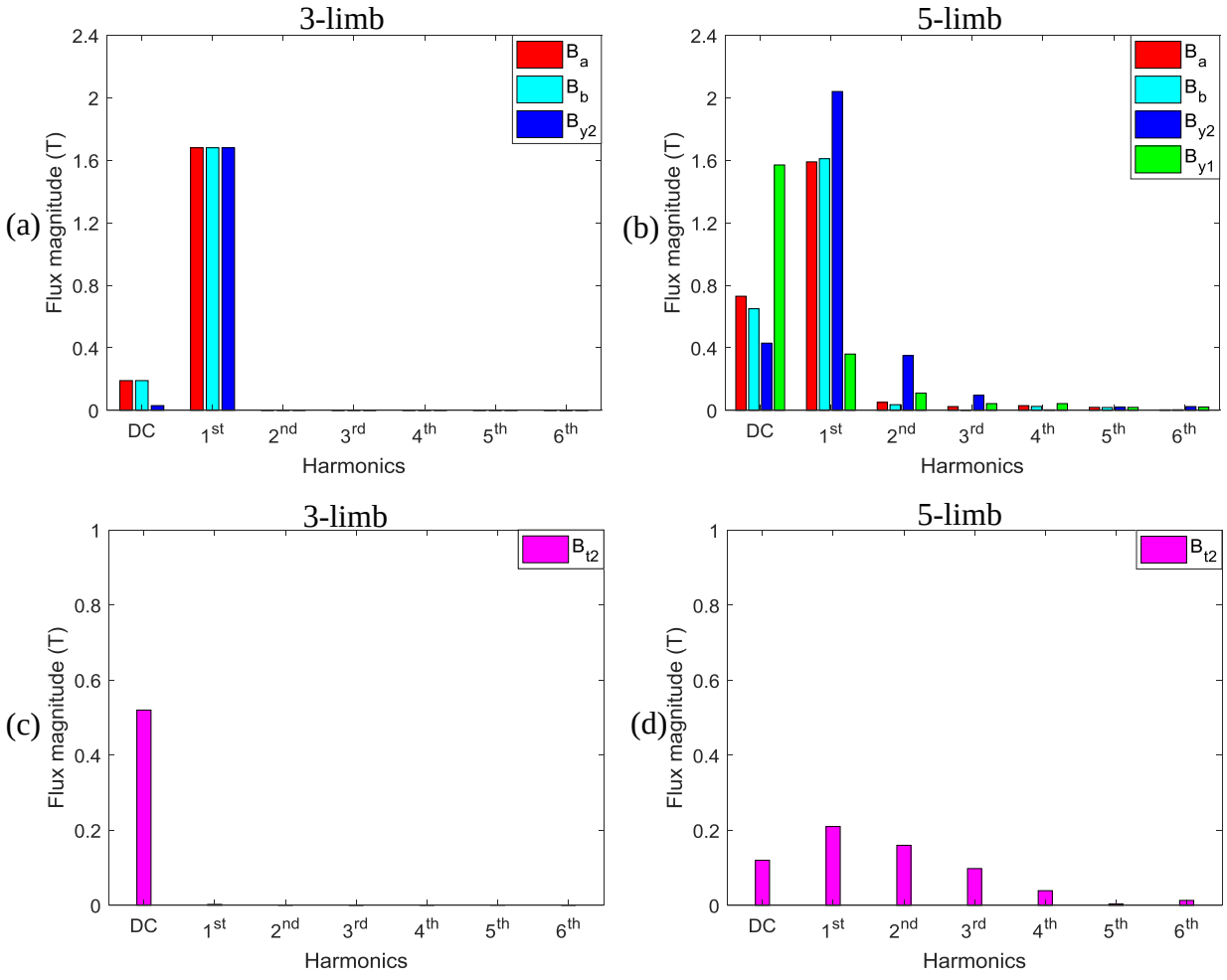

Figure 6-9: Flux density frequency spectrum for (a) 3-limb transformer core (b) 5-limb transformer core (c) 3-limb transformer tank (d) 5-limb transformer tank.

6.4 Comparison of 3-limb and 5-limb transformers under various DC inputs

The 3-limb transformer is considered the type least likely to be affected by GMD events. However, if the electric field produced by GMD events is large enough, the core will also be pushed into the deep saturation operation area. In this section, sensitivity studies are discussed for different magnitudes of DC voltage input on the 3-limb transformer and the 5-limb transformer.

In Figure 6-10 (a), the peak to peak amplitudes of Phase A HV winding currents in the steady state are obtained by the 3-limb model and the 5-limb model under various DC inputs ranging from 0 A to 300 A. The peak-to-peak amplitudes simulated by the 5-limb model significantly exceed the amplitudes simulated by the 3-limb model.

With regard to the 5-limb model simulation results, the peak-to-peak amplitude is nearly proportional to the steady state DC current. The increasing rate shows a slight reduction when the steady state DC current becomes higher. The peak-to-peak amplitude reaches 477.5 A when the neutral DC current is 300 A.

It seems that 3-limb transformers are immune to GIC from Figure 6-10 (a); however, when the steady state neutral DC current increases to 600 A, the peak-to-peak magnitude increases dramatically to 103.5 A as shown in Figure 6-10 (b), which is comparable to the simulation results under 50 A for the 5-limb transformer. Clearly, the peak-to-peak current increases faster after the neutral DC current exceeds 200 A. Therefore, 3-limb transformers still risk being deeply saturated if the GMD events are strong enough.

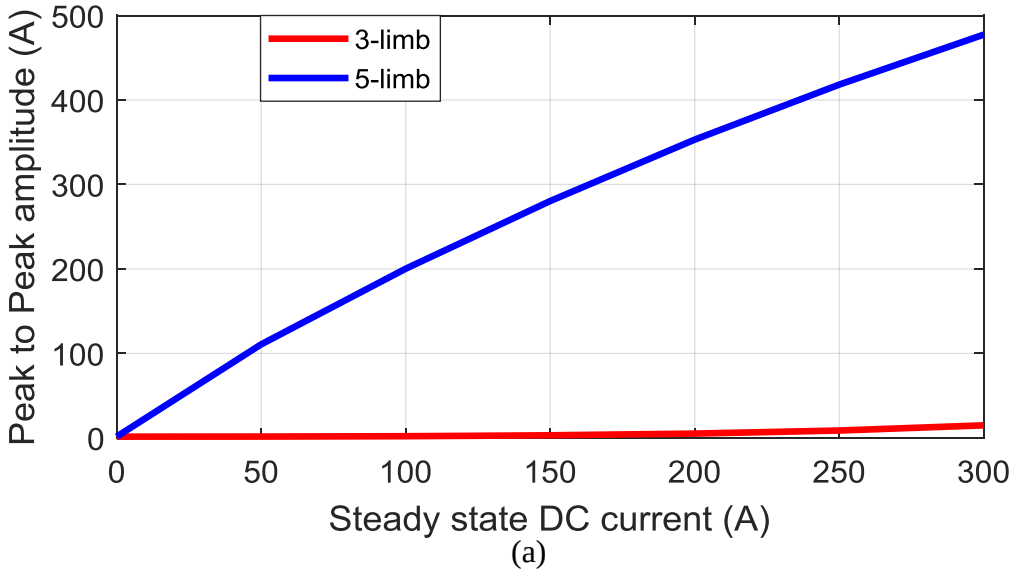

(a)

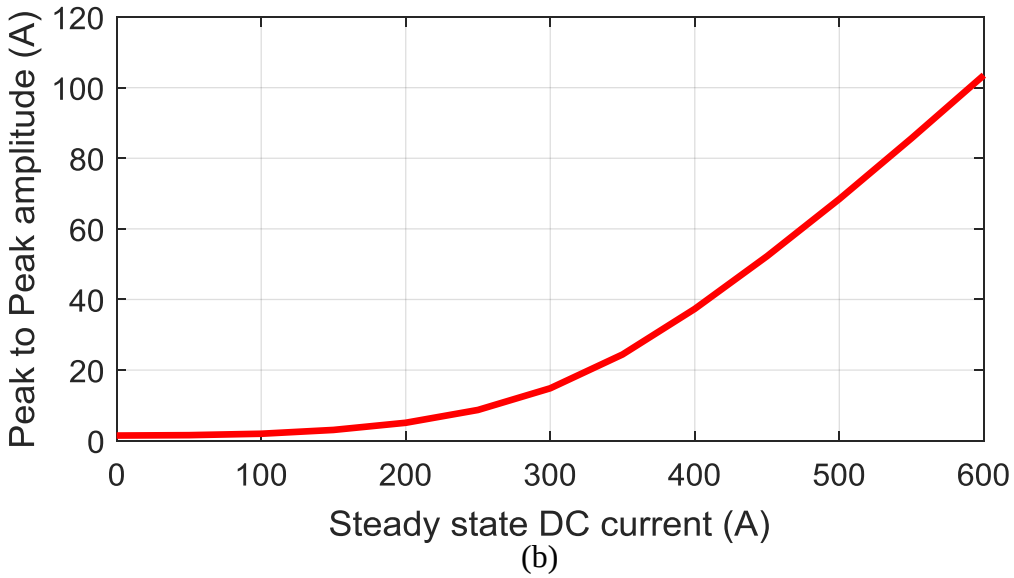

Figure 6-10: Peak-to-peak amplitude of Phase A HV winding current against neutral DC current for (a) 3-limb and 5-limb transformers ranging from 0 A to 300 A (b) 3-limb transformer ranging from 0 A to 600 A.

Figure 6-11 (a) and (b) displays the 2nd harmonics in the HV winding current of the 3-limb transformer and 5-limb transformer respectively. When the neutral DC injection is 50 A and 100 A, the 2nd harmonic in the HV winding current of the 5-limb transformer cannot reach its steady state in 30 s, so the simulation duration extends to 60 s as shown in Figure 6-11 (c). The 2nd harmonics are given in this section because it has great impacts on the relay operation in a power system network.

It is clear that the 2nd harmonic magnitudes simulated by the 5-limb transformer are much higher than those simulated by the 3-limb transformer under the same neutral DC current. However, the 2nd harmonic of the 3-limb transformer increases faster than that of the 5-limb transformer. Overall, 5-limb transformers are more likely to produce high 2nd harmonic, which could cause fault trips of relays.

With regard to the results simulated by the 3-limb transformer, the higher neutral DC current results in the faster increase rate and the higher steady state magnitude of 2nd harmonic. The 2nd harmonic waveforms reach the steady state before 30 s regardless of the neutral DC current.

As for the results simulated by the 5-limb transformer, the 2nd harmonic cannot reach the steady state at the end of 30 s duration when the neutral DC current is 100 A or lower.

It is good news for the transformer designer since the quasi-DC electric field may change its polarity in practical GMD events, and the core saturation state could be reversed. However, when the neutral DC input is high enough, the 2nd harmonic may reach a very high magnitude quickly.

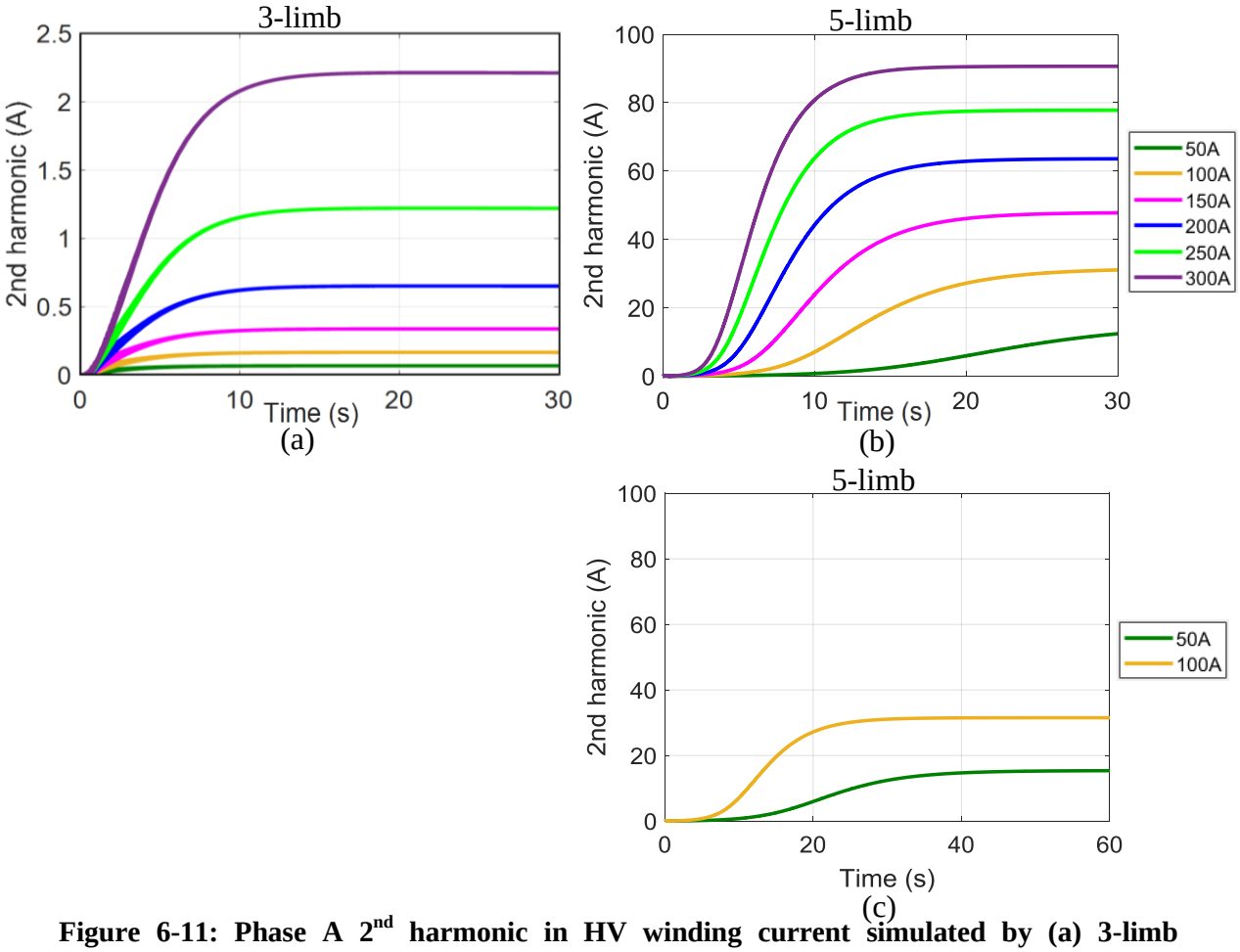

Figure 6-11: Phase A 2nd harmonic in HV winding current simulated by (a) 3-limb transformer over 30 s (b) 5-limb transformer over 30 s (c) 5-limb transformer over 60 s.

Figure 6-12 (a), (b) and (c) provides the DC components contained in Phase A limb flux density simulated by the 3-limb transformer and the 5-limb transformer respectively. Figure 6-12 (a) and (b) indicates that the higher neutral DC currents contribute to the greater flux growth rate and the higher steady state value.

Generally, the 3-limb transformer needs a higher DC injection to be pushed into deep saturation operation area compared with the 5-limb transformer, but the 3-limb transformer is saturated faster than the 5-limb transformer under the same DC input.

As can be seen in Figure 6-12 (b), the limb DC flux density has not reached the steady state in 30 s for the results simulated by the 5-limb transformer with 50 A and 100 A neutral DC injection. When the simulation duration extends to 60 s as shown in Figure 6-

12 (c), the DC flux finally stabilised at 0.49 T and 0.60 T respectively with 50 A and 100 A neutral DC current injection. When 600 A neutral DC current is provided to the 3-limb model, Phase A DC flux reaches 0.488 T which is close to the 5-limb model simulation results with 50 A neutral DC current input.

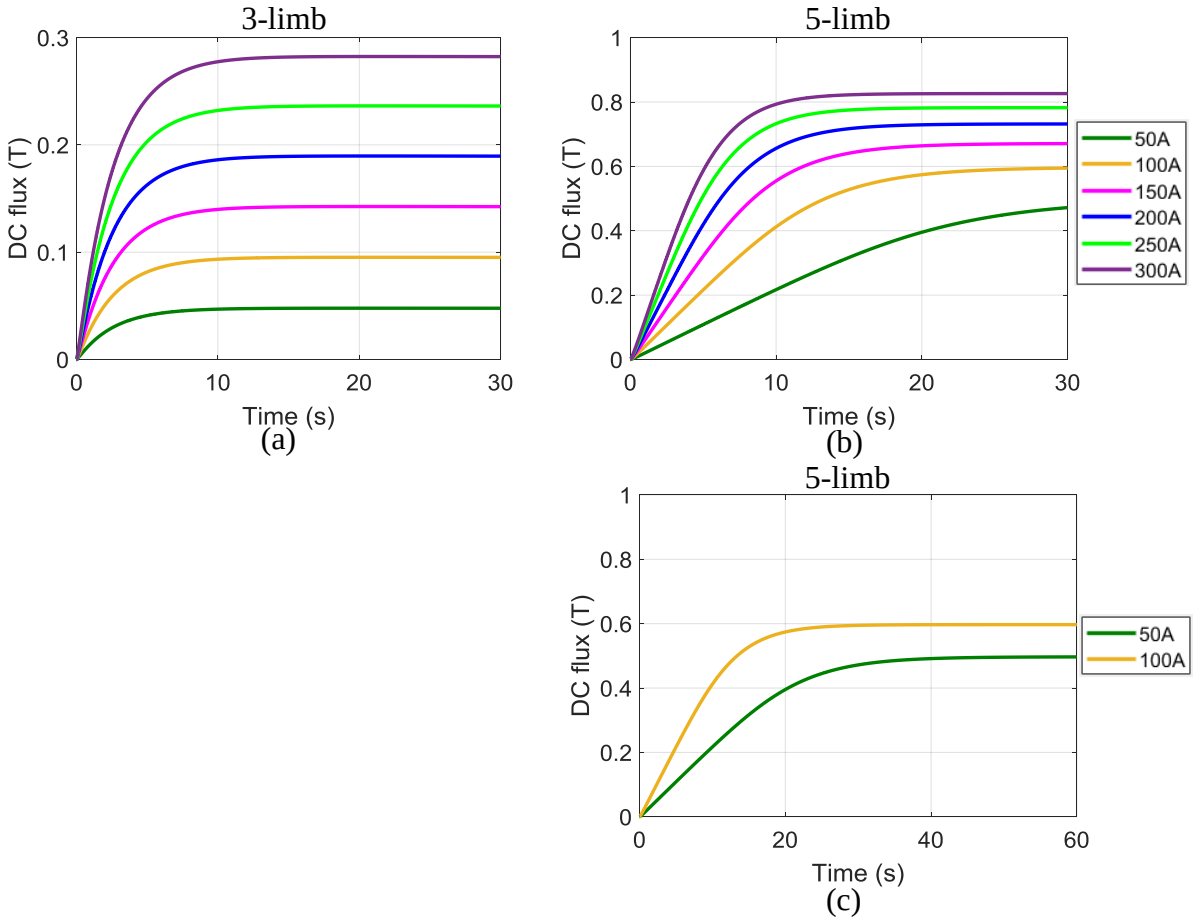

Figure 6-12: Phase A limb DC flux density simulated by (a) 3-limb transformer over 30 s (b) 5-limb transformer over 30 s (c) 5-limb transformer over 60 s.

6.5 Simulation in ATP

In this section, the Hybrid model is implemented to simulate a 3-limb transformer, which has the same parameters as the one used in Section 4.2 except the core type. To model a 3-limb transformer using the Hybrid model, it is necessary to tick the option '3-leg stacked' when setting the model. The length and the area ratios between the limb and the yoke are 1.09 and 1 respectively. In addition, the modelling of a 3-limb transformer using the Hybrid model needs to provide the zero sequence impedance for the leakage paths, which is modelled with a nearly zero number (10^{-4} mH).

6.5.1 Under 200 A DC injection

As shown in Figure 6-13, the Phase A HV winding current of the 3-limb transformer in the steady state is not significantly different from that of the 5-limb. It seems that the zero-sequence flux paths of the 3-limb model are not well described by the Hybrid model. The results of the 3-limb transformer also contain large quantities of harmonics, which indicates that the 3-limb core is also deeply saturated.

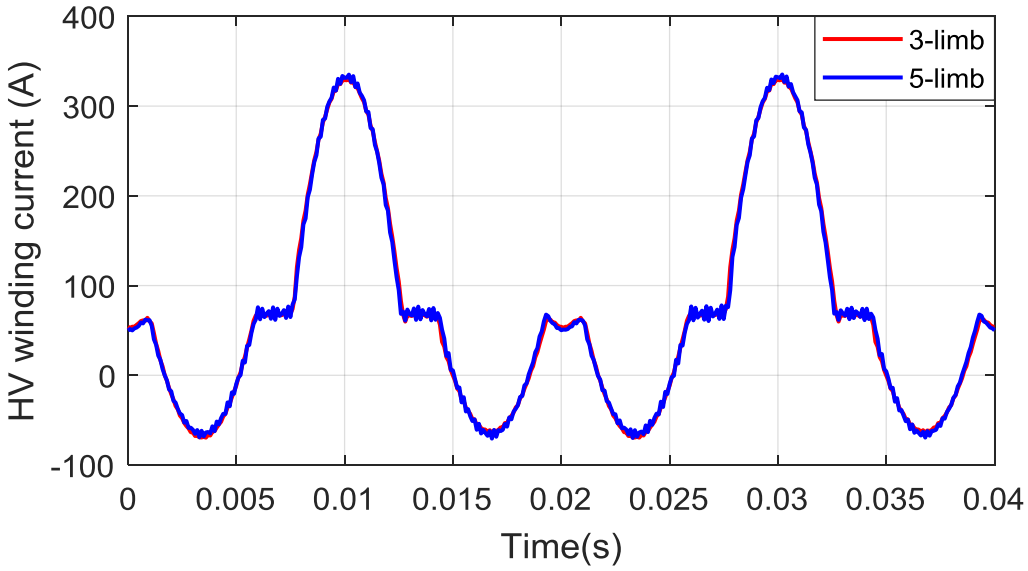

Figure 6-13: Phase A HV winding current of 3-limb transformer and 5-limb transformer simulated by Hybrid model.

6.5.2 Under different levels of DC injection

To determine GIC's impacts on transformers under different levels of DC injection, the neutral DC currents are set ranging from 0 A to 300 A with a step of 50 A. Figure 6-14 compares the results simulated by the new model and the Hybrid model.

As observed in Figure 6-14, when the 3-limb transformer and the 5-limb transformer are modelled by the Hybrid model, they will have similar peak-to-peak amplitude, which can directly reflect their similar core saturation level. When the new model is applied, the 3-limb transformer has a much lower peak-to-peak amplitude than the 5-limb transformer, although the amplitude of the 3-limb transformer booms after the DC injection exceeds 300 A. The new model can illustrate the fact that five-limb transformers are more vulnerable to GMD events than three-limb transformers as illustrated in [3, 90].

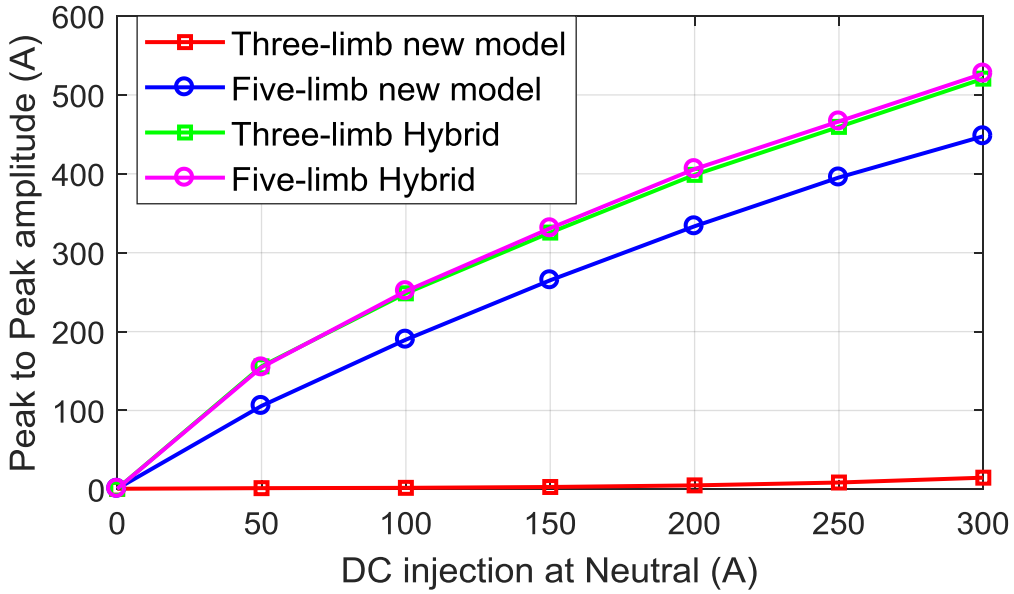

Figure 6-14: Peak-to-peak amplitude simulated by 3-limb transformer and 5-limb transformer by the new model and the Hybrid model under DC injections ranging from 0 A to 300 A.

6.6 Summary

This chapter compares the performance of 3-limb and 5-limb transformers under AC+DC input simulated by the newly developed model and the ATP Hybrid model.

The newly developed model for 3-limb transformer takes into account the different magnetic paths for 3-limb and 5-limb transformers, by using different equivalent magnetic circuits to represent their different core structures; hence it can demonstrate how a 3-limb transformer behaves differently from the 5-limb transformer under GIC as follows:

- The peak-to-peak amplitudes of the currents of the 3-limb transformer are much lower than those of the 5-limb transformer. This indicates that the 5-limb transformer is more seriously saturated and thus the higher harmonic currents are produced.
- The higher 2^{nd} harmonic current produced by the 5-limb transformer has potential to cause relay fault tripping problems.
- The DC currents of the 3-limb transformer increase faster than those of the 5-limb transformer.

- The DC flux and AC flux are both higher in the 5-limb core than the 3-limb core, so the core hotspot problem for a 5-limb transformer may be more severe than a 3-limb transformer.
- There are AC and DC fluxes in the tank of the 5-limb transformer because of the imbalance in the three-phase flux paths, but only high DC flux exists in the tank of the 3-limb transformer.

To conclude, 5-limb transformers are more vulnerable to neutral DC injection. Both types of transformers need to be aware of overheating problems in the core and tank under severe GMD phenomena. As mentioned in Section 3.7.2, the GIC flow in each substation of a power system network can be calculated by the electric field and the equivalent resistances of transformers and transmission lines. For those substations with high GIC flows, it is necessary to assess the GIC risks of the existing transformers by the newly developed model, especially for the 5-limb transformers. If a new transformer is to be installed in a power network, based on the research work done in this PhD thesis, it is advisable to install a 3-limb than 5-limb transformer at the most severe GIC risk substation.

Lastly, the comparison of the results simulated by the newly developed MATLAB model and the ATP Hybrid model reveals that the Hybrid model cannot model 3-limb transformers accurately even when extremely low zero sequence impedance for the leakage flux paths is provided.

Chapter 7: Five-limb Transformer Modelling under Realistic GIC Waveforms

7.1 Introduction

In previous chapters a transformer under the AC+DC input was tested, but in reality GMD phenomena produce quasi-DC time-varying electric field. In this chapter GIC transient simulation studies are conducted on the 5-limb transformer; as seen in Chapter 6 5-limb transformers are more susceptible to the neutral DC input than 3-limb transformers.

Since we are conducting transient simulation, the time constant of saturation is an important parameter for transformers under GIC; this chapter starts with Section 7.2 to describe a study carried out to show the effect of tertiary delta-connected winding on time constant of saturation. It is followed by a study for the 5-limb transformer under a practical neutral time varying injection in Section 7.3. Lastly, the 5-limb transformer simulation results with the full load situation are also provided in Section 7.4.

7.2 Simulation for effects of delta winding

To study the impact of delta winding, an artificial transformer with the same parameters as the previous 5-limb transformer, except without the delta winding, is simulated when 200 A DC steady state current is provided at the neutral point.

Figure 7-1 (a) and (b) show the first 20 s Phase B HV winding current and the delta winding current of the transformer with delta winding and Phase B HV winding current of the transformer without delta winding, respectively. The DC magnitudes are calculated by frequency spectrum in real time. The steady state peak HV winding current for the transformer with delta winding and the transformer without delta winding are 258.0 A and 261.1 A respectively, indicating that the core saturation level is not significantly impacted by the presence of the delta winding.

For the transformer without delta winding, the magnetising current is equivalent to the HV winding current. Regarding the transformer with delta winding, the steady-state magnetising current is 269.5 A which is greater than the value of the transformer without delta winding. However, the delta winding can hold part of the harmonics, so the peak

HV winding current is lower that the peak magnetising current for a transformer with delta winding.

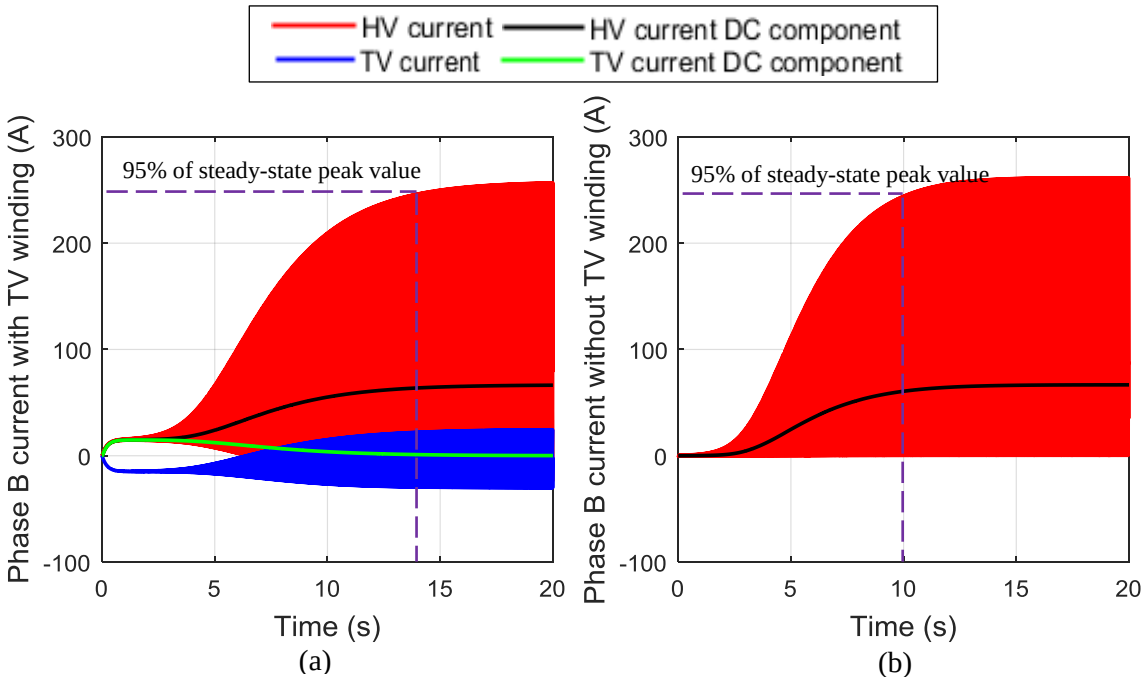

Figure 7-1: Currents and DC components calculated by frequency spectrum (a) with delta winding (b) without delta winding.

However, the peak HV winding current of the transformer with delta winding takes 14 s to reach its 95% steady state value while the transformer without delta winding only takes 10 s, which indicates that the delta winding can delay the core saturation process. Figure 7-1 (a) indicates that the DC current with the magnitude of about 15 A per phase mainly flows in the delta winding in the first 3 seconds, so the DC electromotive force, which saturates the core, will be partly taken by the delta winding. For this reason, the waveform of the DC components in the HV winding current consists of 4 stages, and the core saturation is delayed by the delta winding. The DC current in the delta winding in the first few seconds is determined by the ratio of the HV winding resistance to the TV winding resistance, and the sensitivity study for this factor has been discussed in Chapter 5. Finally, the DC current in the delta winding gradually returns to zero when the core reaches a deeper saturation area, although high order currents still flow in the delta winding.

The different saturation speed of these two transformers can be ideally displayed by the DC flux increase in the limbs. Figure 7-2 shows the DC flux densities in Phase B limb over 20 s. The limb DC flux of the transformer with delta winding has a lower growth

rate than that of the transformer without delta winding. Figure 7-3 (a) and (b) show the simplified DC equivalent circuit for the transformer with delta winding and the transformer without delta winding before reaching the steady state respectively. On the one hand, after the step response stage, the core reactance is large compared to the winding impedance, and the core branch is nearly open-circuit for the transformer with delta winding as expressed in Figure 7-3 (a). The DC electromotive force added on the core in the unsaturated stages can be estimated as Eq. 7.1 for the transformer with delta winding. On the other hand, the DC electromotive force added on the core equals the total DC input for the transformer without delta winding as illustrated in Figure 7-3 (b). According to Faraday's Law, the transformer without delta winding is pushed into the saturation state faster due to its higher DC electromotive force added on the core.

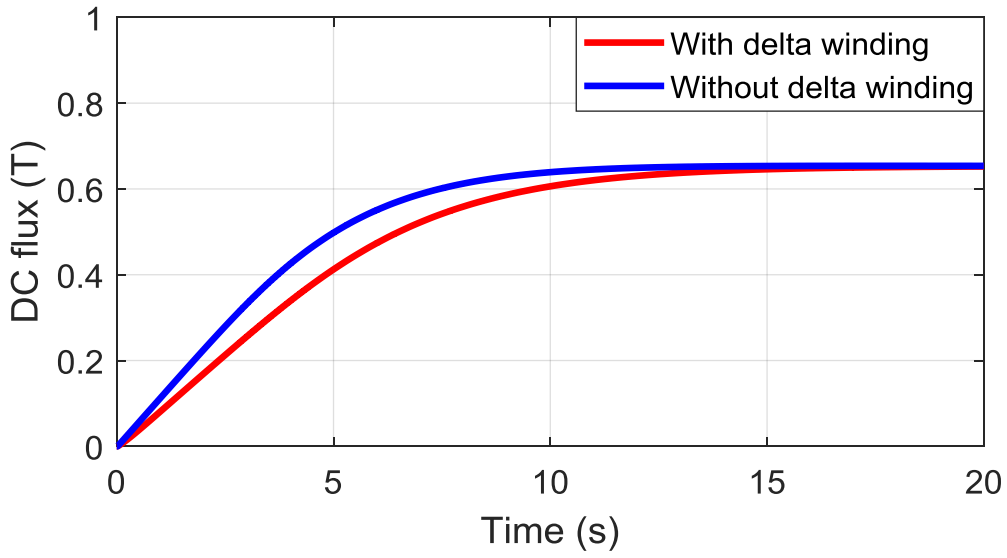

Figure 7-2: Phase B limb DC flux density for the transformer with a delta winding and the transformer without a delta winding.

$$E_1 = V_{DC} \cdot \frac{R_{hv}}{R_{hv} + R'_{tv}} \tag{7.1}$$

where

E_1	Electromotive force added on core (V)
V_{DC}	Total DC voltage (V)
R_{hv}	HV winding resistance (Ω)
R'_{tv}	TV winding resistance referred to TV side (Ω)

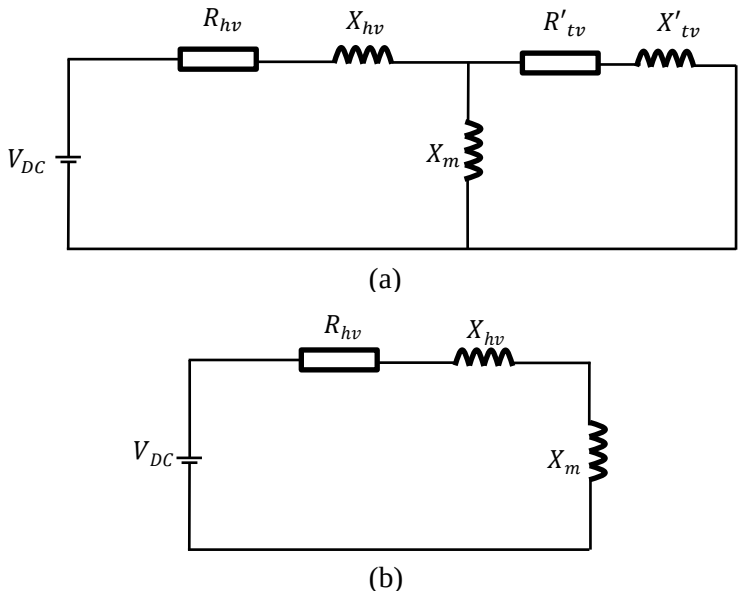

Figure 7-3: Simplified DC equivalent circuit in unsaturated stages for (a) the transformer with delta winding (b) the transformer without delta winding.

The practical GIC is quasi-DC in nature with a low frequency [11], so a longer saturation time means the transformers may avoid being damaged during geomagnetic disturbances because the electric field polarity possibly changes for a short interval of several seconds. Lastly, for a practical network, it is important to have a slower saturation process so that the protection system, such as relays, can have sufficient time to react to GMD events. To conclude, with the delta connected tertiary winding, the transformer may take a longer time to reach saturation, and hence has a better capability of defending itself against GIC.

It is important to mention that the applicability of the above conclusion is also dependent upon the power system where the transformer is installed. Taking the North America and the UK system as an example, the GIC severity in the UK could be much lower than the North America, hence the delta winding can be used in the UK transmission system as one mitigation method as it can delay the saturation. However, it may not be effective in the North America, as the magnitude of GIC could be much higher, so the transformer core would be saturated within a short duration.

7.3 GIC simulation for 5-limb transformer

As introduced in the literature review, the electric fields generated by GMD events are time-varying for both magnitude and direction. The GIC frequency is normally within the

range from 0.01 Hz to 0.5 Hz. However, obtained from the above simulation results, the currents or flux densities need tens of seconds or slightly longer to reach their steady state under certain DC input, so the transformer usually cannot reach its steady state in the transient studies. For this reason, the peak winding currents, harmonic current magnitudes and the flux densities cannot be determined from the neutral DC input directly. For this reason, a typical time varying electric field, based on the waveform provided by IEEE guide [11], is assumed as a 6-step square wave lasting 120 s in this section to conduct a GIC study in real conditions. The 5-limb transformer will be applied in this series of simulations while its LV side is open-circuited.

The analysis in this section is based on the DC components and 2nd harmonic in the HV winding current and DC flux in the main limbs. The DC current in the HV winding current is directly related to GIC and the 2nd harmonic current has great impacts on the relay operation in the power system network. The DC flux is important for analysing the core saturation degree. Section 4.3.3 introduces the 4-stage waveform of the HV winding current that includes the step response stage (Stage I), Pseudo flat stage (Stage II), DC flux build-up stage (Stage III) and steady state stage (Stage IV). This theorem will be applied to explain the waveforms in the GIC studies in this section.

7.3.1 Case study: simulation under a time varying electric field

In Section 7.3.1, the voltage input waveform applied is displayed in Figure 7-4, according to the typical waveform provided in IEEE guide [11]. The IEEE guide provides the GIC profile magnetic field measurements in March 1989. The real GIC waveform is a saw-tooth wave with sharp peaks, and the IEEE guide simplified the saw-tooth waveform into the step waveform according to the GIC magnitudes, as shown in Figure 7-4, for the convenience of simulation. The peak practical GIC in this section is chosen as 200 A to compare the simulation results under practical GIC input with those under pure DC input. The peak of the DC voltage input is 70.7 V which is equivalent to 200 A steady state neutral DC current input. The DC voltage magnitudes for these six steps are various, but the DC voltage keeps positive over the whole duration. The nominal AC voltage will be provided to the 5-limb model on the HV side.

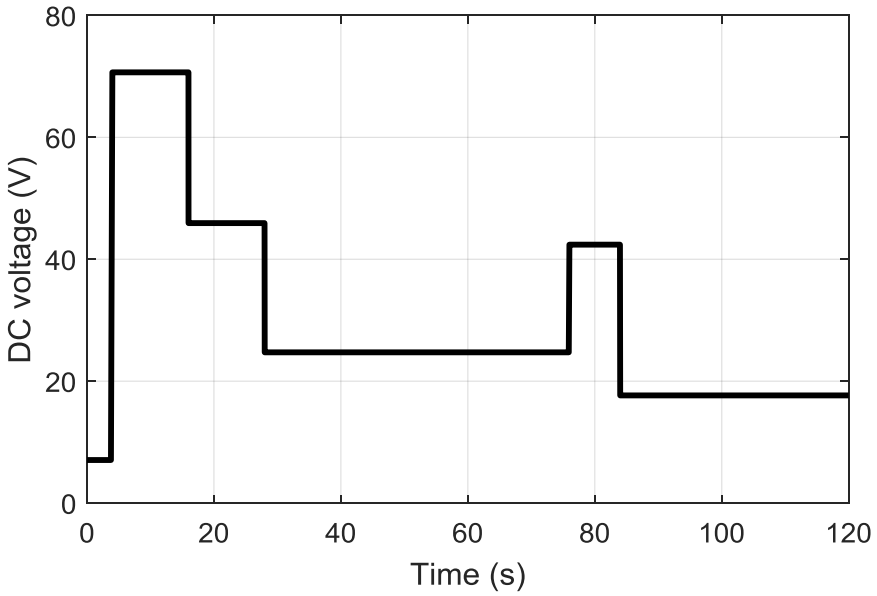

Figure 7-4: DC voltage provided at neutral.

Figure 7-5 shows the DC voltage input and the DC components in Phase A and Phase B HV winding currents. The waveforms are divided into six steps according to the DC voltage input magnitude. Phase A current waveform is similar to that of Phase B, so the following analysis takes Phase A DC current as an example.

In Step 1, the relatively low DC voltage results in a slow saturation progress. After the step response stage, the DC current stabilises at 1.5 A in the pseudo flat stage.

After 4 s, the DC voltage increases dramatically to 70.7 V, which leads to a step response stage in Step 2, and the DC current increases to 15 A shortly. After a short pseudo flat stage, the transformer core gradually enters the deep saturation operation area. Consequently, the DC current increases quickly in the DC flux build-up stage. However, before the DC current reaches its steady state stage, the DC voltage input decreases to 46.0 V. The peak DC current is 58.8 A in Step 2.

At the beginning of Step 3, the DC current exceeds the steady state value of the case with 46.0 V DC voltage input. Therefore, the DC current starts to decrease gradually. The same reason can explain the reduction in the DC current in Step 4. In these two steps, the transformer core will be desaturated and hence contribute to lower harmonic currents and lower flux densities.

In Step 5, the DC current increases again because the DC voltage input jumps to 42.4 V. The step response stage and the pseudo flat stage cannot be found in Step 5, since the DC current at the start of the Step 5 has exceeded the DC value for the pseudo flat stage.

Finally, the DC current decreases to 16.7 A in Step 6 to approach its steady state.

In the whole duration, the peak DC current occurs at the end of Step 2. The magnitude is 58.8 A and is much lower than 66.7 A simulated by the pure DC input case.

Compared with the Phase A results, Phase B DC current waveform is similar, but it has a higher peak magnitude of 61.6 A due to its faster increasing rate.

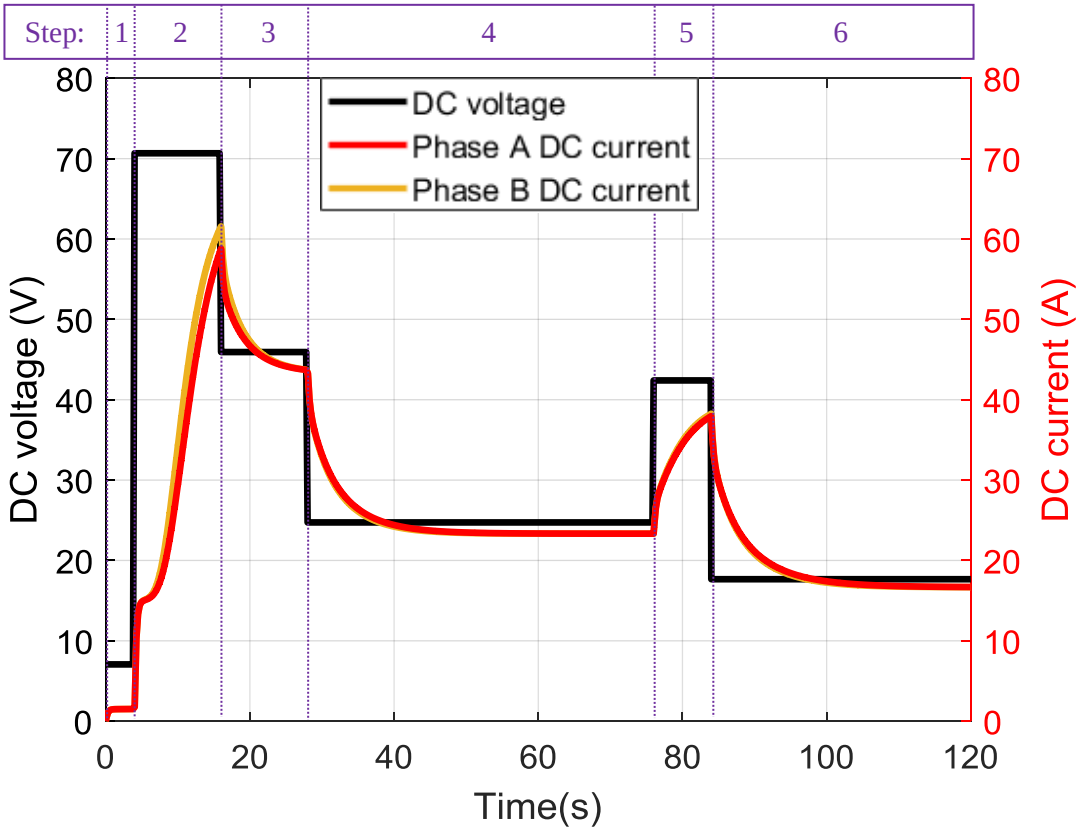

Figure 7-5: DC components in Phase A and Phase B HV winding current under a time varying DC voltage input.

Figure 7-6 displays the 2nd harmonics in Phase A and Phase B HV winding current. Unlike the DC components waveforms, extremely low 2nd harmonic can be found in Step 1. At the beginning of Step 2, the 2nd harmonic increases steadily, and then it rises dramatically till the end of Step 2. Phase A and Phase B 2nd harmonics reach their peaks (54.3 A and 39.8 A) at the end of Step 2. As shown in Section 4.3.3, when the pure DC

voltage input is 70.7 V, the steady state 2nd harmonics of Phase A and Phase B are 64.0 A and 45.0 A, higher than the values achieved in this section. This can be explained as the transformer cannot reach its steady state under this GIC voltage input.

From Step 3 to Step 6, once the DC voltage input changes, the 2nd harmonics will approach the steady state values for the given DC voltage input.

In the whole simulation duration, Phase A and Phase B waveforms have similar trends, but the magnitude of Phase A 2nd harmonic is always higher than that of Phase B.

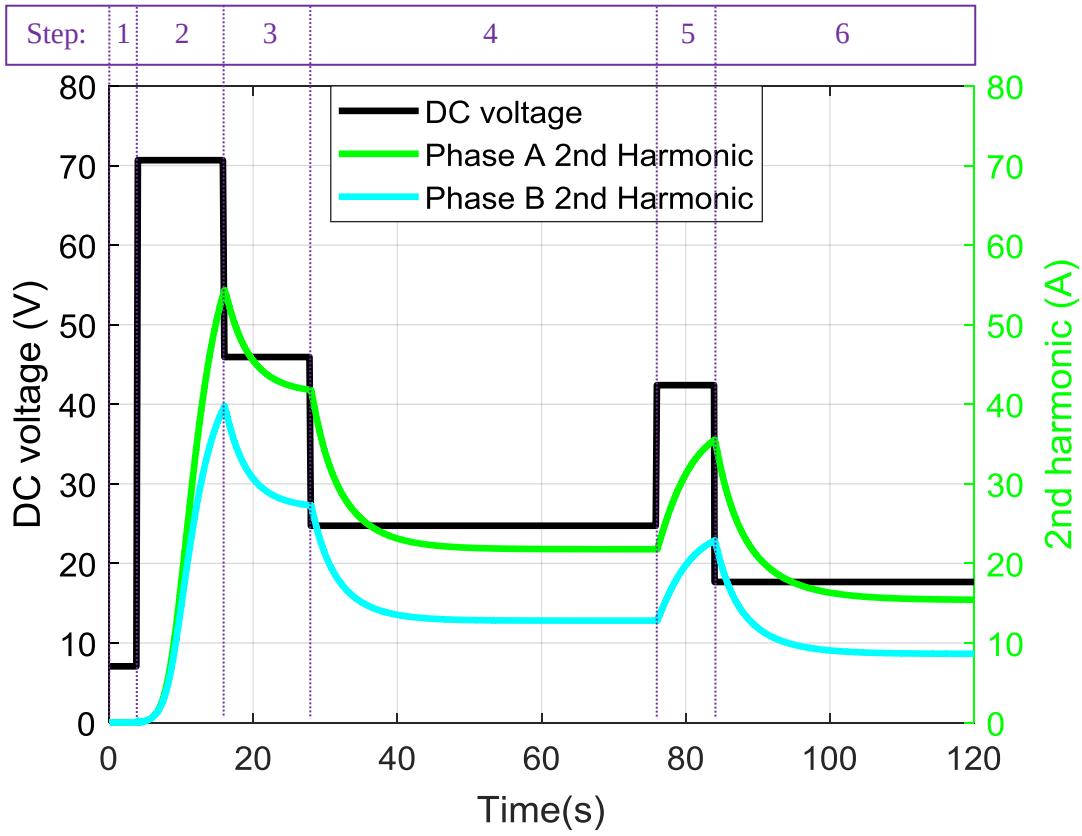

Figure 7-6: 2nd harmonics in Phase A and Phase B HV winding current under a time varying DC voltage input.

Figure 7-7 displays the DC flux in Phase A limb and Phase B limb. The DC limb flux reacts to the DC voltage input faster than the DC components and the 2nd harmonics of the HV winding current, so the DC flux densities increase immediately after the DC voltage input is provided in Step 1. When the DC voltage input rises to 70.7 V at the beginning of Step 2, the growth rate of the flux density increases immediately. Similar to the 2nd harmonic current waveforms, the DC flux of Phase A limb is always higher than

that of Phase B limb from Step 3 to Step 6. During the whole simulation period, the peak DC flux in Phase A limb and Phase B limb is 0.70 T and 0.63 T respectively.

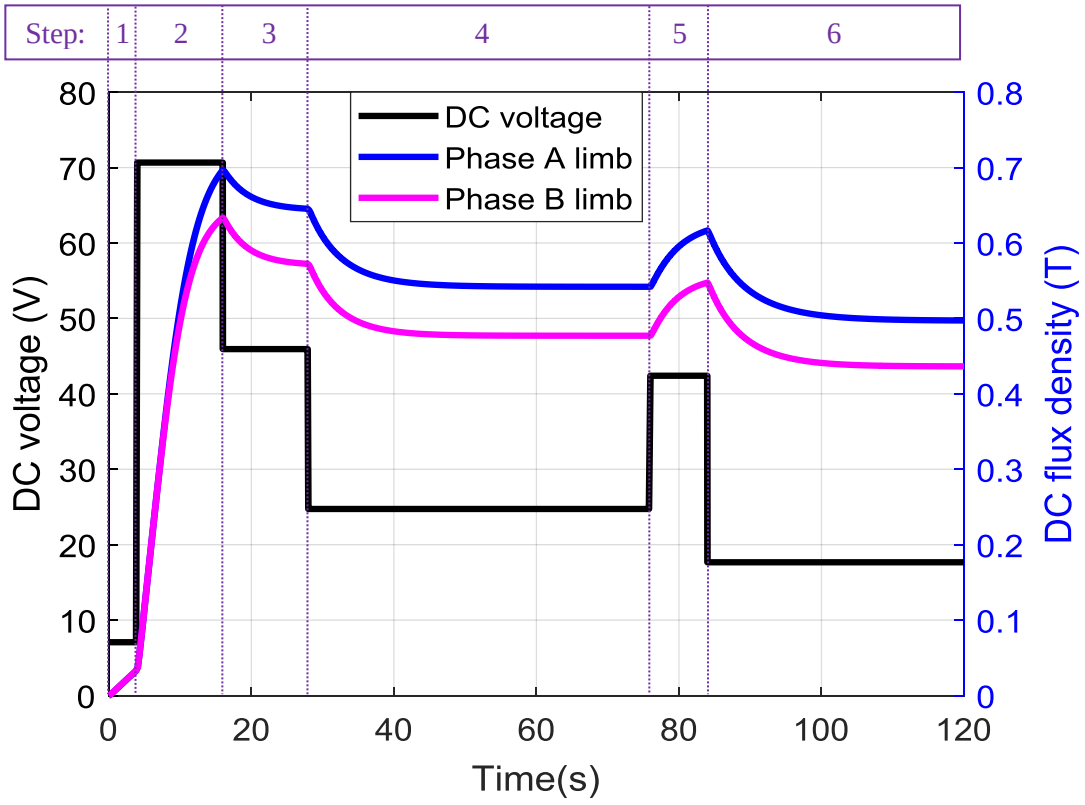

Figure 7-7: DC flux densities in Phase A and Phase B limb under a time varying DC voltage input.

It can be concluded from the above simulation results that the transient simulation is necessary for GIC study. The GIC calculation using the simplified resistance model in the system level study is inaccurate because the steady state results of the maximum DC voltage cannot always be reached. Therefore, the maximum current, harmonic magnitudes and the DC flux cannot be determined from the DC voltage input directly. Compared with the ATP software, the magnetising current, delta winding current and the flux distribution results can be calculated from the new model. The losses in the delta winding current and core loss can be estimated if necessary.

7.3.2 Time varying input waveforms

The waveform of the neutral DC voltage input will significantly impact the simulation results. Another DC voltage waveform is applied in this section as shown in Figure 7-8.

Step II has a reversed magnitude of 45.9 V. The DC voltage magnitude in Step 3 is 70.7 V which equals the maximum magnitude in the waveform in Section 7.3.1.

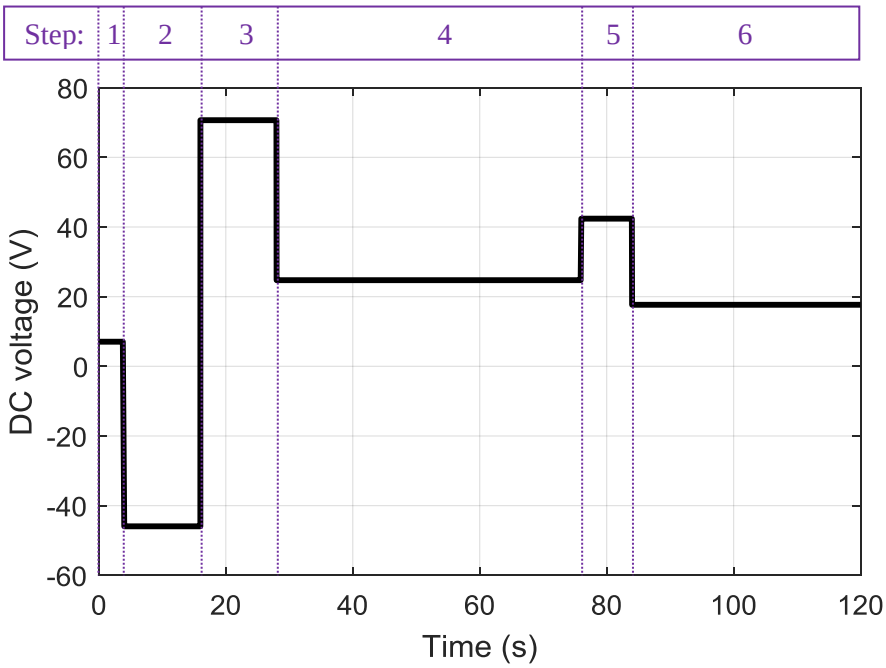

Figure 7-8: DC voltage provided at neutral with reversed step.

Figure 7-9 (a) and (b) shows the Phase A and Phase B DC components in HV winding current with these two waveforms. The results of Phase A and Phase B are similar, and so the Phase A results are analysed in this section.

Figure 7-9 (a) illustrates that the peak of Phase A DC current occurs at the end of Step 5 when the model is simulated under the DC voltage input with the reversed step. In Step 2, the DC current is reversed, and has a step response stage and the pseudo flat stage and then rises quickly. After the DC voltage is reversed again at the beginning of Step 3, the DC current returns to zero and has another step response stage and pseudo flat stage. In Step 4, the DC current is close to the steady state value of the provided DC voltage, so the DC current is steady. In Step 5, the DC current is boosted to the maximum value of 38.0 A which is also the peak value during the whole simulation duration.

As analysed in Section 7.3.1, the peak value for the DC voltage input in Figure 7-9 (b) is obtained at the end of Step 2 with a magnitude of 58.8 A. Clearly, the maximum DC components of Phase A HV winding current are achieved at different steps with different values, although their peak DC voltage inputs are both 70.7 V.

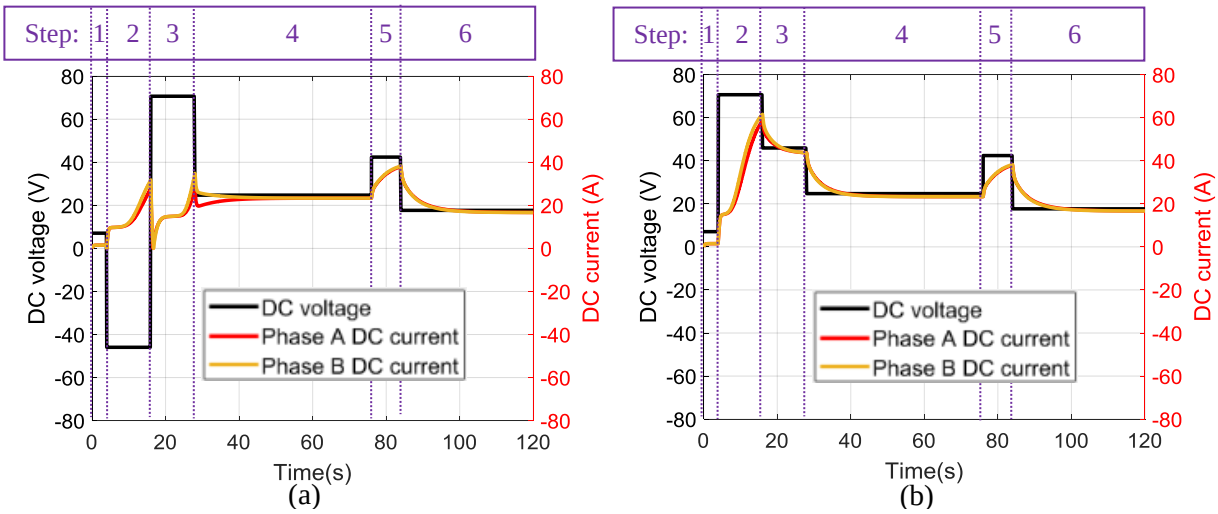

Figure 7-9: DC components in Phase A and Phase B HV winding current under two different time varying DC voltage inputs.

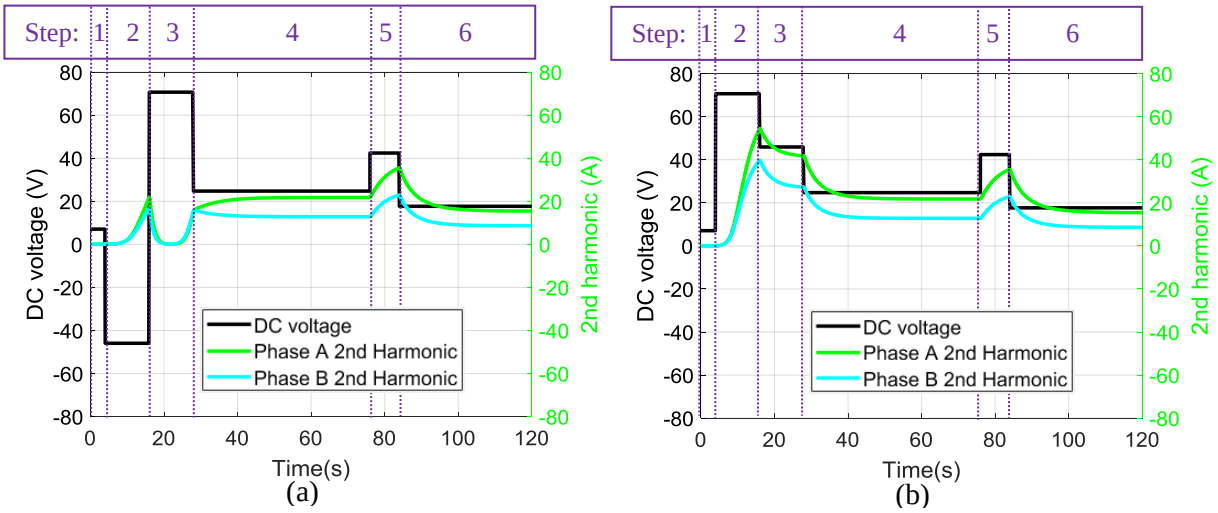

Figure 7-10: 2nd harmonics in Phase A and Phase B HV winding current under two different time varying DC voltage inputs.

As can be seen in Figure 7-10 (a), in Step 2, the DC voltage input becomes negative, and so the transformer is saturated in reversed polarity. After the DC voltage reverses to 70.7 V in Step 3, the saturation state of T1 core is removed gradually, so the 2nd harmonic returns to zero in the early stage of Step 3. With the continuous accumulation of DC flux in the core, the core is pushed into the deep saturation area again. The maximum values of the 2nd harmonics of Phase A and Phase B currents are 35.5 A and 22.9 A respectively occurring at the end of Step 5.

Combining the analysis in Section 7.3.1, Figure 7-10 (b) shows that the peak 2nd harmonics are achieved at the end of Step 2 when the DC voltage input without the

reverse step is provided. In addition, the maximum values of the 2nd harmonics are clearly larger than those shown in Figure 7-10 (a).

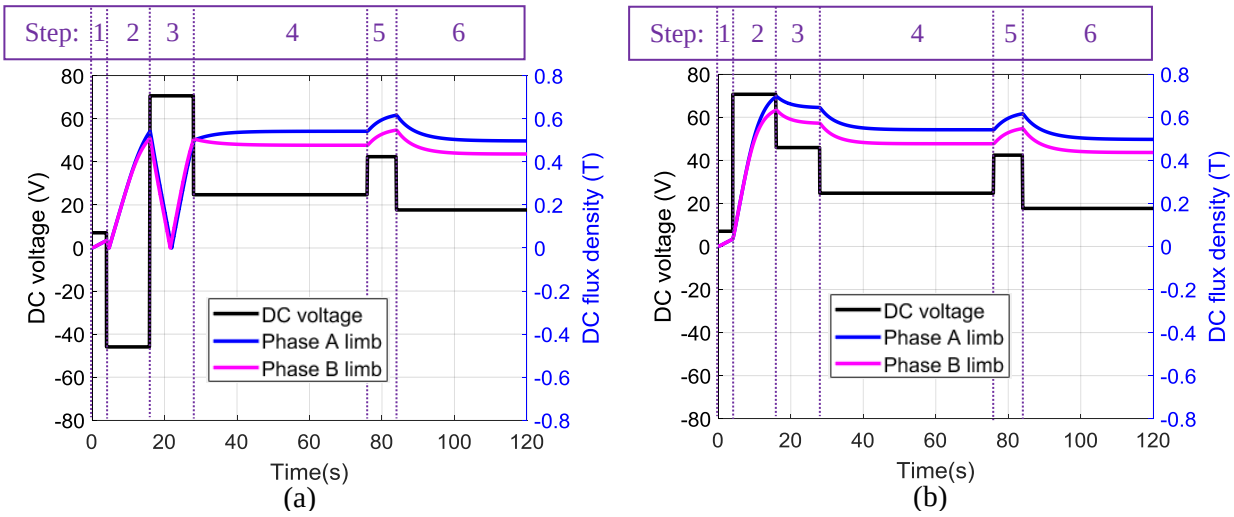

Figure 7-11: DC flux densities in Phase A and Phase B limb under two different time varying DC voltage inputs.

As shown in Figure 7-11 (a), the transformer core is desaturated and saturated again in Step 3. For this reason, Step 3 is too short to reach the steady state for the DC flux densities in the limbs. Therefore, the peak DC flux densities are found at the end of Step 5. As displayed in Figure 7-11 (b), the peak value happens at the end of Step 2, when the DC voltage input without the reversed stage is provided.

This section emphasises the importance of transient simulation in a GIC study. The simulation results could be totally different, even if the peaks of their DC voltage input are the same.

7.3.3 GIC magnitude

The DC voltage input magnitude will influence both the core saturation speed and the peak of the DC components and the 2nd harmonic in the HV winding current and the peak flux density as discussed in Section 6.4. In this section, three time varying DC voltage inputs are provided to determine the impacts of the DC voltage input magnitude on the simulation results.

Figure 7-12 (a) shows the DC voltage inputs with maximum values of 35.4 V, 70.7 V and 106.1 V. Their waveforms are similar, but the magnitude of Curve 2 and Curve 3 are twice and three times that of Curve 1 respectively.

Figure 7-12 (b) displays the DC components in Phase A and Phase B HV winding current simulated under the DC voltage input curves. The peaks of the DC currents occur at the end of Step 2 for the results simulated by Curve 2 and Curve 3, while the peaks are achieved at the end of Step 3 in the case simulated by Curve 1. The low DC voltage input of Curve 1 leads to a slow saturation process, and so the DC current cannot reach a high magnitude at the end of Step 2. The peak DC components in Phase A HV winding current are 20.9 A, 58.8 A and 96.3 A in the results simulated by Curve 1, Curve 2 and Curve 3. Therefore, the peak DC currents are not proportional to the peak DC voltage input.

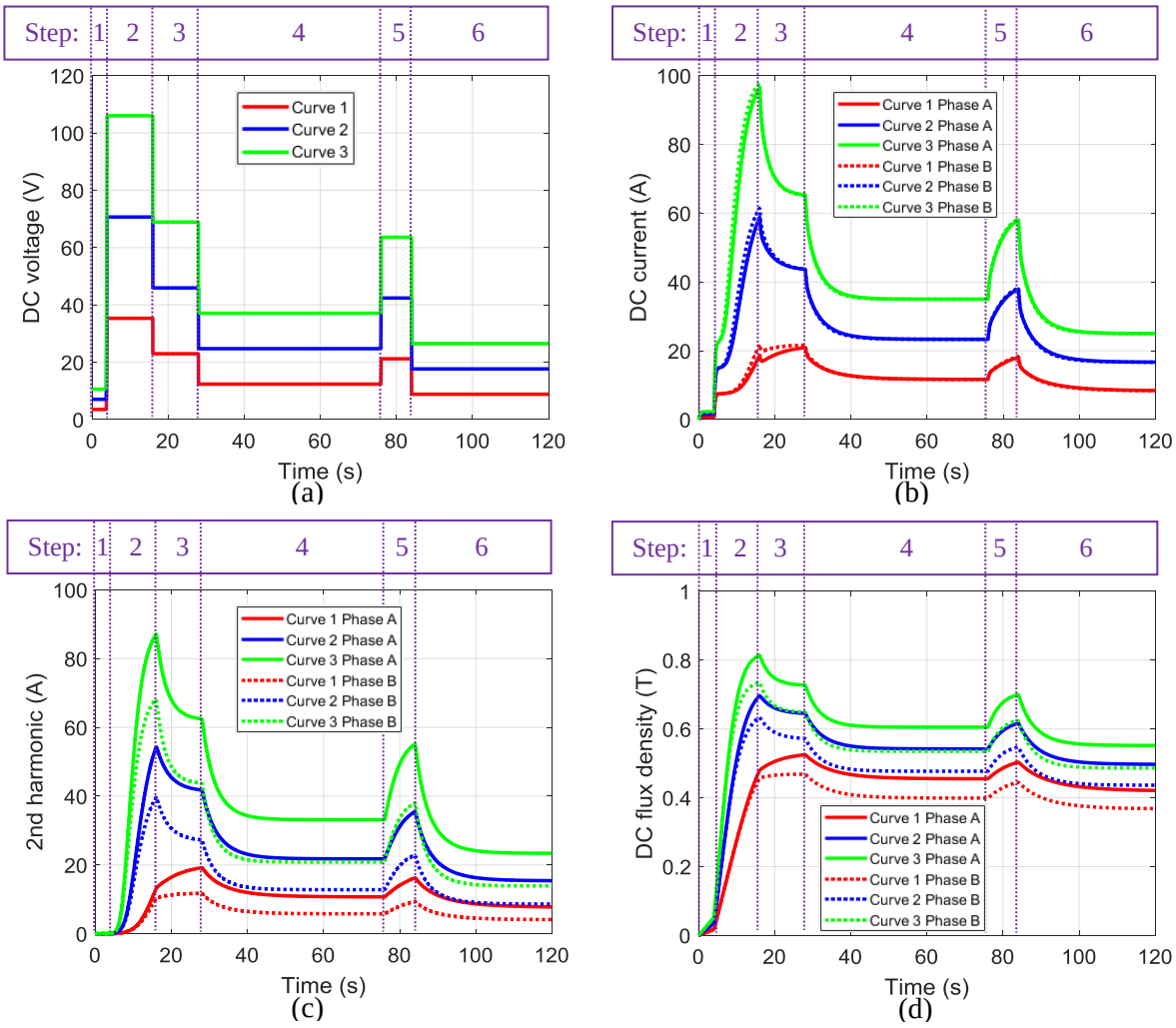

Figure 7-12: (a) DC voltage input at neutral (b) DC components in Phase A and Phase B HV winding current (c) 2nd harmonic in Phase A and Phase B HV winding current (d) DC flux density in Phase A and Phase B limb.

Similarly, as shown in Figure 7-12 (c) and (d), the peaks of the 2nd harmonics in the HV winding current and the limb flux densities are obtained at the end of Step 2 for Curve 2 and Curve 3 and at the end of Step 3 for Curve 1. Regarding the Phase A results, the maximum values of the 2nd harmonics in the whole simulation duration are 19.2 A,

54.4 A and 87.1 A when Curve 1, Curve 2 and Curve 3 are provided as the input. In addition, the peak Phase A limb flux densities are 0.53 T, 0.70 T and 0.81 T for these three cases. For the results simulated by Curve 1, the 2nd harmonic magnitude is acceptable compared to the results simulated by Curve 2 and Curve 3, but the limb flux densities are not significantly superior to the results simulated by Curve 2 and Curve 3.

To conclude, the magnitude of the time varying DC voltage input affects the simulation results. The peaks of the DC components and 2nd harmonics in the HV winding current and the limb flux densities are not proportional to the maximum DC voltage input.

7.4 Simulation with full load

In this section, the 5-limb model is simulated with full load added on the LV side. The power source is assumed strong enough, and the voltage source is not impacted by the excessive reactive power loss due to the GIC injection. *R*, *L* loads (power factor 0.95 lagging) are added on the LV side to investigate the effects of load on the GIC simulation results. The 3-phase neutral DC current in the steady state is 200 A for a fair comparison with open circuit AC+DC simulation results.

The full load impedance per phase can be calculated by the transformer power rating and the HV side nominal line voltage according to Eq. 7.2.

$$Z_{load} = \frac{V_{LL}^2}{S_b} = \frac{(400\ \text{kV})^2}{240\ \text{MVA}} = 666.7\ \Omega \tag{7.2}$$

The currents and the flux densities will reach a steady state in 30 s. Figure 7-13 shows Phase B current waveforms in the steady state. All the current magnitudes have been referred to the HV side. The full load current magnitude is 489.2 A while no neutral DC input is provided. After the DC input is provided, it is clear that the HV winding current contains large quantities of harmonics produced by the core saturation, but the magnitude of the HV winding current is 493.2 A, slightly higher than the no-load simulation. With regard to the magnetising current, three peaks still exist in Phase B waveform as the no-load simulation. However, the magnitude of the highest peak is 276.7 A, slightly higher than 269.6 A of that in the no-load simulation. It indicates that adding the load has limited impact on the core saturation states.

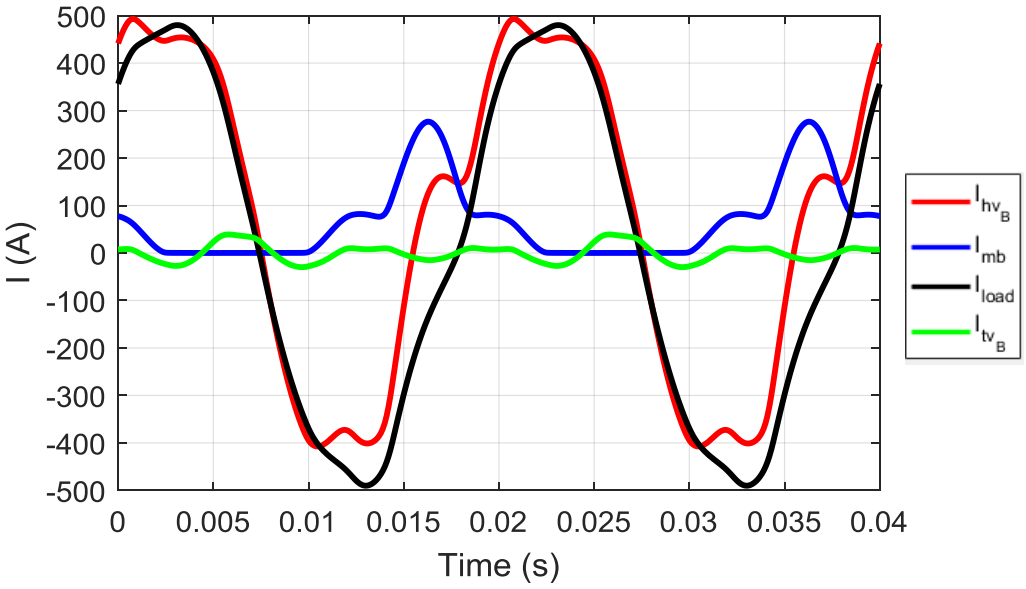

Figure 7-13: Phase B HV winding current, magnetising current, load current and delta winding current referred to the HV side with 95% power factor full load in steady state.

Figure 7-14 (a) indicates that the waveform of Phase B HV winding current under full load is totally different from the waveform simulated in the no-load case. With regard to the magnetising current, the delta winding current and the limb flux density as shown in Figure 7-14 (b), (c) and (d), the apparent phase shifts and slight peak magnitude changes can be found due to the serious distortion of the HV winding current.

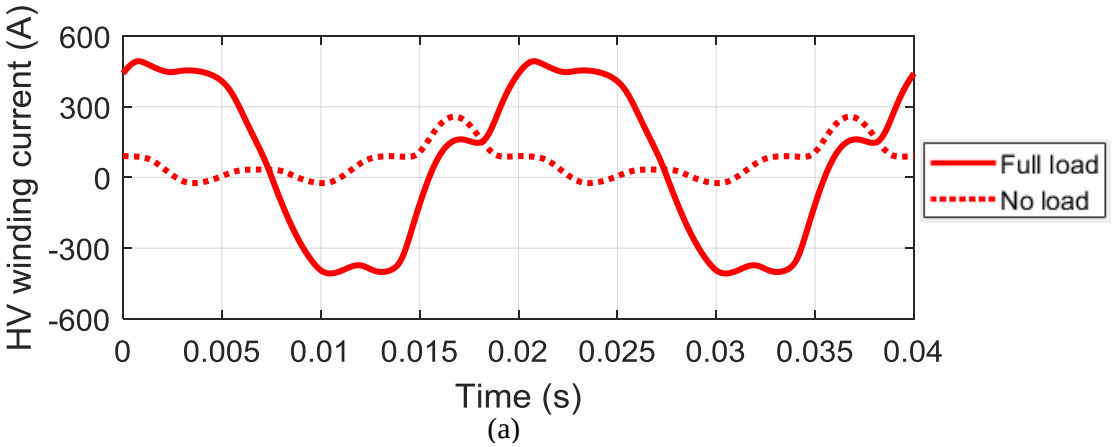

(a)

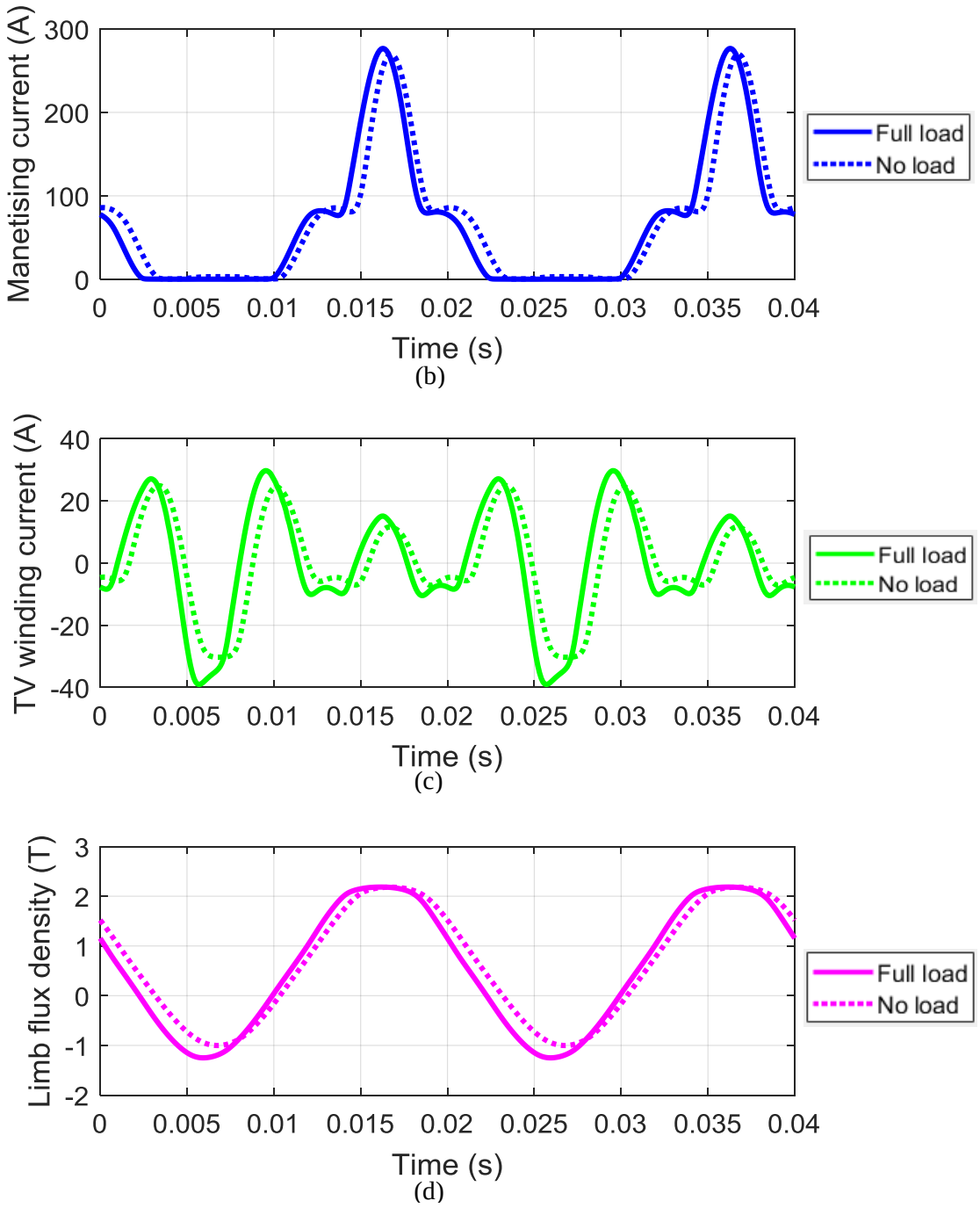

Figure 7-14: Comparison between Phase B results in the full load and no load (a) HV winding current (b) Magnetising current (c) Delta winding current (d) Limb flux density.

Table 7-1 shows the frequency spectrum results of Phase B steady state currents and limb flux density simulated in the full-load case and the no-load case respectively. It is understandable that when the full load is provided on the LV side, the AC fundamental current in the HV winding dramatically increases, which is partly due to the LV winding current. Regarding the TV (delta) winding current, few changes are found in the harmonic magnitude except the 3rd harmonic.

Table 7-1: Comparison between the simulation results under no load and full load.

	$I_{hv\_B}\ (A)$		$I_{mb}\ (A)$		$I_{tv\_B}\ (A)$		$B_b\ (T)$	
Load	Full	No	Full	No	Full	No	Full	No
DC	66.7	66.7	66.7	66.7	4.8e-3	1.6e-7	0.56	0.65
1st	458.4	89.3	99.2	93.4	4.3	4.1	1.74	1.61
2nd	66.8	44.8	41.7	35.0	10.5	9.9	0.054	0.036
3rd	4.9	1.6	20.6	17.5	22.3	18.0	3.9e-3	1.3e-3
4th	52.5	31.6	26.2	27.9	4.5	3.7	0.042	0.025
5th	37.8	22.0	21.4	22.2	1.3	0.3	0.030	0.018
6th	7.1	4.7	6.3	8.4	2.8	3.7	5.6e-3	3.7e-3

The magnetising current of the full-load case contains higher fundamental, 2nd and 3rd currents compared with the no-load case, which is caused by the change of flux density. As observed in Table 7-1, the AC fundamental flux densities are 1.74 T and 1.61 T in the full-load case and the no-load case, while the DC flux densities are 0.56 T and 0.65 T respectively, though the peaks of Phase B limb flux densities are still close. It is clear that the HV winding current will lead to changes in the electromotive force added on the core, and so the changes of the limb flux density are convincing according to Faraday's Law.

7.5 Summary

This chapter mainly discusses the applications of the new model by investigating the GIC's impacts on transformers from the transient aspect.

Firstly, the simulation results of the transformer with a delta winding are compared to those generated by the transformer without a delta winding. The comparison indicates that the delta winding can help to delay the saturation process, which could be very important for transformers defending against GIC.

Secondly, the GIC risks of a transformer are not only determined by the magnitude, but also the waveform and the period of the polarity reversal of the quasi-DC voltage input. Transformer core saturation takes tens of seconds or even a few minutes to reach

the steady state, depending on the many factors of the transformer itself, as well as the applied GIC waveform. For this reason, the peaks of the DC components and the 2nd harmonics in the HV winding current and the DC limb flux cannot be simply decided by the maximum GIC voltage input. Therefore, it is important to apply the transient simulation in a GIC study.

Lastly, the 5-limb transformer is modelled with a full load. There is no doubt that the HV winding current will be significantly different from the simulation results for no-load case; however, the magnitudes of the magnetising current and the delta winding current are only mildly impacted by the load, and adding a load also leads to a phase shift in the current and the flux density waveforms. In addition, it is interesting to note that the main limbs contain less DC flux and more fundamental AC flux after the load is added. In summary, the load characteristics have impacts on the simulation results in the GIC study, especially regarding core losses.

Chapter 8: Conclusion and Future Work

8.1 Research contribution

This thesis carries out a simulation study on geomagnetic induced current (GIC) phenomena when transformers are subjected to a DC magnetisation which pushes the core into deep saturation. The research aims to build a representative model of core saturation and carry out simulation studies to understand the performance of transformer cores in the high flux density region. This in turn helps to identify the design features that need to be taken into account when assessing the capability of a transformer to withstand over-excitation.

The contributions of the research can be highlighted as follows:

- The existing ATP transformer models are tested under GIC scenarios, and only the Hybrid model is verified to be suitable for GIC studies. Even the Hybrid model is unsuitable for severe GIC cases in that it does not take the tank into consideration for 5-limb transformers.
- A new model which consists of an electric circuit and a magnetic circuit is proposed. The electric circuit parameters are calculated using a short circuit test report, and the magnetic circuit bases itself on the physical dimensions and core and properties of the tank materials. The model takes the flux leakage effects into consideration and is able to depict the current waveforms and the flux distribution for over-excitation.
- The design features of core, tank and winding are tested through the sensitivity study, which include the cross-sectional area ratio between yokes and limbs, the equivalent length and area of oil gaps and tank paths and winding impedance.
- The capability to withstand GIC among different transformers is assessed through simulation studies, which include different types of core (3-limb core and 5-limb core) and with/without delta winding.
- Transformers are simulated under realistic GIC waveforms, for situations with and without load.

8.2 Key findings

GMD is produced by space weather with a low frequency normally ranging from 0.01 Hz to 0.5 Hz. GIC is normally regarded as a quasi-DC voltage or current waveform when we need to model its effects on power system networks. Nevertheless, it is vitally important to realise how transformers react to neutral GIC injection is a transient process.

- Comparison of ATP simulation and measurement results using existing models

The research starts with simulations of GIC using the transient software package of ATP. Three widely-used transformer models, the BCTRAN model, the STC model and the Hybrid model are used to model a five-limb transformer as an example, which are under nominal AC input accompanied with 200 A neutral DC input.

The simulation results show that the BCTRAN model and the STC model have poor performance in simulating GIC because non-linear inductances added cannot characterize the DC effect for the BCTAN model and the core non-linear characteristics could be inaccurate beyond the knee point for the STC model. On the other hand, the Hybrid model shows itself as being capable to simulate the transformer over-excitation problems, although the HV winding current waveforms simulated by the Hybrid model somehow show some minor differences from the measurement results. Firstly, the Hybrid model cannot differentiate the magnitudes of Phase B from those of Phase A/C. In addition, when we divide the HV winding current waveforms into 6 zones, the HV winding currents in zone 2, 4 and 6, only contain DC components, which shows that it fails to capture the feature of localized core saturation. However, the Hybrid model is still considered suitable to simulate a 5-limb transformer in the GIC study. It may not be the case for the 3-limb transformer as demonstrated by comparison studies carried out later on.

- Analysis of current and flux density waveforms for GIC

It is essential to understand how the flux is distributed in a transformer during a GIC event because the flux densities directly relates to the power loss and overheating in the core or structure such as a tank. However, the simulation results in ATP cannot provide the detailed waveforms of flux densities. Therefore, a new model is built, which combines

the equivalent electric circuit and the equivalent magnetic circuit, and which takes into account the leakage flux paths consisting of oil gaps and tank paths.

The HV winding currents simulated under nominal AC and 200 A DC neutral input show great agreements with the measurement results. The current waveforms are divided into four stages for better understanding of the core saturation process. Stage I is the step response stage, during which the DC current is formed in the HV winding and the TV winding, while low AC fundamental frequency currents exist. Stage II is the pseudo flat stage because the DC components in the HV winding current and the TV winding current reach the temporary steady state. In Stage I and Stage II, the transformer is still operating in the linear region, and so the DC currents dominate in Stage I and Stage II. The DC flux accumulates in the core due to the DC voltage supply. In Stage III, the core gradually enters saturation, so the AC components increase dramatically. The DC components show an increase in the HV winding current and the magnetising current and a reduction in the delta winding current. Finally, the currents and the flux densities reach a steady state in Stage IV.

In the steady state, a total of 4 peaks and 2 troughs are contained in the HV winding current in each cycle. The peaks and troughs are caused by either the saturation of limbs and yokes or the interaction of delta winding current. The main yoke flux densities (B_{y2}, B_{y3}) and the side yoke flux densities (B_{y1}, B_{y4}) exceed 1.60 T for 52% and 65% of the time respectively in a single period (0.02 s).

- Identifying important design features of core, tank and winding that impact the capability of a transformer to withstand over-excitation.

The research is expected to give recommendations about the design features to minimise damage to transformers during GMD events. The simulation sensitivity studies for a 5-limb transformer indicate that smaller main yoke and side yoke cross-sectional areas are beneficial in decreasing the induced magnetising current during the GMD event. In terms of the leakage paths assumption, the equivalent tank path area, the oil gap length and oil gap area are essential to GIC risks in transformers. It is clear that the reluctance of leakage paths will decrease if the tank path area and the oil gap area expand or the oil gaps shorten, and hence the magnetising current magnitude and peak limb flux densities will increase.

Three-limb transformers are not completely immune to GIC. When the neutral DC current rises to 600 A, the peak-to-peak amplitude of the HV winding current simulated by the 3-limb model reaches 103.5 A. When both the 3-limb model and the 5-limb model are provided with a 200 A neutral DC injection, the peak limb flux density is 1.87 T in the results simulated by the 3-limb model, which is much lower than 2.20 T simulated by the 5-limb model. Other than DC flux, the 3-limb transformer produces little high order harmonic flux. Therefore, it is confirmed that 5-limb transformers are more vulnerable to GIC.

During GMD events, the delta winding holds the triplen harmonic current generated by the half-cycle saturation and the unbalanced current due to various zero sequence reluctance for each phase. In addition, a delta winding can prolong the saturation time of the transformer core.

The model is also applied in the transient simulations under practical quasi-DC neutral input. Both the magnitude and the waveform of the time varying DC input will impact the GIC severities of transformers. It takes tens of seconds or even a few minutes for transformers to reach the steady state, so the peaks of GIC, 2^{nd} harmonics and flux density are not only determined by the peak voltage input. Therefore, the transient study is essential for GIC research.

Finally, the 5-limb transformer model is simulated under full-load. The load results in a phase shift in the magnetising current and the delta winding, but the magnitudes of the currents are similar. However, it is observed that the main limbs contain less DC flux and more fundamental AC flux after the load is added. For this reason, the load effects can be important for the calculation of core losses.

As mentioned in Section 3.7.2, the GIC flow in each substation of a power system network can be calculated by the electric field and the equivalent resistances of transformers and transmission lines. For those substations with high GIC flows, it is necessary to assess the GIC risks of the existing transformers by the newly developed model, especially for the 5-limb transformers. If a new transformer is to be installed in a power network, based on the research work done in this PhD thesis, it is advisable to install a 3-limb than 5-limb transformer at the most severe GIC risk substation.

8.3 Future work

Although the research has built a useful model to accurately present the effect of core saturation under GIC, further work is still needed on the following aspects:

- Core saturation curve

Adding an option of the core material into the new transformer model is recommended. The non-linear characteristics of core material could be diverse, particular for old transformers. B-H curves of core material, as well as tank material, are quite important for the simulation accuracy of the half-cycle saturation problems; hence it is necessary to choose a suitable B-H curve for the transformer to be simulated.

- Core loss and temperature rise simulation

In terms of the simulation of core temperature rise caused by GIC, researchers can either obtain the empirical equations from the transformer test or calculate the temperature distribution by finite element method (FEM). Generally, FEM is time consuming and complex, so it is not widely applied in a GIC system study. There is an example showing the temperature estimated by the empirical equations. Firstly, the tie-plate hotspot temperatures are measured by the manufacturer under different levels of constant GIC input [14]. It also provides the temperature rise curve in 120 *min*. Secondly, the other researchers apply the thermal response related to GIC level directly in order to simulate the core hotspot temperature [110]. In this way, the transformer core temperature can be calculated simply based on the GIC data.

The empirical equation described provides an idea of how to calculate the core temperature rise. The flux distribution in the transformer can be calculated by the new model, so the core losses can be further calculated based on the frequency spectrum calculations for the flux densities. Once we know the power loss, the temperature rise can be calculated by the empirical equation.

The core losses are measured when the transformer core material is operated under AC flux plus a DC flux offset by Cardiff University [66, 111]. The AC flux magnitude ranges from 0 to 1.8 T when the DC flux is provided with maximum 300% of the AC flux magnitude. However, the AC fundamental flux and the DC flux are accompanied with large quantities of harmonic flux due to core saturation; thus it is necessary to include the

core losses produced by the high order harmonics flux in calculating the total core losses. Normally, the core losses for harmonics flux can be divided into the eddy current loss, the hysteresis loss and the anomalous loss, and the calculation formula is included in [112].

Furthermore, Finnish Grid designed a test on two 400 kV transformers under different levels of DC injection up to 200 A [13]. The active power loss under AC and AC+DC test can validate the accuracy of the power loss calculation. It also provides the temperature rise curve as shown in Figure 3-16. Following that, the core temperature rise curves will be fitted by the equations associated with the core losses. With the application of this method, the temperature can be simulated in transient for real GMD events.

The detailed temperature calculation steps are introduced in Appendix V.

- Code the new model into ATP

As discussed in the thesis, ATP is a kind of efficient software to solve transient problems for a network. However, the existing models cannot provide accurate simulation results for GIC study. In addition, the ATP cannot illustrate the flux distribution in the transformer which is essential when analysing transformer behaviours during GMD events. Therefore, the new model developed in this thesis, which is able to produce more precise results including the flux distribution result, should be coded as an external model and connected with the ATP, so that the new transformer model can be used to simulate GMD events for a network in ATP.

A GIC study for the UK Southwest Peninsula power network by using the Hybrid model was conducted and published as attached in Appendix VI. If the Hybrid model is replaced by the newly developed model in the future, it will allow users to obtain the winding currents, magnetising current, flux distribution and further calculate the power losses and reactive power consumption.

Reference

[1] International Standard, IEC 60050-151, International Electrotechnical Vocabulary, Part 151: Electrical and magnetic devices. First edition, 1978.

[2] A. J. Pansini, *Electrical Transformers and Power Equipment*: The Fairmont Press, Inc., 1999.

[3] M. Heathcote, *J&P Transformer Book*, 13th ed.: Newnes, 2007.

[4] National Grid, "Electricity Ten Year Statement 2017", 2017.

[5] Ofgem.gov.uk. (2018). The GB electricity transmission network. [online] Available at: https://www.ofgem.gov.uk/electricity/transmission-networks/gb-electricity-transmission-network [Accessed 14 Aug. 2018].

[6] A. Pors, and N. Browne, "Modelling the energisation of a generator step-up transformer from the high voltage network," in Power Engineering Conference, 2008. AUPEC'08. Australasian Universities, 2008, pp. 1-5.

[7] A. Greenwood, "Electrical transients in power systems," *Ed. John Wisley & Sons Inc.*, pp. 1-5, 1991.

[8] D. A. Jacobson, "Examples of ferroresonance in a high voltage power system," in Power Engineering Society General Meeting, 2003, IEEE, 2003, pp. 1206-1212.

[9] D. Boteler, R. Pirjola, and H. Nevanlinna, "The effects of geomagnetic disturbances on electrical systems at the Earth's surface," *Advances in Space Research*, vol. 22, no. 1, pp. 17-27, 1998.

[10] "Solar Storms and Radiation Exposure on Commercial Flights", NASA, 2018. [Online]. Available: https://www.nasa.gov/topics/aeronautics/features/airline-radiation.html#.VGsbaPl_vig. [Accessed: 14- Aug- 2018].

[11] "IEEE Guide for Establishing Power Transformer Capability while under Geomagnetic Disturbances," *IEEE Std C57.163-2015*, pp. 1-50, 2015.

[12] J. Douglas, "A storm from the sun," *IEEE Power Engineering Review*, vol. 9, no. 12, pp. 11-13, 1989.

[13] M. Lahtinen, and J. Elovaara, "GIC occurrences and GIC test for 400 kV system transformer," *IEEE Transactions on Power Delivery*, vol. 17, no. 2, pp. 555-561, 2002.

[14] R. Girgis, and K. Vedante, "Effects of GIC on power transformers and power systems," in Transmission and Distribution Conference and Exposition (T&D), 2012 IEEE PES, Orlando, FL, 2012, pp. 1-8.

[15] V. Albertson, B. Bozoki, W. Feero *et al.*, "Geomagnetic disturbance effects on power systems," *IEEE transactions on power delivery*, vol. 8, no. 3, pp. 1206-1216, 1993.

[16] T. S. Molinski, "Why utilities respect geomagnetically induced currents," *Journal of atmospheric and solar-terrestrial physics*, vol. 64, no. 16, pp. 1765-1778, 2002.

[17] D. Gubbins, and E. Herrero-Bervera, *Encyclopedia of Geomagnetism and Paleomagnetism*: Springer, 2007.

[18] R. Gummow, and P. Eng, "GIC effects on pipeline corrosion and corrosion control systems," *Journal of Atmospheric and Solar-Terrestrial Physics*, vol. 64, no. 16, pp. 1755-1764, 2002.

[19] N. Takasu, T. Oshi, F. Miyawaki *et al.*, "An experimental analysis of DC excitation of transformers by geomagnetically induced currents," *IEEE Transactions on Power Delivery*, vol. 9, no. 2, pp. 1173-1182, 1994.

[20] S. X. Guo, L. G. Liu, R. J. Pirjola *et al.*, "Impact of the EHV Power System on Geomagnetically Induced Currents in the UHV Power System," *IEEE Transactions on Power Delivery*, vol. 30, no. 5, pp. 2163-2170, 2015.

[21] R. Horton, D. Boteler, T. J. Overbye *et al.*, "A test case for the calculation of geomagnetically induced currents," *IEEE Transactions on Power Delivery*, vol. 27, no. 4, pp. 2368-2373, 2012.

[22] A. Yan, D. Zhou, and L. Marti, "Analysis of Geomagnetically Induced Currents," in 2013 IEEE Power & Energy Society General Meeting, 2013, pp. 1-6.

[23] T. J. Overbye, T. R. Hutchins, K. Shetye *et al.*, "Integration of geomagnetic disturbance modeling into the power flow: A methodology for large-scale system studies," in North American Power Symposium (NAPS), 2012, 2012, pp. 1-7.
[24] E. E. Bernabeu, "Single-Phase Transformer Harmonics Produced During Geomagnetic Disturbances: Theory, Modeling, and Monitoring," *IEEE Transactions on Power Delivery,* vol. 30, no. 3, pp. 1323-1330, 2015.
[25] N. Chiesa, A. Lotfi, H. K. Høidalen *et al.*, "Five-leg transformer model for GIC studies," 2013.
[26] P. R. Price, "Geomagnetically induced current effects on transformers," *IEEE Transactions on Power Delivery,* vol. 17, no. 4, pp. 1002-1008, 2002.
[27] H. W. Dommel, *Electromagnetic Transients Program: Reference Manual:(EMTP theory book)*: Bonneville Power Administration, 1986.
[28] H. K. Høidalen, B. A. Mork, F. Gonzalez *et al.*, "Implementation and verification of the hybrid transformer model in ATPDraw," *Electric Power Systems Research,* vol. 79, no. 3, pp. 454-459, 2009.
[29] I. Commission, "IEC 60076-1: Power Transformers," *General, ed*, 1999, p. 96.
[30] F. Bedell, "History of AC wave form, its determination and standardization," *Electrical Engineering,* vol. 61, no. 12, pp. 864-868, 1942.
[31] P. S. Georgilakis, *Spotlight on modern transformer design*: Springer Science & Business Media, 2009.
[32] "Shell type transformers - Generator step-up transformers (GSU) (Power transformers) | ABB", New.abb.com, 2018. [Online]. Available: http://new.abb.com/products/transformers/power/generator-step-up/shell-type-transformers. [Accessed: 14- Aug- 2018].
[33] V. Sankar, "Preparation of Transformer Specifications," *IEEE Southern Alberta (SAS)-IEEE PES-IAS Seminer. on*, 2012.
[34] J. H. Harlow, *Electric power transformer engineering*: CRC press, 2012.
[35] J. Salsgiver, "A comparison of CGO silicon steels, high performance domain refined silicon steels and amorphous core materials in distribution transformers by Total Ownership Cost (TOC) modeling," *Physica Scripta,* vol. 39, no. 6, pp. 775, 1989.
[36] C. Charalambous, Z. Wang, P. Jarman, and M. Osborne, "Core structure and its association with transformer susceptibility towards ferroresonance," in International Conference on Power Systems Transients, Kyoto, 2009, pp. 3-6.
[37] S. Tumanski, *Handbook of magnetic measurements*: CRC Press, 2016.
[38] Rare-earth-magnets.com, 'Permeability and Saturation', 2015. [Online]. Available: http://www.rare-earth-magnets.com/t-permeability-and-saturation.aspx. [Accessed: 25- Jun- 2015].
[39] M. Pietruszka, and E. Napieralska-Juszczak, "Lamination of T-joints in the transformer core," *IEEE transactions on magnetics,* vol. 32, no. 3, pp. 1180-1183, 1996.
[40] B. Postma, T. Vinay, T. Kangsanant *et al.*, "Electromagnetic flat-faced robot gripper for handling multiple industrial transformer core lamination plates," *IEEE Transactions on magnetics,* vol. 34, no. 3, pp. 700-707, 1998.
[41] R. Pry, and C. Bean, "Calculation of the energy loss in magnetic sheet materials using a domain model," *Journal of Applied Physics,* vol. 29, no. 3, pp. 532-533, 1958.
[42] G. Bertotti, "General properties of power losses in soft ferromagnetic materials," *IEEE Transactions on magnetics,* vol. 24, no. 1, pp. 621-630, 1988.
[43] "Power Transformer Construction – Windings", EEP - Electrical Engineering Portal, 2018. [Online]. Available: http://electrical-engineering-portal.com/power-transformer-construction-windings. [Accessed: 14- Aug- 2018].
[44] R. Girgis, K. Vedante, and G. Burden, "A process for evaluating the degree of susceptibility of a fleet of power transformers to effects of GIC," in T&D Conference and Exposition, 2014 IEEE PES, 2014, pp. 1-5.
[45] S. D. Sudhoff, *Power magnetic devices: a multi-objective design approach*: John Wiley & Sons, 2014.

[46] NERC, "Effects of Geomagnetic Disturbances on the Bulk Power Power System," February 2012.
[47] G. Lakhina, S. Alex, B. Tsurutani *et al.*, "Research on historical records of geomagnetic storms," *Proceedings of the International Astronomical Union,* vol. 2004, no. IAUS226, pp. 3-15, 2004.
[48] "NASA/Marshall Solar Physics", Solarscience.msfc.nasa.gov, 2018. [Online]. Available: http://solarscience.msfc.nasa.gov/predict.shtml. [Accessed: 14- Aug- 2018].
[49] "Spotless Days | SILSO", Sidc.oma.be, 2018. [Online]. Available: http://sidc.oma.be/silso/spotless. [Accessed: 14- Aug- 2018].
[50] R. Arlt, "The sunspot observations by Samuel Heinrich Schwabe," *Astronomische Nachrichten,* vol. 332, no. 8, pp. 805-814, 2011.
[51] M. Ghoorchian, G. Zandesh, F. Foroughian *et al.*, "Unfavorable Effect KP on Power System and Artificial Intelligent Alarm System for It," in Intelligent System Applications to Power Systems, 2009. ISAP'09. 15th International Conference on, 2009, pp. 1-5.
[52] March 13, 1989 Geomagnetic Disturbance, North American Electric Reliability Corporation Final 12 Report, www.nerc.com/files/1989-Quebec-Disturbance.pdf.
[53] T. Hutchins, "Geomagnetically induced currents and their effect on power systems," University of Illinois at Urbana-Champaign, 2012.
[54] S. Chakraborty, R. Hajra, and A. Paul, "Ionosphere near the anomaly crest in Indian zone during magnetic storm on 13-14 March 1989," *Indian J Radio Space Phys,* vol. 37, pp. 396, 2008.
[55] "National Aeronautics and Space Administration Index of/stp/geomagnetic_data/indices/Kp_Ap, "2015.
[56] V. D. Albertson, and J. A. Van Baelen, "Electric and magnetic fields at the Earth's surface due to auroral currents," *IEEE Transactions on Power Apparatus and Systems,* no. 4, pp. 578-584, 1970.
[57] A. McNish, "Magnetic storms," *Edison Electric Institute Bulletin,* 1940.
[58] L. Bolduc, A. Gaudreau, and A. Dutil, "Saturation time of transformers under dc excitation," *Electric Power Systems Research,* vol. 56, no. 2, pp. 95-102, 2000.
[59] D. Boteler, and R. Pirjola, "Nature of the Geoelectric Field Associated with GIC in Long Conductors Such as Power System, Pipelines, and Phone Cables," in IEEE International Symposium on Electromagnetic Compatibility, 1997, pp. 68-71.
[60] B. Carter, E. Yizengaw, R. Pradipta *et al.*, "Geomagnetically induced currents around the world during the 17 March 2015 storm," *Journal of Geophysical Research: Space Physics,* vol. 121, no. 10, 2016.
[61] K. Zheng, D. Boteler, R. J. Pirjola *et al.*, "Effects of system characteristics on geomagnetically induced currents," *IEEE Transactions on Power Delivery,* vol. 29, no. 2, pp. 890-898, 2014.
[62] NERC, "Benchmark Geomagnetic Disturbance Event Description ".
[63] V. D. Albertson, J. Thorson, R. Clayton *et al.*, "Solar-induced-currents in power systems: cause and effects," *IEEE Transactions on Power Apparatus and Systems,* no. 2, pp. 471-477, 1973.
[64] S. Arabi, M. Komaragiri, and M. Tarnawecky, "Effects of geomagnetically-induced currents in power transformers from power systems point of view," *Canadian Electrical Engineering Journal,* vol. 12, no. 4, pp. 165-170, 1987.
[65] A. A. Almeida, D. L. Rodrigues-Jr, L. S. Perassa *et al.*, "Anomalous loss hysteresis loop," *Materials Research,* vol. 17, no. 2, pp. 494-497, 2014.
[66] C. W. Harrison, and P. I. Anderson, "Characterization of Grain-Oriented Electrical Steels Under High DC Biased Conditions," *IEEE Transactions on Magnetics,* vol. 52, no. 5, pp. 1-4, 2016.
[67] R. M. Mathur, and R. K. Varma, *Thyristor-based FACTS controllers for electrical transmission systems*: John Wiley & Sons, 2002.
[68] P. Barnes, D. Rizy, F. Tesche *et al.*, *Electric utility industry experience with geomagnetic disturbances*, DTIC Document, 1991.

[69] V. Albertson, J. Thorson Jr, and S. Miske, "The effects of geomagnetic storms on electrical power systems," *IEEE Transactions on Power Apparatus and Systems*, no. 4, pp. 1031-1044, 1974.

[70] D. Boteler, "Geomagnetic hazards to conducting networks," *Natural Hazards*, vol. 28, no. 2-3, pp. 537-561, 2003.

[71] A. Pesonen, "Effects of solar-induced currents on power systems-a brief survey," in joint meeting of CIGRE SC 36 and SC 23, 1979, pp. 22.

[72] D. Boteler, "Space weather effects on power systems," *Space weather*, pp. 347-352, 2001.

[73] D. Beamish, T. Clark, E. Clarke *et al.*, "Geomagnetically induced currents in the UK: geomagnetic variations and surface electric fields," *Journal of atmospheric and solar-terrestrial physics*, vol. 64, no. 16, pp. 1779-1792, 2002.

[74] I. Erinmez, S. Majithia, C. Rogers *et al.*, "Application of modelling techniques to assess geomagnetically induced current risks on the NGC transmission system," *CIGRE Paper*, no. 39–304, 2002.

[75] D. Crisford, "System harmonic voltage measurements at Harker 275 kV substation," *Technical Audit Unit Report, National Grid Company, TAU*, vol. 1, pp. 92, 1992.

[76] T. Alan, A. McKay, and E. Clarke, "Surface electric fields and geomagnetically induced currents in the Scottish Power grid during the 30 October 2003 geomagnetic storm," *Space Weather*, vol. 3, no. 11, 2005.

[77] P. Persson, "Disturbances in directly earthed transmission power systems caused by geomagnetic storms," in Proceedings of the 3rd Symposium and Technical Exhibition on Electromagnetic Compatibility, 1979, pp. 13-18.

[78] "Effects of geomagnetic disturbances on the bulk power system," *North American Electric Reliability Corporation*, 2012.

[79] J. G. Kappenman, "An overview of the impulsive geomagnetic field disturbances and power grid impacts associated with the violent Sun-Earth connection events of 29–31 October 2003 and a comparative evaluation with other contemporary storms," *Space Weather*, vol. 3, no. 8, 2005.

[80] C. Liu, L. Liu, and R. Pirjola, "Geomagnetically induced currents in the high-voltage power grid in China," *IEEE Transactions on Power Delivery*, vol. 24, no. 4, pp. 2368-2374, 2009.

[81] R. Marshall, H. Gorniak, T. Van Der Walt *et al.*, "Observations of geomagnetically induced currents in the Australian power network," *Space Weather*, vol. 11, no. 1, pp. 6-16, 2013.

[82] J. Kappenman, *Mitigation of geomagnetically induced and dc stray currents. Final report*, Minnesota Power and Light Co., Duluth (USA), 1983.

[83] A. A. Fardoun, E. F. Fuchs, and M. Masoum, "Experimental analysis of a DC bucking motor blocking geomagnetically induced currents," *IEEE Transactions on Power Delivery*, vol. 9, no. 1, pp. 88-99, 1994.

[84] M. Eitzmann, R. Walling, M. Sublich *et al.*, "Alternatives for blocking direct current in AC system neutrals at the Radisson/LG2 complex," *IEEE transactions on power Delivery*, vol. 7, no. 3, pp. 1328-1337, 1992.

[85] L. Bolduc, M. Granger, G. Pare *et al.*, "Development of a DC current-blocking device for transformer neutrals," *IEEE Transactions on Power Delivery*, vol. 20, no. 1, pp. 163-168, 2005.

[86] B. Niu, R. Zeng, B. Zhang *et al.*, "Research and design of the neutral series resistor to restrain the HVDC ground current flowing into transformer," in Power System Technology, 2006. PowerCon 2006. International Conference on, 2006, pp. 1-6.

[87] J. Kappenman, S. Norr, G. Sweezy *et al.*, "GIC mitigation: a neutral blocking/bypass device to prevent the flow of GIC in power systems," *IEEE Transactions on Power Delivery*, vol. 6, no. 3, pp. 1271-1281, 1991.

[88] C. Mao, S. Wang, J. Lu *et al.*, "Measures of restraining DC current through transformer neutral point: A comprehensive survey," in Universities Power Engineering Conference, 2007. UPEC 2007. 42nd International, 2007, pp. 707-711.

[89] W. Viana, R. Micaleff, S. Young *et al.*, "Transformer design considerations for mitigating geomagnetic induced saturation," *IEEE transactions on magnetics*, vol. 35, no. 5, pp. 3532-3534, 1999.

[90] A. Rezaei-Zare, "Enhanced Transformer Model for Low- and Mid-Frequency Transients-Part II: Validation and Simulation Results," *IEEE Transactions on Power Delivery,* vol. 30, no. 1, pp. 316-325, 2015.

[91] P. Picher, L. Bolduc, A. Dutil *et al.*, "Study of the acceptable DC current limit in core-form power transformers," *IEEE Transactions on Power Delivery,* vol. 12, no. 1, pp. 257-265, 1997.

[92] A. J, L. Bolduc, C. E. Association *et al.*, *Detection of Transformer Winding Displacement by the FRSL Diagnosis Method*: Canadian Electrical Association, 1981.

[93] W. Chandrasena, P. McLaren, U. Annakkage *et al.*, "An improved low-frequency transformer model for use in GIC studies," *IEEE Transactions on Power Delivery,* vol. 19, no. 2, pp. 643-651, 2004.

[94] V. Brandwajn, H. Donnel, and I. Dommel, "Matrix representation of three-phase n-winding transformers for steady-state and transient studies," *IEEE Transactions on Power Apparatus and Systems,* no. 6, pp. 1369-1378, 1982.

[95] J. A. Martinez, and B. A. Mork, "Transformer modeling for low-and mid-frequency transients-a review," *IEEE Transactions on Power Delivery,* vol. 20, no. 2, pp. 1625-1632, 2005.

[96] P. Nunes, A. Morched, and M. T. C. d. Barros, "Analysis of generator tripping incidents on energizing nearby transformers," in International Conference on Power Systems Transients (IPST), New Orleans, USA, 2003.

[97] M. M. Duro, and R. Denis, "Parameter uncertainty assessment in the calculation of the overvoltages due to transformer energization in resonant networks," in CIGRE session proceeding, Paris, France, 2012.

[98] R. Zhang, H. Li, S. P. Ang *et al.*, "Complexity of ferroresonance phenomena: sensitivity studies from a single-phase system to three-phase reality," in High Voltage Engineering and Application (ICHVE), 2010 International Conference on, 2010, pp. 172-175.

[99] R. Zhang, J. Peng, S. Ang *et al.*, "Statistical Analysis of Ferroresonance Phenomena for 400 kV Double-Circuit Transmission Systems," in International Conference on Power Systems Transients (IPST 2011) in Delft, the Netherlands, 2011, pp. 14-17.

[100] B. A. Mork, F. Gonzalez, D. Ishchenko *et al.*, "Hybrid transformer model for transient simulation—Part I: Development and parameters," *IEEE Transactions on Power Delivery,* vol. 22, no. 1, pp. 248-255, 2007.

[101] H. K. Høidalen, B. A. Mork, D. Ishchenko *et al.*, "Implementation of the hybrid transformer model in ATP-draw."

[102] G. Slemon, "Equivalent circuits for transformers and machines including non-linear effects," *Proceedings of the IEE-Part IV: Institution Monographs,* vol. 100, no. 5, pp. 129-143, 1953.

[103] D. Boteler, and R. Pirjola, "Modelling geomagnetically induced currents produced by realistic and uniform electric fields," *IEEE Transactions on Power Delivery,* vol. 13, no. 4, pp. 1303-1308, 1998.

[104] A. Haque, J. Vaile, T. Rutkunas *et al.*, "Geomagnetic disturbance storm system impact—A transmission facility owner case study," in Power & Energy Society General Meeting, 2017 IEEE, 2017, pp. 1-5.

[105] X. Dong, Y. Liu, and J. Kappenman, "Comparative analysis of exciting current harmonics and reactive power consumption from GIC saturated transformers," in Power Engineering Society Winter Meeting, 2001. IEEE, 2001, pp. 318-322.

[106] L. Marti, J. Berge, and R. K. Varma, "Determination of geomagnetically induced current flow in a transformer from reactive power absorption," *IEEE Transactions on Power Delivery,* vol. 28, no. 3, pp. 1280-1288, 2013.

[107] Q. Tang, Z. Wang, P. I. Anderson *et al.*, "Approximation and prediction of AC magnetization curves for power transformer core analysis," *IEEE Transactions on Magnetics,* vol. 51, no. 5, pp. 1-8, 2015.

[108] R. L. Burden, and J. D. Faires, "2.2 Fixed-Point Iteration," *Numerical Analysis (3rd ed.). PWS Publishers. ISBN 0-87150-857-5,* 1985.

[109] M. Masoum, and P. Moses, "Impact of balanced and unbalanced direct current bias on harmonic distortion generated by asymmetric three-phase three-leg transformers," *IET Electric Power Applications,* vol. 4, no. 7, pp. 507-515, 2010.
[110] L. Marti, A. Rezaei-Zare, and A. Narang, "Simulation of Transformer Hotspot Heating due to Geomagnetically Induced Currents," *IEEE Transactions on Power Delivery,* vol. 28, no. 1, pp. 320-327, 2013.
[111] P. Marketos, A. J. Moses, and J. P. Hall, "Effect of DC voltage on AC magnetisation of transformer core steel," *J. Elect. Eng,* vol. 61, pp. 123-125, 2010.
[112] Q. Tang, "Investigation of Magnetic Properties of Electrical Steel and Transformer Core at High Flux Densities," 2015.
[113] K. Yamazaki, and S. Watari, "Comparison of methods to calculate iron losses caused by harmonic fields in rotating machines," in Progress in Electromagnetic Research Symposium, 2004, pp. 329-332.
[114] L. T. Mthombeni, and P. Pillay, "Core losses in motor laminations exposed to high-frequency or nonsinusoidal excitation," *IEEE Transactions on Industry Applications,* vol. 40, no. 5, pp. 1325-1332, 2004.

Appendix I

Assume two substations M and N on the map. The latitude and the longitude of Substation M equal X1 and Y1, and the latitude and the longitude of Substation N equal X2 and Y2.

The north-south distance is calculated as

$$l_{N-S} = \frac{\pi}{180} P \cdot (X1 - X2) \quad (A1.1)$$

$$P = \frac{a(1-e^2)}{(1-e^2 \sin^2 \Phi)^{1.5}} \quad (A1.2)$$

$$\Phi = \frac{X1 + X2}{2} \quad (A1.3)$$

where

P is the radius of curvature in the meridian plane

a is the equatorial radius equalling 6378.1 km

b is the polar radius equalling 6356.8 km

e is the eccentricity equalling 0.082

Φ is the average latitude of Substation M and Substation N

The west-east distance is calculated as

$$l_{W-E} = \frac{\pi}{180} Q \cdot (Y1 - Y2) \quad (A1.4)$$

$$Q = \frac{a}{\sqrt{1-e^2 \sin^2 \Phi}} \quad (A1.5)$$

where Q is the radius of curvature on the plane parallel to the latitude

Appendix II

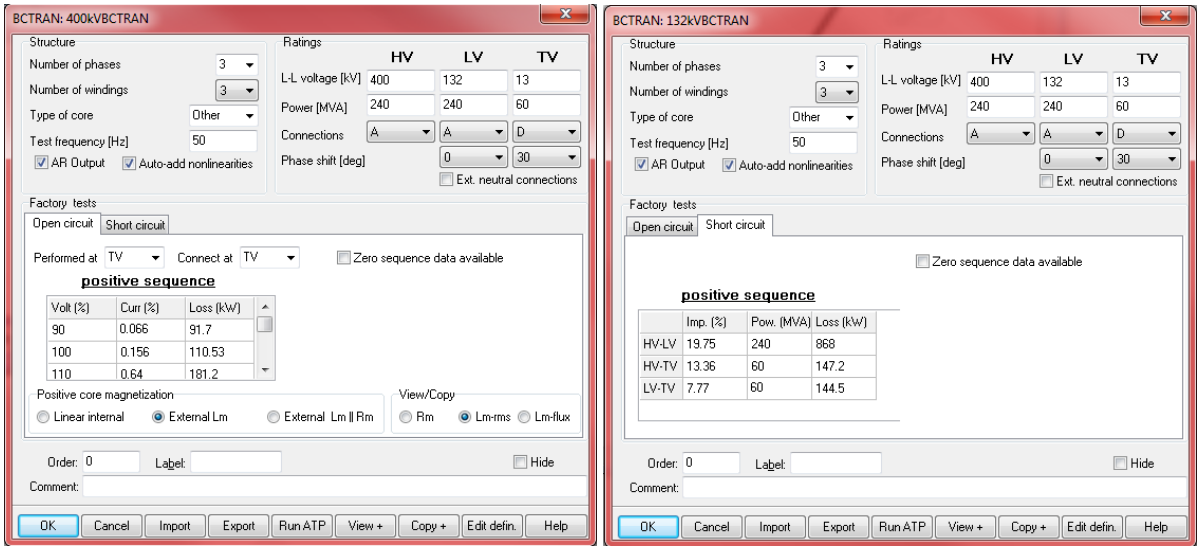

Figure.A 1: BCTRAN input interface for 400 kV transformer.

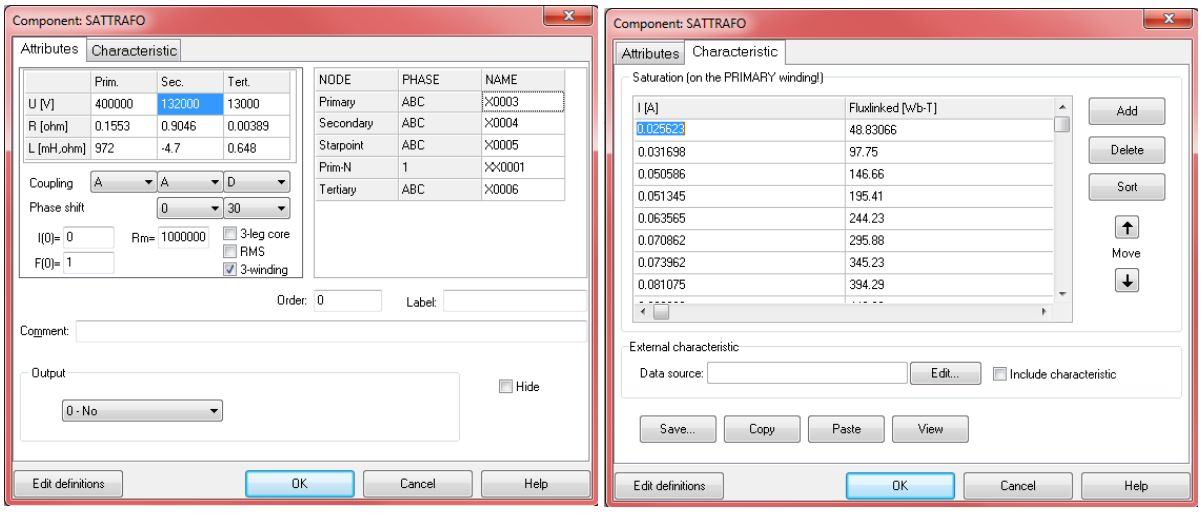

Figure.A 2: STC model input interface for 400 kV transformer.

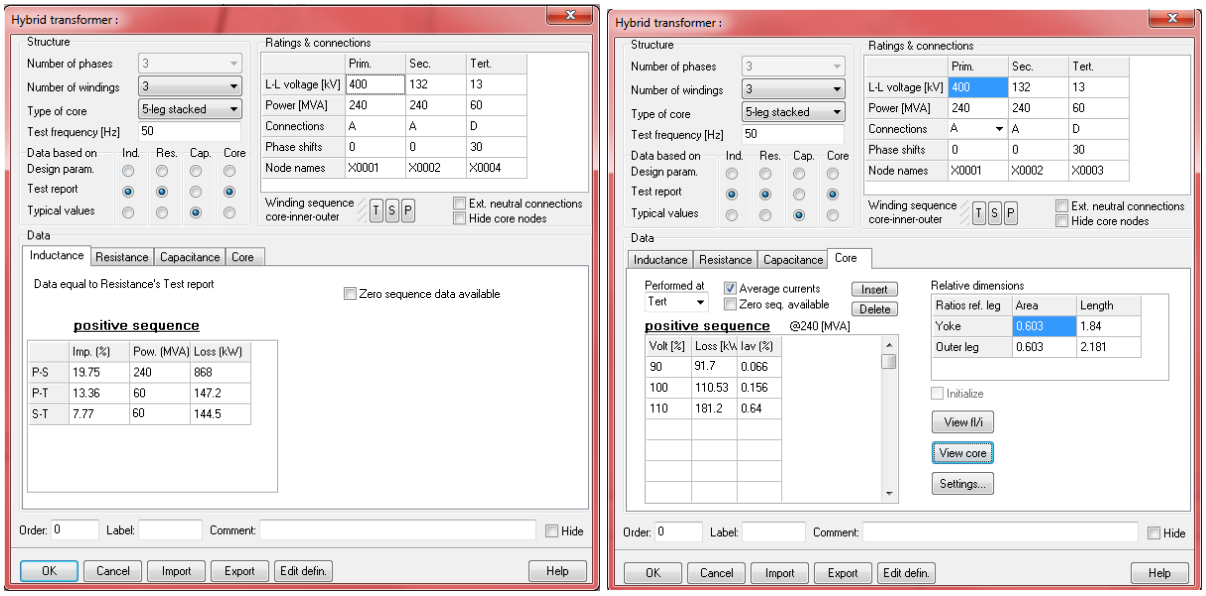

Figure.A 3: Hybrid model input interface for 400 kV transformer.

Appendix III

$S_b = 240$ MVA

$V_h = \frac{400 \text{ kV}}{\sqrt{3}}$

$V_m = \frac{132 \text{ kV}}{\sqrt{3}}$

$V_l = 13 \text{ kV}$

$X_{hm} = 19.63\%$, at 240 MVA

$X_{hl} = 12.3\%$, at 60 MVA

$X_{ml} = 6.71\%$, at 60 MVA

$X_{hm-new} = \frac{240}{240} * 19.63\% = 0.1963$

$X_{hl-new} = \frac{240}{60} * 12.3\% = 0.492$

$X_{ml-new} = \frac{240}{60} * 6.71\% = 0.2684$

$X_h = \frac{1}{2}(X_{hm-new} + X_{hl-new} - X_{ml-new}) = 0.20995$

$X_m = \frac{1}{2}(X_{hm-new} + X_{ml-new} - X_{hl-new}) = -0.01365$

$X_l = \frac{1}{2}(X_{hl-new} + X_{ml-new} - X_{hm-new}) = 0.28205$

If it is auto-transformer, the following steps need to be processed.

$r = \frac{V_h - V_m}{V_h} = \frac{400 - 132}{400} = 0.67$

$X_s = \left(\frac{1}{r}\right)^2 * X_h + \frac{1 - r}{r^2} * X_m = 0.4577$

$X_c = \frac{1}{r} * X_m = -0.02037$

$$X_t = X_l - \frac{1-r}{r} * X_m = 0.2888$$

Appendix IV

Example of bisection method:

Here is an example to calculate the answer of Eq. A4.1:

$$x^3 + 2x - 2 = 0 \qquad (A4.1)$$

Firstly, the interval starts with [0, 1] and the tolerable error is assumed as 0.01. Give function as Eq. A4.2.

$$f(x) = x^3 + 2x - 2 \qquad (A4.2)$$

The lower limit and the upper limit are named as *a* and *b*. *c* is the average value of *a* and *b*. Initially, *f(a)*, *f(b)* and *f(c)* are equal to -2, 1 and -0.875.

The following conditions need to be checked:

1. If *f(a)* f(c)<0*, the root will lie in [*a*, *c*], so give the value of *c* to *b*.
2. If *f(b)* f(c)<0*, the root will lie in [*c*, *b*], so give the value of *c* to *a*.

And then, the iteration process is repeated by updating new values of *a* and *b*.

Table.A1 shows the entire iteration procedure of bisection method:

Table.A.1: Iteration calculation process of bisection method.

Iteration	*a*	*b*	*c=(a+b)/2*	*f(a)*	*f(b)*	*f(c)*	swap	new *b-a*
1	0	1	0.5	-2	1	-0.875	a=c	0.5
2	0.5	1	0.75	-0.875	1	-0.0781	a=c	0.25
3	0.75	1	0.875	-0.0781	1	0.4199	b=c	0.125
4	0.75	0.875	0.8125	-0.0781	0.4199	0.1614	b=c	0.0625
5	0.75	0.8125	0.7813	-0.0781	0.1614	0.0395	b=c	0.0313
6	0.75	0.7813	0.7656	-0.0781	0.0395	-0.0199	a=c	0.0156
7	0.7656	0.7813	0.7734	-0.0199	0.0395	0.0096	b=c	0.0078
8	0.7656	0.7734	0.7695	/	/	/	/	/

Therefore, the root of Equation Eq. A4.1 is 0.7695 when the tolerable error is 0.01. An increase of the iteration times will improve the accuracy of the calculated root.

Appendix V

- **Core loss modelling**

The total core losses are divided into the losses caused by fundamental AC flux and DC flux and the losses produced by high order harmonics flux [113]. For this reason, the frequency spectrum calculation of the flux density is required for each calculation step for the core loss calculation.

The core losses of the transformer core material for fundamental AC flux accompanied with an external DC offset are measured by Cardiff University [66, 111, 114]. An exponential function is assumed in order to obtain the empirical equation for the core losses associated with fundamental AC flux and DC flux. The form of the exponential function is shown as Eq. A5.1.

$$P = a_1 \cdot e^{a_2 \cdot B_{AC} + a_3 \cdot B_{DC}} + a_4 \cdot e^{a_5 \cdot B_{AC}} + a_6 \cdot e^{a_7 \cdot B_{DC}} + a_8 \qquad (A5.1)$$

where

P	Core losses produced by fundamental AC and DC flux (W/kg)
$a_n (n = 1 \text{ to } 8)$	Constant
B_{AC}	Fundamental AC flux density (T)
B_{DC}	DC flux density (T)

Figure.A4 shows the core losses associated with fundamental AC flux and DC flux. The AC flux ranges from 0.5 T to 2.0 T, while the maximum DC flux density flux is 1.5 T. As shown in Figure.A5, the residuals of 80 points for the fitted model are returned as a vector. The error of the equation can be well controlled within the range of 0.11 W/kg. The value is reasonable when the transformer operates in high flux region.

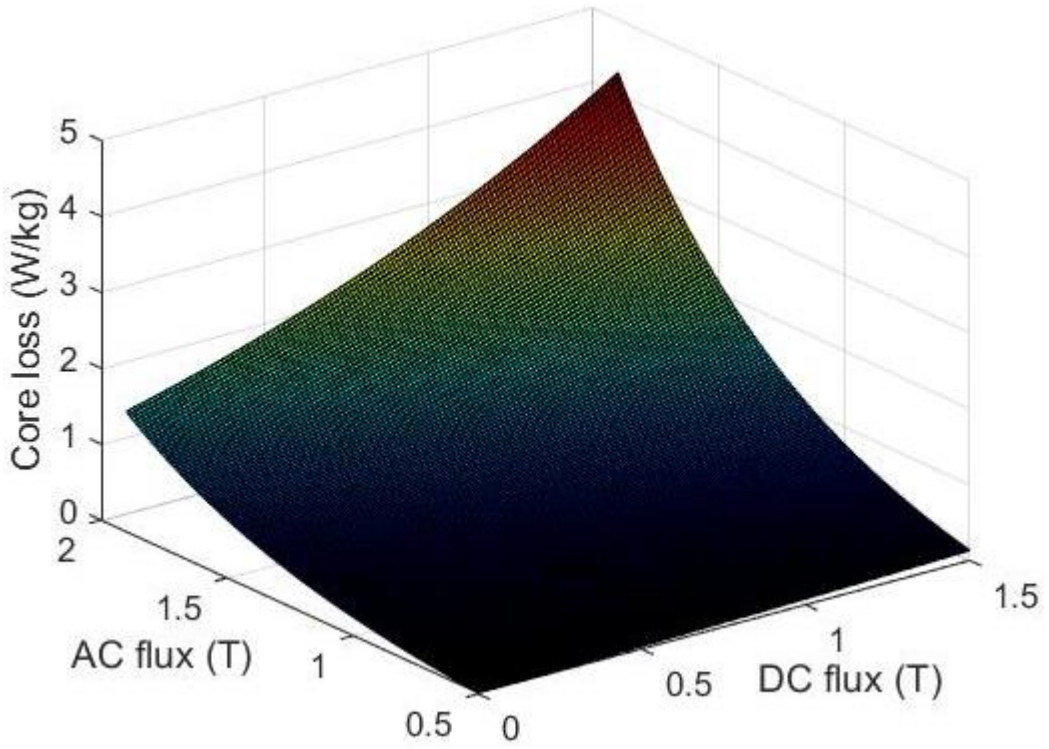

Figure.A4: Power losses caused by nominal AC and DC flux.

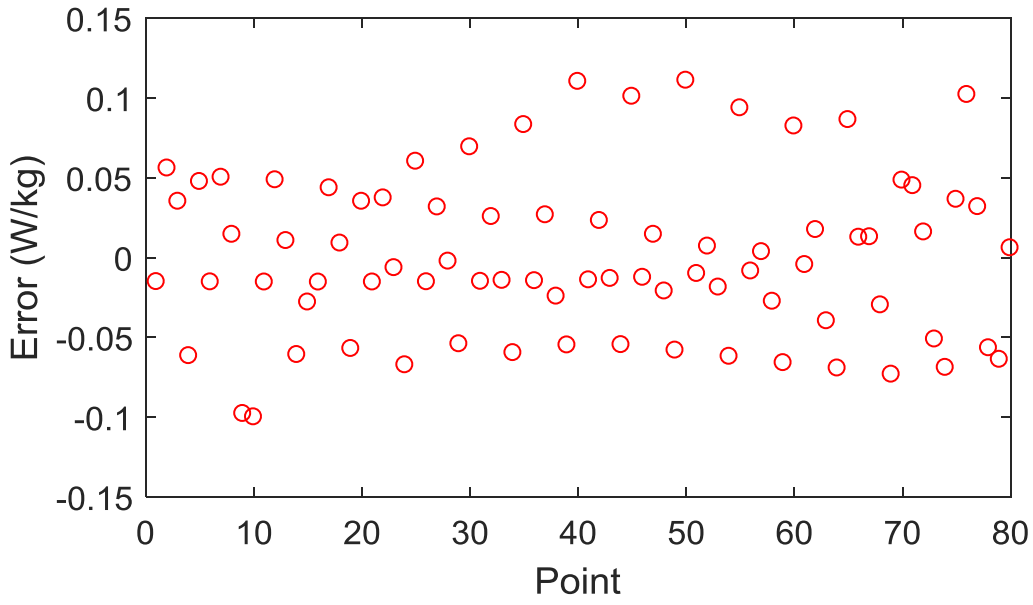

Figure.A5: Error of core losses curve fitting.

The core losses produced by high order harmonic flux, including the hysteresis loss, eddy current loss and anomalous loss, need to be calculated separately. The equations to calculate the typical core losses are shown as Eq. A5.2 –Eq. A5.5.

$$P_{harmonics} = P_{hys} + P_{eddy} + P_{anomalous} \quad (A5.2)$$

$$P_{hys} = k_h f B^n \quad (A5.3)$$

$$P_{eddy} = k_e f^2 B^2 \quad (A5.4)$$

$$P_{anomalous} = k_a f^{1.5} B^{1.5} \quad (A5.5)$$

where

P_{hys}	Hysteresis loss (W/kg)
k_h	Hysteresis loss factor, $k_h = 3.3\text{e} - 4$
B	Flux density (T)
n	Constant
P_{eddy}	Eddy current loss (W/kg)
k_e	Eddy current loss factor, $k_e = 2.7\text{e} - 5$
$P_{anomalous}$	Anomalous loss (W/kg)
k_a	Anomalous loss factor, $k_a = 8.1\text{e} - 4$

The total core loss can be calculated as the sum of these two parts at each time step. The core loss thus can be applied to calculate the temperature rise due to the core saturation during GMD events.

- **Core temperature rise**

The Figure.A6 shows the temperature rise curve in the flitch plate within 150 min under a step-up neutral DC injection up to 200 A provided by the Finnish Grid test, and the new model can calculate the steady state core losses based on the DC input. Since the neutral DC current input keeps steady for a long period at each level, the time constant of the core saturation time is much lower compared to the time constant of the temperature rise curve, thus the power loss curve can be assumed as square wave in this case. In this way, the function of the temperature rise curve under different level of power losses can be calculated Eq. A5.6. The parameters b, c and d are associated with core losses, and their functions need to be derived from the core losses and temperature values in Figure.A6.

$$T = b \cdot e^{-c \cdot t} + d \qquad (A5.6)$$

where

T	Temperature (℃)
t	Time (min)
b, c and d	Parameters associated with core loss P
P	Core loss (W/kg)

The slope of the temperature curve then can be calculated Eq. A5.7.

$$T' = -bc \cdot e^{ln\left(\frac{T-d}{b}\right)} = -cT + cd \qquad (A5.7)$$

This calculation method allows the temperature rise during a short time interval based on the instant core temperature and the core losses. The parameter c is the time constant of the temperature rise curve and d is the steady state temperature. When the time interval is small enough, the core temperature change can be simulated by the new transformer model according to the electric field produced by the GMD events.

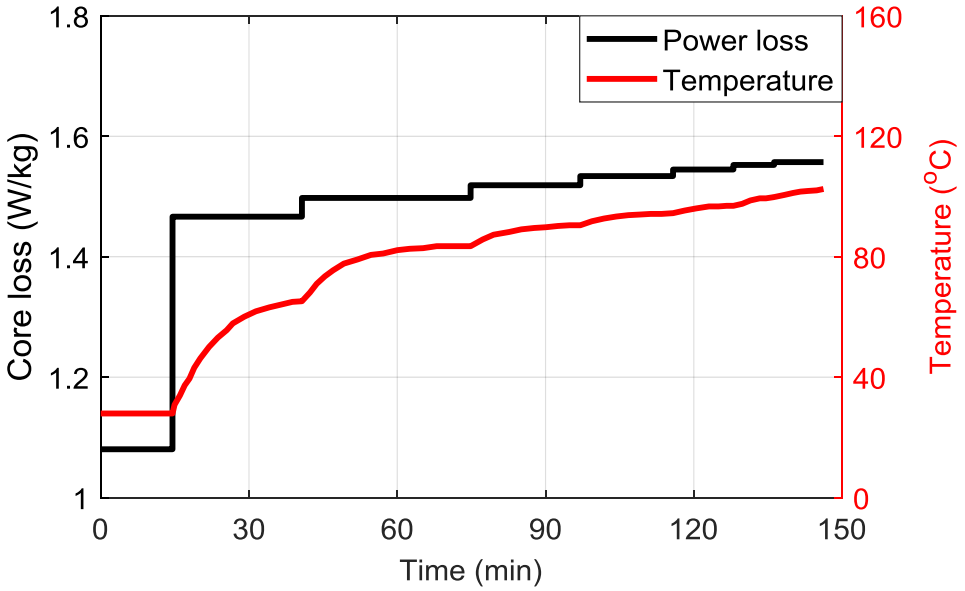

Figure.A6: Transformer flitch plate temperature rise by Finnish Grid measurement and the power loss at each step [13].

Appendix VI

Published IEEE Power & Energy Society General Meeting paper on GIC simulation for part of National Grid transmission system

GIC Simulation Study for Part of UK Transmission System by ATP/EMTP

Y.F. Ni, Z.D. Wang
University of Manchester,
Manchester M13 9PL, UK

P. Jarman
National Grid,
Warwick CV34 6DA, UK

2017

IEEE Power & Energy Society General Meeting 2017, Chicago, US

Published

GIC Simulation Study for Part of UK Transmission System by ATP/EMTP

Y.F. Ni, Z.D. Wang
University of Manchester,
Manchester M13 9PL, UK

P. Jarman
National Grid,
Warwick CV34 6DA, UK

***Abstract*—This paper introduces a network transient simulation study for the UK South-West Peninsula transmission system using the transient software ATP/EMTP. Assume that the system suffers a geomagnetic disturbance with a constant 5 V/km Southwest-Northeast electric field, severities of the GIC in terms of steady state DC current magnitude, extra reactive power losses experienced and time to reach steady state by transformers in the system were firstly quantified. Using typical field waveform in IEEE guide, real-time GIC effects on transformers were simulated to illustrate the importance of transient study, which gave more realistic GIC current magnitudes and extra reactive power losses. The system simulation also revealed that at the same substation the 5-limb transformers are more vulnerable to GIC than 3-limb transformers; and the tertiary delta winding delays the core saturation and results in a lower reactive power loss. It is validated that the GIC level suffered by individual transformer is determined by multiple factors including the location of the substation; the characteristic of the load; the direction, magnitude and waveform of the quasi-DC electric field.**

***Index Terms*—Geomagnetically induced current (GIC), geomagnetic disturbance (GMD), power system analysis, transformer core saturation, transient simulation**

I. Introduction

The geomagnetic disturbance (GMD) and geomagnetically induced current (GIC) have been an interest of investigation since 1960s. When the solar activity maxima occur in every 11 years, the high energy plasmas emitted from the sun reach the earth and impact the magnetic field in the earth atmosphere [1, 2]. Quasi DC geomagnetic fields with the frequency generally below 1Hz are induced within the surface of the earth by the changing magnetic field, leading to the quasi DC current flowing into the transmission lines via transformer neutral points. High-level harmonics are produced by the saturated transformer core due to the DC current flow, which has potential to cause mal-operation of relays and tripping of the Static VAR Compensators. A great deal of reactive power is consumed by the transformers, which could further contribute to a voltage drop in the power system.

The GIC study for a large power system was simulated by a full-node DC model, which simplified the transformers, transmission lines and neutral grounds as constant resistances [3, 4]. Using this method, the GIC current could be calculated at each branch of the system. The reactive power losses of transformers were estimated by empirical functions controlled by the terminal voltage and GIC level [5, 6]. In this way GIC severities at different locations of the system could be evaluated, although its accuracy is hugely dependent upon the constant used in empirical functions.

The transient simulations of small-scale power system with detailed transformer models were able to deliver more accurate results on the transformer performance under GMD events [7, 8]. Simulation could re-produce the transient process of how the quasi-DC currents, flow via the transformer windings and push core into saturation; and transformer harmonics, reactive power demand, and voltage drop could be simulated in real-time.

In this paper, the regional UK South-West Peninsula transmission system network was built in the ATP/EMTP. The Hybrid Transformer Model considers the core topology and the magnetizing characteristics, so it is applicable to solve the transformer core half-cycle saturation problem caused by GIC [9]. The GIC was simulated by injecting the real-time quasi DC voltage calculated by the electric field and substation geography location. To quantify the factors influencing transformers' GIC risks in the network, the GIC current, the transformer primary side voltage drop and the extra reactive power consumption by the transformer were calculated under constant and time varying DC electric fields respectively. In addition, the sensitivity study was carried out on the transformer core type, transformer winding connection and the electric field characteristics.

II. Power System Specifications

In Figure 1, part of the UK South-West Peninsula transmission system to be simulated was composed of 11 substations, being connected by 400 kV double circuit transmission lines. As listed in Table I [10], two categories of lines were applied in this regional system. The rest of the system was represented by two equivalent AC source and equivalent line impedances. The power station F was simulated as an AC source connected with three generator step-up transformers (GSU) modelled by BCTRAN. The interconnected transformers at all substations were autotransformers (400/132/13 kV, 240 MVA, YNa0d11), and these transformers were simulated using Hybrid Transformer Model whose parameters were set based on transformer test reports (Hence the tank effect under core deep saturation status is not explicitly considered in this study). Table II provides the transformer T number and substation load. In the network, only T1, T9 and T10 are 5-limb core transformers, while the rest are

3-limb core transformers. The grounding resistances for the transformers simulated are all assumed to be 0.1 Ω, although it is recognized that the actual values could be varied depending on several factors and a sensitivity study is deemed necessary for future work. The system load, represented by constant resistor and reactor in series, was added at each substation at 132 kV side based on actual local demands. In addition, three capacitor banks were located at Substation A, B and K respectively.

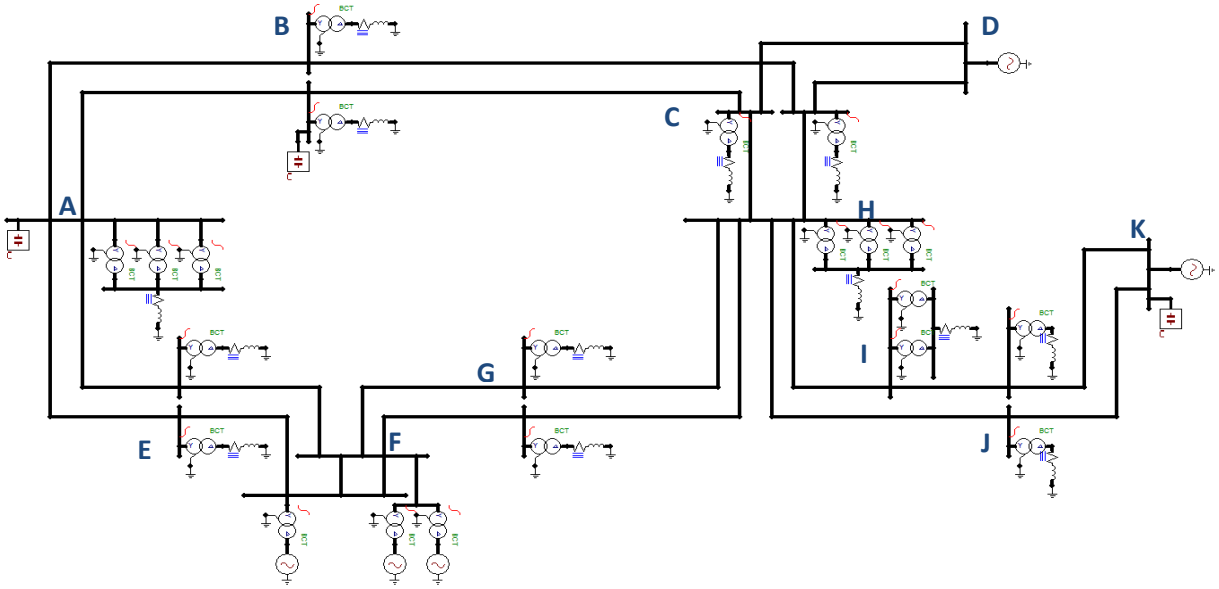

Fig. 1. Scheme diagram of the UK South-West Peninsula transmission system

TABLE I
TRANSMISSION LINE INFORMATION

Conductor name	Material	Outer radius (mm)	AC resistance (Ω/km)
Z=ZEBRA	ACSR	14.31	0.0684
RB=RUBUS	AAAC	15.75	0.0558

TABLE II
SUBSTATIONS, TRANSFORMERS AND SUPPLIED LOAD

Substation	T number	P (MW)	Q (MVar)	R(Ω) @132 kV	L(mH)/ C(μF)@ 132kV
A	**T1-T3**	**316**	**138**	**44.05**	**61.25 mH**
B	**T4-T5**	**188**	**-39**	**101.2**	**151.62 μF**
C	**T6**	**213**	**68**	**66.90**	**67.98 mH**
E	**T7-T8**	**232**	**74**	**65.65**	**66.65 mH**
G	**T9**	**124**	**1.2**	**143.5**	**4.42 mH**
	T10	**128**	**-9.0**	**140.7**	**332.81 μF**
H	**T11-T13**	**331**	**77**	**49.56**	**36.70 mH**
I	**T14**	**209**	**89**	**61.24**	**83.11 mH**
J	**T15**	**52**	**26**	**272.00**	**432.90 mH**
	T16	**52**	**26**	**274.00**	**436.08 mH**

III. INPUT VOLTAGE PARAMETER SETTING

The electric field in this paper was assumed to be in southwest to northeast direction with the angle of 45 ˚. The DC voltage drop was calculated as

$$\Delta V = \overrightarrow{E_{N-S}} * \overrightarrow{L_{N-S}} + \overrightarrow{E_{W-E}} * \overrightarrow{L_{W-E}} \quad (1)$$

where $E_{N\text{-}S}$ is the North-South electric field (V/km), $E_{W\text{-}E}$ is the West-East electric field (V/km), $L_{N\text{-}S}$ is the distance in North-South direction, $L_{W\text{-}E}$ is the distance in West-East direction.

The worst GIC event in human's history caused a wide-range electrical blackout on March 13th 1989 in Quebec Canada, and an electrical field of 5-10 volts per mile was estimated during this event as introduced in [11]. In the UK, the surface electric field reached 5 V/km during the geomagnetic disturbance on 30th October 2003 [12]. The electric field as high as 4 V/km was detected for more than 10 minutes in the UK [13].

Once the latitude and the longitude of the substations were given, the distance between adjacent substations in North-South direction and West-East direction could be calculated respectively as in [4]. Finally, the voltage drops among substations could be obtained by (1).

In this paper, Substation D was selected as the DC voltage reference point, and the neutral DC voltage values at the other substations were determined by the voltage drop. There is no influence on the GIC simulation results when changing the reference point.

IV. Simulation Results

A. Simulation under constant electric field of 5 V/km

In this section, a constant 5 V/km electric field in southwest to northeast direction was applied onto the network. During the GMD events, the DC flux tends to accumulate in the transformer core gradually and the simulation time lasts until the GIC flow and the transformer power consumption reaches stable values.

Table III shows the DC voltage established at the substation with the reference of Substation D, the steady state GIC current and extra reactive power loss of the transformer, and the time for the transformer to reach the GIC steady state respectively. The time to reach the steady state is defined as the time for the extra reactive power loss to reach 95% of its steady state value. The magnitude of DC voltage does not have a direct relevance to the severity of GIC current; instead the magnitude of transformer neutral GIC current largely depends on the location of substation, the direction and the length of the line, and the direction and magnitude of the electric field. Generally, the higher the GIC current, the larger the extra reactive power loss and the faster the saturating speed will be for an individual transformer.

TABLE III
Simulation results under a constant 5 V/km electric field

Sub-station	T number	DC voltage (V)	Neutral DC current (A)	Extra reactive power loss (MVar)	Saturation time (s)
A	T1	760.04	61.92	19.44	26.20
	T2		62.71	19.78	43.94
	T3		62.71	19.78	43.94
C	T6	81.47	-56.13	16.85	52.11
I	T14	111.25	-18.91	5.39	101.16
J	T15	65.48	18.11	5.87	152.58
	T16		17.11	5.55	153.20
H	T11	238.53	13.97	4.28	97.12
	T12		13.97	4.28	97.12
	T13		13.97	4.28	97.12
B	T4	329.31	-14.01	4.43	67.25
	T5		-14.01	3.49	69.73
E	T7	575.44	-7.32	2.08	154.28
	T8		-7.32	2.08	160.01
G	T9	436.42	2.61	2.82	48.50
	T10		2.62	2.70	31.44

The simulation results showed that transformers at Substation A are seen as the ones most at risk. T1 is a 5-limb transformer which failed in 1989 during the geomagnetic disturbance at another substation in this region and was subsequently repaired and reinstalled at Substation A. Under the current simulation scenario, the neutral GIC current of T1 reached 61.92 A whilst its extra reactive power loss reached 19.44 MVar. It took 26.20 s for T1 to reach such a steady state after the electrical field was applied. On the other hand, T2 and T3 had similar neutral GIC current and extra reactive power loss but much longer time to reach steady state (43.94 s). The reason why T1 was saturated much faster than T2 and T3 is that T1 is a 5-limb transformer which is more sensitive to GIC than T2 and T3 (3-limb transformer). However a 3-limb transformer is not necessarily immune to GIC, because the tank and the air gap are able to provide the valid paths for DC flux [14]. At Substation G, T9 was supplying inductive load whilst T10 capacitive load, T9 and T10 had very similar neutral GIC currents and extra reactive power losses, however the time to reach steady state for T9 and T10 were 48.50 s and 31.44 s respectively. This difference could only be caused by the load type.

B. Simulation under time varying electric field with maximum value of 5V/km

In reality quasi DC geomagnetic fields are induced during a GMD event, hence a time varying electric field should be used to validate the importance of real-time simulation. The typical field waveform in IEEE guide [1] was taken as an example and its maximum value is set at 5 V/km as shown in Figure 2, 3 and 4. The corresponding time varying DC voltages were injected into the system and simulate results were obtained. Three transformers, T1, T6 and T11 were used as examples to present high, medium and low saturation rate experienced by the transformers in the network.

Figure 2 provides the time varying electric field, the neutral GIC current and the extra reactive power consumed by T1. Because the GMD event at the maximum electrical field of 5 V/km only lasted for 16 s, which is shorter than the time constant of 26.20 s identified in the previous steady state simulation scenario, the peak of the extra power loss of T1 only reached 16.41 MVar. The steady state extra power loss of T1 for a constant electrical field of 5 V/km was 19.44 MVar as shown in Table III.

Figure 3 provides the time varying electric field, the neutral GIC current and the extra reactive power consumed by T6. T6 saturated much slower than T1, so the extra reactive power consumption reached only 1.94 MVar at 16 s. With electrical field reducing to 3.5 V/km, then 1.75 V/km and then reaching back to 3.5 V/km, the core continued to increase in saturation level and finally reached its peak value of 8.10 MVar at 84 s, which is much lower than the value of the 5 V/km steady state shown in Table III. Note that the time to reach steady state at a constant electrical field of 5 V/km was 52.1 s, and the lower the magnitude of electrical field, the longer the time to reach steady state. Figure 4 provides the time varying electric field, the neutral GIC current and the extra reactive power consumed by T11. The time to reach steady state for T11 at the constant electrical field of 5 V/km was 97.12 s, and it is apparent that the lower the magnitude of electrical field, the longer the time to reach steady state. The DC flux bias kept rising regardless of the fluctuation of the electric field, and the maximum extra reactive power loss occurred at 120 s with 0.92 MVar as shown in Figure 4, in contrast to the steady state value of 4.28 MVar under constant 5 V/km field shown in Table III.

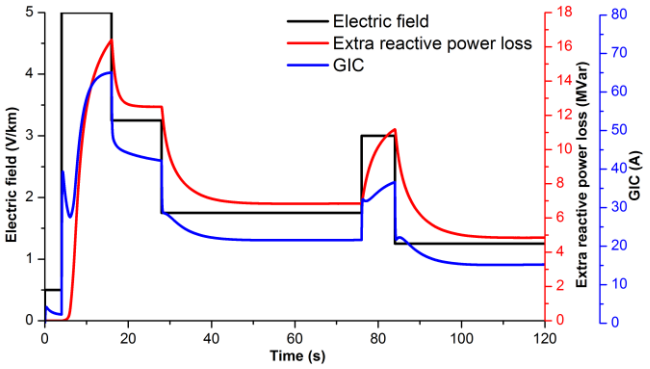

Fig. 2. Neutral GIC and extra reactive power loss for T1 under a time varying electric field

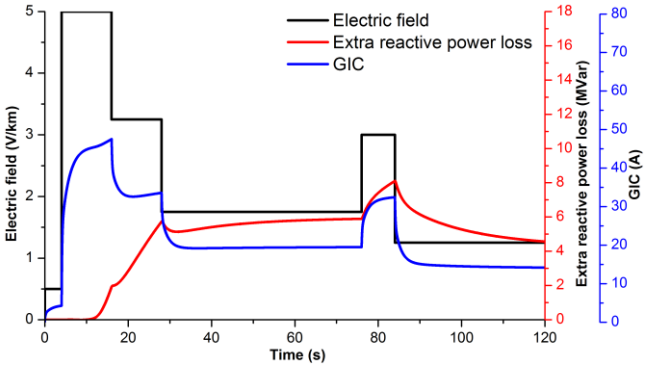

Fig. 3. Neutral GIC and extra reactive power loss for T6 under a time varying electric field

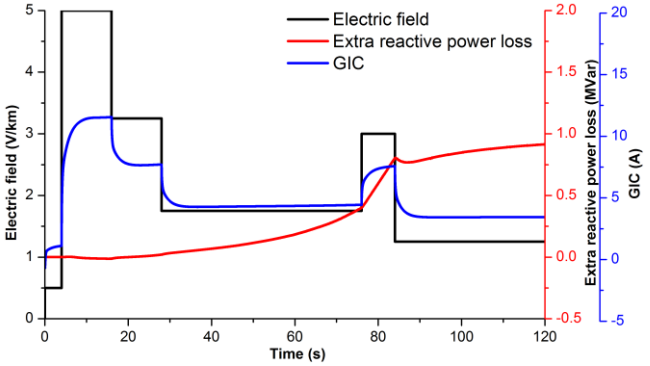

Fig. 4. Neutral GIC and extra reactive power loss for T11 under a time varying electric field

The above results for extra power loss are significantly different from those under constant electrical field simulation, demonstrating the importance of transient simulation.

C. Effect of transformer structure

The effect of transformer core and winding structure on GIC was studied by replacing T6 (a 3-limb YNa0d11 autotransformer installed at Substation C) by a 3-limb YNa0 two-winding transformer or a 5-limb YNa0d11 three-winding transformer respectively, whilst the rest of the parameters was kept the same. Figure 5 shows the extra reactive power losses calculated for the 3-limb core transformers with or without delta winding, and the 5-limb core transformer with delta winding under the time varying electric field.

The simulation results illustrate that the delta winding is able to both significantly decelerate the saturation speed and reduce the saturation level, because the delta winding allows the zero sequence components flow before the core is fully saturated. The 3-limb core structure leads to a slower saturation process as well as a lower peak extra reactive loss absorbed by transformer, because of the large reluctance for the zero sequence flux paths, which are composed of tank and air gaps. The simulation demonstrated that the 3-limb core transformer with delta winding would be the best transformer structure to endure time varying GIC events.

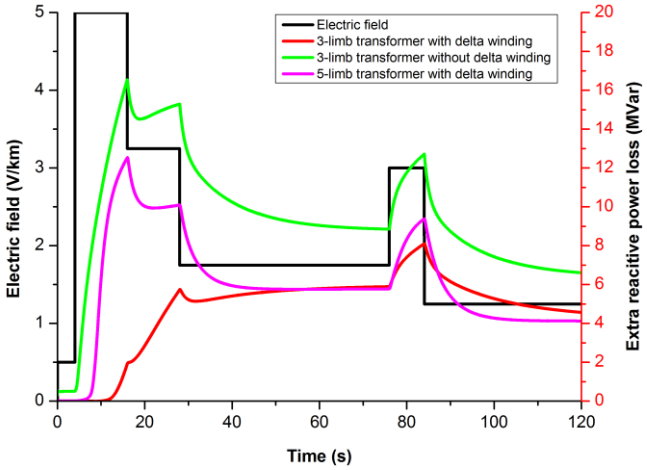

Fig. 5. Effect of core and winding on extra reactive power loss for T6 under a time varying electric field

D. Sensitivity study of electrical field level

The electric field waveform is set as the same as the one used in Figure 2, but the maximum magnitudes were changed to 2.5 V/km, 7.5 V/km or 10 V/km respectively to redo the simulation. Transformer T1 is used as an example to show the sensitivity study results in Table IV, the peak GIC neutral current was almost proportional to the electric field magnitude due to the constant line and transformer winding resistances. The increases of the maximum extra reactive power loss and maximum voltage drop were almost proportional to the increase of the electrical field level.

TABLE IV
SIMULATION RESULTS WITH DIFFERENT MAGNITUDE OF ELECTRIC FIELD INPUT OF TRANSFORMER T1

Max Electric field	Peak GIC neutral current (A)	Max extra reactive power loss (MVar)	Max voltage drop (pu)
2.5V/km	**32.81**	**7.65**	**0.52%**
5V/km	**65.06**	**16.41**	**1.11%**
7.5V/km	**95.42**	**24.76**	**1.84%**
10V/km	**125.81**	**33.11**	**2.74%**

E. Sensitivity study of electric field waveform

As shown in Figure 6, the reverse of electric field to -3.25 V/km occurred in the duration between 4 s to16 s and

the rest of electric field remained the same as the previously applied one. In this case, when the electric field was reversed, the DC flux bias was reversed, and it took a few seconds delay for the core to go into saturation due to the effect of delta tertiary winding. Once the DC flux was established and continuously grew, the core was pushed into saturation and the extra reactive power loss increased again to 13.28 MVar at 28 s, less than the peak extra reactive power loss of 16.41 MVar in Figure 2. In a real GIC event, positive and negative values for real-time electric field exist and alternate, so it is essential to consider the effect of the reversed electric field and various controlling parameters made of resistances, leakage inductances, core characteristics and zero sequence flux paths. Therefore, the real-time transient simulation should be applied. It should be noted for the GIC current to reach steady state, core saturation is of necessity.

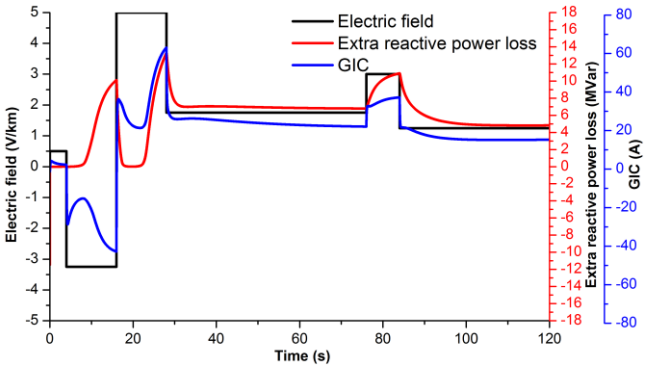

Fig. 6. Effect of the time varying electric field waveform on extra reactive power loss for T1

V. Conclusion

In this paper, part of the UK Southwest Peninsula transmission system was simulated in the ATP/EMTP transient software, which provided a simulation method that enables to consider the core saturation process of individual transformer under GMD events. The core saturation states of individual transformers were able to be monitored, and GIC risks of all the transformers could be analyzed under the time varying electric field.

Under a constant electric field in Southwest-Northeast direction, the transformers operating at substation A and C were the most vulnerable to this electric field. The GIC risks for individual transformers are caused by several factors: the geographic location of substation, the direction and the length of the line, and the direction and magnitude of the electric field, the core structure of the transformer, the delta winding and the characteristic of the load at the secondary side.

While the network was under a time varying electric field, the extra reactive power loss waveforms largely depended on the transformer core saturation level and saturation speed. The sensitivity study was carried out to investigate how the transformer structure may affect its endurance to GIC. The results revealed that the 3-limb core transformer is not as claimed previously, to be immune to GIC due to the accessible flux zero sequence paths provided by the tank and the air gap. However the 3-limb core transformers with delta winding have the best performance in defending against GMD events.

A linear relationship could be found between maximum GMD electric field magnitude and the peak GIC neutral current, the increase of the maximum extra reactive power loss experienced by the transformer and the maximum voltage drop. Furthermore, the simulation results demonstrated that the impacts of electric field waveform were noticeable to transformer saturation status even if the peak electric field was kept the same, it is therefore necessary to conduct network transient study to obtain realistic transformer GIC performance during the GMD events.

VI. References

[1] "IEEE Guide for Establishing Power Transformer Capability while under Geomagnetic Disturbances," *IEEE Std C57.163-2015*, pp. 1-50, 2015.

[2] "Geomagnetic Disturbances: Their Impact on the Power Grid," *IEEE Power and Energy Magazine*, vol. 11, pp. 71-78, 2013.

[3] S. X. Guo, L. G. Liu, R. J. Pirjola, K. R. Wang, and B. Dong, "Impact of the EHV Power System on Geomagnetically Induced Currents in the UHV Power System," *IEEE Trans on Power Del.*, vol. 30, pp. 2163-2170, 2015.

[4] R. Horton, D. Boteler, T. J. Overbye, R. Pirjola, and R. C. Dugan, "A test case for the calculation of geomagnetically induced currents," *IEEE Trans on Power Del.*, vol. 27, pp. 2368-2373, 2012.

[5] A. Yan, D. Zhou, and L. Marti, "Analysis of Geomagnetically Induced Currents," in *Proc. IEEE/Power Eng. Soc. Conf.*, 2013, pp. 1-6.

[6] T. J. Overbye, T. R. Hutchins, K. Shetye, J. Weber, and S. Dahman, "Integration of geomagnetic disturbance modeling into the power flow: A methodology for large-scale system studies," in *North American Power Symposium (NAPS), 2012*, pp. 1-7.

[7] E. E. Bernabeu, "Single-Phase Transformer Harmonics Produced During Geomagnetic Disturbances: Theory, Modeling, and Monitoring," *IEEE Trans. on Power Del.*, vol. 30, pp. 1323-1330, 2015.

[8] N. Chiesa, A. Lotfi, H. K. Høidalen, B. Mork, Ø. Rui, and T. Ohnstad, "Five-leg transformer model for GIC studies," in *Proc. IPST*, 2013.

[9] H. K. Høidalen, B. A. Mork, F. Gonzalez, D. Ishchenko, and N. Chiesa, "Implementation and verification of the hybrid transformer model in ATPDraw," *Electric Power Systems Research*, vol. 79, pp. 454-459, 2009.

[10] "Electrical parameters and impedance characteristics of plant, " National Grid technical guidance note, 2002.

[11] J. Douglas, "A storm from the sun," *IEEE Power Engineering Review*, vol. 9, pp. 11-13, 1989.

[12] A. W. P. Thomson, A. J. Mckay, E. Clarke, and S. J. Reay, "Surface Electric Fields and Geomagnetically Induced Currents in the Scottish Power Grid during the 30 October 2003 Geomagnetic Storm," Space Weather, vol. 3, p. S11002, 2005.

[13] D. Beamish, T. Clark, E. Clarke, and A. Thomson, "Geomagnetically induced currents in the UK: geomagnetic variations and surface electric fields," *Journal of atmospheric and solar-terrestrial physics*, vol. 64, pp. 1779-1792, 2002.

[14] A. Rezaei-Zare, "Enhanced Transformer Model for Low- and Mid-Frequency Transients-Part II: Validation and Simulation Results," *IEEE Trans. on Power Del.*, vol. 30, pp. 316-325, 2015.

Appendix VII

Publication list:

1. Y.F. Ni, Z.D. Wang and P. Jarman, "GIC simulation study for part of UK transmission system by ATP/EMTP," *2017 IEEE Power & Energy Society General Meeting*, Chicago, IL, 2017, pp. 1-5.
2. Y.F. Ni, Z.D. Wang and P. Jarman, "Transformer magnetic models for investigating core saturation process during geomagnetic disturbances," 20th International Symposium on High Voltage Engineering (ISH), Buenos Aires, Argentina, 2017.
3. Y.F. Ni, X. Zhang, Z.D. Wang and P. Jarman, "Transformer modelling for geomagnetically induced current studies," submitted to IEEE Transactions on Power Systems
4. Y.F. Ni, X. Zhang, Z.D. Wang and P. Jarman, "Modelling of core losses and temperature rises in transformers caused by geomagnetically induced current," to be submitted to IEEE Transactions on Power Systems